Summer 7-1-2022

Evaluation of the Energetic Factors in Crystalline Pharmaceuticals Using Solid-state Density Functional Theory and Low-frequency Vibrational Spectroscopy

Margaret P. Davis
Syracuse University

Recommended Citation

Abstract

Due to the importance of maintaining stable and effective pharmaceutical solid doses, it is critical to study the variety of solid forms that active pharmaceutical ingredients can adopt including polymorphs, hydrates, and cocrystals. In this work, low-frequency vibrational spectroscopies and rigorous quantum mechanical simulations are combined to provide a new technique for characterizing and investigating pharmaceutically relevant polymorphs, hydrates, and cocrystals as well as a series of model cocrystals.

Low-frequency spectra in the sub-200 cm^{-1} range provide not only unique and characteristic spectra for all of the systems explored here but, along with X-ray structural parameters, they offer a way to benchmark computational models and ensure that the models are fully capturing essential components such as the packing arrangement and the intermolecular forces present. Accurate quantum mechanical simulations allow us to determine the exact motions associated with specific low-frequency vibrational modes and this work demonstrates that large pharmaceuticals, including ones with multiple species like cocrystals, can be successfully modeled with solid-state density functional theory. Solid-state density functional theory also delivers a way to investigate how the conformations of molecules differ between polymorphs and how manipulation of the hydrogen bonding network of a solid may affect the overall stability. By studying the intermolecular forces present in the different forms, insights into stability can be made to aid future pharmaceutical crystal engineering endeavors.

EVALUATION OF THE ENERGETIC FACTORS IN CRYSTALLINE
PHARMACEUTICALS USING SOLID-STATE DENSITY FUNCTIONAL THEORY AND
LOW-FREQUENCY VIBRATIONAL SPECTROSCOPY

by

Margaret P. Davis

B.S., State University of New York at Geneseo, 2017
M. Phil., Syracuse University, 2019

Dissertation

Submitted in partial fulfillment of the requirements for the degree of

Doctor of Philosophy in Chemistry.

Syracuse University

July 2022

Acknowledgements

This dissertation and my time at Syracuse University would not be what it is without the incredible guidance of Dr. Korter as an advisor. I have learned an innumerable number of things about science, writing, and myself under his guidance and I would not be the scientist I am today without my time in his group. I have been incredibly lucky to have found his group and I am extremely thankful to have done my Ph.D. work in this group. I have not only been able to explore interesting experimental and computational ideas, but he has also given me the opportunity to present my research and learn from fellow scientists around the world. I also would not have been successful in graduate school without the friendship and guidance of Sara and Elyse. I am so glad I landed in a group with you two in it and I cannot imagine getting through my scientific hurdles or traveling the world without you guys. Thanks for always being willing it answer my science questions and making my time in Syracuse fun.

I also want to thank my amazing partner, Alex, for all his support through all the ups and downs on this journey. The last five years would have been much more difficult without your constant support and patience and always being willing to talk to me about whatever was going on. I hope to be able to provide similar support when you are writing your dissertation.

I also could not have done this without my family, specifically my parents, who have always supported me and taught me how to be the independent person I am today. Last, but certainly not least, I am eternally grateful to my cat, Uno, who provides me with cuddles and unconditional love every day.

Table of Contents

Chapter 1: Introduction

1.1 Motivation

Improving the effectiveness of formulated active pharmaceutical ingredients (APIs) can be done in a variety of ways, but one of the most common tactics is crystal engineering of new solids. Crystal engineering involves designing and tuning solid-state structures to have certain advantageous properties such as improved solubility and bioavailability in the case of pharmaceuticals.[1-5] The work presented here focuses on investigating the intermolecular forces involved in polymorphs, hydrates, and cocrystals and how changes in intermolecular forces can affect the stability of different materials.

A variety of experimental tools can be used to investigate these systems. In this work, powder X-ray diffraction (PXRD) is used to confirm sample identity through bulk crystallinity. PXRD is a useful technique since different samples, including different polymorphs, have unique powder patterns.[6-8] Beyond simple sample identification, the unambiguous interpretation of PXRD data becomes much more complicated and it gives little information about the intermolecular forces present in the crystal and how they may affect stability. To further identify and characterize samples as well as investigate the intermolecular forces present, low-frequency vibrational spectroscopy is utilized. The low-frequency region (sub-200 cm^{-1}) can provide a unique fingerprint for each sample and can be sampled at a variety of temperatures, with spectral features becoming better resolved at reduced temperatures.[9-11] The vibrations present in this region are due to motion involving all the atoms within the entire crystal unit cell and can provide insights into the intermolecular forces present as well as the crystal packing arrangement.[12-17] It is impractical (if not impossible) to determine the exact atomic motions associated with individual vibrations simply based on the experimental spectra as might be done at higher frequencies (400-4000 cm^{-1}) with standardized group frequency tables.

Solid-state density functional theory (ss-DFT) allows for the further investigation of the motion involved in individual vibrations.[18-22] Experimental results, both structural and vibrational can be used to benchmark ss-DFT simulations and confirm whether selected modeling parameters correctly simulate the desired system or if further refinement is required.[23]

1.2 Background on Polymorphs, Hydrates, and Cocrystals

Polymorphs are composed of the same molecules but arranged in different three-dimensional ways in the solid (**Figure 1-1**). While polymorphs are the same molecule, they can have different physical and chemical properties, such as different densities, melting points, crystal morphologies, and solubilities. These different properties are due to the fact that they have different intra- and intermolecular interactions, leading to different conformational and cohesive energies. Related to polymorphism, molecules can also crystallize into structures that include specific numbers of solvent molecules (termed "solvates"), and in the case of water these are called hydrates. Hydrates can come in a variety of ratios with respect to the nonaquous species including hemihydrates, monohydrates, dihydrates, trihydrates, etc (**Figure 1-1**). In the instance when two or more non-solvent molecules crystallize together into a new crystal structure, this is referred to as a cocrystal (**Figure 1-1**). Whether cocrystallized solids that include ionic molecules (often referred to as "salts") are considered cocrystals is a matter of debate depending on the source one looks at.[24]
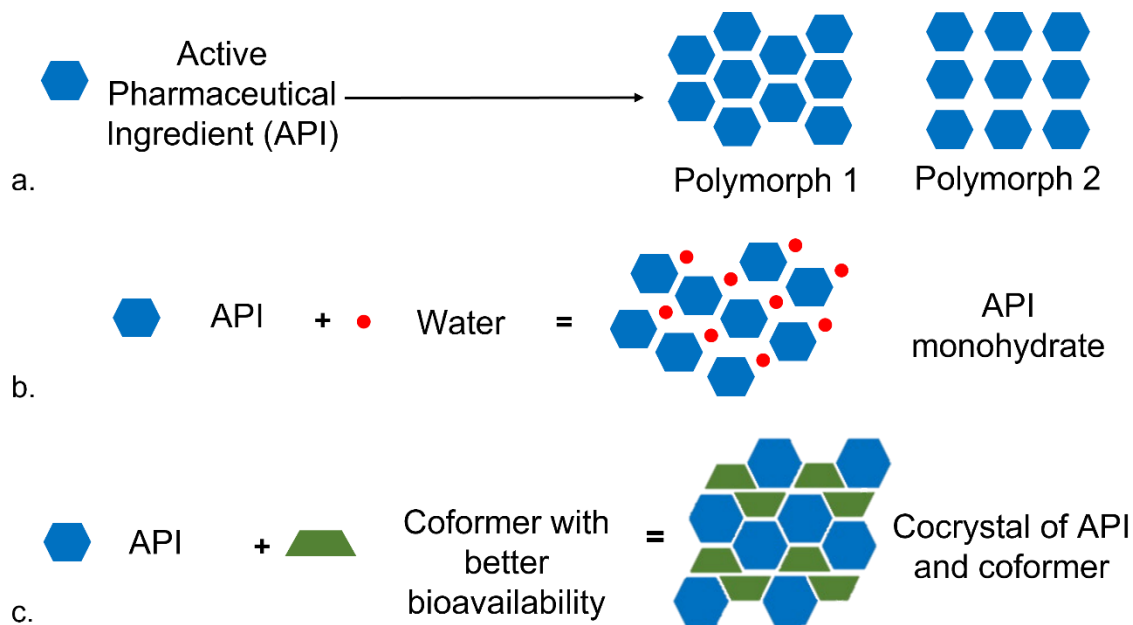
Figure 1-1. Graphical example of **a.** polymorphs, **b.** a monohydrate, and **c.** a cocrystal.

Polymorphs, hydrates, and cocrystals all have major implications for the design and formulation of pharmaceuticals. Due to the fact the different polymorphs can have different chemical and physical properties, it is important to ensure that the desired polymorph is being made in the production of a drug and is preserved during manufacturing and storage. Undesired polymorphs can crystallize in a variety of ways including from different solvents and at different temperatures, humidities, or pressures. The most famous example of this is ritonavir, a drug used to treat HIV that was introduced to the market in 1996. The drug was developed using form I, the only polymorph known at the time, and was marketed as tablets where the drug was dissolved in a hydroalcoholic solution to increase bioavailability. In 1998, form II of ritonavir was discovered when the tablets failed dissolution tests. Form II is more stable than form I and less soluble which resulted in the drug being taken off the market for a year while it was being reformulated in a refrigerated capsule. Continued research and reformulation has occurred over the years to produce a more effective process and formulation that stabilizes form I.[25-27] This example

demonstrates the importance of understanding and screening for different pharmaceutical polymorphs. While in this case form II was less bioavailable, it is also possible that a drug compound may have a previously unknown polymorph that is more bioavailable. Polymorphs can also convert in the solid-state through changes in temperature and pressure as well as through mechanical processes like grinding. The relationship between temperature and polymorph stability, a relationship often looked at here, can reveal either monotropic or enantiotropic relationships. In a monotropic relationship, one polymorph is stable over the entire temperature range and in enantiotropic relationship at some specific temperature the stability of two polymorphs switches.[28, 29] A number of polymorphs are covered in the chapters presented here including polymorphs of enalapril maleate (chapter 5) (**Figure 1-2**), ribavirin (chapter 8), levofloxacin (chapter 7), and urea:glutaric acid (chapter 4).
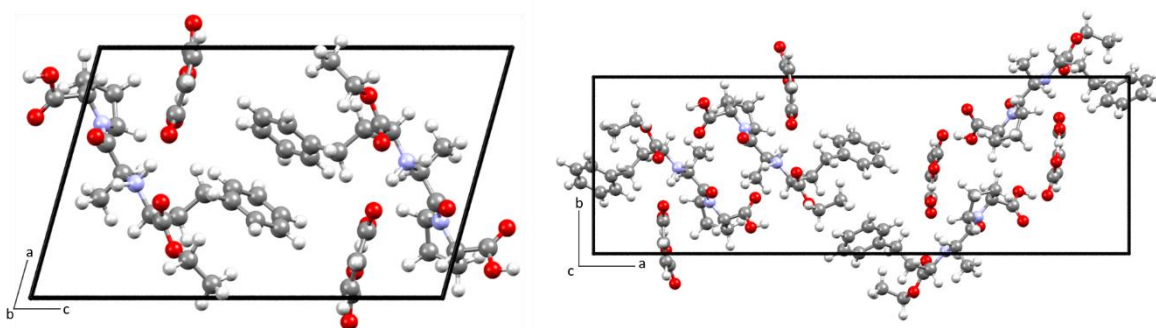
Figure 1-2. Crystallographic unit cells for the two polymorphs of enalapril maleate (EM), EM-I (left) and EM-II (right).

Hydrates are another set of crystal structures that play an important part in the pharmaceutical industry and possible crystal engineering applications. Previous work has postulated that around one third of APIs are naturally found in their hydrated form.[30] Along with hydrates of APIs, hydrates of excipients (inactive molecules in a drug formulation) are also important to consider in formulating pharmaceuticals.[31, 32] Water is an interesting and important

crystalline solvate for a number of reasons including that it is a non-toxic substance and that it may increase the number of possible hydrogen bonds in the solid. It is important to study pharmaceutical hydrates because molecules may hydrate during production and storage, and like polymorph transformation this would cause changes in a variety of chemical and physical properties.[24, 33] Generally, hydrates are less soluble in water than the anhydrous forms because they are more stable and this can be an advantage or a disadvantage depending on the molecule. In some cases, the hydrate being less soluble can be negative for bioavailability but this may be outweighed by the fact that the hydrate is more stable and less likely to degrade during production and storage.[30, 34] One example of a pharmaceutical hydrate is ampicillin trihydrate, an antibiotic, shown in **Figure 1-3** where it is compared to ampicillin anhydrous. It has been shown that the anhydrous form produced a higher blood serum concentration than the trihydrate which could be due to higher solubility of the anhydrous form or to different formulations.[31] This demonstrates why it is important to differentiate between the anhydrous form of an API and any possible hydrates. The differentiation of polymorphs also continues to play a role in pharmaceutical hydrates. Nitrofurantoin monohydrate, an antibacterial, has two polymorphs that can transition during grinding under different rates of relative humidity.[35] Within this work, hydrates of ezetimibe (chapter 6), levofloxacin (chapter 7), and ampicillin and amoxicillin (chapter 9) are investigated.
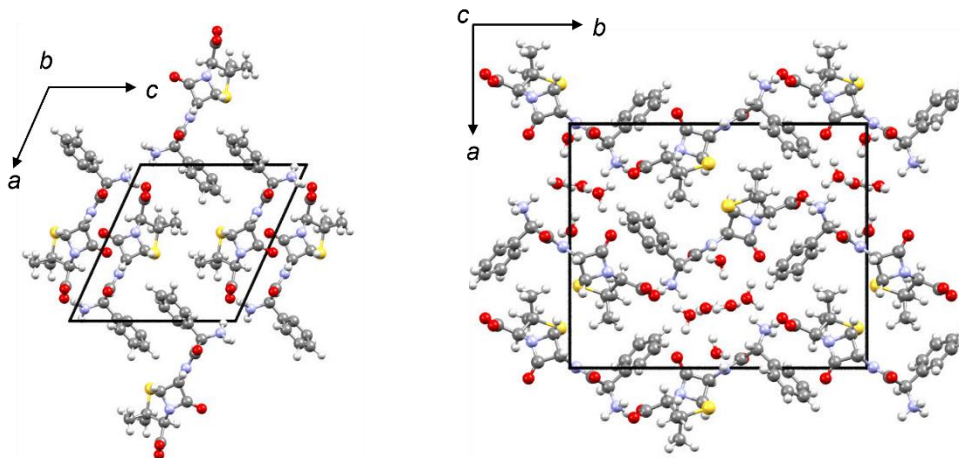
Figure 1-3. Crystallographic unit cells for ampicillin anhydrous (left) and ampicillin trihydrate (right).

Cocrystallization also provides another route to improve specific properties of an API. According to a 2017 article in *Drug Discovery Today*, 40% of approved drugs and 90% of drugs in development consist of poorly soluble molecules.[36, 37] An API can be cocrystallized with a coformer (or more than one coformer) that has a better desired property, such as enhanced solubility or stability.[38, 39] Ideally this leads to a new crystal that has the drug properties of the API while also having increased bioavailability due to the coformer(s). While this can be attempted with any two crystals, the most common molecules to form cocrystals are carboxylic acids, alcohols, and amides.[40] The coformer molecules are often selected from the FDA's "generally recognized as safe" (GRAS) list to avoid health concerns.[41] The main idea of this type of crystal engineering is to modify the non-covalent interactions within the crystal. Most of the cocrystal work presented here focuses on modifying the hydrogen bonding network but forces such as $\pi\ldots\pi$ stacking, van der Waals forces, and halogen bonding could also be manipulated.[42] The literature provides a number of example cocrystals that have demonstrated improvement in the bioavailability of already known pharmaceuticals. Norfloxacin, an antibiotic with low water

solubility, cocrystallized with isonicotinamide showed a 3-fold improvement in solubility when compared to the pure molecule while cocrystalizing it with malonic, succinic, and maleic acids, separately, to form salts showed a 30- to 45-fold increases.[43, 44] Carbamazepine is an anti-epileptic drug that has been shown to have a large number of cocrystals as well as hydrates and solvates. Some of these cocrystals such as carbamazepine-saccharin also have polymorphs which have different solubilities and dissolution rates.[43, 45] Examples such as these demonstrate how cocrystallization can improve pharmaceutical formulations as well as the importance of screening all potential crystals for polymorphism, hydrates, and solvates.[42] The polymorphs of enalapril maleate (chapter 5) along with an assortment of glutaric acid and DL-tartaric acid cocrystals (chapter 4) (**Figure 1-4**) are discussed in this work.
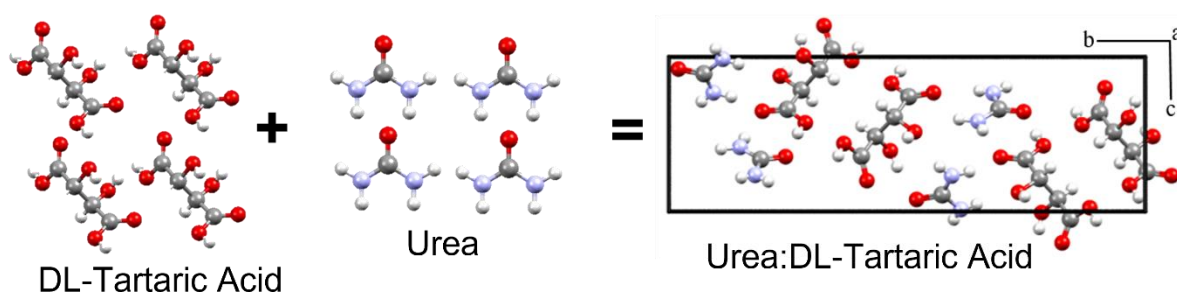
Figure 1-4. DL-tartaric acid cocrystallized with urea to form urea:DL-tartaric acid (right).

1.3 Background of Methods

To investigate the intermolecular forces and energetics involved in polymorphs, hydrates, and cocrystals, the two main methods used here are low-frequency vibrational spectroscopy and solid-state density functional theory (ss-DFT). Powder X-ray diffraction is also used to confirm sample identity and purity.

1.3.1 Low-Frequency Vibrational Spectroscopy

The low-frequency (10-200 cm^{-1}) vibrational region is particularly insightful for

polymorphs, hydrates, and cocrystals because, as discussed above, the vibrations in this region relate to intermolecular forces and crystal packing. While in the higher frequency range, two polymorphs may appear very similar, they have unique low-frequency spectra. Hydrates and their anhydrous forms as well as cocrystals and their pure components also have unique low-frequency spectra. [13-17, 46-48] In this work, terahertz spectroscopy and low-frequency Raman spectroscopy are utilized to provide a complete picture of the low-frequency vibrations of interest. Terahertz (THz) spectroscopy is a type of IR spectroscopy where the observed spectral peaks involve modes that produce dipole moment changes while low-frequency Raman spectroscopy (LFRS) deals with modes that involve a change in polarizability of the molecule (or molecular arrangement in the crystallographic unit cell).[49-52] The different selection rules of these two types of spectroscopies means that they provide complementary information about the system being investigated. Both of these methods are non-destructive and non-ionizing making them suitable for a variety of samples.[53] LFRS is a newer technique, due to more recent technological advances, that presents some advantages over THz spectroscopy because it does not require sample preparation and is not affected by water vapor as THz spectroscopy is.[16, 52, 54] THz spectroscopy, specifically terahertz time-domain spectroscopy (THz-TDS), is a more well-established technique that has been used to investigate molecules from a wide-range of interest areas including pharmaceuticals (the focus here), historical and modern pigments, and explosives.[14, 55-67] **Figure 1-5** demonstrates how polymorphs (**Figure 1-5.a.**), anhydrous crystals and hydrates (**Figure 1-5.b.**), and cocrystals (**Figure 1-5.c.**) have unique low-frequency vibrational spectra.
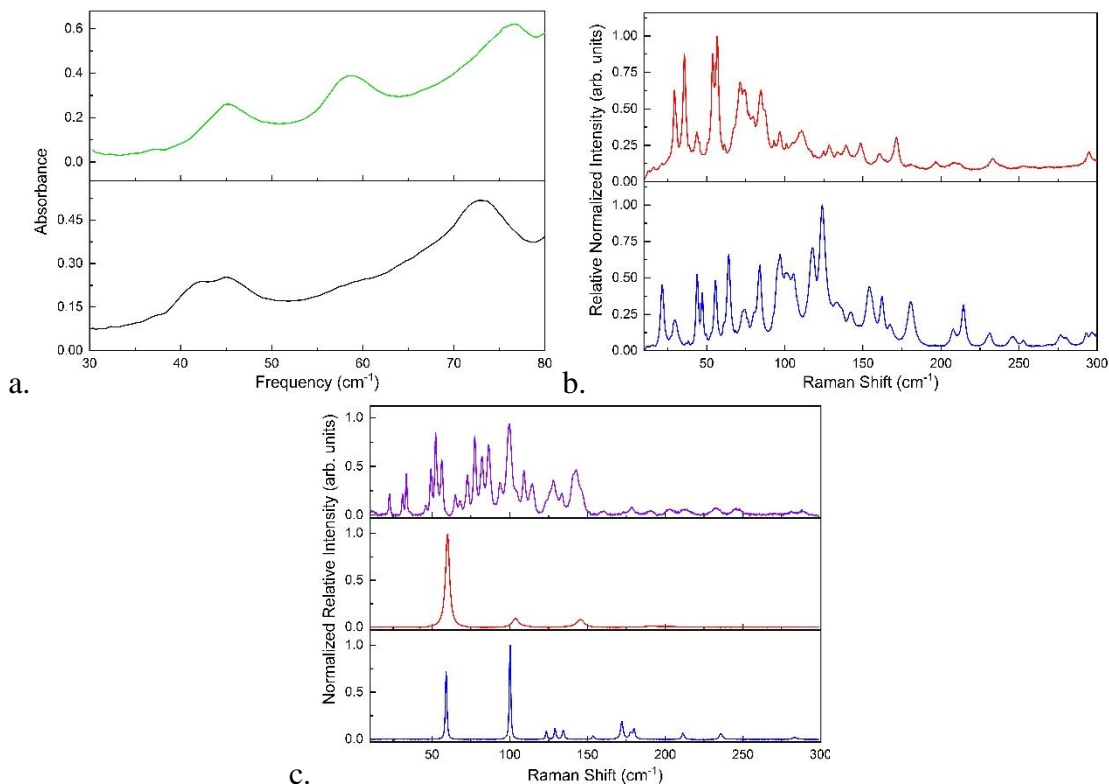
Figure 1-5. a. Experimental THz spectra for EM-I (black, bottom) and EM-II (green, top), **b.** experimental Raman spectra of ampicillin anhydrous (blue, bottom) and ampicillin trihydrate (red, top) and **c.** experimental Raman spectra of DL-tartaric acid (blue, bottom), urea (red, middle), and urea:DL-tartaric acid (purple, top).

1.3.2 Solid-State Density Functional Theory

Solid-state density functional theory (ss-DFT) is the chosen computational method here and these calculations are done using the CRYSTAL17 software package.[68] Solid-state DFT allows for the realistic modeling of three-dimensional crystals helping capture crystal packing, strong intermolecular forces, and weak long-range non-covalent effects such as London dispersion forces. Experimental spectra can be used to identify and differentiate different systems, as discussed above, as well as to benchmark computational methods and determine whether they are fully capturing the forces involved.[23] Part of this benchmarking involves determining the correct methodology to run the calculations including a balance between the most effective and accurate basis set and functional combination. This involves comparing the

solid-state optimized structure to the experimental structure as well as comparing the experimental THz and/or LFRS spectra to the simulated. Success in the benchmarking evaluation process serves to demonstrate that the applied ss-DFT approach can be used to model larger pharmaceutically relevant systems.[20, 22, 69-73]

Once a methodology is established as being effective at modeling the system, ss-DFT allows for the further investigation of the experimental spectra and the energetic factors involved in the system. Individual spectral features can be identified as originating from specific atomic motion giving insight into how certain vibrations may be related to the conformational flexibility of a molecule or polymorphic transitions. Additionally, the total energy can be broken down into conformational and cohesion energies and Gibbs free energy as a function of temperature plots can be constructed. This energy breakdown can be used to deduce why one polymorph is more stable than another or why a hydrate or cocrystal forms over the individual components. Furthermore, changes in conformations or hydrogen bonding can be investigated to see what role this plays in the stability of a particular system.[74-77] This information could be used to optimize cocrystal engineering by giving insights into what intermolecular forces play a significant role in a particular system.

1.4 Summary of Chapters

This work begins by discussing the experimental methods used (**Chapter 2**). First, PXRD is discussed including a brief history of X-ray diffraction, the differences between single-crystal versus powder X-ray diffraction and why PXRD is the primary technique utilized for characterization of samples here. The specific instrumentation used for characterization here is then discussed (**Chapter 2.2**). Then vibrational spectroscopy is discussed in general terms before focusing in on low-frequency vibrational spectroscopy and why the low-frequency modes are of

particular interest (**Chapter 2.3**). The specifics of LFRS (**Chapter 2.3.1**) and THz spectroscopy (**Chapter 2.3.2**) are then discussed along with the instrumentation used. **Chapter 3** goes into the theoretical methods used, specifically density functional theory. It then becomes more specific to focus on ss-DFT and the process of doing ss-DFT in CRYSTAL17.

Chapter 4 presents original research examining a variety of organic cocrystals using low-frequency Raman spectroscopy and ss-DFT. First, a group of known cocrystals, urea:glutaric acid (two polymorphs) and thiourea:glutaric acid are investigated and then urea:DL-tartaric acid, a known cocrystal, and thiourea:DL-tartaric acid, a hypothetical cocrystal, are investigated to explore what causes some of these cocrystals to form experimentally and others not to. This work focuses on using a group of model cocrystals to explore how changes in the hydrogen bonding network effect the overall stability.

Chapter 5 continues the exploration of cocrystals by examining the two polymorphs of enalapril maleate, a cocrystal used to treat hypertension, through terahertz spectroscopy and ss-DFT. This work was done through an ongoing collaboration with Hitachi High-Tech in Hitachi, Japan. Hitachi High-Tech provided the experimental terahertz spectra while I performed the ss-DFT simulations and did the analysis. This work uses a pharmaceutical cocrystal to demonstrate the ability of terahertz spectroscopy to differentiate between polymorphs and for ss-DFT to simulate a real pharmaceutical system. ss-DFT also reveals that Form II of enalapril maleate is the more stable of the two polymorphs due to greater cohesion energy.

Chapter 6 presents the next piece in our collaboration with Hitachi High-Tech which focuses on ezetimibe and ezetimibe monohydrate, a drug used to reduce cholesterol. Hitachi High-Tech were the primary authors of this work since the hydration and dehydration experiments are the focus and our ss-DFT work compliments the experimental presentation. The

goal of this work is to provide critical information about the hydration of ezetimibe and the ss-DFT work provides insights into the stability of ezetimibe versus ezetimibe monohydrate.

Chapter 7 examines ofloxacin, an antibiotic used to treat ear infections, and a series of levofloxacin solids using ss-DFT. This also represents the final piece of my collaboration with Hitachi High-Tech and in the future the simulations shown here will be combined with experimental THz results. This chapter combines the study of polymorphs of an anhydrous solid along with the study of two hydrates and outlines the ss-DFT structural and vibrational simulations for these solids as well as an energetic analysis of ofloxacin and the polymorphs of levofloxacin.

Chapter 8 studies the polymorphs of the antiviral ribavirin and uses a combination of low-frequency vibrational spectroscopies and ss-DFT to explore a critical dihedral angle and how it relates to torsional vibrations present in the low-frequency region. This conformational discussion complements the energetic analysis of the two polymorphs and demonstrates how the conformation of ribavirin in the R-II crystal is due to intermolecular forces present.

Chapter 9 presents our work on ampicillin and amoxicillin, two popular antibiotics. Here LFRS and ss-DFT are used to explore ampicillin anhydrous and the trihydrates of ampicillin and amoxicillin. Computational methods allow for the simulation and assignment of the vibrational spectra as well as for hypothetical amoxicillin anhydrous structures to be constructed and evaluated.

1.5 References

1.   Kumar, S., Pharmaceutical Cocrystals: An Overview. *Indian Journal of Pharmaceutical Sciences* **2018,** *79* (6), 858-871.

2.   Remenar, J. F.; Morissette, S. L.; Peterson, M. L.; Moulton, B.; MacPhee, J. M.; Guzman, H. R.; Almarsson, O., Crystal Engineering of Novel Cocrystals of a Triazole Drug with 1,4-Dicarboxylic Acids. *Journal of the American Chemical Society* **2003,** *125* (28), 8456-8457.

3.   Desiraju, G. R., Crystal Engineering: A Holistic View. *Angewandte Chemie International Edition* **2007,** *46* (44), 8342-8356.

4.   Desiraju, G. R., Crystal Engineering: From Molecule to Crystal. *Journal of the American Chemical Society* **2013,** *135* (27), 9952-9967.

5.   Nangia, A. K.; Desiraju, G. R., Crystal Engineering: An Outlook for the Future. *Angewandte Chemie International Edition* **2019,** *58* (13), 4100-4107.

6.   Jenkins, R.; Snyder, R. L., *Introduction to X-Ray Powder Diffractometry (Volume 138)*. Wiley Online Library: 1996.

7.   Pecharsky, V.; Zavalij, P., *Fundamentals of Powder Diffraction and Structural Characterization of Materials*. Springer Science & Business Media: 2008.

8.   Freitas, J. T.; de Melo, C. C.; Viana, O. M.; Ferreira, F. F.; Doriguetto, A. C., Crystal Structure of Levofloxacin Anhydrates: A High-Temperature Powder X-Ray Diffraction Study Versus Crystal Structure Prediction. *Crystal Growth & Design* **2018,** *18* (6), 3558-3568.

9.   Dampf, S. J.; Korter, T. M., Anomalous Temperature Dependence of the Lowest-Frequency Lattice Vibration in Crystalline Γ-Aminobutyric Acid. *The Journal of Physical Chemistry A* **2019,** *123* (10), 2058-2064.

10.   Zaczek, A. J.; Catalano, L.; Naumov, P.; Korter, T. M., Mapping the Polymorphic Transformation Gateway Vibration in Crystalline 1, 2, 4, 5-Tetrabromobenzene. *Chemical science* **2019,** *10* (5), 1332-1341.

11.   Squires, A.; Zaczek, A. J.; Lewis, R.; Korter, T. M., Identifying and Explaining Vibrational Modes of Quinacridones Via Temperature-Resolved Terahertz Spectroscopy: Absorption Experiments and Solid-State Density Functional Theory Simulations. *Physical Chemistry Chemical Physics* **2020,** *22* (35), 19672-19679.

12.   Bērziņš, K.; Fraser-Miller, S. J.; Gordon, K. C., Recent Advances in Low-Frequency Raman Spectroscopy for Pharmaceutical Applications. *International Journal of Pharmaceutics* **2021,** *592*, 120034.

13.   Parrott, E. P. J.; Zeitler, J. A., Terahertz Time-Domain and Low-Frequency Raman Spectroscopy of Organic Materials. *Applied Spectroscopy* **2015,** *69* (1), 1-25.

14.   Zeitler, J. A.; Taday, P. F.; Newnham, D. A.; Pepper, M.; Gordon, K. C.; Rades, T., Terahertz Pulsed Spectroscopy and Imaging in the Pharmaceutical Setting-a Review. *Journal of Pharmacy and Pharmacology* **2007,** *59* (2), 209-223.

15.   Kimmitt, M. F., Restrahlen to T-Rays - 100 Years of Terahertz Radiation. *J. Biol. Phys.* **2003,** *29* (2-3), 77-85.

16.   Beard, M. C.; Turner, G. M.; Schmuttenmaer, C. A., Terahertz Spectroscopy. *The Journal of Physical Chemistry B* **2002,** *106* (29), 7146-7159.

17.   Larkin, P. J.; Dabros, M.; Sarsfield, B.; Chan, E.; Carriere, J. T.; Smith, B. C., Polymorph Characterization of Active Pharmaceutical Ingredients (Apis) Using Low-Frequency Raman Spectroscopy. *Applied spectroscopy* **2014,** *68* (7), 758-776.

18.   Banks, P. A.; Song, Z.; Ruggiero, M. T., Assessing the Performance of Density

Functional Theory Methods on the Prediction of Low-Frequency Vibrational Spectra. *Journal of*

Infrared, Millimeter, and Terahertz Waves **2020,** *41* (11), 1411-1429.

19.   Ruggiero, M. T.; Sibik, J.; Zeitler, J. A.; Korter, T. M., Examination of L-Glutamic Acid

Polymorphs by Solid-State Density Functional Theory and Terahertz Spectroscopy. *The Journal*

of Physical Chemistry A **2016,** *120* (38), 7490-7495.

20.   Davis, M. P.; Mohara, M.; Shimura, K.; Korter, T. M., Simulation and Assignment of the

Terahertz Vibrational Spectra of Enalapril Maleate Cocrystal Polymorphs. *The Journal of*

Physical Chemistry A **2020,** *124* (47), 9793-9800.

21.   Ruggiero, M. T.; Sutton, J. J.; Fraser-Miller, S. J.; Zaczek, A. J.; Korter, T. M.; Gordon,

K. C.; Zeitler, J. A., Revisiting the Thermodynamic Stability of Indomethacin Polymorphs with

Low-Frequency Vibrational Spectroscopy and Quantum Mechanical Simulations. *Crystal*

Growth & Design **2018,** *18* (11), 6513-6520.

22.   Surov, A. O.; Manin, A. N.; Voronin, A. P.; Boycov, D. E.; Magdysyuk, O. V.;

Perlovich, G. L., New Pharmaceutical Cocrystal Forms of Flurbiprofen: Structural,

Physicochemical, and Thermodynamic Characterization. *Crystal Growth & Design* **2019,** *19*

(10), 5751-5761.

23.   Dampf, S. J.; Korter, T. M., Crystalline Molecular Standards for Low-Frequency

Vibrational Spectroscopies. *Journal of Infrared, Millimeter, and Terahertz Waves* **2020,** *41* (11),

1284-1300.

24.   Elder, D. P.; Holm, R.; De Diego, H. L., Use of Pharmaceutical Salts and Cocrystals to

Address the Issue of Poor Solubility. *International journal of pharmaceutics* **2013,** *453* (1), 88-

100.

25.   Morissette, S. L.; Soukasene, S.; Levinson, D.; Cima, M. J.; Almarsson, Ö., Elucidation of Crystal Form Diversity of the Hiv Protease Inhibitor Ritonavir by High-Throughput Crystallization. *Proceedings of the National Academy of Sciences* **2003,** *100* (5), 2180-2184.

26.   Zhang, C.; Matzger, A. J., A Newly Discovered Racemic Compound of Pioglitazone Hydrochloride Is More Stable Than the Commercial Conglomerate. *Crystal growth & design* **2017,** *17* (2), 414-417.

27.   Chakraborty, D.; Sengupta, N.; Wales, D. J., Conformational Energy Landscape of the Ritonavir Molecule. *The Journal of Physical Chemistry B* **2016,** *120* (19), 4331-4340.

28.   Maheshwari, R.; Chourasiya, Y.; Bandopadhyay, S.; Katiyar, P. K.; Sharma, P.; Deb, P. K.; Tekade, R. K., Chapter 1 - Levels of Solid State Properties: Role of Different Levels During Pharmaceutical Product Development. In *Dosage Form Design Parameters*, Tekade, R. K., Ed. Academic Press: 2018; pp 1-30.

29.   Lee, E. H., A Practical Guide to Pharmaceutical Polymorph Screening & Selection. *asian journal of pharmaceutical sciences* **2014,** *9* (4), 163-175.

30.   Bhatia, A.; Chopra, S.; Nagpal, K.; Deb, P. K.; Tekade, M.; Tekade, R. K., Chapter 2 - Polymorphism and Its Implications in Pharmaceutical Product Development. In *Dosage Form Design Parameters*, Tekade, R. K., Ed. Academic Press: 2018; pp 31-65.

31.   Khankari, R. K.; Grant, D. J., Pharmaceutical Hydrates. *Thermochimica acta* **1995,** *248*, 61-79.

32.   Healy, A. M.; Worku, Z. A.; Kumar, D.; Madi, A. M., Pharmaceutical Solvates, Hydrates and Amorphous Forms: A Special Emphasis on Cocrystals. *Advanced drug delivery reviews* **2017,** *117*, 25-46.

33.	Giron, D.; Goldbronn, C.; Mutz, M.; Pfeffer, S.; Piechon, P.; Schwab, P., Solid State Characterizations of Pharmaceutical Hydrates. *Journal of thermal analysis and calorimetry* **2002,** *68* (2), 453-465.

34.	Jurczak, E.; Mazurek, A. H.; Szeleszczuk, Ł.; Pisklak, D. M.; Zielińska-Pisklak, M., Pharmaceutical Hydrates Analysis—Overview of Methods and Recent Advances. *Pharmaceutics* **2020,** *12* (10), 959.

35.	Tian, F.; Qu, H.; Louhi-Kultanen, M.; Rantanen, J., Mechanistic Insight into the Evaporative Crystallization of Two Polymorphs of Nitrofurantoin Monohydrate. *Journal of crystal growth* **2009,** *311* (8), 2580-2589.

36.	Dalpiaz, A.; Pavan, B.; Ferretti, V., Can Pharmaceutical Co-Crystals Provide an Opportunity to Modify the Biological Properties of Drugs? *Drug Discovery Today* **2017,** *22* (8), 1134-1138.

37.	Steed, J. W., The Role of Co-Crystals in Pharmaceutical Design. *Trends in pharmacological sciences* **2013,** *34* (3), 185-193.

38.	Biscaia, I. F. B.; Gomes, S. N.; Bernardi, L. S.; Oliveira, P. R., Obtaining Cocrystals by Reaction Crystallization Method: Pharmaceutical Applications. *Pharmaceutics* **2021,** *13* (6), 898.

39.	Karimi-Jafari, M.; Padrela, L.; Walker, G. M.; Croker, D. M., Creating Cocrystals: A Review of Pharmaceutical Cocrystal Preparation Routes and Applications. *Crystal Growth & Design* **2018,** *18* (10), 6370-6387.

40.	Bavishi, D. D.; Borkhataria, C. H., Spring and Parachute: How Cocrystals Enhance Solubility. *Progress in Crystal Growth and Characterization of Materials* **2016,** *62* (3), 1-8.

41.   Buddhadev, S. S.; Garala, K. C., Pharmaceutical Cocrystals—a Review. *Multidisciplinary Digital Publishing Institute Proceedings* **2021,** *62* (1), 14.

42.   Qiao, N.; Li, M.; Schlindwein, W.; Malek, N.; Davies, A.; Trappitt, G., Pharmaceutical Cocrystals: An Overview. *International journal of pharmaceutics* **2011,** *419* (1-2), 1-11.

43.   Thakuria, R.; Delori, A.; Jones, W.; Lipert, M. P.; Roy, L.; Rodríguez-Hornedo, N., Pharmaceutical Cocrystals and Poorly Soluble Drugs. *International journal of pharmaceutics* **2013,** *453* (1), 101-125.

44.   Basavoju, S.; Boström, D.; Velaga, S. P., Pharmaceutical Cocrystal and Salts of Norfloxacin. *Crystal growth & design* **2006,** *6* (12), 2699-2708.

45.   Vishweshwar, P.; McMahon, J. A.; Bis, J. A.; Zaworotko, M. J., Pharmaceutical Co-Crystals. *Journal of pharmaceutical sciences* **2006,** *95* (3), 499-516.

46.   Hédoux, A.; Guinet, Y.; Descamps, M., The Contribution of Raman Spectroscopy to the Analysis of Phase Transformations in Pharmaceutical Compounds. *International journal of pharmaceutics* **2011,** *417* (1-2), 17-31.

47.   Inoue, M.; Hisada, H.; Koide, T.; Fukami, T.; Roy, A.; Carriere, J.; Heyler, R., Transmission Low-Frequency Raman Spectroscopy for Quantification of Crystalline Polymorphs in Pharmaceutical Tablets. *Analytical chemistry* **2019,** *91* (3), 1997-2003.

48.   Parrott, E. P.; Zeitler, J. A.; Friščić, T.; Pepper, M.; Jones, W.; Day, G. M.; Gladden, L. F., Testing the Sensitivity of Terahertz Spectroscopy to Changes in Molecular and Supramolecular Structure: A Study of Structurally Similar Cocrystals. *Crystal Growth & Design* **2009,** *9* (3), 1452-1460.

49.   Kaufman, E. D., *Advanced Concepts in Physical Chemistry*. McGraw-Hill: 1966.

50.   Larkin, P., *Infrared and Raman Spectroscopy: Principles and Spectral Interpretation*. Elsevier: 2017.

51.   Colthup, N. B.; Daly, L. H.; Wiberley, S. E., *Introduction to Infrared and Raman Spectroscopy (Second Edition)*. Academic Press: 1975.

52.   Hoffmann, G. G., *Raman Spectroscopy, Volume I: Principles and Applications in Chemistry, Physics, Materials Science, and Biology*. Momentum Press: 2019.

53.   Dexheimer, S. L., *Terahertz Spectroscopy: Principles and Applications*. CRC press: 2017.

54.   Vandenabeele, P., *Practical Raman Spectroscopy: An Introduction*. John Wiley & Sons: 2013.

55.   Liu, H.-B.; Chen, Y.; Zhang, X.-C., Characterization of Anhydrous and Hydrated Pharmaceutical Materials with Thz Time-Domain Spectroscopy. *Journal of pharmaceutical sciences* **2007,** *96* (4), 927-934.

56.   Mohara, M.; Aiko, K.; Shimura, K.; Ono, T. In *Quantitative Analysis and Inspection for Pharmaceutical Polymorphism with Injection-Seeded Terahertz Parametric Generation Technique*, 2018 43rd International Conference on Infrared, Millimeter, and Terahertz Waves (IRMMW-THz), IEEE: 2018; pp 1-2.

57.   Strachan, C. J.; Rades, T.; Newnham, D. A.; Gordon, K. C.; Pepper, M.; Taday, P. F., Using Terahertz Pulsed Spectroscopy to Study Crystallinity of Pharmaceutical Materials. *Chemical Physics Letters* **2004,** *390* (1-3), 20-24.

58.   Strachan, C. J.; Taday, P. F.; Newnham, D. A.; Gordon, K. C.; Zeitler, J. A.; Pepper, M.; Rades, T., Using Terahertz Pulsed Spectroscopy to Quantify Pharmaceutical Polymorphism and Crystallinity. *Journal of Pharmaceutical Sciences* **2005,** *94* (4), 837-846.

59.   Zeitler, J. A. R., Thomas; Taday, Philip F. , Pharmaceutical and Security Applications of Terahertz Spectroscopy. In *Terahertz Spectroscopy: Principles and Applications*, Dexheimer, S. L., Ed. CRC press: 2008; pp 299-320.

60.   Kleist, E. M.; Koch Dandolo, C. L.; Guillet, J.-P.; Mounaix, P.; Korter, T. M., Terahertz Spectroscopy and Quantum Mechanical Simulations of Crystalline Copper-Containing Historical Pigments. *The Journal of Physical Chemistry A* **2019,** *123* (6), 1225-1232.

61.   Kleist, E. M.; Korter, T. M., Quantitative Analysis of Minium and Vermilion Mixtures Using Low-Frequency Vibrational Spectroscopy. *Analytical Chemistry* **2019,** *92* (1), 1211-1218.

62.   Squires, A.; Lewis, R.; Zaczek, A. J.; Korter, T. M., Distinguishing Quinacridone Pigments Via Terahertz Spectroscopy: Absorption Experiments and Solid-State Density Functional Theory Simulations. *The Journal of Physical Chemistry A* **2017,** *121* (18), 3423-3429.

63.   Squires, A.; Lewis, R., Terahertz Analysis of Phthalocyanine Pigments. *Journal of Infrared, Millimeter, and Terahertz Waves* **2019,** *40* (7), 738-751.

64.   Davies, A. G.; Burnett, A. D.; Fan, W.; Linfield, E. H.; Cunningham, J. E., Terahertz Spectroscopy of Explosives and Drugs. *Materials today* **2008,** *11* (3), 18-26.

65.   Allis, D. G.; Prokhorova, D. A.; Korter, T. M., Solid-State Modeling of the Terahertz Spectrum of the High Explosive Hmx. *The Journal of Physical Chemistry A* **2006,** *110* (5), 1951-1959.

66.   Witko, E. M.; Korter, T. M., Terahertz Spectroscopy of the Explosive Taggant 2, 3-Dimethyl-2, 3-Dinitrobutane. *The Journal of Physical Chemistry A* **2012,** *116* (25), 6879-6884.

67.   Taday, P. F.; Bradley, I.; Arnone, D.; Pepper, M., Using Terahertz Pulse Spectroscopy to Study the Crystalline Structure of a Drug: A Case Study of the Polymorphs of Ranitidine Hydrochloride. *Journal of pharmaceutical sciences* **2003,** *92* (4), 831-838.

68.   Dovesi, R.; Erba, A.; Orlando, R.; Zicovich-Wilson, C. M.; Civalleri, B.; Maschio, L.; Rérat, M.; Casassa, S.; Baima, J.; Salustro, S., Quantum-Mechanical Condensed Matter Simulations with Crystal. *Wiley Interdisciplinary Reviews: Computational Molecular Science* **2018**, e1360.

69.   Aytekin, Y. S.; Köktürk, M.; Zaczek, A.; Korter, T. M.; Heilweil, E. J.; Esenturk, O., Optical Properties of Meloxicam in the Far-Infrared Spectral Region. *Chemical physics* **2018,** *512*, 36-43.

70.   Mazurek, A. H.; Szeleszczuk, Ł.; Pisklak, D. M., Periodic Dft Calculations—Review of Applications in the Pharmaceutical Sciences. *Pharmaceutics* **2020,** *12* (5), 415.

71.   Surov, A. O.; Vasilev, N. A.; Vener, M. V.; Parashchuk, O. D.; Churakov, A. V.; Magdysyuk, O. V.; Perlovich, G. L., Pharmaceutical Salts of Fenbendazole with Organic Counterions: Structural Analysis and Solubility Performance. *Crystal Growth & Design* **2021,** *21* (8), 4516-4530.

72.   Delaney, S. P.; Korter, T. M., Terahertz Spectroscopy and Computational Investigation of the Flufenamic Acid/Nicotinamide Cocrystal. *The Journal of Physical Chemistry A* **2015,** *119* (13), 3269-3276.

73.   Delaney, S. P.; Pan, D.; Galella, M.; Yin, S. X.; Korter, T. M., Understanding the Origins of Conformational Disorder in the Crystalline Polymorphs of Irbesartan. *Crystal growth & design* **2012,** *12* (10), 5017-5024.

74.   Delaney, S. P.; Pan, D.; Yin, S. X.; Smith, T. M.; Korter, T. M., Evaluating the Roles of Conformational Strain and Cohesive Binding in Crystalline Polymorphs of Aripiprazole. *Crystal growth & design* **2013,** *13* (7), 2943-2952.

75.   Dierks, T. M.; Korter, T. M., Comparison of Intermolecular Forces in Anhydrous Sorbitol and Solvent Cocrystals. *The Journal of Physical Chemistry A* **2017,** *121* (30), 5720-5727.

76.   Dierks, T. M.; Korter, T. M., Origins of the Relative Stabilities of Anhydrous and Hydrated D-Mannitol Crystals. *The Journal of Physical Chemistry A* **2016,** *120* (33), 6629-6636.

77.   Greenwell, C.; McKinley, J. L.; Zhang, P.; Zeng, Q.; Sun, G.; Li, B.; Wen, S.; Beran, G. J., Overcoming the Difficulties of Predicting Conformational Polymorph Energetics in Molecular Crystals Via Correlated Wavefunction Methods. *Chemical science* **2020,** *11* (8), 2200-2214.

Chapter 2: Experimental Methods

2.1 Introduction

A number of different experimental techniques are used here. The main technique is low-frequency vibrational spectroscopy including low-frequency Raman spectroscopy and terahertz spectroscopy. Powder X-ray diffraction (PXRD) is used at the very beginning of a project to characterize the samples in question (whether bought from a chemical manufacturer or crystallized in the laboratory). By comparing the PXRD pattern generated to those found in databases, such as the Cambridge Structural Database (CSD)[1], it can be confirmed that the samples are what was expected. This step is critical in ensuring that the low-frequency spectra taken are reliably representative of the proper sample and the correct structure is being used for computational simulations. Low-frequency Raman spectroscopy (LFRS) and terahertz (THz) spectroscopy are then used to probe the low-frequency vibrational modes present in the sample. These spectroscopies probe the Raman- and IR-active modes in the sub-200 cm^{-1} region that are indicative of intermolecular forces and three-dimensional crystal packing, both critical ideas in the works presented here.[2-5]

2.2 Powder X-Ray Diffraction (PXRD)

X-ray diffraction has long been used to characterize samples and determine the structure of crystals. The basis of our understanding of X-ray diffraction is Bragg's Law (Eq. 2.1), which was developed in 1913 to help explain the patterns seen when X-rays scattered off crystalline samples:

$$n\lambda = 2d \sin \theta \qquad (2.1)$$

where n is an integer, λ is the wavelength of radiation, d is the spacing between parallel lattice planes, and 2θ is the angle of the scattered X-rays (diffraction angle).[6, 7] Bragg's Law is based on

the fact that crystalline samples have planes of atoms, called lattice planes, and when X-rays

scatter off of the electrons in these planes they can constructively or destructively interfere.

When they constructively interfere, and therefore satisfy Bragg's Law, a significant increase in

X-ray scattering intensity (a peak) can be seen by a detector.[7-9] X-ray radiation is produced by

hitting a metal anode with electrons and characteristic emission lines are produced when specific

electronic transitions occur in the metal anode. The most common metals used as X-ray sources

are Cu and Mo while other sources can be used for specific applications. The two common

characteristic emissions that are utilized in X-ray diffraction are the Kα and Kβ emission lines,

with Kβ being weaker. Kα occurs when an electron goes from 2p to 1s and has a λ=1.54056 Å in

Cu. Kβ occurs when an electron goes from 3p to 1s and it occurs at λ=1.392 Å in Cu. Cu Kα

radiation is one of the most common sources for X-ray diffraction.[10]

X-ray diffraction experiments can be done on a single crystal or a powder sample. The

same principles apply to both of these techniques, but they produce different results and can be

utilized in different ways (**Figure 2-1**).
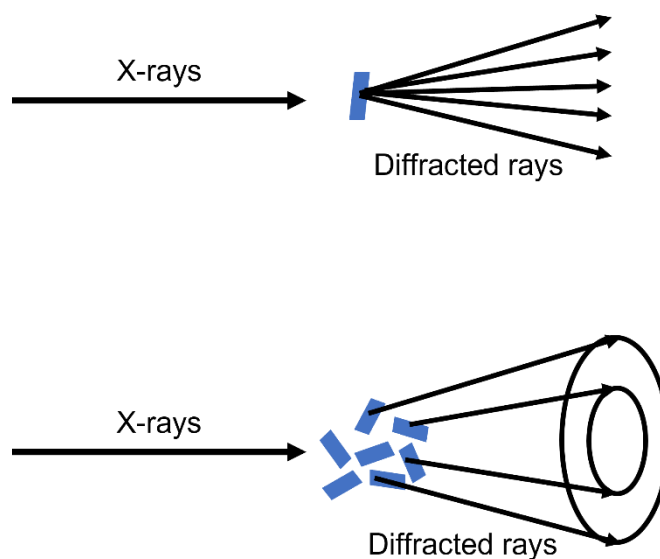
Figure 2-1. Diagram of single crystal X-ray diffraction which produces spots (top) and powder X-ray diffraction which produces Debye-Scherrer cones (bottom).

Single-crystal X-ray diffraction produces discrete spots when X-ray radiation reflects off a plane of atoms. These discrete spots are called reflections and can be used to determine a complete crystal structure.[11] While I have solved single-crystal X-ray structures, the main technique that is utilized here is PXRD.

PXRD was developed in 1916 by Debye and Scherrer and produces Debye-Scherrer cones which can be translated into a two-dimensional pattern with the 2θ diffraction angle on the x-axis and the X-ray scattering intensity on the y-axis.[7] Here PXRD is used to confirm samples by comparing the experimental PXRD pattern to those generated from data contained in the CSD.[1] PXRD can also be used to solve crystal structures by using mathematical algorithms, though those have large uncertainties in the exact molecular structures in comparison to single-

crystal measurement.[8] This is especially useful for samples that are hard to grow single crystals of adequate size.

      All the PXRD measurements shown here were done on a Bruker D2 Phaser diffractometer (**Figure 2-2.a.**). This is a benchtop system that is easy to use and produces excellent PXRD patterns with simple sample preparation. A sample is first ground to a powder using a mortar and pestle so that the X-rays hit a mixture of randomly oriented crystals and then is loaded into the sample holder (**Figure 2-2.b.**). The sample holder can then be put into one of the six sample spots within the D2 Phaser (**Figure 2-2.c.**).

a.   b.

c.

Figure 2-2. a. Bruker D2 Phaser, **b.** sample holder, and **c.** inside the Bruker D2 Phaser with two samples.

The Bruker D2 Phaser uses Cu Kα radiation and the acquisition settings can be configured in a variety of ways depending on the sample and the pattern one wishes to produce. Generally, 2θ angles from 5° to 70° are run with a 0.02° step taking 0.5 s per step. This setup takes 28 minutes to run and can be viewed on the DIFFRAC.SUITE software on the D2 Phaser monitor.[12] The experimental PXRD pattern can then be compared to one from the CSD by using visualization software called Mercury to calculate a powder pattern.[13] In **Figure 2-3**, an example is shown of an experimental PXRD pattern for urea compared to the predicted PXRD pattern from the published crystal structure.
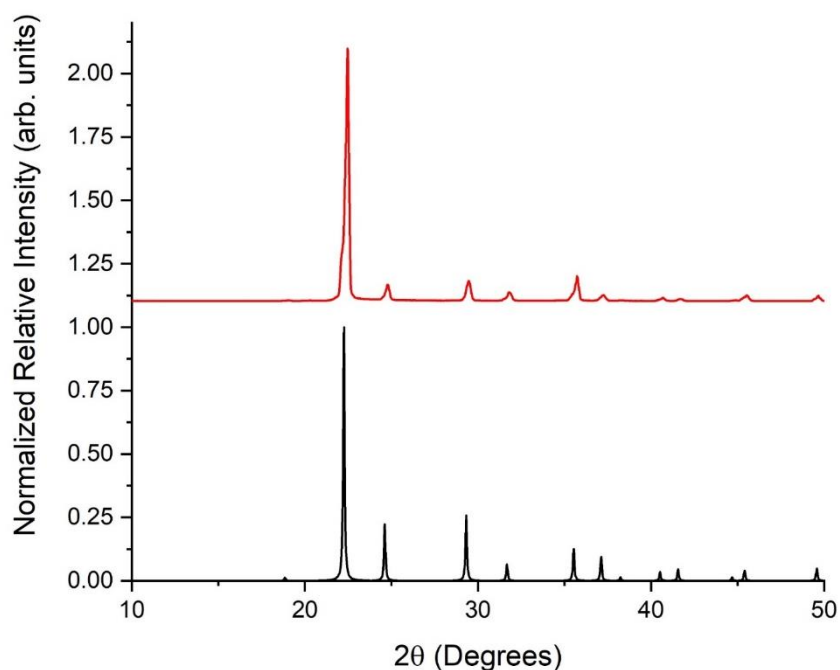
Figure 2-3. PXRD patterns of urea experimental sample (red) and urea predicted from published data[14] (black) (patterns offset for clarity).

2.3 Vibrational Spectroscopy

The majority of the work shown here focuses on LFRS and in some works THz spectroscopy (far-IR) is used as a complementary technique to further investigate the low-frequency modes. The vibrations present in the low-frequency (sub-200 cm^{-1}) region are lattice modes that come from the large-amplitude motion of molecules within the crystal and are influenced by the three-dimensional packing of the crystal.[2, 3, 15, 16] These modes are especially sensitive to the intermolecular forces and packing arrangements present which makes them ideal for the study of polymorphs, cocrystals, and hydrates. Both LFRS and THz spectroscopy have been used to identify and examine polymorphs of a variety of compounds including solid-state pharmaceuticals.[4, 17-23]

The number of ways that a molecule can vibrate can be defined by the vibrational degrees of freedom. A linear molecule has 3N-5, where N is the number of atoms, degrees of vibrational freedom and non-linear molecules have 3N-6 degrees of vibrational freedom. The minus 5 comes from the three translational modes and two rotational modes present in a linear molecule and a non-linear molecule has one additional rotational mode. Each of these vibrational degrees of freedom has a normal mode vibration that corresponds with the specific atomic motion of that vibration.

The vibrations studied here all occur within the solid-state, meaning they become more complex because there can be internal, which involve molecular motion, and external modes, which involve lattice motion. In the case of a three-dimensional solid, there are three acoustic modes and 3n-3 optical modes, where n is the number of atoms in the unit cell. The optical modes are what we focus on and can be broken down into internal modes, (3n-6)Z where Z is the number of formula units per unit cell, and external modes, 6Z-3. Unlike higher-frequency modes which can be assigned to specific motions, such as O-H stretching, through group frequency

tables, the lower-frequency modes generally consist of motion involving the whole unit cell making the low-frequency modes very complex. Generally, the modes discussed here are broken down into three descriptions, translational, rotational, and torsional motion.[24]

Spectroscopy can probe these normal mode vibrations if the energy coming in matches the difference between the energy levels in the molecule or crystalline assembly.[25] These energy levels and the potential energy surface can be modeled in a variety of ways. The most common way is using the harmonic oscillator. The Schrodinger equation, discussed further in chapter 3, can be defined for the harmonic oscillator as:

$$-\frac{\hbar^2}{2m}\frac{d^2\psi}{dx^2} + \frac{1}{2}m\omega^2x^2\psi = E\psi \tag{2.2}$$

where ħ is Planck's constant, m is the mass, and ω is the angular frequency of oscillation

($\omega = \sqrt{\frac{k}{m}}$, where k is the force constant).[26] From this the energy levels, n, can be defined as:

$$E_n = \left(n + \frac{1}{2}\right)\hbar\omega \tag{2.3}$$

Within the harmonic oscillator approach, the approximation for the potential energy takes the form of a parabola and the energy levels are equally spaced beginning at the zero-point energy, $E_0 = (\frac{1}{2})\hbar\omega$ (**Figure 2-4**). While this is a useful approximation in many ways because it has an analytical solution, it fails as the distance between two atoms gets further from the equilibrium position (q). In reality, the potential energy surface is anharmonic, meaning the potential well is asymmetric and the energy levels get closer together as the energy increases (**Figure 2-4**). The shape of the anharmonic well can be represented by a Morse potential.[27, 28] Normal mode vibrations occur when the radiation hitting the sample can excites a vibrational state n=±1 energy levels.[25]
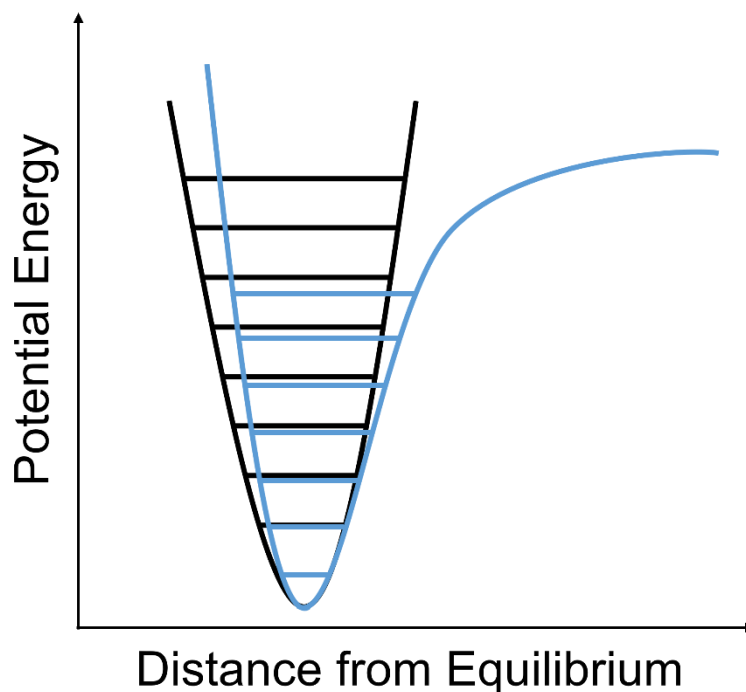
Figure 2-4. The harmonic oscillator potential (black) with energy levels and the Morse potential (blue) with anharmonic energy levels.

Whether a normal mode is detectable also depends on how that vibration interacts with the light coming in. These rules are called selection rules and are different for IR and Raman spectroscopies. For a mode to be IR-active, the vibration must cause a change in the dipole moment of the molecule or crystallographic unit cell and for a mode to be Raman-active the vibration must cause a change in polarizability. Depending on the symmetry of the vibrational mode it can be either IR-active, Raman-active, both, or neither. The symmetry of a vibrational mode can be determined by using character tables, but this gets very complicated as the molecules and crystals get larger. In practice here, the software used to perform solid-state density functional theory calculations (chapters 3) is used to determine the symmetry of the different normal modes.[27, 29]

2.3.1 Low-Frequency Raman Spectroscopy (LFRS)

As stated above, Raman spectroscopy can be used when the normal mode vibration causes a change in polarizability of the molecule. In a practical sense, monochromatic radiation is directed at a sample.[30] Most of the radiation scatters elastically, at the same frequency as the incident radiation, called Rayleigh scattering and produces a large intensity peak at 0 cm^{-1} Raman shift. A small portion is scattered inelastically, 1 in 10^8 photons, and at a different frequency than the incident radiation, called Raman scattering. The Raman scattered light can be lower (Stokes) or higher (anti-Stokes) in energy.[31] Primarily the Stokes peaks are used to analyze and identify samples though in some cases anti-Stokes are used as well. LFRS refers to Raman spectroscopy done in the sub-200 cm^{-1} where the vibrations involve torsions, translations, and rotations which give information about the intermolecular forces and crystal packing. To access this region, strong filters are needed to help reject the Rayleigh scattering so it does not overwhelm the instrument and obscure the Raman scattering in this region.

Raman spectroscopy is an advantageous technique for a number of reasons including the ease at which it can be done. Raman spectroscopy is a non-destructive technique where water (liquid or vapor) does not cause any significant interference and, typically, there is also no sample preparation.

2.3.1.1 Coherent (Ondax) THz-Raman System (Santa Clara, CA)

All the Raman data presented here was taken on a Coherent (Ondax) THz-Raman system (Santa Clara, CA). This system has a 225 mW frequency-stabilized (12 MHz linewidth) semiconductor diode laser with excitation centered at 784.7 nm. The scattered light is analyzed with an Andor Shamrock SR-750 spectrograph and detected with an iDus 416 CCD detector. Using a laser centered at ~785 nm is a good choice for most organic samples and helps balance

factors such as signal strength, fluorescence, and cost.[31] Typically, 225 acquisitions are run with a 3 s exposure time but the number of acquisitions is sometimes increased to decrease noise and reveal weaker peaks. The typical setup yields a useable spectral range of 10-300 cm^{-1} with a spectral resolution of 0.6 cm^{-1}. Our laboratory has two sample setups with this system, an attached powder sample holder and a cryostat holder that allows for the samples to be cooled to 78 K (**Figure 2-5**).

a.

b.

c.
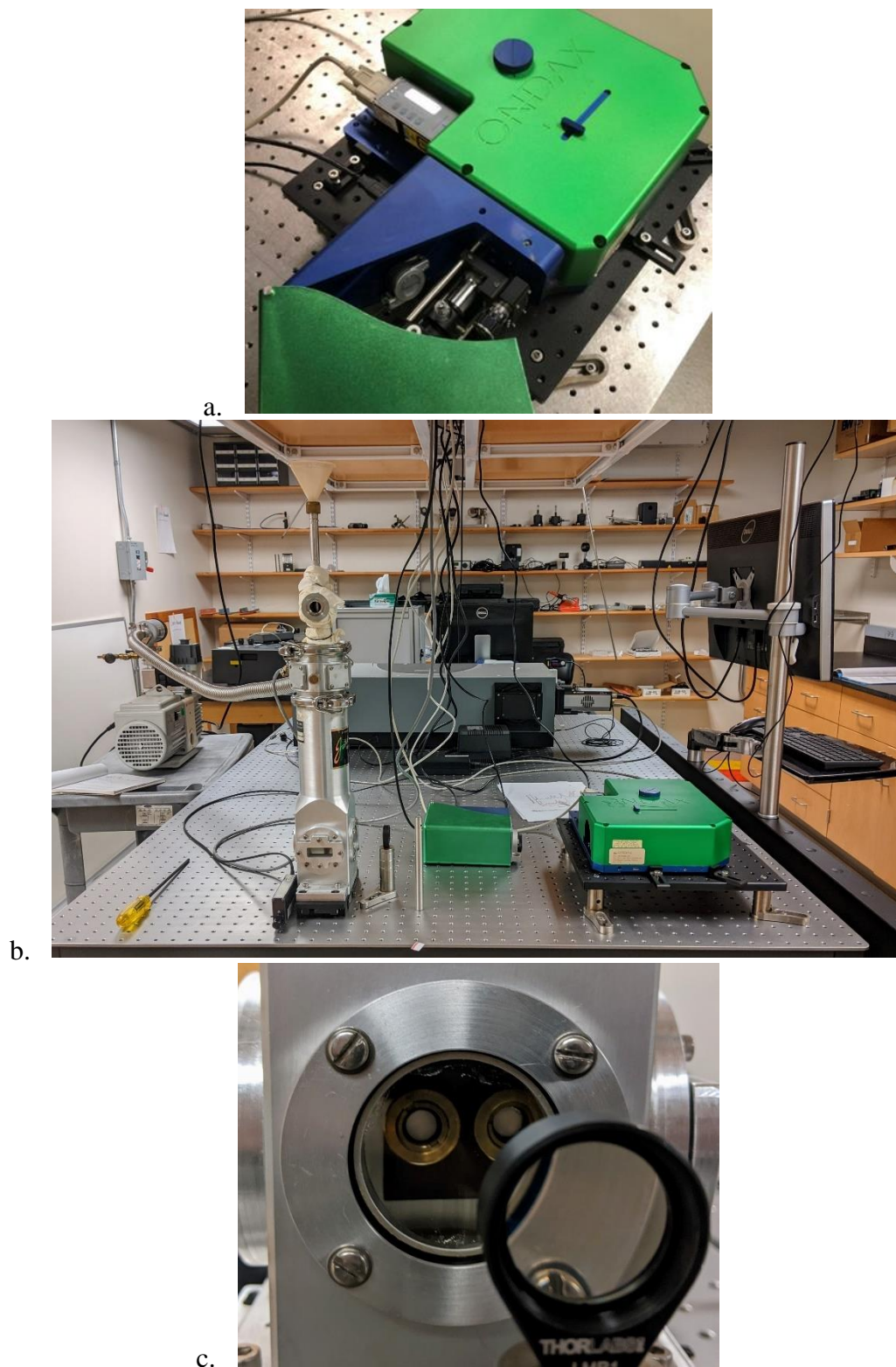
Figure 2-5. a. attached powder sample holder, **b.** cryostat set up, and **c.** the cryostat-mounted brass cuvette system inside the cryostat.

For either sample handling setup, the samples are ground using a mortar and pestle before a spectrum is taken. The attached powder sample holder can run samples at room temperature, 290 K, and has a high signal-noise ratio while the cryostat setup can be run at room temperature, 290 K, or with liquid nitrogen, 78 K, but has a worse signal-noise ratio because of the longer path length the laser light has to travel and the less efficient optical collection of the scattered light. The cryostat setup has optically clear glass windows with a brass cuvette system, so that powder samples can be mounted inside the cryostat. In some cases, when the cryostat system is used, the rotational spectrum of air (specifically N_2 and O_2) can be seen and this then has to subtracted out to produce a clean Raman spectrum of the desired sample.

2.3.2 Terahertz Spectroscopy

IR-active modes occur when the vibration causes a change in the dipole moment of the sample. IR spectroscopy can be done in numerous ways with a variety of different instruments. Here the focus is on terahertz or far-infrared spectroscopy, which has historically been more difficult to perform than higher-frequency IR spectroscopy but advances in terahertz detection and generation has made this region more accessible. Terahertz spectroscopy is a non-ionizing and non-destructive method that can be useful in detecting and identifying diverse materials such as pharmaceuticals, explosives, and biomaterials, and can even penetrate through pharmaceutical tablets and clothing.[32, 33]

2.3.2.1 Terahertz Time-Domain Spectroscopy (THz-TDS)

All of the THz-TDS shown here was taken in Prof. Michal Ruggiero's research group at the University of Vermont using a Toptica Photonics TeraFlash (Munich, Germany) (**Figure 2-6.a.**) with a bandwidth of 10-167 cm^{-1}. The TeraFlash is a time-domain (not time-resolved) instrument and is based on a pulsed λ=1.5 µm femtosecond fiber laser. For THz generation, it

uses an InGaAs 25 µm strip-line photoconductive antenna and for detection it uses a 25 µm

InGaAs dipole photoconductive antenna. Samples were ground and mixed with

polytetrafluoroethylene (PTFE) (usually at 1-3% w/w) before they were pressed into a 13 mm

diameter x 3 mm thick pellet (**Figure 2-6.b.**). A blank reference pellet was also made and was

used to ratio out the matrix absorption by the PTFE in the sample pellet. All data was taken

within a closed-cycle helium cryostat from Cryocool Industries with TPX polymer windows. The

acquisition settings for each sample and blank measurement were a 50 ps time window to sample

the time-domain THz waveform and then averaged over 20,000 scans which takes approximately

30 minutes.

a.   b.
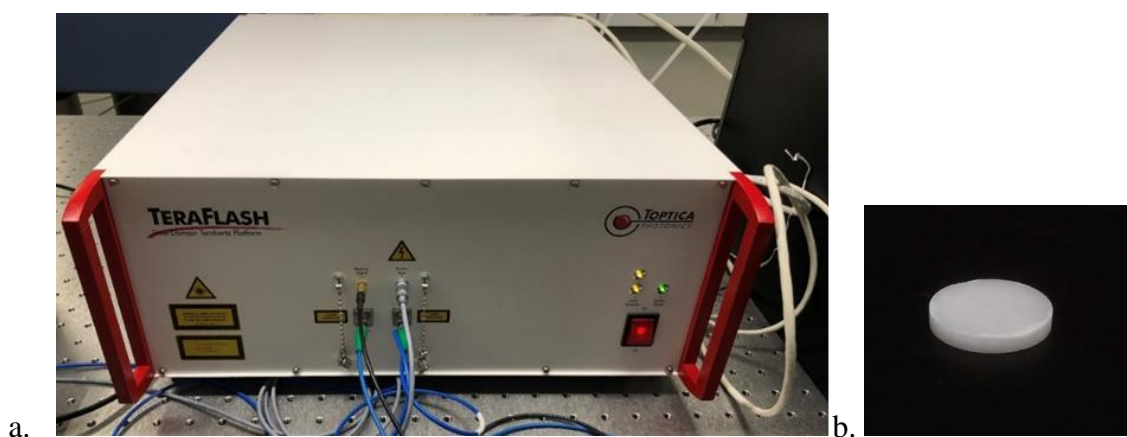
Figure 2-6. a. Toptica TeraFlash and **b.** a THz pellet.

2.3.2.2 Terahertz Frequency-Domain Spectroscopy (THz-FDS)

All terahertz frequency-domain spectroscopy was taken at Hitachi High-Tech in

Hitachinaka, Japan at 295 K. The following description of their setup was provided by Dr.

Mizuki Mohara and Dr. Kei Shimura at Hitachi High-Tech: "The frequency-domain THz

spectrometer uses an injection-seeded THz parametric generation (is-TPG) source. Amplified

light from the Q-switched Nd:YAG microchip laser (wavelength: 1064 nm) was used as the

pump light for is-TPG. This pump beam and a continuous-wave (CW) tunable diode laser beam

were focused on the MgO doped LiNbO3 crystal. The CW beam was used as an injection seeder

to generate narrowband THz waves parametrically. The THz waves from 0.8 to 2.5 THz were

generated by scanning the wavelength of the seeder laser from 1067.5 to 1074.0 nm. The angle

of the seeding beam to the pumping beam was adjusted by a galvano mirror for every

wavelength during the scanning. Generated THz waves were focused on the sample tablet.

Mixing the transmitted THz wave with pump light in another MgO doped LiNbO3 crystal

generates an upconverted signal. The upconverted signal is detected using a 2D-CMOS sensor

(**Figure 2-7**)."[34, 35]
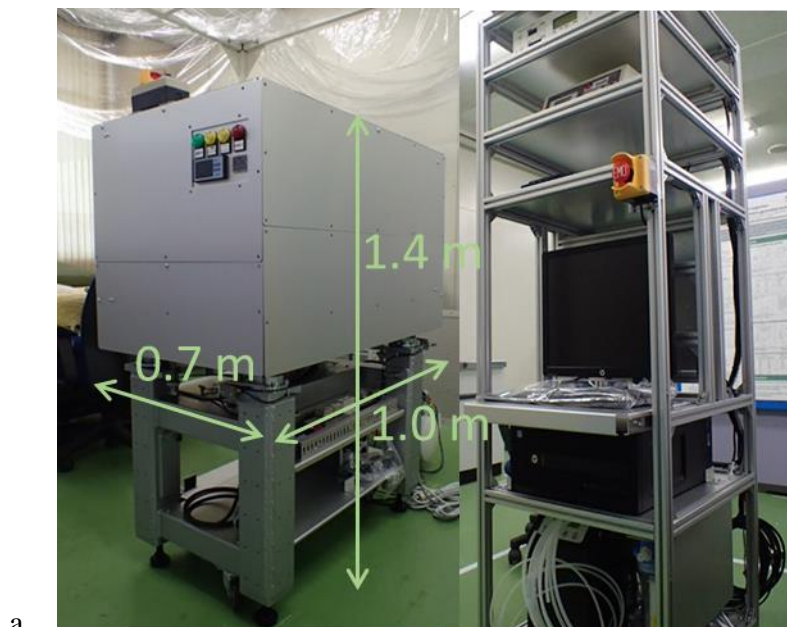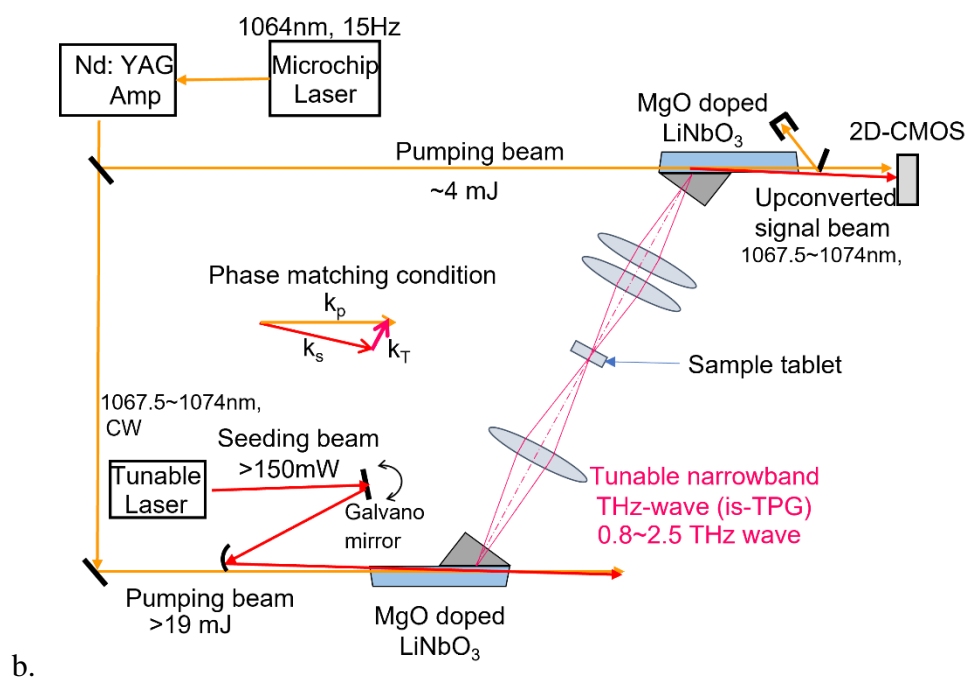
Figure 2-7. a. Hitachi High-Tech frequency-domain THz spectrometer and **b.** diagram of the frequency-domain THz spectrometer set up. (Both images provided by Hitachi High-Tech.)

2.4 References

1.   Groom, C. R.; Bruno, I. J.; Lightfoot, M. P.; Ward, S. C., The Cambridge Structural Database. *Acta Crystallographica Section B: Structural Science, Crystal Engineering and Materials* **2016,** *72* (2), 171-179.

2.   Beard, M. C.; Turner, G. M.; Schmuttenmaer, C. A., Terahertz Spectroscopy. *The Journal of Physical Chemistry B* **2002,** *106* (29), 7146-7159.

3.   Kimmitt, M. F., Restrahlen to T-Rays - 100 Years of Terahertz Radiation. *J. Biol. Phys.* **2003,** *29* (2-3), 77-85.

4.   Larkin, P. J.; Dabros, M.; Sarsfield, B.; Chan, E.; Carriere, J. T.; Smith, B. C., Polymorph Characterization of Active Pharmaceutical Ingredients (Apis) Using Low-Frequency Raman Spectroscopy. *Applied spectroscopy* **2014,** *68* (7), 758-776.

5.   Dierks, T. M.; Korter, T. M., Comparison of Intermolecular Forces in Anhydrous Sorbitol and Solvent Cocrystals. *The Journal of Physical Chemistry A* **2017,** *121* (30), 5720-5727.

6.   Bragg, W. H.; Bragg, W. L., The Reflection of X-Rays by Crystals. *Proceedings of the Royal Society of London. Series A, Containing Papers of a Mathematical and Physical Character* **1913,** *88* (605), 428-438.

7.   Dinnebier, R. E.; Billinge, S. J., Principles of Powder Diffraction. In *Powder Diffraction: Theory and Practice*, Dinnebier, R. E.; Billinge, S. J., Eds. Royal society of chemistry: 2008.

8.   Pecharsky, V.; Zavalij, P., *Fundamentals of Powder Diffraction and Structural Characterization of Materials*. Springer Science & Business Media: 2008.

9.   Jenkins, R.; Snyder, R. L., *Introduction to X-Ray Powder Diffractometry (Volume 138)*. Wiley Online Library: 1996.

10.   Cockcroft, J. K.; Fitch, A. N., Experimental Setups. In *Powder Diffraction: Theory and Practice*, Dinnebier, R. E.; Billinge, S. J., Eds. Royal society of chemistry: 2008.

11.   Harris, K. D., Powder Diffraction Crystallography of Molecular Solids. *Advanced X-ray crystallography* **2011**, 133-177.

12.   BRUKER Diffrac.Suite Software Family. https://www.bruker.com/en/products-and-solutions/diffractometers-and-scattering-systems/x-ray-diffractometers/diffrac-suite-software.html.

13.   Macrae, C. F.; Sovago, I.; Cottrell, S. J.; Galek, P. T.; McCabe, P.; Pidcock, E.; Platings, M.; Shields, G. P.; Stevens, J. S.; Towler, M., Mercury 4.0: From Visualization to Analysis, Design and Prediction. *Journal of applied crystallography* **2020,** *53* (1), 226-235.

14.   Svane, B.; Tolborg, K.; Jørgensen, L. R.; Roelsgaard, M.; Jørgensen, M. R. V.; Brummerstedt Iversen, B., Multipole Electron Densities and Atomic Displacement Parameters in Urea from Accurate Powder X-Ray Diffraction. *Acta Crystallographica Section A: Foundations and Advances* **2019,** *75* (4), 600-609.

15.   Bērziņš, K.; Fraser-Miller, S. J.; Gordon, K. C., Recent Advances in Low-Frequency Raman Spectroscopy for Pharmaceutical Applications. *International Journal of Pharmaceutics* **2021,** *592*, 120034.

16.   Parrott, E. P. J.; Zeitler, J. A., Terahertz Time-Domain and Low-Frequency Raman Spectroscopy of Organic Materials. *Applied Spectroscopy* **2015,** *69* (1), 1-25.

17.   Zeitler, J. A.; Taday, P. F.; Newnham, D. A.; Pepper, M.; Gordon, K. C.; Rades, T., Terahertz Pulsed Spectroscopy and Imaging in the Pharmaceutical Setting-a Review. *Journal of Pharmacy and Pharmacology* **2007,** *59* (2), 209-223.

18.   Inoue, M.; Hisada, H.; Koide, T.; Fukami, T.; Roy, A.; Carriere, J.; Heyler, R., Transmission Low-Frequency Raman Spectroscopy for Quantification of Crystalline Polymorphs in Pharmaceutical Tablets. *Analytical chemistry* **2019,** *91* (3), 1997-2003.

19.   Inoue, M.; Hisada, H.; Koide, T.; Carriere, J.; Heyler, R.; Fukami, T., In Situ Monitoring of Crystalline Transformation of Carbamazepine Using Probe-Type Low-Frequency Raman Spectroscopy. *Organic Process Research & Development* **2017,** *21* (2), 262-265.

20.   Delaney, S. P.; Korter, T. M., Terahertz Spectroscopy and Computational Investigation of the Flufenamic Acid/Nicotinamide Cocrystal. *The Journal of Physical Chemistry A* **2015,** *119* (13), 3269-3276.

21.   Lipiäinen, T.; Fraser-Miller, S. J.; Gordon, K. C.; Strachan, C. J., Direct Comparison of Low-and Mid-Frequency Raman Spectroscopy for Quantitative Solid-State Pharmaceutical Analysis. *Journal of pharmaceutical and biomedical analysis* **2018,** *149*, 343-350.

22.   Robert, C.; Fraser-Miller, S. J.; Berzins, K.; Okeyo, P. O.; Rantanen, J.; Rades, T.; Gordon, K. C., Monitoring the Isothermal Dehydration of Crystalline Hydrates Using Low-Frequency Raman Spectroscopy. *Molecular Pharmaceutics* **2021,** *18* (3), 1264-1276.

23.   Parrott, E. P.; Zeitler, J. A.; Friščić, T.; Pepper, M.; Jones, W.; Day, G. M.; Gladden, L. F., Testing the Sensitivity of Terahertz Spectroscopy to Changes in Molecular and Supramolecular Structure: A Study of Structurally Similar Cocrystals. *Crystal Growth & Design* **2009,** *9* (3), 1452-1460.

24.   Sherwood, P. M. A., *Vibrational Spectroscopy of Solids*. CUP Archive: 1972.

25.   Larkin, P., *Infrared and Raman Spectroscopy: Principles and Spectral Interpretation*. Elsevier: 2017.

26.   Griffiths, D. J., *Introduction to Quantum Mechanics*. Pearson International Edition (Pearson Prentice Hall, Upper Saddle River, 2005): 1962.

27.   Harris, D. C.; Bertolucci, M. D., *Symmetry and Spectroscopy: An Introduction to Vibrational and Electronic Spectroscopy*. Courier Corporation: 1989.

28.   Kaufman, E. D., *Advanced Concepts in Physical Chemistry*. McGraw-Hill: 1966.

29.   Wilson, E. B.; Decius, J. C.; Cross, P. C., *Molecular Vibrations: The Theory of Infrared and Raman Vibrational Spectra*. Courier Corporation: 1980.

30.   Hoffmann, G. G., *Raman Spectroscopy, Volume I: Principles and Applications in Chemistry, Physics, Materials Science, and Biology*. Momentum Press: 2019.

31.   Jones, R. R.; Hooper, D. C.; Zhang, L.; Wolverson, D.; Valev, V. K., Raman Techniques: Fundamentals and Frontiers. *Nanoscale research letters* **2019,** *14* (1), 1-34.

32.   Zeitler, J. A. R., Thomas; Taday, Philip F. , Pharmaceutical and Security Applications of Terahertz Spectroscopy. In *Terahertz Spectroscopy: Principles and Applications*, Dexheimer, S. L., Ed. CRC press: 2008; pp 299-320.

33.   Neu, J.; Schmuttenmaer, C. A., Tutorial: An Introduction to Terahertz Time Domain Spectroscopy (Thz-Tds). *Journal of Applied Physics* **2018,** *124* (23), 231101.

34.   Mohara, M.; Aiko, K.; Shimura, K.; Ono, T. In *Quantitative Analysis and Inspection for Pharmaceutical Polymorphism with Injection-Seeded Terahertz Parametric Generation Technique*, 2018 43rd International Conference on Infrared, Millimeter, and Terahertz Waves (IRMMW-THz), IEEE: 2018; pp 1-2.

35.   Davis, M. P.; Mohara, M.; Shimura, K.; Korter, T. M., Simulation and Assignment of the Terahertz Vibrational Spectra of Enalapril Maleate Cocrystal Polymorphs. *The Journal of Physical Chemistry A* **2020,** *124* (47), 9793-9800.

Chapter 3: Computational Methods

3.1 Introduction

In this work, quantum mechanical computational techniques are used to investigate the

energies, structures, and vibrations of a variety of polymorphs, hydrates, and cocrystals. At their

core, these computational techniques have the concept of wave-particle duality which allows any

entity to be described as either a wave or a particle and for the full investigation of the quantum

mechanics of a system. When describing a particle as a wave, the wave function can illustrate all

the physical properties of a system.[1] Schrödinger proposed an equation to solve for the wave

function of a system (ψ) and this equation can be given as time-independent or dependent

depending on the desired use.[2] The time-independent Schrödinger equation is:

$$H\psi = E\psi \tag{3.1}$$

Eq. 3.1 is the general time-independent Schrödinger equation where H is the Hamiltonian

operator that gives the energy of the system, ψ is the eigenstate of the Hamiltonian, and E is an

eigenvalue (in this case the energy). For a many-particle system, such as the ones studied here,

the motion of all the particles is correlated which makes the Schrödinger equation difficult to

understand and express.[3] To make this simpler, Born and Oppenheimer proposed separating the

nuclei wave functions and the electron wave functions, since protons and neutrons have a much

larger mass than electrons. This allows for the electronic Schrödinger equation to be defined for

fixed nuclei positions:[1, 4]

$$\left[-\frac{\hbar}{2m} \sum_{i=1}^{N} \nabla_i^2 + \sum_{i=1}^{N} V(\boldsymbol{r_i}) + \sum_{i=1}^{N} \sum_{j<i} U(r_i, r_j) \right] \psi = E\psi \tag{3.2}$$

Eq. 3.2 is a more complicated equation than eq. 3.1 but is a more descriptive representation of the time-independent Schrödinger equation for the case where there are many atoms and, therefore, many electrons and nuclei. In eq. 3.2, the three terms on the left side of the equation represent the kinetic energy of each electron, the interaction between each electron and the nuclei, and the interaction between the electrons, respectively.

3.2 Density Functional Theory

Eq 3.2 can be solved to fully describe the system; however, further approximations and theorems are needed to make the problem tractable. One property that becomes critical in developing density functional theory is the electron density, ρ, or the probability of finding an electron in a certain region of space. The electron density gives us all the information needed to define the Hamiltonian. In 1964, Hohenberg and Kohn developed two theorems that help define the electron density, based off electrons interacting with each other and the attraction from the nuclei (otherwise known as an external potential). The first theorem is that the ground state electron density uniquely determines the Hamiltonian operator and, therefore, all properties of the ground state. The second theorem helps us determine the ground state electron density through the variational principle, which states that the ground state electron density is the one that minimizes the total energy. In combination, these two theorems give us a way to determine the electron density of a system which, in turn, determines all properties of the system.[5] To apply these theorems to chemical systems, Kohn and Sham developed a series of equations for a system of non-interacting electrons that have the same electron density as a system of interacting electrons.[6] The energy functional, a function that defines the total energy of the system, can then be divided as shown below:

$$E[\rho(\mathbf{r})] = T_{ni}[\rho(\mathbf{r})] + V_{ne}[\rho(\mathbf{r})] + V_{ee}[\rho(\mathbf{r})] + \Delta T[\rho(\mathbf{r})] + \Delta V_{ee}[\rho(\mathbf{r})] \qquad (3.3)$$

where T_{ni} is the kinetic energy of the non-interacting electrons, V_{ne} is the potential energy of the nuclear-electron interaction, V_{ee} is the potential energy of the classical electron-electron repulsion, and then the last two terms are a correction to account for the fact that electrons do in fact interact with each other, ΔT is a correction to the kinetic energy and ΔV_{ee} is a correction for all non-classical electron-electron interactions.[7] These correction terms cannot be calculated exactly and are generally put together and labeled as the exchange-correlation energy, E_{xc}.

3.2.1 Density Functionals

Density functionals come into DFT as a way to approximate the exchange-correlation energy. In many cases, a functional for the exchange and a functional for the correlation energy are combined. The ranking of different functionals, from least to most complex, can be represented by "Jacob's Ladder" proposed by Perdew in 2001 based on the biblical Jacob's ladder that led to heaven (**Figure 3-1**).[8]
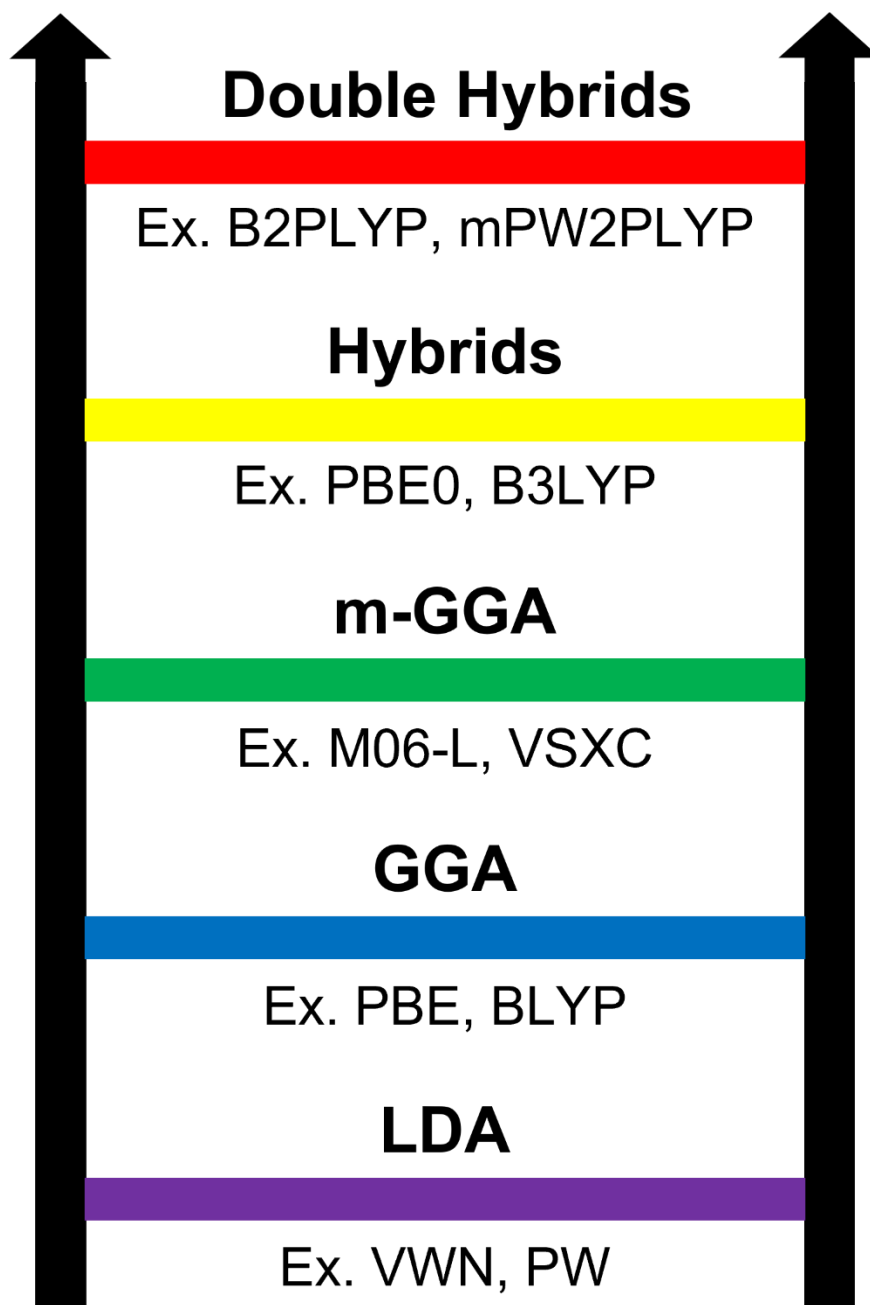
Figure 3-1. Jacob's Ladder of density functionals.

Local Density Approximation (LDA) functionals are the lowest rung of Jacob's Ladder and are based on the fact that the energy density can be calculated at a specific point using only the electron density at that position (known as the local value of the electron density). Usually

this is derived from the uniform electron gas model, a model where the positive charge from the nuclei is uniformly distributed throughout the space.[7] Since this uniform electron gas model is not an accurate representation of the molecular systems studied here, where the electron density can varied throughout the system, LDAs lead to poor results when used for solids. For example, LDAs tend to lead to lattice constants being too small due to an increase in cohesion energy which can be off by 20-30%.[9, 10] The accurate simulation of cohesion energy is critical in helping predict why one crystalline solid may form over another arrangement.

Generalized Gradient Approximation (GGA) functionals are the next rung of the ladder and the one most commonly used here. GGA functionals improve on LDA functionals by depending on the gradient of the density as well as the electron density. These functionals have been developed in a variety of ways, most commonly by adding a correction term to an LDA functional (eq. 3.4).

$$\varepsilon_{X/C}^{GGA}[\rho(\boldsymbol{r})] = \varepsilon_{X/C}^{LDA}[\rho(\boldsymbol{r})] + \Delta\varepsilon_{X/C}\left[\frac{|\nabla\rho(\boldsymbol{r})|}{\rho^{\frac{4}{3}}(\boldsymbol{r})}\right] \qquad (3.4)$$

Some GGAs include empirically-optimized terms while others do not. PBE, developed by Perdew, Burke, and Ernzerhof (1996), is an example of a GGA functional that does not contain any empirically optimized terms and is the functional most commonly used in this work. PBE works well across a variety of systems and with a variety of basis sets (discussed in section 3.3) including large ones.[11]

The next step in the development of GGA functionals was to include the second derivative of the density, i.e. the Laplacian, and these functionals are called meta-GGA

functionals. meta-GGA functionals provide some improvements over GGA functionals but they also have drawbacks due to the Laplacian.[7]

The next rung on the ladder are hybrid functionals. These functionals are called hybrid functionals because they combine Hartree-Fock methods with DFT methods. These functionals use the adiabatic connection method to show that the exchange-correlation energy can be a combination of the Hartree-Fock exchange energy and the DFT exchange-correlation energy.[12] In our group's experience, hybrids such as B3LYP and PBE0 can lead to more accurate results but in the ss-DFT program used here, CRYSTAL17, they often have electronic convergence issues especially when using larger basis sets.[13-15] It should also be noted that as the accuracy of the calculation is increased, the more computational time a calculation will take. A hybrid functional such as PBE0 also runs significantly slower due to the added burden of evaluating the integrals in the periodic Hartree-Fock exchange term. Generally, with the systems studied here PBE provides a balance of accuracy and computational time.

The rungs of the ladder continue upwards to functionals such as double hybrids and random phase approximation. However, functionals are also continuously being developed and improved upon. This means that new functionals are always becoming available and future work in this research group will always include the evaluation of these approaches in relevant chemical systems.

3.2.2 London Dispersion Force Issues

One critical factor in the systems and properties studied here are London dispersion forces. Many functionals have trouble correctly accounting for these forces and therefore, dispersion corrections have been developed to help DFT better account for these important

forces. These dispersion corrections can come in a variety of forms with the most prominent being a series of corrections developed by Grimme. The correction that is used here is Grimme's D3 (DFT-D3) correction term with Becke-Johnson (BJ) damping.[16-18] The inclusion of damping helps correct for the behavior of dispersion at short-range distances and improves on DFT-D3(0), which is the D3 correction with zero damping. Additionally, the pair-wise two-body interaction is corrected to include three-body interactions using the Axilrod-Teller-Muto three-body term (ABC).[19, 20]

3.3 Basis Sets

Basis sets are the mathematical functions that are used to model the molecular orbitals during the calculations. Finite basis sets can be broken down into two main categories: plane-wave basis sets and atom-centered basis sets. Plane-wave basis sets are constructed using a sum of continuous plane-waves to model the molecular orbitals and an energy cutoff is used to determine how many plane-waves are necessary. In practice, a large number of plane-waves are required to model the core and valence electrons. Pseudopotentials have been developed to help solve this problem, but these limit the utility of the plane-wave approach.[21, 22]

In our work, atom-centered basis sets, where the functions used to model the atomic orbitals are centered on the atomic nuclei, are used. Early work on atom-centered basis sets used Slater-type orbitals (STOs) to construct the basis functions.[7] This approach, however, is challenging to scale beyond atomic and diatomic molecules because of the computational time required to evaluate the two-electron integrals.[12] In 1950, Boys developed Gaussian-type orbitals (GTOs) to help solve the computational issues involving STOs.[23] In early GTO basis sets, GTOs were used to approximate the shape of the STOs to combine some of the favorable attributes of

both. Individual or 'primitive' Gaussians can be used to form a linear combination in what are called 'contracted' basis sets. Minimal GTO basis sets, also known as single-ζ, are ones that have one basis function for each orbital up to the valence orbitals. GTO basis sets continued to be developed into double-ζ, triple-ζ, etc. as computational resources increased and more accuracy was desired. The next step in improving these basis sets was the understanding that core electrons are not heavily affected during chemical bonding but valence electrons are and, therefore, the functions defining core electrons can be more fixed while the ones defining valence electrons need more flexibility. This led to 'split-valence' or 'valence-multiple-ζ' basis sets. The Pople basis sets such as 6-31G and 6-311G are still popular basis sets today.[24-29] Further improvements to basis set design include the addition of polarization and diffuse functions. In the work presented here, the two basis sets that are most commonly used are Ahlrichs' VTZ (valence-triple-ζ) basis set with additional polarization functions[30] and def2-TZVP (valence-triple-ζ with polarization).[31] Both Ahlrichs' VTZ basis set with additional polarization functions and def2-TZVP are considered larger basis sets with def2-TZVP being the larger of the two. We have also seen good agreement between theory and experimental work with the slightly smaller basis set of 6-311G(d,p). To give an example of the size differences, for the example system 5-fluorouracil form 2, 6-311G(d,p) has 720 atomic orbitals, Ahlrichs' VTZ basis set with additional polarization functions has 792 atomic orbitals, and def2-TZVP has 1188 atomic orbitals.

One important consideration when choosing a basis set is the amount of basis set superposition error (BSSE) present. BSSE comes from the fact that basis functions from different atoms on different molecules can overlap and one atom can 'borrow' basis functions from another.[32] This can artificially change the energy of the system. Larger basis sets are

advantageous because they have less BSSE.[33-35] BSSE can be corrected for using a standard Boys-Bernardi counterpoise correction and this correction can be seen in many of the works shown here.[12, 36]

3.4 Periodic Boundary Conditions and Reciprocal Space

The calculations here focus on solid-state density functional theory (ss-DFT) as opposed to gas or liquid phase calculations since the systems studied are crystalline solids. One of the most important considerations in modeling solid-state systems is correctly replicating the periodicity of crystalline systems. This is done through periodic boundary conditions (PBC). A three-dimensional crystal can be viewed as a series of repeating chemical units in all directions, essentially to infinity.[1] The infinite structure can be reduced to a unit cell and further to an asymmetric unit within the unit cell. By knowing the asymmetric unit and the symmetry operators that define the unit cell, the entire three-dimensional array can be created (**Figure 3-2**).[37-39]
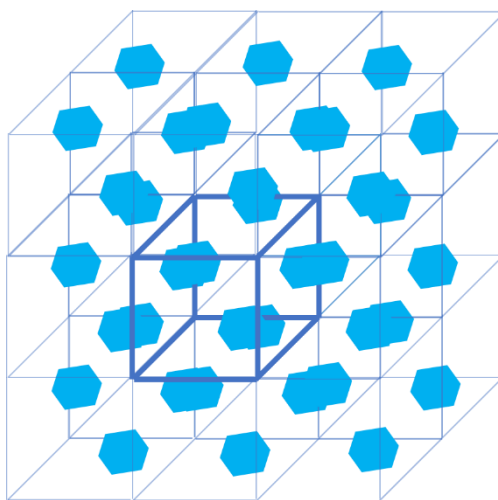
Figure 3-2. Periodic Boundary Conditions: The blue hexagon represents the asymmetric unit, it is replicated to form the unit cell shown in bolded blue lines and that can be replicated in all three-dimensions.

The symmetry present in crystalline solids allows us to make the useful conversion to reciprocal space and utilize Bloch's theorem.[40] The real-space lattice vectors can be transformed into reciprocal space by taking the Fourier transform and this results in the reciprocal lattice.[41] Bloch's theorem states that due to the translation invariance of a periodic crystal, the wave function will change by a phase factor when translation between equivalent lattice positions occurs:

$$\Psi(r + R) = e^{ikR}\Psi(r) \tag{3.5}$$

Bloch's theorem is shown above (eq. 3.5) where k is the wave vector and r is the position vector under translational invariance where $U(r + R) = U(r)$ where R is the lattice vector.[40] In ss-DFT, it is much easier to solve for many properties in reciprocal space (**k**-space) rather than in real space. The primitive unit cell can be transformed into reciprocal space, called the first Brillouin zone.[42] To do calculations within this space, a certain number of points must be chosen to sample the Brillouin zone. There are a number of methods to determine what k-points to use.[43, 44] The method that is used in all the calculations shown here is the Pack-Monkhorst net.[45-47]

3.5 Solid-State Density Functional Theory in CRYSTAL17

3.5.1 Initial Keyword Settings

CRYSTAL17[48] is the program used here to do ss-DFT calculations. The first step in this process is using single point energy calculations to determine the necessary shrinking factor that the Pack-Monkhorst method utilizes to determine the k-points.[46, 47] This is done by performing single point energies using the experimentally determined crystal structure, usually found in the Cambridge Structural Database[49], with incrementally increasing shrinking factors (keyword

SHRINK) and taking the energy difference between the single point energies until the energy change is converged, usually 10^{-10} hartree (**Figure 3-3**).
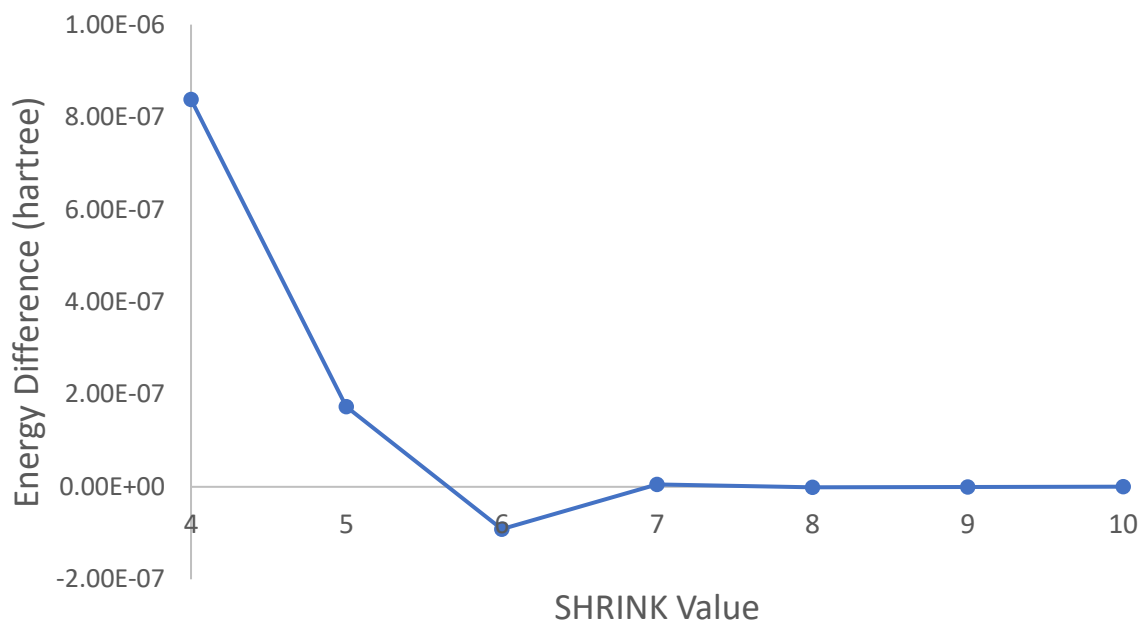
Figure 3-3. An example of energy convergence as a function of SHRINK value.

The initial input file used to perform SHRINK testing includes the experimental crystal structure, a basis set, and a functional along with other keywords (an example single point input file can be found in **Figure 3-4**). Basis sets can be found on the Basis Set Exchange.[50] In terms of dispersion corrections, Grimme's D3 correction[16-18] is included in the functional name (ex. PBE-D) and in the DFTD3 input block the keyword ABC is included to take the three-body dispersion term into account.[19, 20] The TOLINTEG keyword sets the overlap-based truncation criteria for the bielectronic integrals (Coulomb and exchange) and includes five numbers with the last one, generally, being double the first four when using a GGA functional. If during shrinking factor testing or geometry optimization electronic convergence issues are seen, the TOLINTEG may need to be increased. This is especially common when using a hybrid

functional. The energy convergence threshold is set using the TOLDEE keyword and is, generally, set to $\Delta E < 10^{-10}$ hartree for single point energy, vibrational frequency, and other energy calculations and $\Delta E < 10^{-8}$ hartree for geometry optimizations.

```
Urea GeoOpt UREAXX13 SinglePoint
CRYSTAL
0 0 0
113
5.570    4.688
5
6 0.00000 0.50000 0.32650
8 0.00000 0.50000 0.59540
7 0.14550 0.64550 0.17710
1 0.25690 0.75690 0.28320
1 0.14380 0.64380 -0.03710
BASISSET
def2-TZVP
DFT
PBE-D
XXLGRID
END
DFTD3
ABC
END
EXCHSIZE
80000000
BIPOSIZE
80000000
MAXCYCLE
600
SCFDIR
TOLINTEG
10 10 10 10 20
POLEORDR
6
TOLDEE
10
SHRINK
8 8
END
END
```

Figure 3-4. Single point input example for CRYSTAL17.

3.5.2 Geometry Optimizations

After a SHRINK value has been determined, a geometry optimization can be performed. A geometry optimization varies the initial structure to find a structure that minimizes the total energy of the system. In CRYSTAL, this is done using a Quasi-Newton optimization scheme by including the OPTGEOM input block after the crystal structure in the input file. There are a number of different types of geometry optimizations that are included in the following chapters. The most common type is the full optimization where the lattice dimensions and atomic positions are allowed to optimize (this is the default). Atom-only and constant volume optimizations are also used here. In atom-only optimizations (ATOMONLY keyword) only the atomic positions are optimized and the lattice dimensions are kept constant. In a constant volume optimization (CVOLOPT) the volume is kept constant and the lattice dimensions and atomic positions are allowed to optimize within that constraint (examples of all of these can be seen in **Figure 3-5**).

```
                      OPTGEOM          OPTGEOM
   OPTGEOM            ATOMONLY         CVOLOPT
   TOLDEG            TOLDEG           TOLDEG
   0.000010          0.000010         0.000010
   TOLDEX            TOLDEX           TOLDEX
   0.000040          0.000040         0.000040
   END              END              END
a. BASISSET      b. BASISSET      c. BASISSET
```

Figure 3-5. Examples of **a.** a full optimization, **b.** an atom-only optimization, and **c.** a constant volume optimization.

Once a geometry optimization is done, the optimized structure can be analyzed to see how close it is to the experimental structure. A good starting point is to calculate the percent error between the optimized structure and the experimental structure lattice dimensions and

volume as well as the root-mean-square-deviation between the bond lengths, bond angles, torsions, and intermolecular hydrogen bond lengths and angles (if applicable) of the two structures. Depending on the system studied, some values may be more important than others. These comparisons should be done carefully, remembering that the optimized structure is essentially a 0 K structure and the experimental structure may be a low temperature structure (easier to compare to), a room temperature, or even a higher temperature structure (harder to compare to). If the experimental structure was solved via powder X-ray diffraction, errors may also be higher since the structure may not be as accurate as a single-crystal X-ray structure. One may also see higher errors if the hydrogen atoms were not solved for in the initial structure and had to be added in Mercury, a visualization software, or if any of the atomic positions needed to be corrected because they did not make chemical sense.[51]

3.5.3 Vibrational Frequencies

After a geometry optimization, generally, a vibrational frequency calculation is the next step. The FREQCALC keyword calculates the vibrational frequencies using the harmonic approximation. By default, only the intensity of IR-active vibrational frequencies are calculated and this is done using the Berry phase method.[52, 53] To calculate the intensity of the Raman-active modes, one must include the INTRAMAN keyword along with the RAMEXP keyword which allows for the experimental temperature and laser wavelength to be inputted. Generally, when doing Raman intensities, the INTCPHF keywords is included so that the intensities (both IR and Raman) are calculated using the Coupled-Perturbed Hartree–Fock/Kohn–Sham method (examples can be seen in **Figure 3-6**).[54-57] An important option within the frequency input block is the choice between the 1-point or 2-point numerical derivative (keyword NUMDERIV). The 1-point numerical derivative means that the calculation uses the difference quotient formula and

displaces each atom once along each Cartesian axis. The 2-point numerical derivative uses the central-difference formula and does two displacements along each Cartesian axis for each atom (examples can be seen in **Figure 3-6**). The 2-point numerical derivative is more accurate, but slower by a factor of two. If negative (imaginary) modes are seen with a calculation done with the 1-point numerical derivative it should be restarted with the 2-point numerical derivative to see if this improves the calculation. Negative (imaginary) modes can indicate that the structure is not a minimum on the potential energy surface. The energy difference listed in the output file for each atomic displacement is also a good indicator of any issues within the calculation. Energy changes should be positive for all displacements; however, it is not unusual to see negative energy differences. This could be indicative of a variety of issues but improvements have been seen by including the POLEORDR keyword. The POLEORDR keyword determines the maximum order of the multipolar expansion and is by default set to 4 with a maximum value of 6. Increasing it to 6 increases the numerical accuracy of the calculation and has been seen to decrease the occurrence of negative energy differences (can be seen in **Figure 3-4**).

```
                                 FREQCALC
                                 NUMDERIV
                                 2
                                 INTENS
                                 INTRAMAN
                                 RAMEXP
                                 295.0 785.0
        FREQCALC                 INTCPHF
        NUMDERIV                 ANDERSON
        1                        ANDERSON2
        INTENS                   END
        END                      END
        BASISSET                 BASISSET
    a.                       b.
```

Figure 3-6. Example of **a.** a frequency input block for only IR intensities with the 1-point numerical derivative and **b.** for IR and Raman intensities with the 2-point numerical derivative.

The simulated vibrational frequencies and intensities can be convolved with a normalized Lorentzian line shape to produce a spectrum that can be compared to the experimental results. The normalized Lorentzian line shape can be modified with the empirical full width at half maximum (FWHM) which can be determined by fitting the experimental peaks with a Lorentzian and determining a reasonable FWHM. When comparing a simulated Raman spectrum to an experimental Raman spectrum, the y-axis units (intensity) can be normalized (**Figure 3-7b.**). When comparing a simulated IR spectrum to an experimental terahertz spectrum, the intensities are converted to molar extinction coefficient ($M^{-1}cm^{-1}$) (**Figure 3-7a.**).

a.   b.
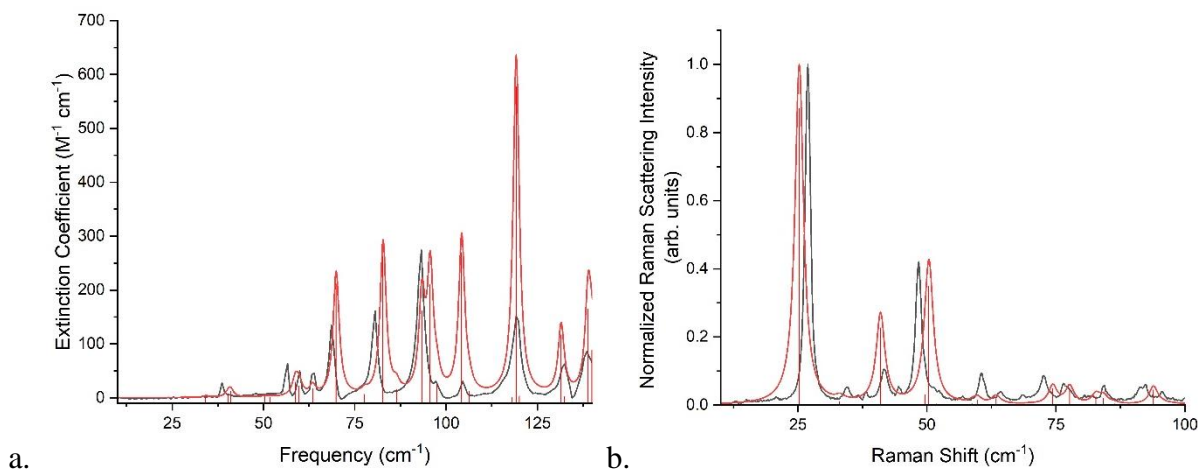
Figure 3-7. Ribavirin form II **a.** experimental 20 K THz spectrum (left, black) and the fully-optimized ss-DFT simulated (linewidth 1) (left, red) and **b.** 78 K low-frequency Raman spectrum (right, black) and the 78 K ss-DFT simulated (linewidth 1) (right, red).

3.5.4 Energy Analysis

3.5.4.1 Conformational and Cohesion Energy

ss-DFT allows for the total energy of the solid to be broken down into the conformational and cohesion energies. The total energy can be found by running a single point energy calculation on the optimized structure.

Conformational energy depends on the three-dimensional arrangement of the atoms of the individual molecule in the crystal. This can be determined by including the MOLECULE keyword after the structure part of the input file (an example MOLECULE input block can be found in **Figure 3-8**). After the MOLECULE keyword appears, the number of molecules to be extracted from the crystal (usually 1) is listed along with the label of an atom in the molecule to be extracted and the integer coordinates of the cell containing the atom (usually 0 0 0). The default value of the atomic covalent radii may also need to be modified so that the entire molecule is extracted (keyword RAYCOV). This job will run similarly to a typical single point energy, but just on the extracted molecule.

Issues can occur with this procedure when performing it on zwitterions or other charged molecules. If there are two molecules with opposite charges present in the system (such as in enalapril maleate), the best course of action is to run the MOLECULE job on a dimer of the two molecules. If this is not possible, moving to a hybrid functional sometimes also works.

```
RAYCOV
1
1 0.70
MOLECULE
1
1 0 0 0
END
```

Figure 3-8. Example of the MOLECULE keyword.

Cohesion energy is calculated by subtracting the total conformational energy of the molecules in the unit cell from the total energy of the unit cell (eq. 3.5).

$$E_{cohesive} = E_{total} - \sum_{a}^{N} E_{conformational} \tag{3.5}$$

Cohesion energy represents the energy that is coming from intermolecular forces (**Figure 3-9**).
The conformational and cohesion energy can be useful in determining whether a polymorph is
more likely to be kinetically or thermodynamically formed.
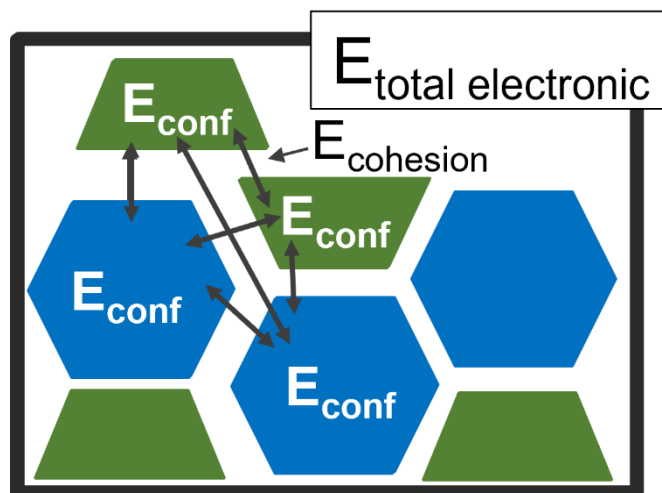
Figure 3-9. A graphical representation of total electronic energy ($E_{total\ electronic}$), conformational
energy (E_{conf}), and cohesion energy ($E_{cohesion}$). The blue and green shapes represent individual
molecules.

3.5.4.1.1 Correcting for BSSE

To correct for BSSE, the MOLEBSSE keyword is used, which is similar to the
MOLECULE keyword used above but has an additional parameter for the number of ghost
atoms (an example MOLEBSSE input block can be found in **Figure 3-10**). Generally, one starts
with 50 ghost atoms and continues to increase by 25 ghost atoms until the correction energy
plateaus and the estimated amount of BSSE not accounted for is under 1% (not all BSSE can be
accounted for in an infinite crystal). This allows for the BSSE per unit cell to be calculated and
this can be used to correct the determined cohesion energy. The maximum size of a cluster may
also need to be increased as the number of ghost atoms is increased (keyword CLUSTSIZE). As
stated in the basis set section (3.3), for large basis sets such as def2-TZVP[31] and Ahlrichs' VTZ

basis set with additional polarization[30] functions the contribution from BSSE is not large. It

becomes more important to correct for BSSE when using a smaller basis set. Generally, for the

6-311G(d,p) basis set BSSE accounts for around 20% of the cohesion energy, for the Ahlrichs'

VTZ basis set with additional polarization functions BSSE accounts for around 10% of the

cohesion energy, and for the def2-TZVP basis set it accounts for around 5% of the cohesion

energy. A BSSE correction could be applied for every step of the geometry and frequency

calculations, but this is unrealistic in terms of computational time and in most scenarios would

have a small enough effect to not warrant the greatly increased run times. It is more important to

correct for BSSE when comparing systems such as polymorphs of the same molecule that are

close in energy where the energetic ordering could be altered.

```
RAYCOV
1
1 0.35
CLUSTSIZE
10000
MOLEBSSE
1
1 0 0 0
50 10
END
```

Figure 3-10. Example of the MOLEBSSE keyword.

3.5.4.2 Gibbs Free Energy

Gibbs free energy values and curves can also be calculated from the vibrational analysis.

Gibbs free energy is important because it includes factors such as vibrational energy and entropy.

Eq. 3.6 shows the equation for Gibbs free energy (G) where E is the electronic energy, E^{ZPE} is

the zero-point energy, E^T is the thermal contribution to the vibrational energy, PV is pressure x

volume, and TS is temperature x entropy:

$$G = E + E^{ZPE} + E^T + PV - TS \tag{3.6}$$

The frequency analysis will by default report the electronic energy and the zero-point energy as well as the Gibbs free energy at 298.15 K. To obtain the Gibbs free energies over a certain temperature range, restart a completed frequency calculation with the TEMPERAT keyword (an example of using the TEMPERAT keyword can be found in **Figure 3-11**). Generally, the temperature range should at least go past the melting point of the system. This will produce an output with all of the frequency analysis information as well as the Gibbs free energy values at every 1 K between the temperature range given.

```
FREQCALC
RESTART
TEMPERAT
701 0.0 700.0
NUMDERIV
2
INTENS
INTRAMAN
RAMEXP
78.0 785.0
INTCPHF
ANDERSON
ANDERSON2
END
END
```

Figure 3-11. Example of TEMPERAT keyword in the frequency block.

Once this output has been produced, the Linux command "grep 'EL+E0+ET' output.out>newoutput.out" can be used to extract all lines in the output that begin with EL+E0+ET. These energetic values should be divided by the crystallographic Z value (the number of formula units in the unit cell) and plotted versus the temperature. Gibbs free energy curves are useful for comparing the stability of polymorphs at different temperatures as well as for comparing the stability of a cocrystal to its pure components (**Figure 3-12**).
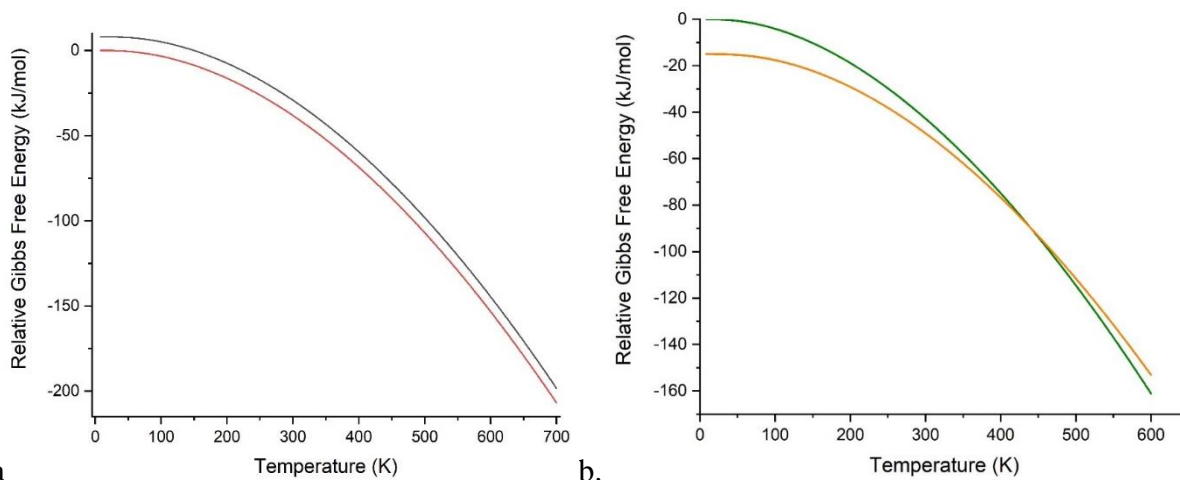
Figure 3-12. a. Relative Gibbs free energy curve for ribavirin form II (red) and ribavirin form I (black). **b.** Relative Gibbs free energy curve for cocrystallized thiourea:DL-tartaric acid (green) and the linear combination of relative Gibbs free energies of pure thiourea and pure DL-tartaric acid (orange). All energies are per asymmetric unit. For clarity, the energy values have been set relative to a common zero.

3.6 References

1.   Sholl, D.; Steckel, J. A., *Density Functional Theory: A Practical Introduction*. John Wiley & Sons: 2011.

2.   Schrödinger, E., Quantisierung Als Eigenwertproblem. *Annalen der physik* **1926,** *385* (13), 437-490.

3.   Schrödinger, E., An Undulatory Theory of the Mechanics of Atoms and Molecules. *Physical review* **1926,** *28* (6), 1049.

4.   Born, M.; Oppenheimer, R., Zur Quantentheorie Der Molekeln. *Annalen der physik* **1927,** *389* (20), 457-484.

5.   Hohenberg, P.; Kohn, W., Inhomogeneous Electron Gas. *Physical review* **1964,** *136* (3B), B864.

6.   Kohn, W.; Sham, L. J., Self-Consistent Equations Including Exchange and Correlation Effects. *Physical review* **1965,** *140* (4A), A1133.

7.   Cramer, C. J., *Essentials of Computational Chemistry: Theories and Models*. John Wiley & Sons: 2013.

8.   Perdew, J. P.; Schmidt, K. In *Jacob's Ladder of Density Functional Approximations for the Exchange-Correlation Energy*, AIP Conference Proceedings, American Institute of Physics: 2001; pp 1-20.

9.   Zhang, G.-X.; Reilly, A. M.; Tkatchenko, A.; Scheffler, M., Performance of Various Density-Functional Approximations for Cohesive Properties of 64 Bulk Solids. *New Journal of Physics* **2018,** *20* (6), 063020.

10.   Tran, F.; Stelzl, J.; Blaha, P., Rungs 1 to 4 of Dft Jacob's Ladder: Extensive Test on the Lattice Constant, Bulk Modulus, and Cohesive Energy of Solids. *The Journal of chemical physics* **2016,** *144* (20), 204120.

11.   Perdew, J. P.; Burke, K.; Ernzerhof, M., Generalized Gradient Approximation Made Simple. *Physical Review Letters* **1996,** *77* (18), 3865.

12.   Lewars, E. G., Computational Chemistry: Introduction to the Theory and Applications of Molecular and Quantum Mechanics. *Springer, New York* **2011,** *43*, 44-45.

13.   Becke, A. D., A New Mixing of Hartree–Fock and Local Density-Functional Theories. *The Journal of chemical physics* **1993,** *98* (2), 1372-1377.

14.   Stephens, P. J.; Devlin, F. J.; Chabalowski, C. F.; Frisch, M. J., Ab Initio Calculation of Vibrational Absorption and Circular Dichroism Spectra Using Density Functional Force Fields. *The Journal of physical chemistry* **1994,** *98* (45), 11623-11627.

15.   Adamo, C.; Barone, V., Toward Reliable Density Functional Methods without Adjustable Parameters: The Pbe0 Model. *The Journal of chemical physics* **1999,** *110* (13), 6158-6170.

16.   Grimme, S.; Antony, J.; Ehrlich, S.; Krieg, H., A Consistent and Accurate Ab Initio Parametrization of Density Functional Dispersion Correction (Dft-D) for the 94 Elements H-Pu. *The Journal of Chemical Physics* **2010,** *132* (15), 154104.

17.   Grimme, S.; Ehrlich, S.; Goerigk, L., Effect of the Damping Function in Dispersion Corrected Density Functional Theory. *Journal of computational chemistry* **2011,** *32* (7), 1456-1465.

18.   Grimme, S.; Hansen, A.; Brandenburg, J. G.; Bannwarth, C., Dispersion-Corrected Mean-Field Electronic Structure Methods. *Chemical Reviews* **2016,** *116* (9), 5105-5154.

19.   Axilrod, B.; Teller, E., Interaction of the Van Der Waals Type between Three Atoms. *The Journal of Chemical Physics* **1943,** *11* (6), 299-300.

20.   Muto, Y., Force between Nonpolar Molecules. *J. Phys. Math. Soc. Jpn* **1943,** *17*, 629-631.

21.   Kohanoff, J., *Electronic Structure Calculations for Solids and Molecules: Theory and Computational Methods*. Cambridge university press: 2006.

22.   Marx, D.; Hutter, J., *Ab Initio Molecular Dynamics: Basic Theory and Advanced Methods*. Cambridge University Press: 2009.

23.   Boys, S. F., Electronic Wave Functions-I. A General Method of Calculation for the Stationary States of Any Molecular System. *Proceedings of the Royal Society of London. Series A. Mathematical and Physical Sciences* **1950,** *200* (1063), 542-554.

24.   Krishnan, R.; Binkley, J. S.; Seeger, R.; Pople, J. A., Self-Consistent Molecular Orbital Methods. Xx. A Basis Set for Correlated Wave Functions. *The Journal of chemical physics* **1980,** *72* (1), 650-654.

25.   Hehre, W. J.; Ditchfield, R.; Pople, J. A., Self—Consistent Molecular Orbital Methods. Xii. Further Extensions of Gaussian—Type Basis Sets for Use in Molecular Orbital Studies of Organic Molecules. *The Journal of Chemical Physics* **1972,** *56* (5), 2257-2261.

26.   Dill, J. D.; Pople, J. A., Self-Consistent Molecular Orbital Methods. Xv. Extended Gaussian-Type Basis Sets for Lithium, Beryllium, and Boron. *The Journal of Chemical Physics* **1975,** *62* (7), 2921-2923.

27.   Francl, M. M.; Pietro, W. J.; Hehre, W. J.; Binkley, J. S.; Gordon, M. S.; DeFrees, D. J.; Pople, J. A., Self-Consistent Molecular Orbital Methods. Xxiii. A Polarization-Type Basis Set for Second-Row Elements. *The Journal of Chemical Physics* **1982,** *77* (7), 3654-3665.

28.   Rassolov, V. A.; Pople, J. A.; Ratner, M. A.; Windus, T. L., 6-31g* Basis Set for Atoms K through Zn. *The Journal of chemical physics* **1998,** *109* (4), 1223-1229.

29.   Hariharan, P. C.; Pople, J. A., The Influence of Polarization Functions on Molecular Orbital Hydrogenation Energies. *Theoretica chimica acta* **1973,** *28* (3), 213-222.

30.   Schäfer, A.; Horn, H.; Ahlrichs, R., Fully Optimized Contracted Gaussian Basis Sets for Atoms Li to Kr. *The Journal of Chemical Physics* **1992,** *97* (4), 2571-2577.

31.   Weigend, F.; Ahlrichs, R., Balanced Basis Sets of Split Valence, Triple Zeta Valence and Quadruple Zeta Valence Quality for H to Rn: Design and Assessment of Accuracy. *Physical Chemistry Chemical Physics* **2005,** *7* (18), 3297-3305.

32.   Van Duijneveldt, F. B.; van Duijneveldt-van de Rijdt, J. G.; van Lenthe, J. H., State of the Art in Counterpoise Theory. *Chemical Reviews* **1994,** *94* (7), 1873-1885.

33.   Sancho-Garcia, J.-C.; Pérez-Jiménez, A.; Olivier, Y., Determining the Cohesive Energy of Coronene by Dispersion-Corrected Dft Methods: Periodic Boundary Conditions Vs. Molecular Pairs. *The Journal of Chemical Physics* **2015,** *142* (5), 054702.

34.   Schwenke, D. W.; Truhlar, D. G., Systematic Study of Basis Set Superposition Errors in the Calculated Interaction Energy of Two Hf Molecules. *The Journal of chemical physics* **1985,** *82* (5), 2418-2426.

35.   Mayer, I.; Turi, L., An Analytical Investigation into the Bsse Problem. *Journal of Molecular Structure: THEOCHEM* **1991,** *227*, 43-65.

36.   Boys, S. F.; Bernardi, F., The Calculation of Small Molecular Interactions by the Differences of Separate Total Energies. Some Procedures with Reduced Errors. *Molecular Physics* **1970,** *19* (4), 553-566.

37.   Mazurek, A. H.; Szeleszczuk, Ł.; Pisklak, D. M., Periodic Dft Calculations—Review of Applications in the Pharmaceutical Sciences. *Pharmaceutics* **2020,** *12* (5), 415.

38.   Makov, G.; Payne, M., Periodic Boundary Conditions in Ab Initio Calculations. *Physical Review B* **1995,** *51* (7), 4014.

39.   Banks, P. A.; Burgess, L.; Ruggiero, M. T., The Necessity of Periodic Boundary Conditions for the Accurate Calculation of Crystalline Terahertz Spectra. *Physical Chemistry Chemical Physics* **2021,** *23* (36), 20038-20051.

40.   Ashcroft, N. W.; Mermin, N. D., Solid State Physics. holt, rinehart and winston, new york London: 1976.

41.   Martin, R. M., *Electronic Structure: Basic Theory and Practical Methods*. Cambridge university press: 2020.

42.   Pisani, C., *Quantum-Mechanical Ab-Initio Calculation of the Properties of Crystalline Materials*. Springer Science & Business Media: 2012; Vol. 67.

43.   Brandenburg, J. G.; Grimme, S., Dispersion Corrected Hartree–Fock and Density Functional Theory for Organic Crystal Structure Prediction. *Prediction and Calculation of Crystal Structures* **2013**, 1-23.

44.   Kratzer, P.; Neugebauer, J., The Basics of Electronic Structure Theory for Periodic Systems. *Frontiers in chemistry* **2019,** *7*, 106.

45.   Dovesi, R.; Saunders, V.; Roetti, C.; Orlando, R.; Zicovich-Wilson, C.; Pascale, F.; Civalleri, B.; Doll, K.; Harrison, N.; Bush, I., Crystal17 User's Manual. **2017**.

46.   Monkhorst, H. J.; Pack, J. D., Special Points for Brillouin-Zone Integrations. *Physical review B* **1976,** *13* (12), 5188.

47.   Pack, J. D.; Monkhorst, H. J., " Special Points for Brillouin-Zone Integrations"—a Reply. *Physical Review B* **1977,** *16* (4), 1748.

48.   Dovesi, R.; Erba, A.; Orlando, R.; Zicovich-Wilson, C. M.; Civalleri, B.; Maschio, L.; Rérat, M.; Casassa, S.; Baima, J.; Salustro, S., Quantum-Mechanical Condensed Matter Simulations with Crystal. *Wiley Interdisciplinary Reviews: Computational Molecular Science* **2018**, e1360.

49.   Groom, C. R.; Bruno, I. J.; Lightfoot, M. P.; Ward, S. C., The Cambridge Structural Database. *Acta Crystallographica Section B: Structural Science, Crystal Engineering and Materials* **2016,** *72* (2), 171-179.

50.   Pritchard, B. P.; Altarawy, D.; Didier, B.; Gibson, T. D.; Windus, T. L., New Basis Set Exchange: An Open, up-to-Date Resource for the Molecular Sciences Community. *Journal of chemical information and modeling* **2019,** *59* (11), 4814-4820.

51.   Macrae, C. F.; Sovago, I.; Cottrell, S. J.; Galek, P. T.; McCabe, P.; Pidcock, E.; Platings, M.; Shields, G. P.; Stevens, J. S.; Towler, M., Mercury 4.0: From Visualization to Analysis, Design and Prediction. *Journal of applied crystallography* **2020,** *53* (1), 226-235.

52.   Noel, Y.; Zicovich-Wilson, C.; Civalleri, B.; D'arco, P.; Dovesi, R., Polarization Properties of Zno and Beo: An Ab Initio Study through the Berry Phase and Wannier Functions Approaches. *Physical Review B* **2001,** *65* (1), 014111.

53.   Pascale, F.; Zicovich-Wilson, C. M.; López Gejo, F.; Civalleri, B.; Orlando, R.; Dovesi, R., The Calculation of the Vibrational Frequencies of Crystalline Compounds and Its Implementation in the Crystal Code. *Journal of computational chemistry* **2004,** *25* (6), 888-897.

54.   Ferrero, M.; Rérat, M.; Kirtman, B.; Dovesi, R., Calculation of First and Second Static Hyperpolarizabilities of One-to Three-Dimensional Periodic Compounds. Implementation in the Crystal Code. *The Journal of chemical physics* **2008,** *129* (24), 244110.

55.   Ferrero, M.; Rérat, M.; Orlando, R.; Dovesi, R., Coupled Perturbed Hartree-Fock for Periodic Systems: The Role of Symmetry and Related Computational Aspects. *The Journal of chemical physics* **2008,** *128* (1), 014110.

56.   Ferrero, M.; Rérat, M.; Orlando, R.; Dovesi, R., The Calculation of Static Polarizabilities of 1-3d Periodic Compounds. The Implementation in the Crystal Code. *Journal of computational chemistry* **2008,** *29* (9), 1450-1459.

57.   Zicovich-Wilson, C.; Pascale, F.; Roetti, C.; Saunders, V.; Orlando, R.; Dovesi, R., Calculation of the Vibration Frequencies of A-Quartz: The Effect of Hamiltonian and Basis Set. *Journal of computational chemistry* **2004,** *25* (15), 1873-1881.

Chapter 4: Evaluating Hydrogen Bonding in Organic Cocrystals Using Low-Frequency Raman Vibrational Spectroscopy and Quantum Mechanical Simulations

The material contained within this chapter is published in Crystal Growth & Design and has been reproduced with permission of American Chemical Society.

Abstract

Cocrystallization can provide a potential route to usability for active pharmaceutical ingredients that are eliminated in the drug discovery process due to their low bioavailability. In this work, cocrystals of urea and thiourea with glutaric acid and tartaric acid were used as model systems to experimentally and computationally investigate the intermolecular energy factors within heterogeneous molecular crystals. The tools employed in this study were low-frequency Raman vibrational spectroscopy and solid-state density functional theory (ss-DFT). The sub-200 cm^{-1} Raman spectra give insight into vibrations that are characteristic of the crystal packing and the intermolecular forces within the samples. ss-DFT allows for analysis of these vibrations and of the specific energies involved in the collective cocrystal. Moreover, ss-DFT permits the computational investigation of hypothetical cocrystals, utilized here to predict the properties of the unrealized thiourea:DL-tartaric acid cocrystal. These analyses demonstrated that it is both experimentally and computationally favorable for the urea and thiourea glutaric acid cocrystals to form, as well as the urea:DL-tartaric acid cocrystal, when compared to crystallization of the pure component materials. However, changes in the hydrogen bonding network yield a

thiourea:DL-tartaric acid cocrystal that corresponds to an energetic minimum on the potential

energy surface, but has a Gibbs free energy that prevents it from experimental formation under

ambient conditions.

4.1 Introduction

Crystal engineering is a concept applied in various fields to improve a material by tuning its physical and chemical properties through manipulation of the solid-state structure.[1,2] This is done through rational selection of crystal components and control of growth conditions to yield crystal packing arrangements with desired properties. The pharmaceutical industry heavily utilizes crystal engineering ideas and methods in the quest to optimize drug effectiveness, improving important factors such as stability, permeability, and solubility.[3] Cocrystallization is an appealing approach that combines the positive attributes of two (or more) components to produce a single solid that serves as a superior drug formulation. In this context, a cocrystal generally consists of an active pharmaceutical ingredient (API) cocrystallized with a second organic molecular species (differentiated from solvates and most salts) that is typically an inactive excipient or occasionally a complementary API, though more complex cocrystalline pharmaceuticals have been reported.[4,5,6] Cocrystals are also the focus of considerable research since they increase the practicality of the many APIs that are discarded in the drug development process due to lack of bioavailability.[7] To help make cocrystal design more effective, research is necessary on the structures and thermodynamics of both successful and unsuccessful cocrystal formations to better understand what determines ideal candidates for cocrystallization.

The intermolecular forces between cocrystal components are a critical aspect to study in the formation of cocrystals and how this phenomenon is favored over recrystallization of simply the pure initial compounds. Low-frequency Raman spectroscopy (LFRS) in the sub-200 cm^{-1} region enables the direct exploration of the intermolecular vibrations and thus the intermolecular potential energy surfaces that significantly define the physical properties of solids. Vibrational spectroscopy in the sub-200 cm^{-1} region permits measurement of the lattice vibrations resulting

from the three-dimensional crystal packing and also the large-amplitude motions within the molecules themselves that are sensitive to interactions present in the crystallographic unit cell.[8,9, 10] The importance of this low-frequency spectral region has become apparent with numerous studies related to crystal engineering being published, including both Raman and terahertz (far-infrared) spectroscopic investigations of polymorphs and cocrystals.[11,12,13,14,15]

However, the correct interpretation of low-frequency vibrational spectra can be challenging since the vibrations being probed cannot be assigned using traditional characteristic group frequency tables as is done at higher frequencies. The sub-200 cm^{-1} vibrations are not the product of an isolated molecule, but rather a complex set of motions that result from the bulk sample and therefore the entire solid must be considered for realistic spectral analyses. Solid-state density functional theory (ss-DFT) has been established as a key tool for understanding these spectra by enabling assignments to specific translations, rotations, torsions, etc. in the crystal, while simultaneously providing new insights into the energetic factors underlying crystal formation.[16-18] The assignment of observed spectral features with ss-DFT is important, but the successful simulation of these often convoluted spectra also clearly signifies that the applied computational model is correctly representing the forces within and between the molecules. Once the models are validated in this manner, there is greater confidence in the reliability of various calculated solid-state parameters including free energies, conformational energies, and cohesive energies. Accurate modeling of the low-frequency modes directly reflects the quality of the intermolecular forces in the applied model and therefore the cohesion energy of the solid. To a lesser extent, the intermolecular forces affect the conformational energies of the molecules. In terms of the overall Gibbs free energy the high-frequency vibrations are the largest contributor.

This work focuses on the study of small organic acids cocrystallized with urea (CH_4N_2O) and thiourea (CH_4N_2S) as model systems of pharmaceutically relevant molecules. The comparison of a urea cocrystal and a thiourea cocrystal allows for the investigation of non-standard O-H•••S hydrogen bond interactions (present in thiourea cocrystals) as opposed to O-H•••O interactions (present in urea cocrystals) as a potential modifier to cocrystal formation and properties. Four unique 1:1 cocrystals are investigated here using both experimental and computational methods, and consist of cocrystals of urea and thiourea with either glutaric acid ($C_5H_8O_4$) or DL-tartaric acid ($C_4H_6O_6$).[19-23] Initial study began with the glutaric acid cocrystals as these have well established experimental crystal structures. The urea:glutaric acid cocrystal is designated as U:GA-I[19] or U:GA-II[20] to represent the two known polymorphs, while thiourea:glutaric acid (T:GA[21]) has only a single reported solid form (**Figure 4-1**).
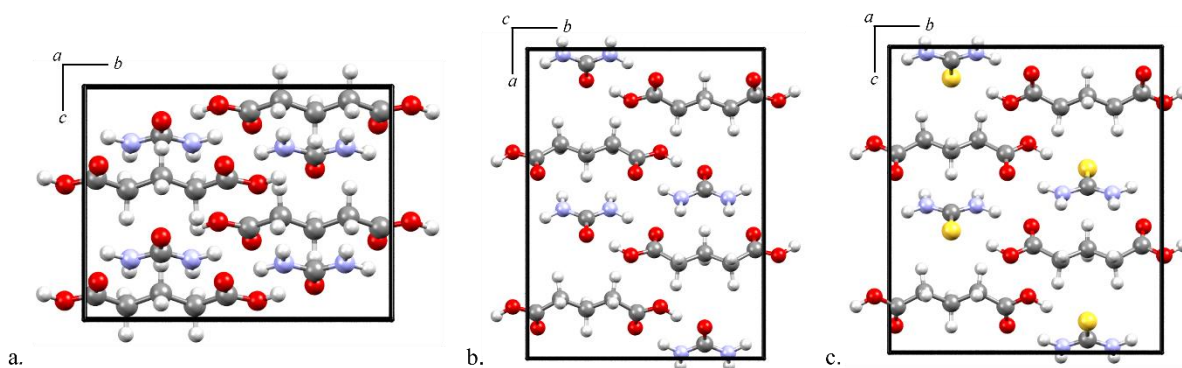
Figure 4-1. Unit cells for **a.** U:GA-I, **b.** U:GA-II, and **c.** T:GA with sulfur atoms shown in yellow, carbon shown in grey, oxygen shown in red, nitrogen shown in blue, and hydrogen shown in white.

Using these experimental glutaric acid urea and thiourea cocrystals as a base of knowledge, DL-tartaric acid ($C_4H_6O_6$) cocrystals were also explored, specifically urea:DL-tartaric acid (U:TA) and thiourea:DL-tartaric acid (T:TA) (**Figure 4-2**).[22, 23] U:TA is an experimentally known cocrystal, while T:TA is a hypothetical system produced in the current study by computationally

substituting thiourea for urea in the U:TA cocrystal. The alterations that occur in the hydrogen bonding network with the exchange of sulfur for oxygen give insights into how specific modifications in the van der Waals interactions can be used to alter cocrystal formation and properties in two different carboxylic acid cocrystal systems.
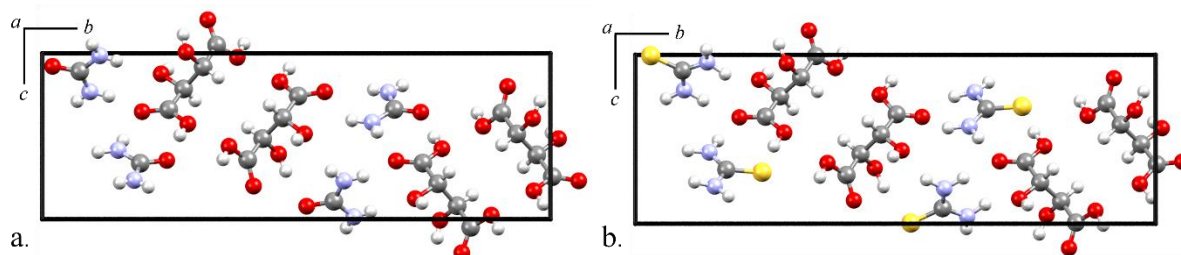
Figure 4-2. Unit cells for **a.** U:TA and **b.** T:TA with sulfur atoms shown in yellow, carbon shown in grey, oxygen shown in red, nitrogen shown in blue, and hydrogen shown in white.

4.2 Experimental Methods

4.2.1 Sample Preparation

All pure samples were purchased from Sigma-Aldrich. The as-received samples of urea (99.0-100.5%), thiourea ($\geq$99.0%), glutaric acid (99%), and DL-tartaric acid (99%) were evaluated at room temperature using powder X-ray diffraction (PXRD) with a Bruker D2 Phaser diffractometer (Cu Kα radiation, λ=1.54060 Å, 5° to 70° with 0.5 s per step). PXRD data are provided in the **Supporting Information** and comparison to data from the Cambridge Structural Database (CSD)[24] confirmed the crystal structures of all the starting materials. Specifically, the samples were consistent with published crystallographic data with space group symmetries of P$\bar{4}2_1$m (Z=2) for urea[25], Pbnm (Z=4) for thiourea[26], C2/c (Z=4) for glutaric acid[27], and P$\bar{1}$ (Z=2) for DL-tartaric acid.[28] U:GA (U:GA-I; P2_1/n, Z=4[19] and U:GA-II; Pnma, Z=4[20]), T:GA (Pc2_1n, Z=4)[21], and U:TA (P2_1, Z=4)[22,23] were all crystallized by dissolving a 1:1 molar ratio of the two components in an aqueous solution and allowing for slow evaporation at ambient conditions. The

two U:GA polymorphs formed simultaneously during the room temperature crystallization. Higher or lower temperature crystallization may influence the relative populations of the two polymorphs. The formation of all cocrystals was confirmed with PXRD and detailed in the **Supporting Information**. Despite numerous attempts, cocrystals of T:TA could not be grown under similar conditions.

4.2.2 Low-Frequency Raman Spectroscopy (LFRS)

Raman data were taken using a Coherent (Ondax) THz-Raman system (Santa Clara, CA) with laser excitation centered at 784.7 nm. The scattered light was analyzed with an Andor Shamrock SR-750 spectrograph with an iDus 416 CCD detector. The system has a 0.5 mm laser spot size. Each Raman spectrum consisted of 225 acquisitions of 3 s exposure time windows, yielding a usable spectral range of 10 to 300 cm^{-1} and a spectral resolution of 0.6 cm^{-1}. Low-frequency Raman spectra were obtained for powder samples of T:GA, U:TA, and the U:GA-I/U:GA-II mixture. Samples were prepared by grinding in a mortar and pestle before being placed in a brass cuvette system. Sample homogeneity was not tested here. Experiments were done at both 290 K and 78 K using a cryostat-mounted brass cuvette system with optically-clear glass windows that allowed for the samples to be cooled via liquid nitrogen.

4.3 Theoretical Methods

CRYSTAL17[29] was used to perform solid-state density functional theory calculations using the Perdew−Burke−Ernzerhof (PBE)[30] density functional and the def2-TZVP[31] basis set. The calculations were augmented with Grimme's London dispersion correction (D3) utilizing the Becke-Johnson damping correction[32,33,34] and included three-body Axilrod-Teller-Muto contributions (program keyword "ABC").[35,36] All calculations used a pruned integration grid of

99 radial points and 1454 angular points. This computational approach was used to perform geometry optimizations, to simulate the low-frequency IR-active and Raman-active vibrational frequencies, and to calculate cohesive and conformational energies. For all simulations, the experimental crystal structures from the CSD (with the exception of T:TA) were used as the starting point for the geometry optimization with an energy convergence of $\Delta E < 10^{-8}$ hartree. The hypothetical T:TA starting structure was created by replacing the oxygens present in the urea molecules of the optimized U:TA structure with sulfur atoms. Normal mode vibrational analyses were performed on the optimized structures with a tighter energy convergence of $\Delta E < 10^{-10}$ hartree. The central-difference formula was used to calculate the numerical derivatives of the Hessian matrix, with each atom having two displacements along each Cartesian axis. Raman intensities were calculated using the Coupled-Perturbed Hartree-Fock/Kohn-Sham (CPHF) approach with parameters for experimental laser wavelength and sample temperature included.[37,38]

Conformational and cohesive energies for U:GA-I, U:GA-II, T:GA, U:TA, and T:TA, along with Gibbs free energy versus temperature curves, were also calculated. Each symmetry-unique molecule within the optimized unit cell of the cocrystal was extracted and its fixed conformational energy calculated. The sum of the molecular conformational energies of each individual molecule in the unit cell was subtracted from the total electronic energy of the same unit cell to obtain the cohesive energy of the cocrystal. All energy calculations were performed with a convergence of $\Delta E < 10^{-10}$ hartree. A standard Boys-Bernardi counterpoise correction[39] was applied to the simulations to address basis set superposition error (BSSE), although this error is low with the use of the large def2-TZVP basis set.

Molecular dimer calculations were performed to estimate the binding energy between specific molecular pairs within the cocrystals. These calculations utilized the non-periodic MOLECULE keyword within CRYSTAL17 as opposed to the fully periodic CRYSTAL keyword used for all other calculations.

4.4 Results and Discussion

4.4.1 Urea-Glutaric Acid and Thiourea-Glutaric Acid

The pure glutaric acid, urea, and thiourea structures were optimized and found to correspond to minima on their respective potential energy surfaces through vibrational frequency analyses (all eigenvalues were positive). Geometry optimizations and vibrational frequency analyses were then performed on U:GA-I, U:GA-II, and T:GA. After the ss-DFT geometry optimization of U:GA-I, the average unsigned overall percent error in the unit cell dimensions was 2.0%. U:GA-II optimized similarly and also had an error of 2.0% in the unit cell dimensions. U-GA-I exhibited root-mean-square deviation (rmsd) values of 0.02 Å for the bond lengths, 0.83° for the bond angles, and 2.02° for the torsions, taking into account only nonhydrogen atoms. U-GA-II showed the same performance, with rmsd values of 0.01 Å for the bond lengths, 1.00° for the bond angles, and 1.73° for the torsions.

U:GA-I and U:GA-II have nearly identical hydrogen bonding patterns despite their different crystallographic symmetries. Chadwick *et al.* described the main difference in the two polymorphs to be how two dimensional hydrogen bonded groups of urea and glutaric acid packed. In U:GA-I they pack in a 'dovetail' pattern while in U:GA-II they pack in a 'herringbone' patter.[20] **Figure 4-3** shows the hydrogen bonds present in both polymorphs. Comparing the ss-DFT results to experiment shows similar quality along the intermolecular

hydrogen bonds for both solids. The hydrogen bonds in U:GA-I showed rmsd values of 0.05 Å

for the heavy-atom hydrogen bond lengths, while the rmsd for U:GA-II was 0.04 Å. Considering

the hydrogen bond angles (X-H•••O), U:GA-I and U:GA-II yielded similar rmsd values of 4.04°

and 3.71°, respectively. The hydrogen bond angles show a larger deviation from experiment than

observed for the covalent structure, primarily because the experimental hydrogen positions are

not well resolved using X-ray diffraction. Due to the high accuracy of the simulated structures,

these calculations can be used to gauge the relative energies of the U:GA polymorphs. In

accordance with their structural similarities, U:GA-I and U:GA-II are very close in energy, with

U:GA-I being slightly lower in total electronic energy by 0.04 kJ/mol per formula unit (one urea

and one glutaric acid). The energy difference between the two polymorphs is so close that

definitive ranking can not be established.
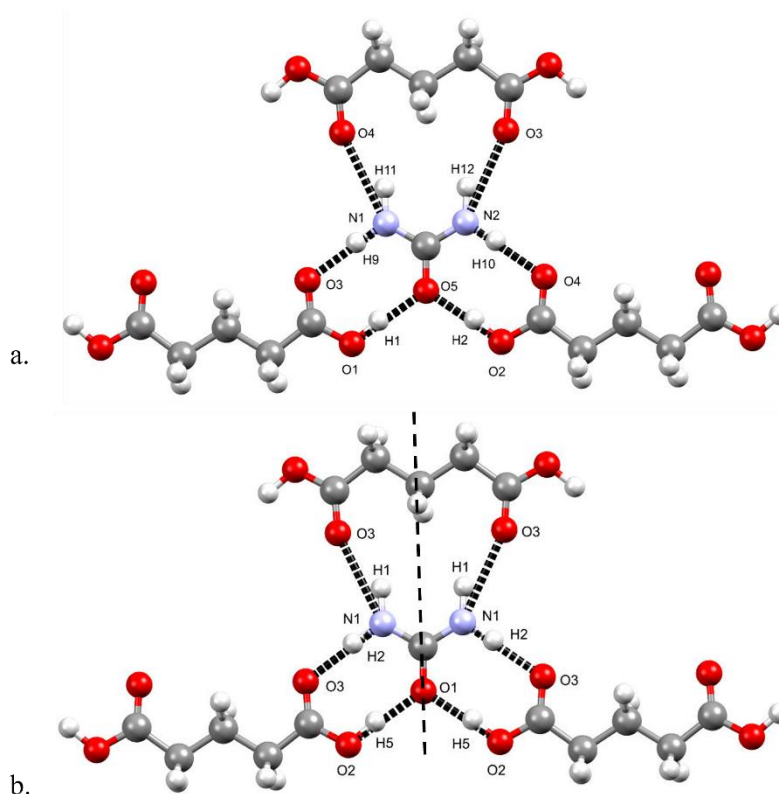
Figure 4-3. Portion of the ss-DFT optimized U:GA-I **(a)** and U:GA-II **(b)** crystals to illustrate the hydrogen bonding pattern. The vertical dashed line represents the mirror plane present in U:GA-II, but absent in U:GA-I.

The simulated Raman spectra of the U:GA polymorphs along with the experimental 78 K data are shown in **Figure 4-4**. Since both polymorphs appeared simultaneously during crystallization, the experimental spectrum is of a mixture of U:GA-I and U:GA-II. A combination of the simulated spectra of both U:GA-I and U:GA-II is also shown in **Figure4-4** (40% U:GA-I, 60% U:GA-II determined from PXRD relative intensities) demonstrating that individual simulations can be combined to replicate the spectrum of the polymorph mixture. While the U:GA polymorphs exhibit similar vibrational spectra, the lowest frequency modes with appreciable intensities actually represent different types of motion. The mode calculated at 49.30 cm^{-1} in U:GA-I is a translation, while the mode at 60.05 cm^{-1} in U:GA-II is a rotation. However, the most intense observed spectral features arise from the mode at 67.17 cm^{-1} in

U:GA-I and the mode at 74.99 cm^{-1} in U:GA-II which are both very similar rotations. A full list

of simulated IR-active and Raman-active vibrational modes can be found in the **Supporting**

Information (Tables A-11-A-14).
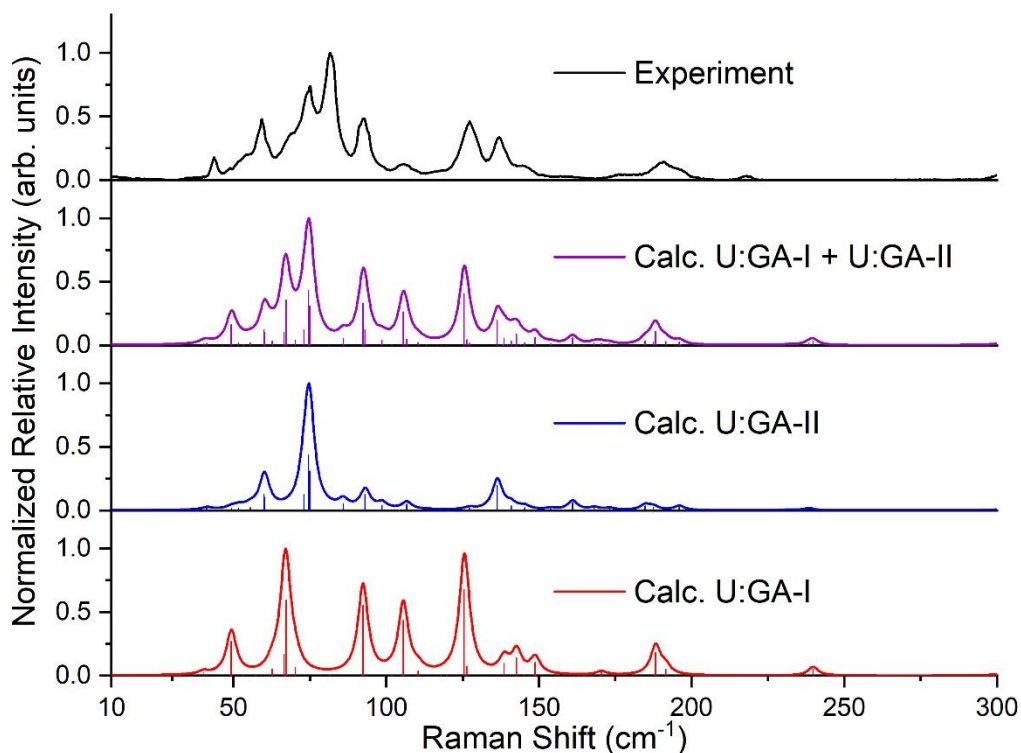
Figure 4-4. From top to bottom: 78 K experimental Raman spectrum of U:GA-I/U:GA-II mixture (black), simulated Raman spectrum of a U:GA-I and U:GA-II mixture (purple), simulated Raman spectrum of U:GA-II (blue), and simulated Raman spectrum of U:GA-I (red).

The accuracy of the U:GA-I and U:GA-II frequency analyses also allows for Gibbs free

energies to be calculated. The Gibbs free energy curves indicate that the two polymorphs have a

monotropic relationship, with U:GA-I being more stable over the entire 0 to 600 K temperature

range. However, they do remain close in energy with U:GA-I being 0.53 kJ/mol per formula unit

lower at 0 K and 0.98 kJ/mol per formula unit lower at 298 K. While these results indicate that

U:GA-I is stable and U:GA-II is metastable, the very close energies may be why both forms

were crystallized during experiments. This further suggests that the formation of U:GA-II is a kinetically driven phenomenon here and in previous experiments.[20]

The T:GA ss-DFT simulations ultimately produced excellent results, but only after corrections were made to the published hydrogen atom positions of the carboxylic acid. Two of the hydrogen atoms in the original structure (those in the glutaric acid end groups) were oriented towards the carbon chain of the glutaric acid, rather than outward for intermolecular hydrogen bonding. This is an unlikely positioning of these two atoms from a chemical perspective, and ss-DFT geometry optimizations confirmed that the atom positions were not correctly identified. These two hydrogen atoms in glutaric acid were repositioned and this modification produced a lower energy structure and reduced the average unsigned overall percent error in the unit cell dimensions from 2.3% to 1.4%. The corrected T:GA structure yielded rmsd values of 0.02 Å for the bond lengths, 3.08° for the bond angles, and 2.58° for the torsions, taking into account only nonhydrogen atoms. The hydrogen bonds in T:GA have rmsd values of 0.07 Å for the heavy-atom hydrogen bond lengths and 5.56° for the hydrogen bond angles.

Figure 4-5 shows the 78 K Raman spectrum of T:GA, as well as the simulated spectrum. A full list of simulated IR-active and Raman-active vibrational modes can be found in the **Supporting Information (Tables A-15 and A-16)**.
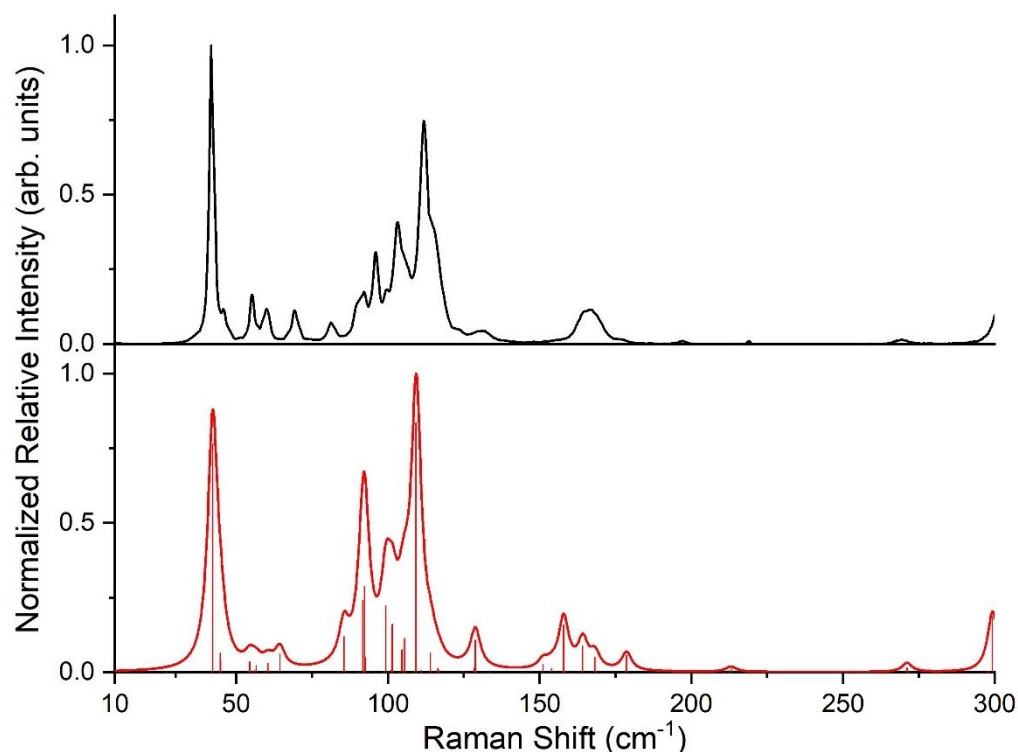
Figure 4-5. 78 K experimental (black) and simulated (red) Raman spectra of T:GA.

4.4.2 Comparison of U:GA-II and T:GA Structures

When the crystal structures of the U:GA polymorphs and T:GA were compared, it was found that U:GA-II and T:GA have almost superimposable crystal packing arrangements, while U:GA-I has a very different crystal structure (**Figure 4-1b.** and **4-1c.**). When a space group analysis was performed on the optimized T:GA structure (Pc2₁n) using the ISOCIF software, the U:GA-II space group (Pnma) was found as an alternate symmetry solution and demonstrates that U:GA-II and T:GA are functionally isomorphic.[40]

Table 4-1. Unit cell dimensions (Å) and volumes (Å^3) for U:GA-II and T:GA experimental and ss-DFT optimized structures, along with percent errors.

	U:GA-II			T:GA		
	Exp.[a]	ss-DFT	Percent Error	Exp.[a]	ss-DFT	Percent Error
a	14.77	15.226	3.1%	14.64	14.206	-3.0%
b	11.74	11.667	-0.6%	12.81	12.708	-0.8%
c	5.07	4.953	-2.4%	5.26	5.242	-0.3%
Volume	879.29	879.886	0.1%	986.18	946.401	-4.0%

[a] Experimental data for U:GA-II from ref. 20 and for T:GA from ref. 21.

The T:GA structure has a larger volume (+7.6%) and two larger unit cell dimensions than U:GA-II due to the increased radius of the sulfur atom present in T:GA as opposed to the oxygen in U:GA-II (**Table 4-1**). One of the most notable changes between these two structures is that the addition of the sulfur pushes the heavy atoms of the neighboring glutaric acid molecules further away from each other by over 1 Å, as shown in **Figure 4-6**.

a.

b.
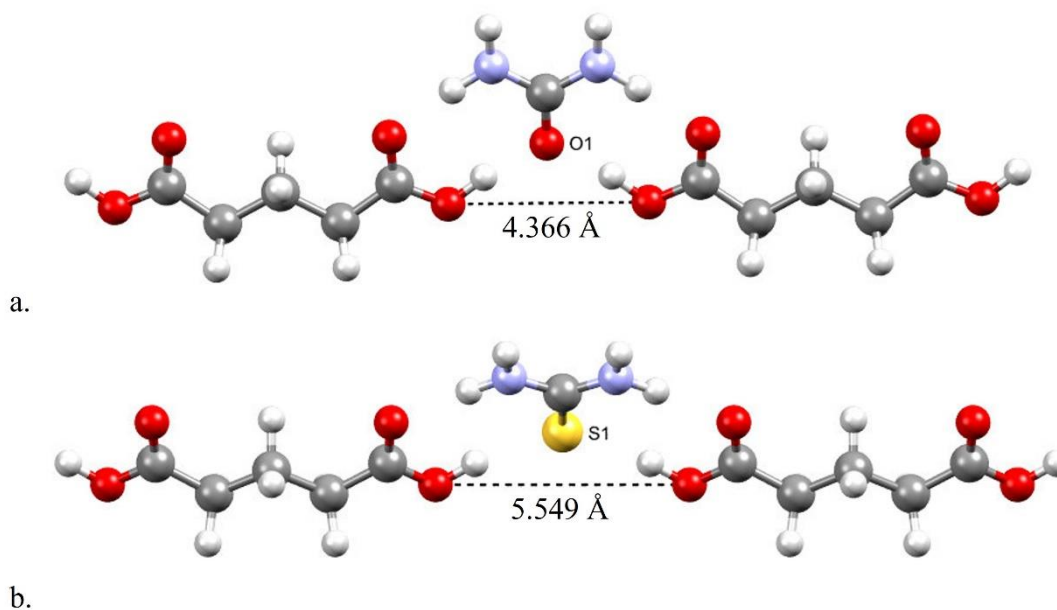
Figure 4-6. Calculated ss-DFT intermolecular packing change in **a.** U:GA-II compared to **b.** T:GA.

U:GA-II and T:GA have three comparable symmetry-unique hydrogen bonds (each doubled with symmetry), one of which involves the O1/S1 atom (**Figure 4-3** and **Figure 4-6**). The hydrogen bond that involves O1 lengthens significantly when thiourea is present instead of urea (**Table 4-2**). This corresponds with the lengthening noted in **Figure 4-6** since this hydrogen bond involves the carboxylic acid hydrogens of the glutaric acid chain termini. When the sulfur is introduced, the planar glutaric acid chains must move away from each other to accommodate the sulfur, creating a longer distance between not only the glutaric acids, but also the sulfur and the terminal hydrogens of the glutaric acid chain. One of the two N-H•••O bonds also lengthens significantly, while the other bond remains relatively unchanged. With sulfur, the packing has to expand along the plane of the heavy atoms of the glutaric acid molecules and this causes the lengthening in the N1-H2•••O3 hydrogen bonds as the two glutaric acid molecules involved move apart (**Figure 4-3b**). However, the N1-H1•••O3 hydrogen bonds change very little because the carbonyl oxygens involved do not move with the introduction of the sulfur. These structural changes may be one reason that, despite the fact that U:GA-II and T:GA have similar structures, they have very different Raman vibrational spectra.

Table 4-2. Hydrogen bonding heavy atom distances (Å) and angles (degrees) for equivalent positions in ss-DFT optimized U:GA-II and T:GA.

	U:GA-II				T:GA[a]			
	Heavy Atom Distance (Å)		Angle		Heavy Atom Distance (Å)		Angle	
	Exp.[b]	ss-DFT	Exp.[b]	ss-DFT	Exp.[b]	ss-DFT	Exp.[b]	ss-DFT
O2-H5•••O1/S1	2.715	2.660	165.7°	171.5°	3.128	3.051	168.8	167.0°
					3.030	3.051	179.5	167.0°
N1-H1•••O3	2.935	2.912	142.3°	144.7°	2.995	2.923	137.0	140.4°
					2.997	2.922	139.4	140.4°
N1-H2•••O3	2.818	2.792	173.3°	174.7°	3.043	2.962	169.7	172.9°
					3.051	2.962	174.7	172.9°

[a] T:GA has two non-equivalent bonds in the Pc21n space group setting.
[b] Experimental data for U:GA-II from ref. 20 and T:GA from ref. 21.

4.4.3 Urea-DL-Tartaric Acid

Optimizations and vibrational frequency analyses were performed on pure DL-tartaric acid, as well as the urea-DL-tartaric acid cocrystal. The average unsigned overall percent error in the unit cell dimensions for U:TA was 0.90% with the largest error (2.08%) occurring on the longest axis (b=23.0797 Å). The rmsd values, considering only nonhydrogen atoms, for U:TA are 0.01 Å for the bond lengths, 0.81° for the bond angles, and 2.80° for the dihedral angles. The LFRS data (**Figure 4-7**) for U:TA has a particularly high density of spectral peaks due to the complexity and low symmetry of the unit cell contents.

The simulated Raman spectrum shows good agreement with the experimental spectrum in both peak placement and intensity (**Figure 4-7**). A full list of simulated IR-active and Raman-active vibrational modes can be found in the **Supporting Information** (**Tables A-17** and **A-18**).
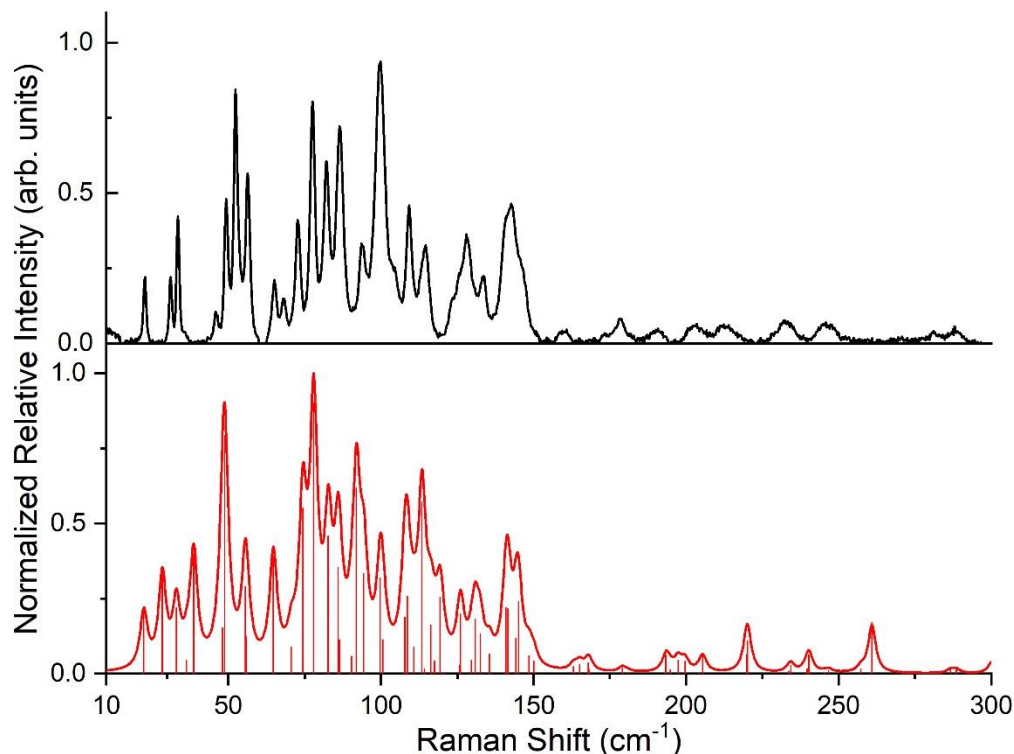
Figure 4-7. 78 K experimental (black) and simulated (red) Raman spectra of U:TA.

4.4.4 Comparison of U:TA and T:TA Structures

To compare the cocrystal structures between experimental U:TA and hypothetical T:TA, the optimized structure of U:TA was used as a starting point and the oxygens on the urea molecules were replaced with sulfurs to generate the T:TA solid. This structure was then optimized using the same conditions as the U:TA cocrystal. During the initial optimization, T:TA was kept in the same space group symmetry as the U:TA structure, $P2_1$. Once this optimization was completed, the final structure was reduced to P1 symmetry and re-optimized. The full P1 optimization did not result in any significant structural changes and maintained the original $P2_1$ symmetry, confirming it to be a reasonable crystal packing symmetry for this hypothetical system. A vibrational frequency analysis indicated that this proposed T:TA structure corresponds to a minimum on the potential energy surface.

The T:TA optimization yielded slightly increased expansion in its lattice cell parameters compared to U:TA (+9.5% volume) than what was found in the U:GA-II and T:GA comparison (+7.6% volume). **Table 4-3** lists the unit cell dimensions of U:TA and T:TA.

Table 4-3. Unit cell dimensions (Å) and volumes (Å^3) for the U:TA experimental and ss-DFT optimized structures along with the percent errors. Values are also provided for the T:TA ss-DFT optimized hypothetical structure.

	U:TA			T:TA
	Exp.[a]	ss-DFT	Percent Error	ss-DFT
a	4.81	4.820	0.2%	4.853
b	23.08	23.559	2.1%	24.365
c	7.65	7.612	-0.4%	7.998
Volume	833.294	851.174	2.2%	931.682

[a] Experimental data for U:TA from ref. 22.

The hydrogen bonding network also shows changes when replacing the traditional O-H•••O hydrogen bonds with thiourea having O-H•••S interactions. As anticipated, the majority of the hydrogen bonds become longer and deviate from linearity in T:TA (**Figure 4-8** and **Table 4-4**), indicating that the hydrogen bonding network becomes weaker in T:TA. However, four of the N-H•••O hydrogen bonds do not follow this trend, suggesting that since all the O-H•••S and O-H•••O bonds in T:TA are weaker than their equivalent O-H•••O bonds in U:TA, four of the N-H•••O bonds may be preferentially promoted (bolded in **Table 4-4**). However, it is important to note that the four N-H•••O bonds that are enhanced are among the weaker hydrogen bonds present in the solid (they are all further from 180° than the average and two of them are longer than average for both U:TA and T:TA).
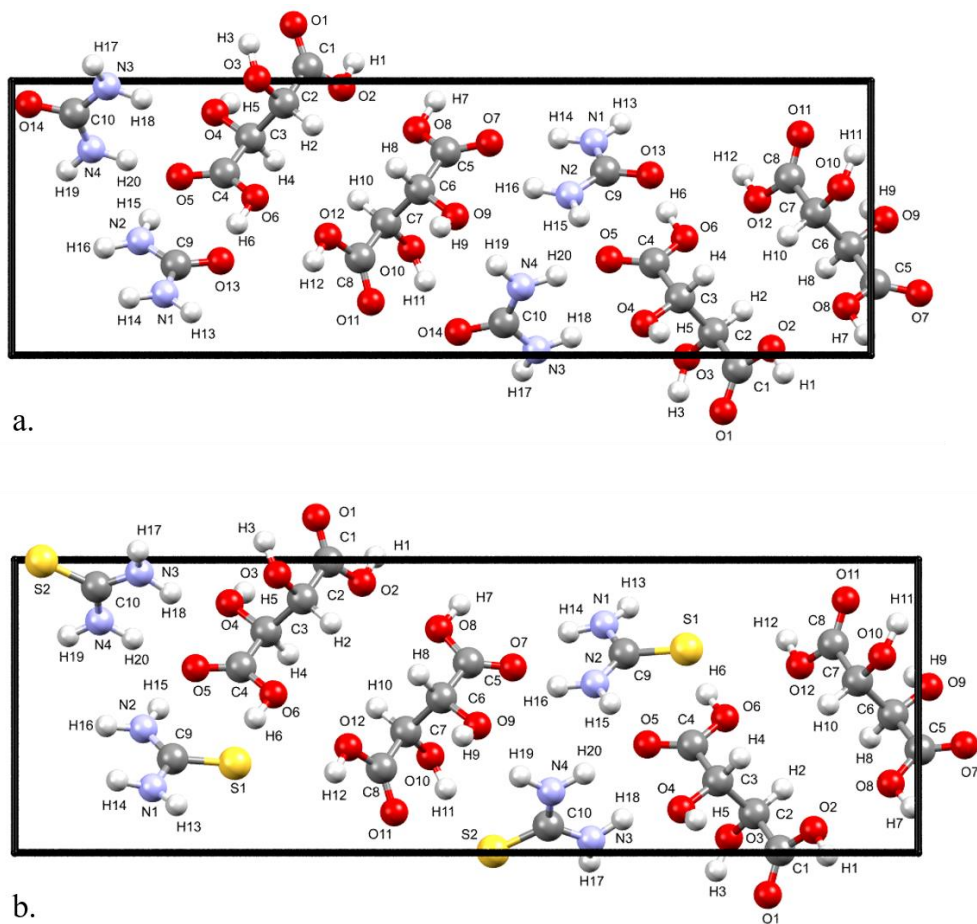
Figure 4-8. Labeled unit cells for **a.** U:TA and **b.** T:TA.

Table 4-4. Hydrogen bond heavy atom distances (Å) and angles (degrees) for equivalent positions in experimental and ss-DFT optimized U:TA and T:TA structures. N-H•••O bonds that shorten in T:TA are bolded.

	U:TA				T:TA	
	Heavy Atom Distance (Å)		Angle		Heavy Atom Distance (Å)	Angle
	Exp.[a]	Calc.	Exp.[a]	Calc.	Calc.	Calc.
O3-H3•••O13/S1	2.759	2.715	155.6°	152.6°	3.061	144.8°
O6-H6•••O13/S1	2.537	2.506	173.0°	171.0°	2.959	168.0°
O8-H7•••O14/S2	2.585	2.546	175.7°	175.2°	3.109	170.3°
O10-H11•••O14/S2	2.695	2.633	161.3°	158.8°	3.078	148.6°
O2-H1•••O11	2.628	2.564	175.8°	177.8°	2.596	177.6°
O4-H5•••O3	2.769	2.693	168.6°	170.2°	2.746	172.8°
O9-H9•••O10	2.735	2.698	173.7°	174.3°	2.722	172.8°
O12-H12•••O1	2.678	2.603	175.2°	177.6°	2.607	178.7°
N1-H13•••O4	3.049	2.984	128.5°	138.2°	3.633	135.1°
N1-H14•••O7	**2.902**	**2.883**	**141.8°**	**142.3°**	**2.735**	**150.9°**
N2-H15•••O5	2.913	2.877	168.7°	165.7°	3.030	172.7°
N2-H16•••O7	2.951	2.951	140.2°	141.9°	2.971	133.9°
N2-H16•••O9	3.123	3.194	144.9°	143.5°	3.365	153.4°
N3-H17•••O7	3.121	3.064	174.0°	172.9°	4.619	142.08°
N3-H18•••O4	**3.369**	**3.482**	**141.5°**	**133.6°**	**3.236**	**137.2°**
N3-H18•••O5	**3.180**	**3.181**	**134.3°**	**135.8°**	**2.988**	**140.6°**
N4-H19•••O9	**3.058**	**2.990**	**164.2°**	**171.9°**	**2.970**	**158.0°**
N4-H20•••O5	3.341	2.971	143.1°	141.0°	3.200	132.4°

[a] Experimental data for U:TA from ref. 22.

Table 4-5 lists the average hydrogen bond heavy atom distances and bond angles across all the solids studied in this work. When urea is switched out for thiourea in the glutaric acid cocrystal, the average heavy atom distance increases and the bond angle decreases, however, neither changes as greatly as in the urea/thiourea-glutaric acid cocrystal comparison. It is worth noting that in this analysis it is assumed that T:TA and U:TA are isomorphic, though this may not be true.

Table 4-5. Average hydrogen bond heavy atom distances (Å) and bond angles (degrees) for U:GA-II, T:GA, U:TA, and T:TA.

	Average distance (Å)	Average angle
Exp. U:GA-I[a]	2.823	161.5°
ss-DFT U:GA-I	2.788	163.6°
Exp. U:GA-II[a]	2.822	160.4°
ss-DFT U:GA-II	2.788	163.6°
Exp. T:GA[a]	3.041	161.5°
ss-DFT T:GA	2.979	160.1°
Exp. U:TA[a]	2.916	156.7°
ss-DFT U:TA	2.863	158.0°
ss-DFT T:TA	2.994	155.6°

[a] Experimental data for U:GA-I from ref. 19, U:GA-II from ref. 20, T:GA from ref. 21, and U:TA from ref. 22.

4.4.5 Intermolecular Forces in U:GA-II and T:GA versus U:TA and T:TA

To further explore the intermolecular forces present in the glutaric acid cocrystals and the tartaric acid cocrystals, a dimer interaction approach was taken. By isolating the intermolecular environment surrounding a single glutaric acid or tartaric acid molecule inside the solid structures (chosen to be within 3 Å), certain interactions can be identified as being particularly sensitive to the differences between the urea and the thiourea cocrystals. These interactions point to key structural changes within T:TA that lead to its destabilization compared to U:TA, while comparable structural changes are not seen between U:GA-II and T:GA.

First, using the fully-optimized ss-DFT crystal structures, the 3 Å environment around a specific glutaric acid or tartaric acid molecule was identified and then the individual dimer pairs that involve the central molecule were analyzed for their interaction (binding) energies. When comparing structurally equivalent dimers in U:TA versus T:TA, it was found that the binding energies of two specific dimer pairs decreased significantly more than the others. All of the

binding energies decreased when the oxygen was switched out for a sulfur, with most decreasing

by <4 kJ/mol, but the two dimer interactions identified in **Figure 4-9a** and 4-**9b** exhibited a

reduction of ~30 kJ/mol (dimer pair I) and ~20 kJ/mol (dimer pair II). These two dimer pairs also

relate to two of the three largest hydrogen bond elongations (more than 0.5 Å longer) observed

when urea was replaced with thiourea (O8-H7•••O14/S2 and N3-H17•••O7 in **Table 4-4**).

Figure 4-9a and **4-9b** shows these two dimer pairs in U:TA and T:TA, with each dimer pair

involving one of the urea or thiourea molecules interacting with the central tartaric acid. The

structural change can be further seen in **Figure 4-9c** where the central tartaric acid molecules

have been overlaid.
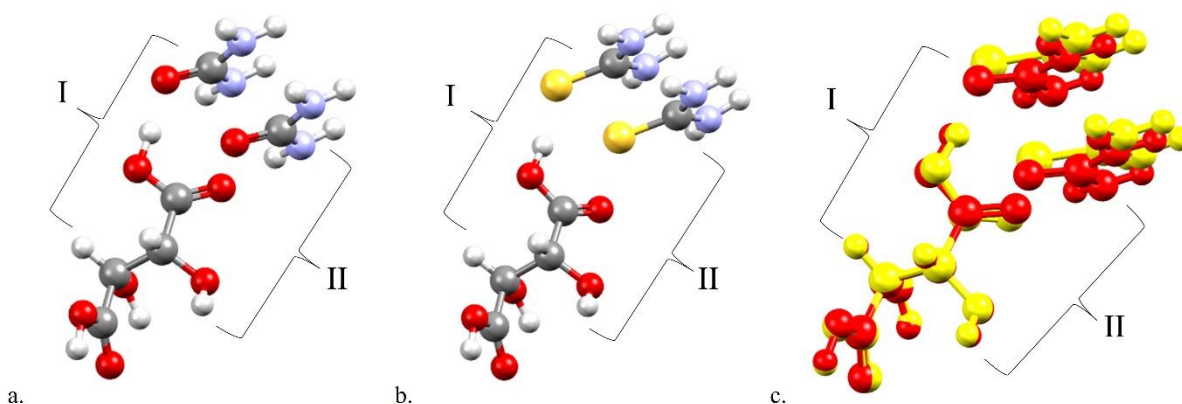
Figure 4-9. a. Dimer pairs for U:TA (labeled as dimers I and II), **b.** dimer pairs for T:TA
(labeled as dimers I and II), and **c.** the superposition of the U:TA and T:TA dimers with the
central DL-tartaric acid molecules directly overlaid. U:TA is shown in red and T:TA is shown
in yellow.

When a similar set of calculations was performed on U:GA-II and T:GA, there was no

comparable dimer set that decreased significantly in binding energy when urea was replaced with

thiourea. While the majority of the binding energies do decrease when this change occurs, there

is no equivalent decrease in binding energy of specific dimer pairs as seen in the U:TA/T:TA

solids. This may be one factor that contributes to the fact that U:GA-II, T:GA, and U-TA form under ambient conditions, but T:TA crystal growth does not occur.

4.4.6 Energy Factors of the Cocrystals

4.4.6.1 Cohesive and Conformational Energies

The electronic energies involved in cocrystal formation can be investigated by focusing on factors such as cohesive and conformational energies of the complete solids, rather than considering dimeric interactions. In glutaric acid and DL-tartaric acid cocrystals, the cohesive energy decreases when the urea oxygen is replaced with the thiourea sulfur (**Table 4-6**). However, the percent change in cohesive energy from U:TA to T:TA (-9.53% change) is greater than when compared to U:GA-II and T:GA (-4.17% change). This finding for the complete solid is consistent with the dimer interaction analysis where a greater decrease in binding energies between U:TA and T:TA was found as compared to between U:GA-II and T:GA.

Table 4-6. BSSE-corrected cohesive energies per formula unit (kJ/mol) and per atom (kJ/mol) for the U:GA-I, U:GA-II, T:GA, U:TA, and T:TA cocrystals. A formula unit is one urea or thiourea molecule and one glutaric acid or tartaric acid molecule.

	Cohesive Energy per Formula Unit (kJ/mol)	Cohesive Energy per Atom (kJ/mol)
U:GA-I	-294.44	-11.78
U:GA-II	-293.21	-11.73
T:GA	-281.00	-11.24
U:TA	-352.59	-14.69
T:TA	-318.97	-13.29

In terms of conformational energy, the conformation of glutaric acid is more favorable in T:GA than in either U:GA-I or U:GA-II by -8.95 kJ/mol. A similar trend can be seen for the conformational energies of the two unique tartaric acids within U:TA and T:TA, being more

favorable by -16.22 and -8.42 kJ/mol in T:TA than in U:TA. The lower cohesion in the thiourea containing solids may provide an opportunity for the acid molecules to take on more relaxed conformations in the crystals. This is important to note because these conformational factors in some cases could help stabilize the thiourea cocrystals. In the case of T:TA however, it does not appear to be enough of a driving factor to allow the cocrystal to form. While cohesive and conformational energies can highlight trends between the urea cocrystals and the thiourea cocrystals, they do not provide a complete picture of stability and it is necessary to include factors such as vibrational energy and entropy which can be represented by calculating Gibbs free energy curves.

4.4.6.2 Gibbs Free Energy Curves

Figure 4-10 shows the calculated cocrystal Gibbs energy differences as a function of temperature. These difference curves are constructed by taking the cocrystal Gibbs free energy curves, then subtracting the Gibbs free energy curves of their individual components, thus creating a single curve for each cocrystal that are all directly comparable. The figure demonstrates that U:GA-I is the more stable of the two U:GA polymorphs across all temperatures and that the cocrystal polymorphs are more stable at all temperatures compared to the linear combination of pure glutaric acid and pure urea. T:GA is also more stable across the entire temperature range compared to a linear combination of its component molecules. These Gibbs free energies help illustrate why both urea and thiourea glutaric acid cocrystals form over their individual components. The full Gibbs free energy versus temperature curves from 0 to 600 K for the data presented in **Figure 4-10** can be found in the **Supporting Information (Figures A-8-A-11)**.
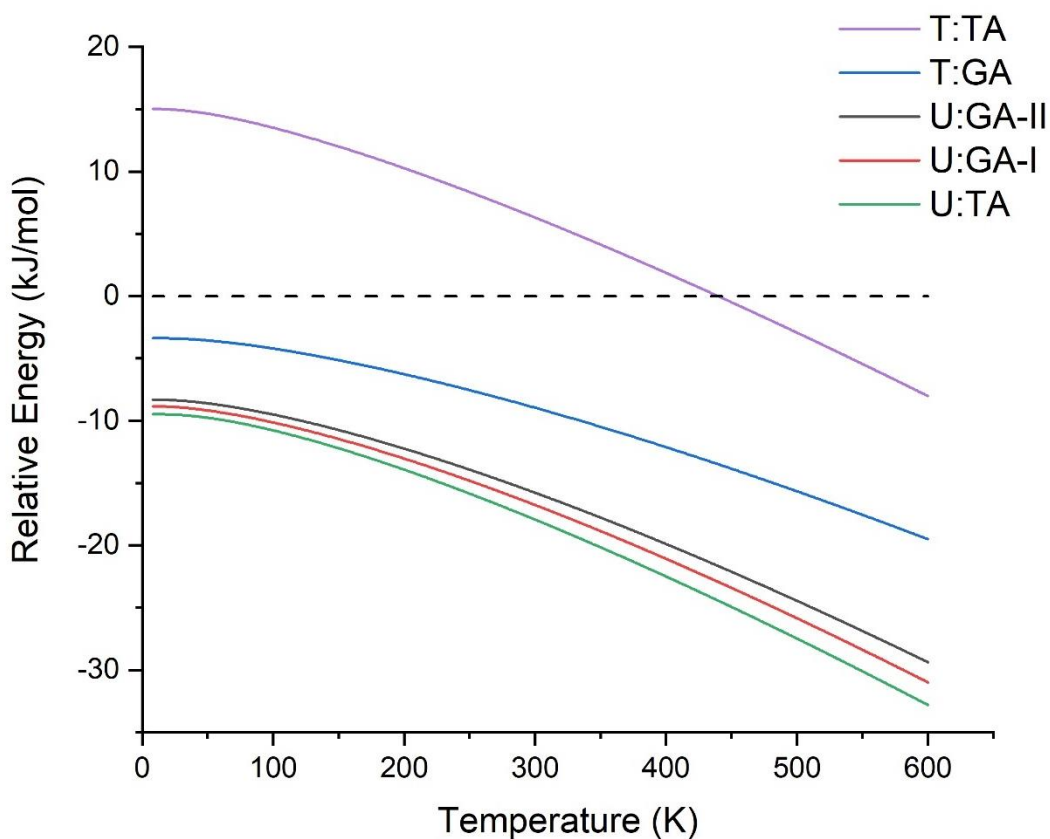
Figure 4-10. Different plots of the cocrystal Gibbs free energy curves minus the Gibbs free energy curves of the individual components for all studied cocrystals.

This same process was applied to the DL-tartaric acid cocrystals and leads to additional information about why T:TA does not appear to form under standard conditions. **Figure 4-10** shows a similar trend for U:TA as was seen with the U:GA polymorphs and T:GA, with U:TA being more stable than its individual components across the entire temperature range. However, a different trend is seen for T:TA than any of the previous cocrystals. At both 0 K and 298 K, the pure thiourea and DL-tartaric acid components have a collectively lower Gibbs free energy than the T:TA cocrystal, leading to positive energy values for T:TA. This is maintained until 439 K, where the T:TA curve crosses the zero line (an event unseen in the other solids). Above that temperature, the T:TA cocrystal becomes more favorable than its individual components. This

high temperature is close to the melting points of both DL-tartaric acid (479 K)[41] and thiourea (454 K)[42] and suggests that T:TA will be unlikely to form experimentally, though possibly through crystallization of the melted mixture. Ultimately, the Gibbs free energies show that the changes in the hydrogen bonding network induced by sulfur make T:TA formation energetically less favorable than the readily grown U:TA cocrystalline solid.

4.5 Conclusions

It is common for the crystal engineering of new cocrystalline materials to leverage modified hydrogen bonding motifs in order to achieve desired functionality. Low-frequency Raman spectroscopy combined with rigorous computational models such as ss-DFT provide detailed information that can help guide the rational design and evaluation of future cocrystals. A demonstration of this powerful combination of techniques has been described here with a focus on the impact of replacing an oxygen hydrogen bond acceptor with sulfur. In particular, U:GA-II and T:GA were used as experimental standards to directly compare the structural and energy differences found between urea and thiourea cocrystals. The validation of the computational approach for U:GA and T:GA established the basis for the investigation of U:TA and furthermore enabled the prediction of properties for the hypothetical T:TA cocrystal. Computationally, compared to U:TA, T:TA compensates for its non-traditional, weaker O-H•••S bonds and longer O-H•••O bonds by creating shorter N-H•••O bonds. However, the stronger N-H•••O bonds in T:TA do not fully offset the loss of the O-H•••O bonds present in U:TA, making U:TA more energetically favorable. Simulations provide information about changing hydrogen bond strengths not fully captured by prior empirical evidence. The comparison of U:TA to the hypothetical T:TA cocrystal gives important insights into the possible crystal engineering of related hydrogen-bonded cocrystals through modifications of their van der Waals interactions.

4.6 Supporting Information (see Appendix A)

Powder X-ray diffraction (PXRD) patterns for urea, thiourea, glutaric acid, U:GA-I, U:GA-II, T:GA, DL-tartaric acid, and U:TA, solid-state DFT optimized lattice parameters and atomic positions in fractional coordinates for U:GA-I, U:GA-II, T:GA, U:TA, and T:TA, list of solid-state DFT IR-active and Raman-active frequencies, intensities, and mode symmetries for U:GA-I, U:GA-II, T:GA, U:TA, and T:TA, relative Gibbs free energy curves for U:GA-I, U:GA-II, T:GA, U:TA, and T:TA.

4.7 Acknowledgements

4.8 References

1.   Desiraju, G. R., Crystal Engineering: From Molecule to Crystal. *Journal of the American Chemical Society* **2013,** *135* (27), 9952-9967.

2.   Nangia, A. K.; Desiraju, G. R., Crystal Engineering: An Outlook for the Future. *Angewandte Chemie International Edition* **2019,** *58* (13), 4100-4107.

3.   Qiao, N.; Li, M.; Schlindwein, W.; Malek, N.; Davies, A.; Trappitt, G., Pharmaceutical Cocrystals: An Overview. *International Journal Of Pharmaceutics* **2011,** *419* (1-2), 1-11.

4.   Aitipamula, S.; Chow, P. S.; Tan, R. B., Polymorphism in Cocrystals: A Review and Assessment of Its Significance. *CrystEngComm* **2014,** *16* (17), 3451-3465.

5.   Clarke, H. D.; Hickey, M. B.; Moulton, B.; Perman, J. A.; Peterson, M. L.; Wojtas, Ł.; Almarsson, O. r.; Zaworotko, M. J., Crystal Engineering of Isostructural Quaternary Multicomponent Crystal Forms of Olanzapine. *Crystal Growth & Design* **2012,** *12* (8), 4194-4201.

6.   Tothadi, S.; Desiraju, G. R., Designing Ternary Cocrystals with Hydrogen Bonds and Halogen Bonds. *Chemical Communications* **2013,** *49* (71), 7791-7793.

7.   Dalpiaz, A.; Pavan, B.; Ferretti, V., Can Pharmaceutical Co-Crystals Provide an Opportunity to Modify the Biological Properties of Drugs? *Drug Discovery Today* **2017,** *22* (8), 1134-1138.

8.   Kimmitt, M. F., Restrahlen to T-Rays - 100 Years of Terahertz Radiation. *Journal of Biological Physics* **2003,** *29* (2-3), 77-85.

9.   Beard, M. C.; Turner, G. M.; Schmuttenmaer, C. A., Terahertz Spectroscopy. *The Journal of Physical Chemistry B* **2002,** *106* (29), 7146-7159.

10.   Parrott, E. P. J.; Zeitler, J. A., Terahertz Time-Domain and Low-Frequency Raman Spectroscopy of Organic Materials. *Applied Spectroscopy* **2015,** *69* (1), 1-25.

11.   Zeitler, J. A.; Taday, P. F.; Newnham, D. A.; Pepper, M.; Gordon, K. C.; Rades, T., Terahertz Pulsed Spectroscopy and Imaging in the Pharmaceutical Setting-a Review. *Journal of Pharmacy and Pharmacology* **2007,** *59* (2), 209-223.

12.   Larkin, P. J.; Dabros, M.; Sarsfield, B.; Chan, E.; Carriere, J. T.; Smith, B. C., Polymorph Characterization of Active Pharmaceutical Ingredients (APIs) Using Low-Frequency Raman Spectroscopy. *Applied Spectroscopy* **2014,** *68* (7), 758-776.

13.   Inoue, M.; Hisada, H.; Koide, T.; Fukami, T.; Roy, A.; Carriere, J.; Heyler, R., Transmission Low-Frequency Raman Spectroscopy for Quantification of Crystalline Polymorphs in Pharmaceutical Tablets. *Analytical Chemistry* **2019,** *91* (3), 1997-2003.

14.   Delaney, S. P.; Korter, T. M., Terahertz Spectroscopy and Computational Investigation of the Flufenamic Acid/Nicotinamide Cocrystal. *The Journal of Physical Chemistry A* **2015,** *119* (13), 3269-3276.

15.   Parrott, E. P.; Zeitler, J. A.; Friščić, T.; Pepper, M.; Jones, W.; Day, G. M.; Gladden, L. F., Testing the Sensitivity of Terahertz Spectroscopy to Changes in Molecular and Supramolecular Structure: A Study of Structurally Similar Cocrystals. *Crystal Growth & Design* **2009,** *9* (3), 1452-1460.

16.   Ruggiero, M. T.; Sutton, J. J.; Fraser-Miller, S. J.; Zaczek, A. J.; Korter, T. M.; Gordon, K. C.; Zeitler, J. A., Revisiting the Thermodynamic Stability of Indomethacin Polymorphs with Low-Frequency Vibrational Spectroscopy and Quantum Mechanical Simulations. *Crystal Growth & Design* **2018,** *18* (11), 6513-6520.

17.   Neu, J.; Nikonow, H.; Schmuttenmaer, C. A., Terahertz Spectroscopy and Density Functional Theory Calculations of DL-Norleucine and DL-Methionine. *The Journal of Physical Chemistry A* **2018,** *122* (28), 5978-5982.

18.   Ruggiero, M. T.; Bardon, T.; Strlic, M.; Taday, P. F.; Korter, T. M., Assignment of the Terahertz Spectra of Crystalline Copper Sulfate and Its Hydrates Via Solid-State Density Functional Theory. *The Journal of Physical Chemistry A* **2014,** *118* (43), 10101-10108.

19.   Videnova-Adrabińska, V., Pre-Designed Structural Building Blocks of a (1: 1) Urea–Glutaric Acid Co-Crystal. *Journal of Materials Chemistry* **1995,** *5* (12), 2309-2311.

20.   Chadwick, K.; Davey, R.; Sadiq, G.; Cross, W.; Pritchard, R., The Utility of a Ternary Phase Diagram in the Discovery of New Co-Crystal Forms. *CrystEngComm* **2009,** *11* (3), 412-414.

21.   Thirumurugan, R.; Babu, B.; Anitha, K.; Chandrasekaran, J., Synthesis, Growth, Characterization and Quantum Chemical Investigations of a Promising Organic Nonlinear Optical Material: Thiourea-Glutaric Acid. *Journal of Molecular Structure* **2018,** *1171*, 915-925.

22.   Kostyanovsky, R. G.; Kostyanovsky, V. R.; Kadorkina, G. K., The Enigma of a (±)-Tartaric Acid–Urea Cocrystal. *Mendeleev Communications* **2009,** *1* (19), 17-18.

23.   Lue, M. K.; Meng, F. Q.; Yang, Z. H.; Yu, W. T.; Zeng, H., Growth and Characterization of Urea-(DL) Tartaric Acid Single Crystals. *Crystal Research and Technology* **1996,** *31* (7), 833-836.

24.   Groom, C. R.; Bruno, I. J.; Lightfoot, M. P.; Ward, S. C., The Cambridge Structural Database. *Acta Crystallographica Section B: Structural Science, Crystal Engineering and Materials* **2016,** *72* (2), 171-179.

25.   Swaminathan, S.; Craven, B.; McMullan, R., The Crystal Structure and Molecular Thermal Motion of Urea at 12, 60 and 123 K from Neutron Diffraction. *Acta Crystallographica Section B: Structural Science, Crystal Engineering and Materials* **1984,** *40* (3), 300-306.

26.   Takahashi, I.; Onodera, A.; Shiozaki, Y., Structural Changes of Thiourea in Connection with Its Phase Transitions: Reappraisal of Rigidity and Libration of the Molecule. *Acta Crystallographica Section B: Structural Science, Crystal Engineering and Materials* **1990,** *46* (5), 661-664.

27.   Thalladi, V. R.; Nüsse, M.; Boese, R., The Melting Point Alternation in A, Ω-Alkanedicarboxylic Acids. *Journal of the American Chemical Society* **2000,** *122* (38), 9227-9236.

28.   Falvello, L. R., CSD-ZZZDUI02. *Cambridge Structural Database Communication* **2016**.

29.   Dovesi, R.; Erba, A.; Orlando, R.; Zicovich-Wilson, C. M.; Civalleri, B.; Maschio, L.; Rérat, M.; Casassa, S.; Baima, J.; Salustro, S., Quantum-Mechanical Condensed Matter Simulations with Crystal. *Wiley Interdisciplinary Reviews: Computational Molecular Science* **2018**, e1360.

30.   Perdew, J. P.; Burke, K.; Ernzerhof, M., Generalized Gradient Approximation Made Simple. *Physical Review Letters* **1996,** *77* (18), 3865.

31.   Weigend, F.; Ahlrichs, R., Balanced Basis Sets of Split Valence, Triple Zeta Valence and Quadruple Zeta Valence Quality for H to Rn: Design and Assessment of Accuracy. *Physical Chemistry Chemical Physics* **2005,** *7* (18), 3297-3305.

32.   Grimme, S.; Antony, J.; Ehrlich, S.; Krieg, H., A Consistent and Accurate Ab Initio Parametrization of Density Functional Dispersion Correction (DFT-D) for the 94 Elements H-Pu. *The Journal of Chemical Physics* **2010,** *132* (15), 154104.

33.   Grimme, S.; Ehrlich, S.; Goerigk, L., Effect of the Damping Function in Dispersion Corrected Density Functional Theory. *Journal of Computational Chemistry* **2011,** *32* (7), 1456-1465.

34.   Grimme, S.; Hansen, A.; Brandenburg, J. G.; Bannwarth, C., Dispersion-Corrected Mean-Field Electronic Structure Methods. *Chemical Reviews* **2016,** *116* (9), 5105-5154.

35.   Axilrod, B.; Teller, E., Interaction of the Van Der Waals Type between Three Atoms. *The Journal of Chemical Physics* **1943,** *11* (6), 299-300.

36.   Muto, Y., Force between Nonpolar Molecules. *Proceedings of the Physico-Mathematical Society of Japan* **1943,** *17*, 629-631.

37.   Pascale, F.; Zicovich-Wilson, C. M.; López Gejo, F.; Civalleri, B.; Orlando, R.; Dovesi, R., The Calculation of the Vibrational Frequencies of Crystalline Compounds and Its Implementation in the Crystal Code. *Journal of Computational Chemistry* **2004,** *25* (6), 888-897.

38.   Zicovich-Wilson, C.; Pascale, F.; Roetti, C.; Saunders, V.; Orlando, R.; Dovesi, R., Calculation of the Vibration Frequencies of A-Quartz: The Effect of Hamiltonian and Basis Set. *Journal Of Computational Chemistry* **2004,** *25* (15), 1873-1881.

39.   Boys, S.; Bernardi, F., Molecular Physics: An International Journal at the Interface between Chemistry and Physics. *Molecular Physics* **1970,** *19*, 553-566.

40.   Stokes, H.; Hatch, D.; Campbell, B., Isocif, Isotropy Software Suite, iso.byu.edu. 2021.

41.   Likhitha, U.; Narayana, B.; Sarojini, B.; Kumar, S. M.; Karthick, T., Crystallographic and Theoretical Interpretation of Supramolecular Architecture in a New Salt Hydrate of DL-Tartaric Acid and Dimethylamine (DLTA-DA). *Journal of Molecular Structure* **2021,** *1225*, 129284.

42.   Bauer, L.; Gardella Jr, L. A., Addition of Thiourea to 2-and 4-Vinylpyridines. *The Journal of Organic Chemistry* **1961,** *26* (1), 82-85.

Chapter 5: Simulation and Assignment of the Terahertz Vibrational Spectra of Enalapril Maleate Cocrystal Polymorphs

The material contained within this chapter is published in The Journal of Physical Chemistry A and has been reproduced with permission of American Chemical Society.

Abstract

The identification of crystalline drug polymorphs using terahertz vibrational spectroscopy is a powerful approach for the non-destructive and non-invasive characterization of solid-state pharmaceuticals. However, a complete understanding of the terahertz spectra of molecular solids is challenging to obtain due to the complex nature of the low-frequency vibrational motions found in the sub-3 THz (sub-100 cm-1) range. Unambiguous assignments of the observed spectral features can be achieved through quantum mechanical solid-state simulations of crystal structures and lattice vibrations utilizing the periodic boundary condition approach. The terahertz spectra of two polymorphs of enalapril maleate are presented here to demonstrate that even large pharmaceuticals can be successfully modeled using solid-state density functional theory, including cocrystalline solids comprised of multiple distinct species. These simulations enable spectral assignments to be made, but also provide insights into the conformational and cohesion energies that contribute to the polymorph stabilities. The results reveal that the Form II

polymorph of enalapril maleate is the more stable of the two under ambient conditions, and that

this stability is driven by a greater intermolecular cohesion energy as compared to Form I.

5.1 Introduction

The varied three-dimensional packing arrangements of molecules in crystalline solids, referred to as polymorphism[1, 2], can substantially alter their physical and chemical properties. This issue is of immense concern to the pharmaceutical industry where these properties need to be strictly monitored and controlled to ensure the safety and quality of drugs.[3] Polymorphic changes of an active pharmaceutical ingredient (API) can affect drug effectiveness by modifying factors such as stability, permeability, and solubility.[4] Polymorphism has been studied in many homogeneous crystal pharmaceuticals such as ritonavir[5] and aripiprazole[6], but is also present in heterogeneous cocrystalline systems, such as carbamazepine[7] with nicotinamide and saccharin.[8,9]

Cocrystals are formed when two or more molecules are crystallized together to form an entirely new crystal structure, as opposed to a simple mixture of the individual component crystals. Cocrystallization is an aspect of crystal engineering that has been utilized in the pharmaceutical industry to design new drug formulations and improve existing ones.[10] By cocrystallizing an API with an inactive conformer or another API, a formulation can be developed that is more effective in terms of bioavailability or stability, or can combine the medical effects of compatible APIs.[11-15] However, as often found with homogeneous crystal structures, heterogeneous cocrystalline structures can also exist as multiple polymorphs. A pharmaceutical example of this is enalapril maleate, an important angiotensin-converting-enzyme (ACE) inhibitor used to treat hypertension, which is a cocrystal of enalapril ($[C_{20}H_{29}N_2O_5]^{+1}$) and hydrogen maleate ($[C_4O_4H_3]^{-1}$) (**Figure 5-1**). Enalapril maleate exists in two polymorphic forms generally cited as Form I[16] and Form II[17], referred to in this work as EM-I and EM-II, respectively.[18, 19]
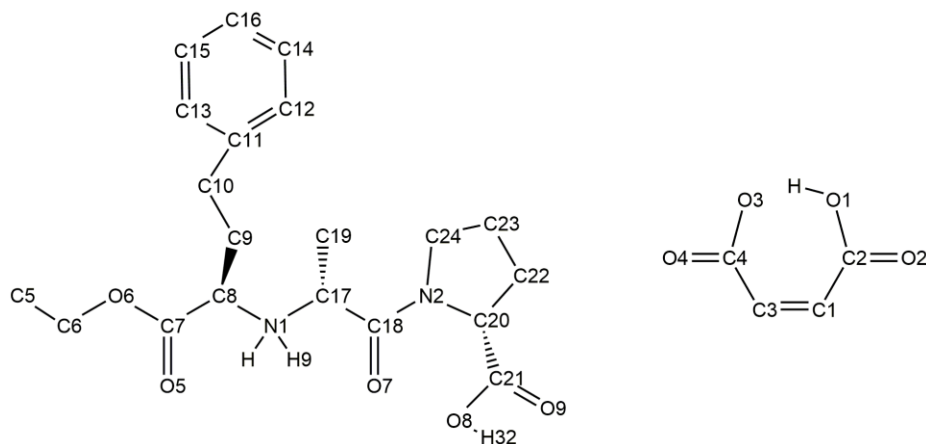
Figure 5-1. Enalapril ($[C_{20}H_{29}N_2O_5]^{+1}$) (left) and maleate ($[C_4O_4H_3]^{-1}$) (right). Only hydrogen-bonding hydrogens are labeled.

For almost two decades, terahertz spectroscopy has been an important tool used to differentiate and identify polymorphs, with one of the first major studies being on the solid-state forms of ranitidine hydrochloride.[20] Unlike mid-infrared spectroscopy and other high-frequency techniques, the vibrations present in the terahertz region (sub-6 THz or sub-200 cm^{-1}) are remarkably responsive to the packing arrangements of molecules in the crystallographic unit cell and the intermolecular interactions present within the solids.[21, 22] This unique sensitivity means that terahertz spectroscopy can provide distinct characteristic spectra for different polymorphs of the same compound, and can be utilized for both homogeneous and heterogeneous cocrystalline polymorphs.[23-26] The ability of terahertz spectroscopy to distinguish between polymorphs has been previously demonstrated with many solid-state structures, including for the two polymorphs of enalapril maleate.[24, 27, 28] However, the assignment and interpretation of the observed features in the EM-I and EM-II THz spectra have not yet been reported.

The vibrations present in the terahertz region result from the interplay of the three-dimensional packing of the crystal components and the intermolecular forces between species.

Therefore, the specific motions associated with each spectral peak cannot be determined using group frequency tables as is done at higher frequencies in the mid-infrared. Solid-state density functional theory (ss-DFT) has become an important approach for accurately simulating THz spectra, enabling spectral assignments to be made and the nature of the motions within the unit cell to be established as rotational, torsional, or translational. Use of ss-DFT can also provide valuable insights into polymorphic systems through analysis of the energetic contributors that govern polymorph and cocrystal formation and stability. The ability of ss-DFT to augment and expand on terahertz spectroscopy has been previously demonstrated with other polymorphic and cocrystalline systems such as sorbitol solvates and diclofenac acid polymorphs.[29, 30]

In this work, the two polymorphs of enalapril maleate are used as a demonstration of how terahertz spectroscopy and ss-DFT can be used in complementary roles. Together, they help to enhance analytical methods for differentiating polymorphs, reveal the chemical origins of the observed terahertz spectra, and permit the complex factors influencing the stability of polymorphic cocrystals to be understood.

5.2 Methods

5.2.1 Terahertz Frequency-Domain Spectroscopy (THz-FDS)

The frequency-domain THz spectrometer uses an injection-seeded THz parametric generation (is-TPG) source. Amplified light from the Q-switched Nd:YAG microchip laser (wavelength: 1064 nm) was used as pump light for is-TPG. This pump beam and a continuous-wave (CW) tunable diode laser beam were focused on the MgO doped $LiNbO_3$ crystal. The CW beam was used as an injection seeder to generate narrowband THz waves parametrically. The THz waves from 0.8 to 2.5 THz were generated by scanning the wavelength of the seeder laser from 1067.5 to 1074.0 nm. The angle of the seeding beam to the pumping beam was adjusted by

a galvano mirror for every wavelength during the scanning. Generated THz waves were focused on the sample tablet. Mixing the transmitted THz wave with pump light in another MgO doped LiNbO$_3$ crystal generates an upconverted signal. The upconverted signal is detected by a 2D-CMOS sensor. All experimental data was taken at Hitachi High-Tech in Hitachinaka, Japan at 295 K.[31]

EM-II was purchased from Tokyo Chemical Industry Co. Ltd.. EM-I was obtained by recrystallization from ethyl acetate in the presence of methanol. These forms were confirmed by powder x-ray diffraction (PXRD). EM-I and EM-II pellets were made with 25% by weight of the sample and 75% by weight of polyethylene (PE) for a total weight of 198 mg and pressed into 2.9 mm thick pellets.

5.2.2 Theoretical Methods

CRYSTAL17[32] was used to complete quantum mechanical simulations of the two polymorphs of enalapril maleate including geometry optimizations, frequency simulations and assignments, and energetic analyses. For all of the calculations, Ahlrichs' VTZ basis set with additional polarization[33] functions (VTZP) was used along with the Perdew-Burke-Ernzerhof (PBE)[34] density functional. The calculations were augmented with Grimme's London dispersion correction (D3) utilizing the Becke-Johnson damping correction[35-37] and also included three-body Axilrod-Teller-Muto repulsion contributions (program keyword "ABC").[38] The calculations used a pruned DFT integration grid of 99 radial points and 1454 angular points and a sampling of 170 k-points in the irreducible Brillouin zone (SHRINK=8) for EM-I and 64 k-points in the irreducible Brillouin zone (SHRINK=7) for EM-II. Appropriate k-point sampling was determined for each crystal by monitoring the convergence ($\Delta E < 10^{-10}$ hartree) of the unit cell energies while systematically incrementing the SHRINK values. The overlap-based

truncation criteria for the bielectronic integrals (Coulomb and exchange) (TOLINTEG) were set

to 10^{-9}, 10^{-9}, 10^{-9}, 10^{-9}, and 10^{-18} for the optimization, frequency, and energy calculations.

Experimental crystal structures from the Cambridge Structural Database (CSD)[39] (DIVHOF01[16]

and DIVHOF02[17] for EM-I and EM-II, respectively) were used as the starting points for the

geometry optimizations with an energy convergence of $\Delta E < 10^{-8}$ hartree. Normal mode

vibrational analyses utilized the central-difference formula to calculate the numerical derivative

of the Hessian matrix, with two displacements along each Cartesian axis for each atom and an

energy convergence of $\Delta E < 10^{-10}$ hartree. Along with each normal mode vibrational analysis, IR

intensities were calculated using the Berry phase method.[40, 41]

CRYSTAL17 was also used to perform energetic analyses on the EM-I and EM-II crystalline

solids. Conformational energies were determined by extracting a dimer of enalapril and its

closest maleate counterion from the optimized unit cell, and calculating the energy of this

isolated pair. All fixed position energy calculations were done with an energy convergence of ΔE

$< 10^{-8}$ hartree. Cohesion energies of the cocrystals were calculated by subtracting the

conformational energy of the extracted dimer from the total solid-state electronic energy of the

same unit cell. Basis set superposition error (BSSE) is present in finite atom-centered basis set

calculations, but is expected to be small given the size of the basis set used here. An estimate of

BSSE was made using the standard Boys-Bernardi counterpoise correction[42] method and

revealed to be approximately 5% of the cohesion energy. Therefore, energies reported here have

not been corrected for BSSE. For reference, test calculations of enalapril maleate using the

6-31G(d,p) basis set revealed BSSE values of approximately 20% of the cohesion energy and

would require correction.[43] Gibbs free energies, which include electronic energy, zero-point

energy, and vibrational energy contributions, were also calculated from 0 K to 600 K for each

solid.

5.3 Results and Discussion

5.3.1 Experimental Terahertz Vibrational Spectra
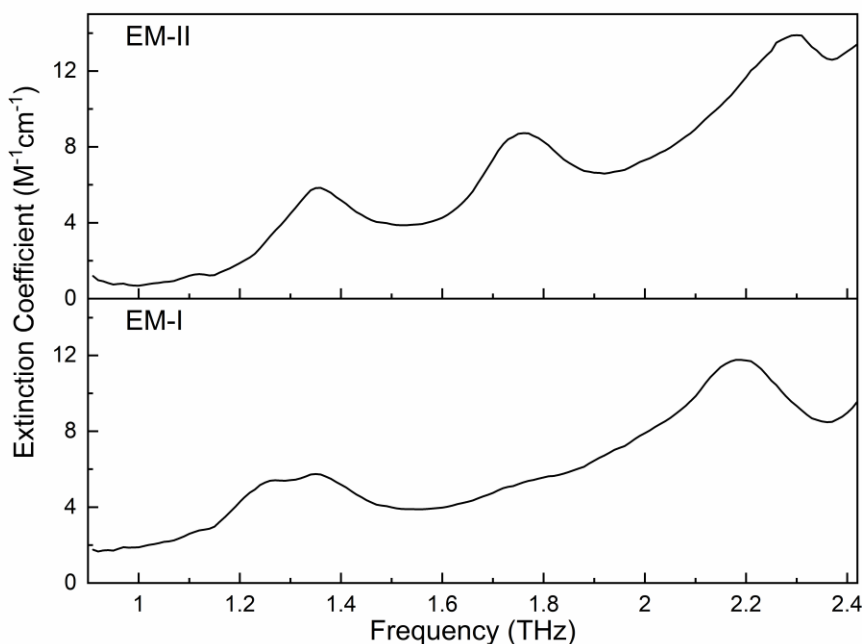
Figure 5-2. Experimental THz spectra for EM-I (bottom) and EM-II (top).

Each polymorph of enalapril maleate has a distinct terahertz spectrum that can be used to differentiate between the two forms. The experimental spectra have rising baselines, most likely due to Mie scattering and the presence of high-intensity peaks at frequencies slightly beyond the experimental range.[24] **Figure 5-2** shows the THz-FDS spectra of EM-I and EM-II from 0.9 to 2.4 THz. Between 1.2 to 1.4 THz, the EM-I spectrum has what appears to be two closely-spaced overlapping peaks with maxima at 1.26 and 1.34 THz, and a third distinct peak at 2.18 THz. The EM-II spectrum is clearly different than what was observed for EM-I and has three major features at 1.35, 1.75, and 2.27 THz. The THz-FDS results for both polymorphs of enalapril maleate are consistent with those reported in earlier works.[24, 27, 28]

5.3.2 Polymorph Differences and Optimized Structures

The enalapril maleate polymorphs have clear structural differences that help define the crystallographic symmetries of each form. The main structural difference is in the C7-O6-C6-C5 dihedral angle (**Figure 5-1**) in enalapril, which is -166.65° in EM-I and -87.44° in EM-II. The molecular structure differences contribute to EM-I crystallizing in the monoclinic space group $P2_1$ (Z=2)[16, 19], and EM-II exhibiting orthorhombic symmetry with space group $P2_12_12_1$ (Z=4) (**Figure 5-3**).[17] In both forms, the asymmetric unit of each polymorph is comprised of one enalapril and one maleate. It is worth noting that the EM-I structure was solved using single-crystal X-ray diffraction, while the EM-II structure was determined from powder X-ray diffraction experiments and lacked the same level of detail. The Mercury software package[44] was used to manually add hydrogens to the EM-II crystal structure prior to any ss-DFT calculations.

The only perceived ambiguity in the enalapril maleate crystal structures is the position of one of the hydrogen atoms at the $-NH_2-$ site of the enalapril molecule. There is a possibility that it could transfer to the maleate ion to yield maleic acid. This scenario was investigated through two structural optimizations, one starting with the expected $-NH_2-$ enalapril and maleate counterion in the crystal, the other starting with a deprotonated enalapril and maleic acid. The results showed that only the $-NH_2-$ paired with a maleate ion was stable in the solid state. This finding is consistent with the differing experimental C–O bond lengths identified in the maleate ion.
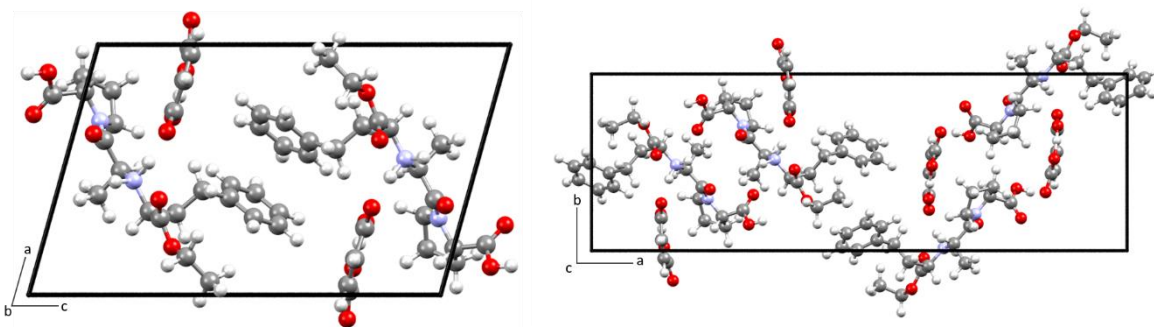
Figure 5-3. Crystallographic unit cells for EM-I (left) and EM-II (right).

Internal structure, crystal packing, and intermolecular forces are incredibly important to the accurate simulation of vibrations in the low-frequency range. The ss-DFT simulations of both the EM-I and EM-II structures yielded good agreement with experimental reports in terms of lattice parameters and molecular geometries. The average observed error in the calculated unit cell dimensions across both polymorphs was -0.91%. This is a small deviation from experiment and consistent with the published structural data being at room temperature and the simulations being at 0 K. **Table 5-1** summarizes the crystal packing results, with the largest lattice dimension errors for both structures appearing in the *c* axes of their unit cells, with a -1.49% error for EM-I and a -1.23% error for EM-II.

Table 5-1. Lattice dimensions (Å) of EM-I and EM-II from experiments[16,17], after ss-DFT optimization, and the percent error between the two.

EM-I			
Lattice Dimension	Experimental	Calculated	Percent Error
a	11.224	11.15766	-0.59%
b	6.645	6.59589	-0.74%
c	17.824	17.55754	-1.49%
EM-II			
Lattice Dimension	Experimental	Calculated	Percent Error
a	33.9898	33.72019	-0.79%
b	11.2109	11.14380	-0.60%
c	6.64195	6.55968	-1.23%

The accuracy of the simulated internal covalent bonding structure is also important in judging the computational model. Considering only non-hydrogen atoms, the EM-I simulated structure has RMSD values of 0.03 Å in the bond lengths, 1.78° in the bond angles, and 3.97° in the dihedral angles. The EM-II simulated structure has RMSD values of 0.07 Å in the bond lengths, 6.83° in the bond angles, and 7.64° in the dihedral angles. The higher RMSD values for EM-II may initially appear concerning, but are expected because the published crystal structure for EM-II is limited by the fact that it is based on powder X-ray diffraction measurements.[17]

The hydrogen-bonding network is an important part of the crystal structure and the simulated intermolecular hydrogen-bonding geometries need to also be compared to experimental data. The EM-I and EM-II polymorphs have very similar hydrogen bonds. In both there are two primary hydrogen bonds between the enalapril and maleate molecules, one an O-H•••O type and the other being an N-H•••O bond. **Figure 5-4** shows the two primary intermolecular hydrogen bonds in EM-I and EM-II, as well as the overall hydrogen-bonding pattern in both polymorphs. As the bottom panel illustrates, the individual hydrogen bonds present are similar in both solid forms, but differences in the crystallographic packing of the two polymorphs leads to global differences in the hydrogen-bonding networks.
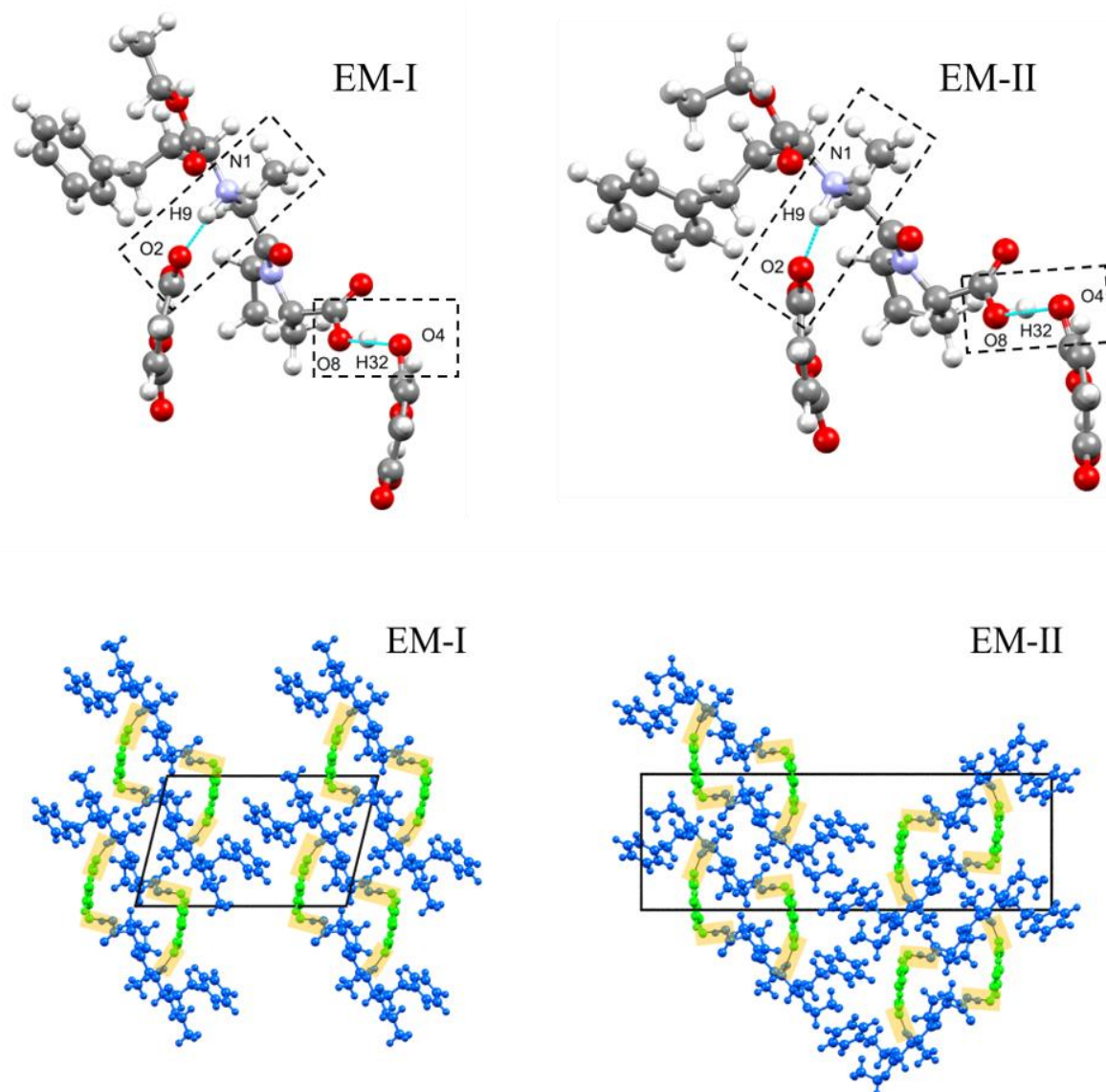
Figure 5-4. Top: Key intermolecular hydrogen bonds (light blue lines within dashed boxes) in the two enalapril maleate polymorphs. Bottom: Expanded view of the hydrogen-bonding patterns in the two enalapril maleate polymorphs with enalapril in blue, maleate in green, and the hydrogen bonds highlighted in yellow.

Table 5-2 shows the experimental and ss-DFT optimized heavy-atom distances of the two symmetry-unique hydrogen bonds in each polymorph, along with the percent error. The average hydrogen bond heavy-atom distance percent error in EM-I was 1.00%, while in EM-II it was 1.90%, demonstrating that the hydrogen-bonding network is well modeled in the ss-DFT

optimized structures of both. **Table 5-2** also shows the computational hydrogen bond angles that are not available from the existing experimental X-ray diffraction studies. It is clear that the O-H•••O interactions have larger deviations from experiment as compared to N-H•••O. Previous work has demonstrated that hydrogen bonds that are further from linearity (180°) are generally less well modeled and this may be contributing to the larger errors in the O-H•••O bonds.[45] Overall, all of the observed differences between the experimental and calculated structures are minor and are certainly of high enough quality to use as the basis for the calculation of the normal modes of vibration for both polymorphs.

Table 5-2. The hydrogen bond experimental[16,17] and computational heavy atom distances (Å) for EM-I and EM-II along with percent errors and computational hydrogen bond angles.

	Exp. Heavy Atom Distance (Å)	ss-DFT Heavy Atom Distance (Å)	Percent Error	ss-DFT Angle
	EM-I			
O8-H32•••O4	2.654	2.605	-1.85%	156.7°
N1-H9•••O2	2.753	2.757	0.15%	171.7°
	EM-II			
O8-H32•••O4	2.657	2.587	-2.63%	156.1°
N1-H9•••O2	2.749	2.781	1.16%	172.6°

5.3.3 Simulated Terahertz Vibrational Spectra
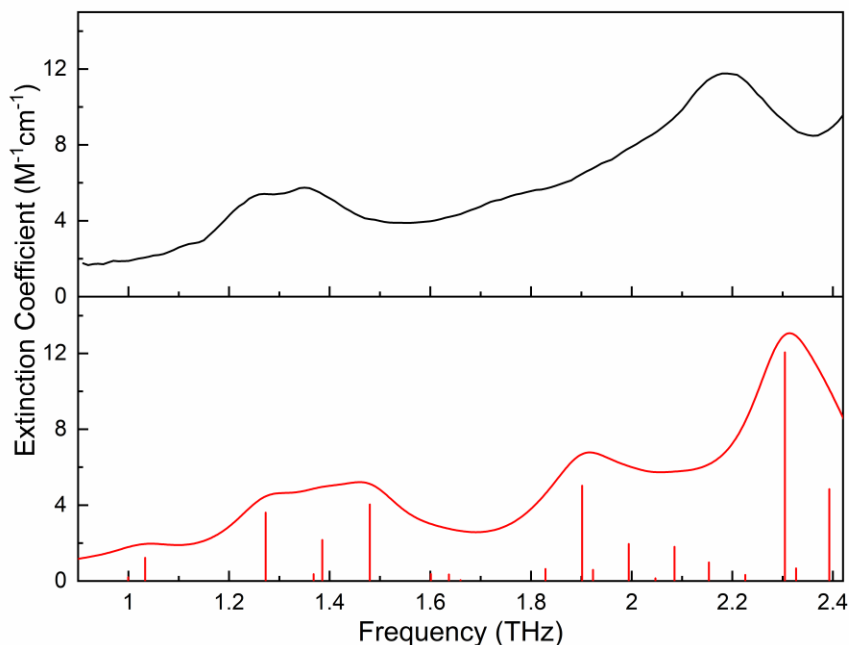
Figure 5-5. Experimental THz spectrum for EM-I (top, black) and the ss-DFT simulated THz spectrum (bottom, red). The simulated intensities have been scaled down by a factor of 5. A 3 cm^{-1} FWHM Lorentzian line shape has been convolved into the simulation to aid comparison.

Vibrational analyses of the ss-DFT optimized polymorph structures yielded no negative vibrational frequencies, indicating that both structures corresponded to energetic minima on their respective potential energy surfaces. The simulated infrared intensities for enalapril maleate were consistently overestimated by the applied theory. The simulated spectra presented here for both EM-I and EM-II have been scaled down by a factor of five from their calculated values. The origin of this intensity mismatch could be issues with the calculation of the atomic charges in these charged solid-state species, however, no negative consequences of this are evident in the simulated structures. Another possible explanation is the temperature difference between simulation and experiment, where line narrowing with cooling would tend to increase the experimental intensities and bring them closer to the 0 K simulations. The simulated spectra in

this work do not account for any scattering effects though this should have a minor influence on intensity comparisons. **Figure 5-5** compares the simulated spectrum of EM-I to the experimental data. The two features at 1.26 and 1.34 THz are reproduced in the simulation as a grouping of three peaks at 1.27, 1.39, and 1.48 THz. The small peak at 1.74 THz is likely attributable to the calculated 1.90 THz vibration, although the simulated intensity is too strong. The most intense experimental peak at 2.18 THz is found at 2.31 THz in the ss-DFT results and this is likely due to the fact that the simulated spectrum is based on a 0 K structure, while the experimental spectrum was recorded at room temperature. A complete list of simulated IR-active vibrational modes can be found in the **Supporting Information**.
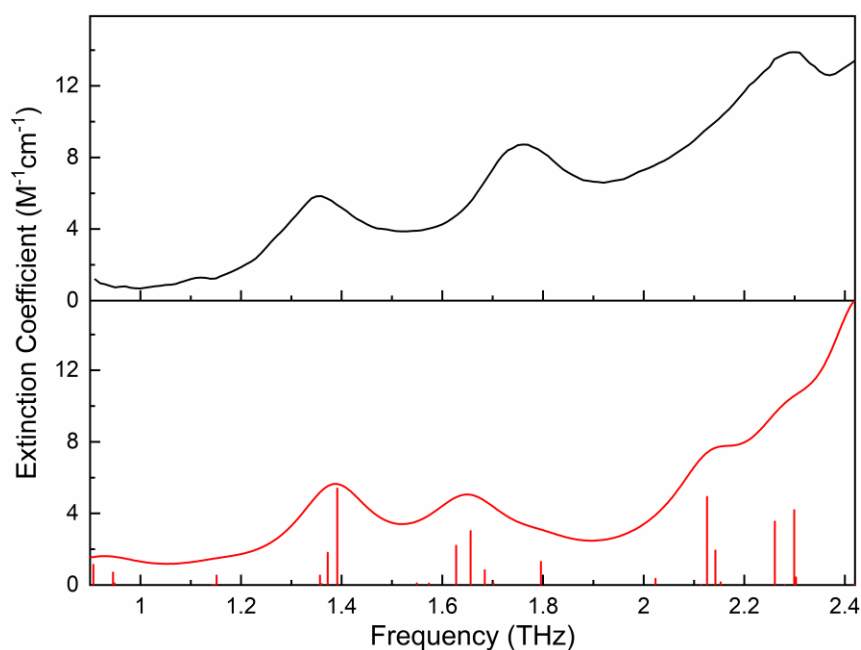
Figure 5-6. Experimental THz spectra for EM-II (top, black) and the ss-DFT simulated (bottom, red)). The simulated intensities have been scaled down by a factor of 5. A 3 cm^{-1} FWHM Lorentzian line shape has been convolved in the simulation to facilitate comparison.

The experimental spectrum for EM-II is shown in **Figure 5-6** along with the ss-DFT simulation. The clearly defined peak at 1.35 THz is reproduced in the simulated spectrum at 1.39

THz, a small shift that is again likely due to temperature effects. The experimental feature at 1.76 THz is seen shifted to a lower value of 1.66 THz in the simulated spectrum, which is unlike the shifting seen in the other position comparisons and less straightforward to attribute to temperature differences. A number of intense features appear between 2.10 and 2.40 THz in the simulated spectrum and just outside the range of the experimental data, specifically an intense simulated peak at 2.43 THz. This grouping is one possible reason for the notable rise in absorbance in the higher end of the experimental EM-II spectrum and makes for a difficult interpretation of the absorption feature observed at 2.27 THz. This 2.27 THz peak is tentatively assigned to the vibration calculated at 2.29 THz. It is possible that the simulated structure and spectrum of EM-II could be improved if single-crystal X-ray diffraction data was available for comparison and indicated some deficiency in the calculated data. However, it is more likely that the challenges associated with assigning all of the observed spectral features arises from thermal shifting of the peaks that is not accounted for in the current simulations. Thermal effects in vibrational spectroscopy can be approximated with computational methods such as the quasi-harmonic approximation, but these are prohibitively slow to apply to large pharmaceutical systems.[46] A complete list of simulated IR-active vibrational modes can be found in the **Supporting Information**.

The simulations present an opportunity to assign the experimental absorption features to particular motions of the molecules in the polymorphic solids. The majority of the vibrational modes in the terahertz region for both EM-I and EM-II are a mixture of external lattice and internal molecular motions. In EM-I, the vibrations with calculated frequencies of 1.27 and 2.31 THz are primarily rotational motion, while the modes at 1.48 and 1.90 THz are primarily torsional motion. In EM-II, the 1.39, 1.66, and 2.13 THz modes are all primarily rotational

motion. The complicated nature of these vibrations is due to enalapril being a large, flexible

molecule that is strongly paired with maleate in the cocrystalline solids and therefore it is

difficult for the terahertz motions to be limited to localization within only the enalapril or

maleate components. For example, by analyzing the eigenvector displacements of all the atoms

in the crystallographic unit cell the rotational vibration at 1.27 THz in EM-I, can be identified as

being composed of 39% maleate motion and 61% enalapril motion. **Table 5-3** details the

motions that are responsible for the four highest intensity peaks predicted in EM-I and EM-II

between 0.9 and 2.4 THz and indicate the majority motion type and the percentage of atomic

motion in the modes arising from the cocrystal components.

Table 5-3. Four more intense peaks in the EM-I and EM-II simulated spectra between 0.9 and
2.4 THz along with the motion type and the percent motion in enalapril and maleate of the
cocrystal.

EM-I			
Frequency (THz)	Motion Type	% Enalapril	% Maleate
1.27	Rotational	39%	61%
1.48	Torsional	55%	45%
1.90	Torsional	64%	36%
2.31	Rotational	37%	63%
EM-II			
Frequency (THz)	Motion Type	% Enalapril	% Maleate
1.39	Rotational	34%	66%
1.66	Rotational	59%	41%
2.13	Rotational	36%	64%
2.30	Rotational	36%	64%

5.3.4 Polymorph Energy Analysis

The low errors in the simulated structures of EM-I and EM-II, along with the accuracy of

the low-frequency vibrational simulations, add confidence in the ss-DFT model being used and

allows for the investigation of the energetics involved in the two polymorphs of enalapril

maleate. The dimer and cohesion energies, along with the Gibbs free energies, of the two

polymorphs can give important insights into the polymorph and cocrystal formation mechanisms and relative stabilities. In terms of 0 K total electronic energies, EM-II is lower in energy than EM-I by 2.91 kJ/mol per asymmetric unit. The electronic energy results match ranking with experimental data that show EM-II is stable, but EM-I is metastable.[17] When the energy is further broken down into dimer and crystal cohesion energies, EM-I is lower in dimer energy by 1.03 kJ/mol, but EM-II has a stronger cohesion energy by 3.94 kJ/mol. **Table 5-4** lists the relative values for the various energy components in EM-I and EM-II. Considering cohesion energy as an indicator of solubility, the numbers suggest that EM-I might be the more water soluble of the two crystal forms, but this prediction is only weakly supported by published dissolution data.[18]

Table 5-4. Relative total electronic, dimer, cohesion, and Gibbs free energies (0 K and 298 K) for EM-I and EM-II per asymmetric unit (one enalapril and one maleate). Bolded values are energetically favorable.

	EM-I (kJ/mol)	EM-II (kJ/mol)
Total Electronic Energy	+2.91	**0.00**
Dimer Energy	**0.00**	+1.03
Cohesion Energy (total)	+3.94	**0.00**
Gibbs Free Energy (0 K)	+2.52	**0.00**
Gibbs Free Energy (298 K)	+6.00	**0.00**

The Gibbs free energies calculated at 0 K and 298 K help provide a more holistic description of energetic stability by including temperature-dependent factors such as vibrational energy and entropy. The Gibbs free energy of EM-II is lower (more stable) than that of EM-I at both 0 K and 298 K and **Figure 5-7** shows that the Gibbs free energy curves do not cross at any temperature (monotropic relationship). The difference in the calculated Gibbs free energies is in good agreement with previous thermodynamic measurements that indicated EM-I and EM-II are similar in energy, but that EM-II is 0.6 kcal/mol (2.5 kJ/mol) more stable.[18] Based on the

complete energy analysis, EM-I is likely a kinetically formed polymorph, forming first during

crystallization due to a more favorable conformational energy and then remains trapped in the

metastable state due to barriers prohibiting relaxation into EM-II. On the other hand, EM-II is the

thermodynamically stable crystal form of enalapril maleate due to more favorable cohesion

energy, but its initial growth may be limited by its less favorable molecular conformation. This

behavior is in agreement with Ostwald's rule for polymorph formation which states that a

metastable polymorph will form before the most stable polymorph.[3]
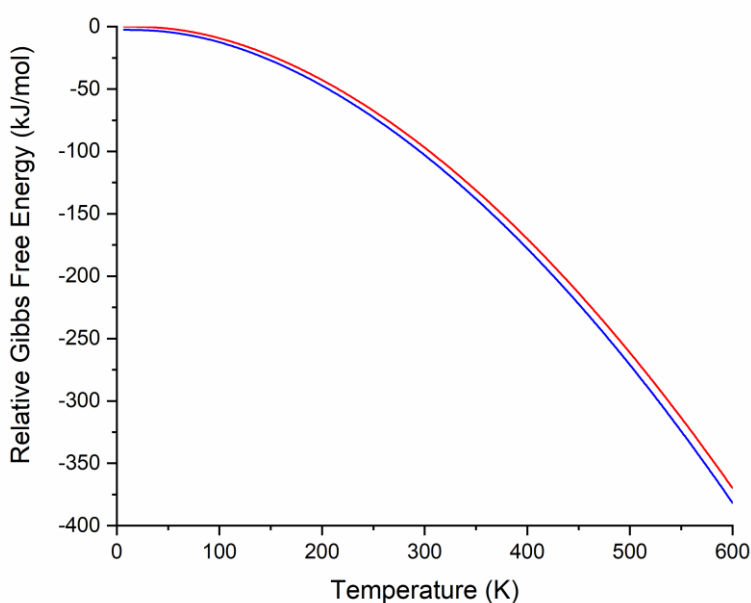
Figure 5-7. Relative Gibbs free energy curve for EM-I (red) and EM-II (blue). All energies
are per asymmetric unit. For clarity, the energy values have been set relative to a common
zero.

5.4 Conclusions

The powerful combination of terahertz spectroscopy and ss-DFT has allowed for the

experimental differentiation of enalapril maleate cocrystalline polymorphs, as well as the

computational assignment of their observed spectra to specific motions within the solid samples.

The sub-3 THz vibrations of both enalapril maleate polymorphs are complex, with significant amounts of rotational and torsional motion occurring simultaneously in the enalapril and maleate moieties. The successful simulation of the EM-I and EM-II structures and vibrations provides confidence in the ability of the calculations to yield useful details of the energetic factors underlying the observed stability rankings of the polymorphs. Experimentally, it has been shown that under ambient conditions, EM-II is the more stable of the two enalapril maleate polymorphs and ss-DFT analyses is able to explain this stability ranking as originating from the stronger cohesion energy of the EM-II crystal.

5.5 Supporting Information (see Appendix B)

Solid-state DFT optimized lattice parameters for EM-I and EM-II, list of solid-state DFT optimized atomic positions in fractional coordinates for the asymmetric unit cell for EM-I and EM-II, list of solid-state DFT IR-active vibrational frequencies, mode symmetries, IR intensities for EM-I and EM-II, CRYSTAL-formatted input files for geometry optimizations and frequency calculations for EM-I and EM-II, and CIFs of the EM-I and EM-II optimized structures.

5.6 Acknowledgements

5.7 References

1.   Cruz-Cabeza, A. J.; Reutzel-Edens, S. M.; Bernstein, J., Facts and Fictions About Polymorphism. *Chemical Society Reviews* **2015,** *44* (23), 8619-8635.

2.   Cruz-Cabeza, A. J.; Bernstein, J., Conformational Polymorphism. *Chemical Reviews* **2013,** *114* (4), 2170-2191.

3.   Lee, E. H., A Practical Guide to Pharmaceutical Polymorph Screening & Selection. *Asian Journal of Pharmaceutical Sciences* **2014,** *9* (4), 163-175.

4.   Lawrence, X. Y.; Furness, M. S.; Raw, A.; Outlaw, K. P. W.; Nashed, N. E.; Ramos, E.; Miller, S. P.; Adams, R. C.; Fang, F.; Patel, R. M., Scientific Considerations of Pharmaceutical Solid Polymorphism in Abbreviated New Drug Applications. *Pharmaceutical Research* **2003,** *20* (4), 531-536.

5.   Bauer, J.; Spanton, S.; Henry, R.; Quick, J.; Dziki, W.; Porter, W.; Morris, J., Ritonavir: An Extraordinary Example of Conformational Polymorphism. *Pharmaceutical Research* **2001,** *18* (6), 859-866.

6.   Delaney, S. P.; Pan, D.; Yin, S. X.; Smith, T. M.; Korter, T. M., Evaluating the Roles of Conformational Strain and Cohesive Binding in Crystalline Polymorphs of Aripiprazole. *Crystal Growth & Design* **2013,** *13* (7), 2943-2952.

7.   Kobayashi, Y.; Ito, S.; Itai, S.; Yamamoto, K., Physicochemical Properties and Bioavailability of Carbamazepine Polymorphs and Dihydrate. *International Journal of Pharmaceutics* **2000,** *193* (2), 137-146.

8.   Porter Iii, W. W.; Elie, S. C.; Matzger, A. J., Polymorphism in Carbamazepine Cocrystals. *Crystal Growth & Design* **2008,** *8* (1), 14-16.

9.   Aitipamula, S.; Chow, P. S.; Tan, R. B., Polymorphism in Cocrystals: A Review and Assessment of Its Significance. *CrystEngComm* **2014,** *16* (17), 3451-3465.

10.   Kumar, S., Pharmaceutical Cocrystals: An Overview. *Indian Journal of Pharmaceutical Sciences* **2017,** *79* (6), 858-871.

11.   Dalpiaz, A.; Pavan, B.; Ferretti, V., Can Pharmaceutical Co-Crystals Provide an Opportunity to Modify the Biological Properties of Drugs? *Drug Discovery Today* **2017,** *22* (8), 1134-1138.

12.   Remenar, J. F.; Morissette, S. L.; Peterson, M. L.; Moulton, B.; MacPhee, J. M.; Guzman, H. R.; Almarsson, O., Crystal Engineering of Novel Cocrystals of a Triazole Drug with 1,4-Dicarboxylic Acids. *Journal of the American Chemical Society* **2003,** *125* (28), 8456-8457.

13.   Vioglio, P. C.; Chierotti, M. R.; Gobetto, R., Pharmaceutical Aspects of Salt and Cocrystal Forms of Apis and Characterization Challenges. *Advanced Drug Delivery Reviews* **2017,** *117*, 86-110.

14.   Clarke, H. D.; Hickey, M. B.; Moulton, B.; Perman, J. A.; Peterson, M. L.; Wojtas, Ł.; Almarsson, O. r.; Zaworotko, M. J., Crystal Engineering of Isostructural Quaternary Multicomponent Crystal Forms of Olanzapine. *Crystal Growth & Design* **2012,** *12* (8), 4194-4201.

15.   Yousef, M. A.; Vangala, V. R., Pharmaceutical Cocrystals: Molecules, Crystals, Formulations, Medicines. *Crystal Growth & Design* **2019,** *19* (12), 7420-7438.

16.   Précigoux, G.; Geoffre, S.; Leroy, F., N-(1-Ethoxycarbonyl-3-Phenylpropyl)-L-Alanyl-L-Prolinium–Hydrogen Maleate (1/1), Enalapril (Mk-421). *Acta Crystallographica Section C: Crystal Structure Communications* **1986,** *42* (8), 1022-1024.

17.   Kiang, Y.-H.; Huq, A.; Stephens, P. W.; Xu, W., Structure Determination of Enalapril Maleate Form Ii from High-Resolution X-Ray Powder Diffraction Data. *Journal of Pharmaceutical Sciences* **2003,** *92* (9), 1844-1853.

18.   Ip, D. P.; Brenner, G. S.; Stevenson, J. M.; Lindenbaum, S.; Douglas, A. W.; Klein, S. D.; McCauley, J. A., High Resolution Spectroscopic Evidence and Solution Calorimetry Studies on the Polymorphs of Enalapril Maleate. *International Journal of Pharmaceutics* **1986,** *28* (2-3), 183-191.

19.   In, Y.; Shibata, M.; Doi, M.; Ishida, T.; Inoue, M.; Sasaki, Y.; Morimoto, S., Conformational Similarities of Angiotensin-Converting Enzyme Inhibitors: X-Ray Crystal Structures. *Journal of the Chemical Society, Chemical Communications* **1986,** (6), 473-474.

20.   Taday, P. F.; Bradley, I.; Arnone, D.; Pepper, M., Using Terahertz Pulse Spectroscopy to Study the Crystalline Structure of a Drug: A Case Study of the Polymorphs of Ranitidine Hydrochloride. *Journal of Pharmaceutical Sciences* **2003,** *92* (4), 831-838.

21.   Beard, M. C.; Turner, G. M.; Schmuttenmaer, C. A., Terahertz Spectroscopy. *The Journal of Physical Chemistry B* **2002,** *106* (29), 7146-7159.

22.   Parrott, E. P. J.; Zeitler, J. A., Terahertz Time-Domain and Low-Frequency Raman Spectroscopy of Organic Materials. *Applied Spectroscopy* **2015,** *69* (1), 1-25.

23.   Parrott, E. P.; Zeitler, J. A.; Friščić, T.; Pepper, M.; Jones, W.; Day, G. M.; Gladden, L. F., Testing the Sensitivity of Terahertz Spectroscopy to Changes in Molecular and Supramolecular Structure: A Study of Structurally Similar Cocrystals. *Crystal Growth & Design* **2009,** *9* (3), 1452-1460.

24.	Strachan, C. J.; Taday, P. F.; Newnham, D. A.; Gordon, K. C.; Zeitler, J. A.; Pepper, M.; Rades, T., Using Terahertz Pulsed Spectroscopy to Quantify Pharmaceutical Polymorphism and Crystallinity. *Journal of Pharmaceutical Sciences* **2005,** *94* (4), 837-846.

25.	Zeitler, J. A.; Taday, P. F.; Newnham, D. A.; Pepper, M.; Gordon, K. C.; Rades, T., Terahertz Pulsed Spectroscopy and Imaging in the Pharmaceutical Setting-a Review. *Journal of Pharmacy and Pharmacology* **2007,** *59* (2), 209-223.

26.	Delaney, S. P.; Korter, T. M., Terahertz Spectroscopy and Computational Investigation of the Flufenamic Acid/Nicotinamide Cocrystal. *The Journal of Physical Chemistry A* **2015,** *119* (13), 3269-3276.

27.	Strachan, C. J.; Rades, T.; Newnham, D. A.; Gordon, K. C.; Pepper, M.; Taday, P. F., Using Terahertz Pulsed Spectroscopy to Study Crystallinity of Pharmaceutical Materials. *Chemical Physics Letters* **2004,** *390*, 20-24.

28.	Rutz, F.; Wilk, R.; Kleine-Ostmann, T.; Grunenberg, J.; Koch, M. Experimental and Theoretical Study of the Thz Absorption Spectra of Selected Tripeptides. In *Terahertz and Gigahertz Electronics and Photonics IV, International Society for Optics and Photonics*: **2005**; 12-19.

29.	Dierks, T. M.; Korter, T. M., Comparison of Intermolecular Forces in Anhydrous Sorbitol and Solvent Cocrystals. *The Journal of Physical Chemistry A* **2017,** *121* (30), 5720-5727.

30.	King, M. D.; Buchanan, W. D.; Korter, T. M., Identification and Quantification of Polymorphism in the Pharmaceutical Compound Diclofenac Acid by Terahertz Spectroscopy and Solid-State Density Functional Theory. *Analytical Chemistry* **2011,** *83* (10), 3786-3792.

31.   Mohara, M.; Aiko, K.; Shimura, K.; Ono, T. Quantitative Analysis and Inspection for Pharmaceutical Polymorphism with Injection-Seeded Terahertz Parametric Generation Technique. In *Proceedings of 43rd International Conference on Infrared, Millimeter, and Terahertz Waves (IRMMW-THz), IEEE*: **2018**; 265-266.

32.   Dovesi, R.; Erba, A.; Orlando, R.; Zicovich-Wilson, C. M.; Civalleri, B.; Maschio, L.; Rérat, M.; Casassa, S.; Baima, J.; Salustro, S., Quantum-Mechanical Condensed Matter Simulations with Crystal. *Wiley Interdisciplinary Reviews: Computational Molecular Science* **2018**, e1360.

33.   Schäfer, A.; Horn, H.; Ahlrichs, R., Fully Optimized Contracted Gaussian Basis Sets for Atoms Li to Kr. *The Journal of Chemical Physics* **1992,** *97* (4), 2571-2577.

34.   Perdew, J. P.; Burke, K.; Ernzerhof, M., Generalized Gradient Approximation Made Simple. *Physical Review Letters* **1996,** *77* (18), 3865.

35.   Grimme, S.; Antony, J.; Ehrlich, S.; Krieg, H., A Consistent and Accurate Ab Initio Parametrization of Density Functional Dispersion Correction (Dft-D) for the 94 Elements H-Pu. *The Journal of Chemical Physics* **2010,** *132* (15), 154104.

36.   Grimme, S.; Ehrlich, S.; Goerigk, L., Effect of the Damping Function in Dispersion Corrected Density Functional Theory. *Journal of Computational Chemistry* **2011,** *32* (7), 1456-1465.

37.   Grimme, S.; Hansen, A.; Brandenburg, J. G.; Bannwarth, C., Dispersion-Corrected Mean-Field Electronic Structure Methods. *Chemical Reviews* **2016,** *116* (9), 5105-5154.

38.   Donà, L.; Brandenburg, J. G.; Bush, I. J.; Civalleri, B., Cost-Effective Composite Methods for Large Scale Solid-State Calculations. *Faraday Discussions* **2020**.

39.   Groom, C. R.; Bruno, I. J.; Lightfoot, M. P.; Ward, S. C., The Cambridge Structural Database. *Acta Crystallographica Section B: Structural Science, Crystal Engineering and Materials* **2016,** *72* (2), 171-179.

40.   Noel, Y.; Zicovich-Wilson, C.; Civalleri, B.; D'arco, P.; Dovesi, R., Polarization Properties of Zno and Beo: An Ab Initio Study through the Berry Phase and Wannier Functions Approaches. *Physical Review B* **2001,** *65* (1), 014111.

41.   Pascale, F.; Zicovich-Wilson, C. M.; López Gejo, F.; Civalleri, B.; Orlando, R.; Dovesi, R., The Calculation of the Vibrational Frequencies of Crystalline Compounds and Its Implementation in the Crystal Code. *Journal of Computational Chemistry* **2004,** *25* (6), 888-897.

42.   Boys, S.; Bernardi, F., Molecular Physics: An International Journal at the Interface between Chemistry and Physics. *Molecular Physics* **1970,** *19*, 553-566.

43.   Hariharan, P. C.; Pople, J. A., The Influence of Polarization Functions on Molecular Orbital Hydrogenation Energies. *Theoretica Chimica Acta* **1973,** *28* (3), 213-222.

44.   Macrae, C. F.; Sovago, I.; Cottrell, S. J.; Galek, P. T.; McCabe, P.; Pidcock, E.; Platings, M.; Shields, G. P.; Stevens, J. S.; Towler, M., Mercury 4.0: From Visualization to Analysis, Design and Prediction. *Journal of Applied Crystallography* **2020**.

45.   Ireta, J.; Neugebauer, J.; Scheffler, M., On the Accuracy of Dft for Describing Hydrogen Bonds: Dependence on the Bond Directionality. *The Journal of Physical Chemistry A* **2004,** *108* (26), 5692-5698.

46.   Dampf, S. J.; Korter, T. M., Anomalous Temperature Dependence of the Lowest-Frequency Lattice Vibration in Crystalline Γ-Aminobutyric Acid. *The Journal of Physical Chemistry A* **2019,** *123* (10), 2058-2064.

Chapter 6: Study on Hydration and Dehydration of Ezetimibe by Terahertz Spectroscopy with Humidity-Controlled Measurements and Theoretical Analysis

The material contained within this chapter is published in Journal of Physical Chemistry A and has been reproduced with permission of American Chemical Society.

This paper was in collaboration with Hitachi High-Tech and they wrote the majority of this paper with my contributions being the theoretical portion.

Abstract

Understanding the solid-state transitions of active pharmaceutical ingredients (APIs) is essential for quality control since differences in their forms affect the bioavailability of APIs. Terahertz (THz) frequency-domain spectroscopy is suitable for such an application since it can sensitively probe the lattice phonon modes originating in the crystal structures. THz absorption spectra were obtained for ezetimibe (EZT) and ezetimibe monohydrate (EZT-MH), which have similar crystalline structures and belong to the same space group. The observed absorption spectrum of EZT matched well with the solid-state density functional theory (ss-DFT)-simulated spectrum for the structures at 0 K and room temperature (modeled using constrained unit cell volumes). However for EZT-MH, the ss-DFT spectrum of the room-temperature structure showed better correlation with the experimental THz spectrum than that of the simulated spectrum of the 0 K structures, suggesting that the EZT-MH crystal has greater anharmonic character. Gibbs free-energy curves were calculated, and EZT-MH was found to be more stable

than pure EZT and water in a broad temperature range. The hydrate stability may be influenced by the existence of more hydrogen bonds in EZT-MH. The hydration and dehydration of EZT in a pure API tablet and formulation tablets were monitored using a THz spectrometer with a humidity-controlled sample chamber. The effect of the excipient in the formulation tablet on hydration was successfully confirmed by showing that the solid-state transition of the API with excipients is significantly slower than that without it. Under a relative humidity of 60%, hydration of EZT in a pure EZT tablet occurred in 200 min, while the hydration of EZT in a formulation tablet was 50 times slower.

6.1 Introduction

Analyzing crystalline forms, such as polymorph and hydrate/ anhydrous forms, of active pharmaceutical ingredients (APIs) in formulation tablets is essential for quality control of pharmaceutical tablets. Different crystalline forms of an API can produce different properties, such as altered solubility, melting point, and density.[1] Transition between crystalline forms during pharmaceutical manufacturing processes such as mixing, granulation, drying, and tableting processes have been reported.[2] In addition, unstable and metastable forms could be transformed to a stable form under standard storage conditions. Therefore, identifying a stable form of an API and confirming it in formulation tablets and after production processes are necessary for ensuring quality of pharmaceutical products.[3]

Approximately one-third of pharmaceutical molecules are thought to be capable of forming crystalline hydrates.[4] Hydrates usually have lower dissolution rates than anhydrates,[5] and pharmaceutical excipients affect hydration and dehydration reactions in formulations that contains API and some excipients.[6] However, very few spectroscopic studies on the crystalline form in pharmaceutical formulations have been reported because of the difficulties of understanding the complex spectra resulting from multiple compounds. Also, monitoring and understanding the hydration and dehydration reactions of APIs in formulations are important for pharmaceutical manufacturers to select suitable excipients. Crystal structures of hydrates transform upon dehydration since removal of water induces the change in the internal structure, and some hydrates also become amorphous when dehydrated.[7] Others retain their three-dimensional packing arrangements with hydration and dehydration transitions.[7] For example, erythromycin A is a widely used macrolide antibiotic and is known for having structural

similarity between its dihydrate and anhydrate forms, and similar powder X-ray diffraction (PXRD) patterns between the hydrate and anhydrate forms are observed.[6,8]
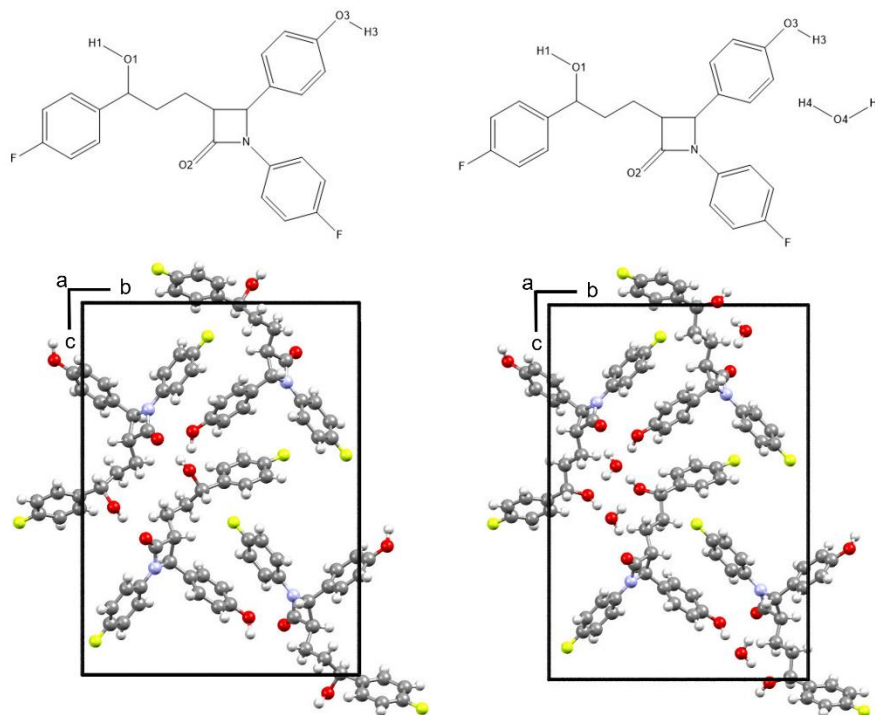
Figure 6-1. EZT (top, left), EZT-MH (right, top), and crystallographic unit cells for EZT (bottom, left) and EZT-MH (bottom, right). Only atoms involved in hydrogen bonding are labeled in the two-dimensional representations.

PXRD is widely used to identify crystalline forms in the pharmaceutical field and determine crystal structures directly. The combination of PXRD and calorimetric techniques such as differential scanning calorimetry and thermogravimetric analyses are powerful tools for evaluating the formation of hydrates and dehydrates of APIs.[6,8,9] Mid- and low-frequency Raman spectroscopy is sensitive to the solid-state structure and applied to identify hydrates.[10,11] Since terahertz (THz) radiation is located at the far-infrared region, THz spectroscopy can directly probe the lattice phonon modes originating from the crystal structure contents and specific packing. Using THz time-domain spectroscopy (THz-TDS), the identification of hydrates and

anhydrates has been reported.[12–14] Also, novel solid-state density functional theory (ss-DFT) calculations for hydrate and anhydrate organic crystals have been performed to assign the vibrational modes of their THz absorption spectra.[12,15]

An injection-seeded THz parametric generation (is-TPG) technique has been developed for realizing a high-peak-power THz wave source,[16] and it has been used for THz frequency-domain spectroscopy (THz-FDS).[17–19] Although THz-TDS generally has a high dynamic range below 1 THz, an is-TPG source has the highest dynamic range between 1.5 and 2.0 THz,[17] where a number of characteristic absorption peaks exist. Its high-peak-power THz wave and large dynamic range over a wide frequency range make it applicable to inspecting crystal structures in a formulation tablet without sample damage. The transmission THz spectrometer with an intense THz source such as this makes it possible to inspect a whole sample tablet,[19] not only the surface of the sample or a small portion of the sample like in other microscopic methods. Thus, it has another advantage, the ability to detect changes in crystalline forms directly in a formulation tablet.

In this work, we theoretically analyze the crystal structures and THz absorption spectra of ezetimibe anhydrous (EZT) and ezetimibe monohydrate (EZT-MH) and identify the solid-state transition between the two using THz-FDS with an is-TPG technique. EZT is used for cholesterol and lipid reduction in blood and is considered as Class II in the Biopharmaceutical Classification System, which means the API has low solubility in water but high permeability.[20,21] EZT exists in the solid state in both anhydrous[22] and monohydrate[23] forms with very similar crystalline morphologies, with both belonging to the same $P2_12_12_1$ space group (**Figure 6-1**). Although several pieces of research on improving the solubility of EZT have been reported, studies in the literature about different crystalline forms of EZT are limited.[21,24,25] Here,

we have demonstrated monitoring of the hydration and dehydration of ezetimibe in real time using THz-FDS with the is-TPG source and a humidity-controlled sample chamber and verified the effect of excipients in the pharmaceutical formulation on the solid-state phase transformation. Additionally, ss-DFT calculations were used to simulate the crystal structures and vibrations of EZT and EZT-MH to assign the THz spectra. In order to understand the stability of EZT-MH, the Gibbs free-energy curves for EZT-MH and EZT were calculated using ss-DFT to better define the temperature dependence of the different forms.

6.2 Methods

6.2.1 Materials

EZT was purchased from Toronto Research Chemicals. EZT-MH was obtained by keeping EZT at room temperature at a relative humidity (RH) of 55−75% overnight.[21] The EZT-MH form was confirmed by PXRD (Rigaku, MiniFlex600), as shown in the **Supporting Information**. The PXRD peaks at 7.82 and 24.46° matched with those of previous study about EZT-MH.[21] The sample powders were weighed and mixed, as shown in **Table 6-1**, and pressed into 10 mm diameter tablets at a pressure of 4.9 kN in 10 s for the measurement of the THz absorption spectra of pure EZT and EZT-MH. Ultra-high-molecular-weight polyethylene (Sigma-Aldrich) was used as the diluent. Since the THz-wave absorption of EZT-MH is low, the tablet thickness was about twice that of EZT. To measure the hydration and dehydration of a pharmaceutical formulation tablet, a sample tablet was used that contained 10% EZT as an API and lactose monohydrate (Wako Pure Chemical Corporation, guaranteed reagent) and crystalline cellulose (Asahi Kasei Corporation, ST-100, particle size: 50 μm) as additives. A placebo (no API) tablet was prepared to compare the absorption spectra of the formulation tablet and the placebo tablet. The sample powder of the formulation and placebo tablets were pressed into 10

mm diameter tablets at a pressure of 49 kN in 2 min. The high pressure was needed to avoid the disintegration of the sample tablets due to the absorption of humidity by additives. The thickness of the pure EZT tablets normalized by its weight was thicker than that of the formulation tablets. This may come from the differences in density between EZT and the additives.

Table 6-1. Compositions of sample tablets (wt%)

Tablet name	Ezetimibe		Polyethylene	Lactose monohydrate	Crystalline cellulose	Thickness (mm)	weight (mg)
	anhydrate	monohydrate					
Pure EZM	80	-	20	-	-	1.3	109
Pure EZT-MH	-	80	20	-	-	2.5	197
Formulation	10	-	-	45	45	2.5	226
Placebo	-	-	-	50	50	2.5	226

6.2.2 Terahertz Spectrometer

Figure 6-2 shows the developed frequency-domain THz (FD-THz) spectrometer with isTPG.[19] Light emitted from a Q-switched Nd:YAG microchip laser (L11038-11, Hamamatsu Photonics) at a 15 Hz repetition rate (wavelength: 1064 nm) was amplified up to 26 mJ by double-pass Nd:YAG amplifiers (POD-CS3/300PNY3, PHLUXi). This amplified high-peak-power light was focused on a MgO-doped LiNbO3 (LN) crystal and used as a pump light for generating is-TPG waves. The output light of a continuous-wave (CW) tunable diode laser with a single longitudinal mode (TLB6722-P, Newport) was also amplified up to 150 mW by a fiber amplifier (CTFA-PB, Keopsys). This amplified CW beam was introduced into the LN crystal as a seed light to generate is-TPG waves parametrically. The relationship among the pump light, seed light, and generated is-TPG waves satisfies the non-collinear phase-matching condition, as

shown in the inset of **Figure 6-2**. The is-TPG waves from 0.8 to 2.5 THz were generated by scanning the wavelength of the seeder laser from 1067.5 to 1074 nm. The angle of the seeding beam to the pumping beam was adjusted with high accuracy using a galvano mirror for every wavelength during the scanning. The relationship between the surface of the crystal and the galvano mirror was designed to be optically conjugate using a concave mirror in order to make the beam position of the seed light stay on the surface of the crystal at the same position when the angle of the seeding beam was changed using the galvano mirror for a selected wavelength. The surface of the LN crystal was cut off at an angle of 4° to avoid optically damaging the seed optical system using the pump light reflected at the front surface of the crystal. Adopting the galvano mirror makes it possible to establish a compact and practical seed optical system. A Si prism placed on the side of the LN crystal was used as an efficient output coupler for the THz waves. A slit mounted on a linear stage was inserted in the THz optics between the LN crystal and a sample to effectively expand the spectral range of the spectrometer.

When an is-TPG wave was generated at the first LN crystal, a weak and broadband unseeded TPG wave was simultaneously generated by the intense pulsed pump beam without the effect of the seeding beam. This broadband TPG wave was generated preferentially in a region of the seeded frequency but less than 1.2 THz and higher than 2.5 THz, where the is-TPG conversion efficiency was low. The intensity of this TPG wave was unstable and affected the dispersion of the signal intensity of the spectra. To eliminate this TPG wave with an emission angle different from that of the is-TPG wave, the generated THz waves were focused on the slit, and the position of the slit was adjusted by a linear stage so that the is-TPG wave passed through the slit, and the TPG wave was blocked. Using this configuration in the frequency region with a

lower conversion efficiency for is-TPG waves, and even if the is-TPG light transmitted through the sample tablet was weak, the signal light could be detected.

Generated high-purity is-TPG waves were focused on a sample tablet that was mounted on a holder in a humidity-controlled chamber. The RH in the chamber was controlled to lower than 1% for dry measurements and approximately 60% for non-dry measurements. Mixing the THz waves transmitted through the sample tablet with the pump light in another MgO-doped LiNbO3 crystal generated an upconverted signal. The upconverted signal light was attenuated by multiple neutral density (ND) filters after being separated from the pump light and was detected by a 2D-CMOS camera in synchronization with the emission of the pump light. All absorption spectra in this work were smoothed using a Savitzky−Golay filtering method. In the case of non-dry measurements, the absorption peaks of water vapor in the measured data were removed by preprocessing the spectra. The frequency calibration of the absorption spectra measured with this THz spectrometer was accomplished using the known frequencies of the absorption peaks of water vapor (**Figure 6-2**).[26,27]
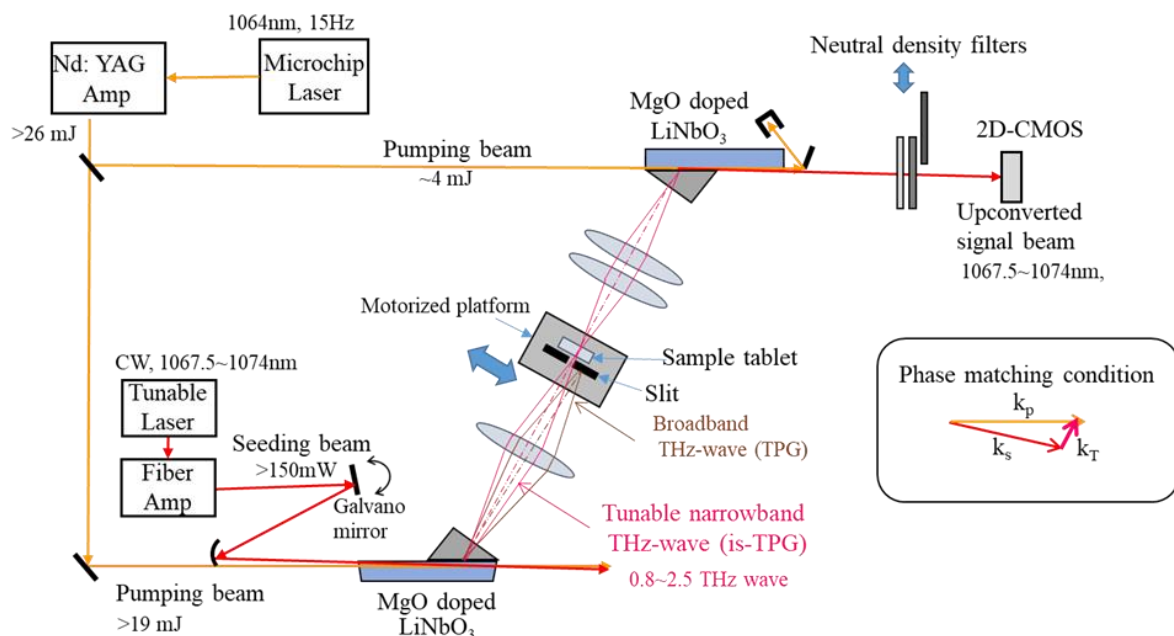
Figure 6-2. Schematic of FD-THz spectrometer with is-TPG. Slit for eliminating TPG waves is placed in front of the sample and moved dependent of the wavelength of the is-TPG. Footprint is 0.7 m^2.

6.2.3 Theoretical Analysis

CRYSTAL17[28] was used to complete ss-DFT simulations of EZT and EZT-MH including geometry optimizations, frequency simulations and assignments, and energetic analyses. For all of the calculations, Ahlrichs' VTZ basis set with additional polarization functions[29] was used with the Perdew−Burke−Ernzerhof[30] density functional. Grimme's London dispersion correction[31−33] (D3) utilizing the Becke−Johnson damping correction and three-body Axilrod−Teller−Muto repulsion contributions[34] (program keyword "ABC") were included. For EZT and EZTMH, the number of k-points in the irreducible Brillouin zone was set to 125 (program keyword SHRINK 8 8). For all calculations with both systems, the overlap-based truncation criteria for the bielectronic integrals (Coulombic and exchange, program keyword TOLINTEG) were set to 10^{-10}, 10^{-10}, 10^{-10}, 10^{-10}, and 10^{-20}.

The crystal structure of EZT has been deduced from using PXRD methods, while single-crystal X-ray diffraction measurements have been reported for EZT-MH. There is a published single-crystal structure for EZT; however, it is a different chirality (R, S, R instead of the correct S, R, S) from the clinically administered form used in this work.[25] The starting structures for EZT and EZT-MH geometry optimizations were obtained from the Cambridge Structural Database[35] (CSD) with reference codes QUWYIR22 and QATNEF01,[23] respectively. The energy convergence criteria for geometry optimizations were set to $\Delta E < 10^{-8}$ hartree. Two types of geometry optimizations were performed. First, geometry optimizations were performed where the lattice parameters and the atomic positions were allowed to freely optimize (the only constraint being the crystal space group), with results referred to as the "fully optimized" structure and representative of the structures at 0 K. Second, geometry optimizations were performed where only the atomic positions were allowed to optimize, and the lattice parameters were held constant to their experimental values, referred to here as the "fixed-lattice" structure (program keyword ATOMONLY). Since both previously reported experimental structures were solved at room temperature (293 K, unit cell volume = 2019.688 Å^3 for EZT[22] and 296 K, unit cell volume = 2161.395 Å^3 for EZTMH[23]), the fixed-lattice calculations were an approximation used to better simulate the properties of the room-temperature samples studied in this work. Frequency analyses were performed on both the fully optimized and fixed-lattice structures of EZT and EZT-MH with energy convergence criteria of $\Delta E < 10^{-10}$ hartree. The central difference formula was employed to calculate the numerical derivative of the Hessian matrix with each atom having two displacements along each Cartesian axis. Infrared spectral intensities were calculated using the Berry phase method.[36,37]

CRYSTAL17 was also used to perform energy analyses on the EZT and EZT-MH crystals (both fully optimized and fixed-lattice structures). Conformational energies of ezetimibe were calculated by performing a single-point molecular energy calculation on an isolated molecule extracted from each periodic system. For the EZT crystal, cohesive energies were calculated by subtracting the conformational energy of the isolated ezetimibe molecule from the total electronic energy of the solid. In the EZT-MH, the conformational energies of both the isolated ezetimibe and water molecules were subtracted from the total electronic energy of the hydrated crystal. The final aspect of energy analysis was the construction of Gibbs free-energy curves from 0 to 700 K for the ezetimibe samples using both the fully optimized and fixed-lattice simulated structures and vibrational frequencies.

6.3 Results and Discussion

6.3.1 Experimental Terahertz Vibrational Spectra

Figure 6-3 shows the THz frequency-domain absorption spectra of the pure EZT and EZT-MH tablets. Extinction was calculated for the vertical axis on the basis of the concentration of the sample and the thickness of the tablets and represents both the absorption and scattering of THz waves in the tablets. The base line of these spectra gradually increased in the high-frequency region, most likely because of Mie scattering inside the tablets. Main cause of the scattering was assumed to be difference in the refractive index between EZT and EZT-MH since the particle size of EZT-MH, which is prepared from the EZT powder, is expected to be the same as that of the EZT sample. Absorption peaks of EZT appeared at 1.75, 1.98, and 2.42 THz, and those of EZT-MH appeared at 1.24 and 1.88 THz. Anhydrate and hydrate were clearly identified on the basis of the differences in these characteristic absorption peak positions, which corresponded to the difference in vibrational modes between the crystal structures.
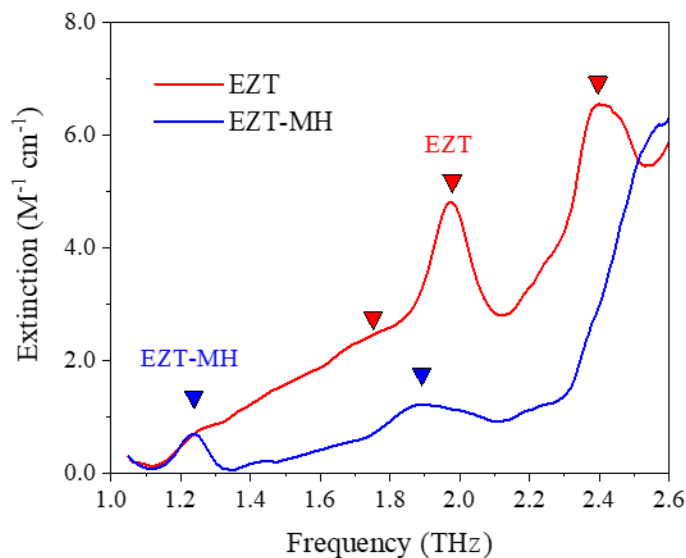
Figure 6-3. FD-THz absorption spectra of pure EZT (thickness = 1.3 mm) and EZT-MH (thickness = 2.5 mm) tablets.

Absorption spectra of a pure EZT-MH tablet were repeatedly measured while keeping the tablet in a dry condition (**Figure 6-4a**). The absorption peaks of EZT-MH at 1.24 and 1.88 THz decreased gradually, and those of EZT at 1.75, 1.98, and 2.42 THz increased. EZT-MH completely dehydrated after 900 min. On the other hand, keeping the EZT tablet at RH 25%, the absorption peaks of EZT decreased, and those of EZT-MH increased, which means that the hydration of EZT was observed (**Figure 6-4b**) over a span of 200 min. Under non-dry measurement conditions, strong narrow absorption peaks of water vapor appeared. These peaks could be removed, and the data interpolated linearly since the widths of the absorption peaks of water vapor were much narrower than those of EZT and EZT-HM.
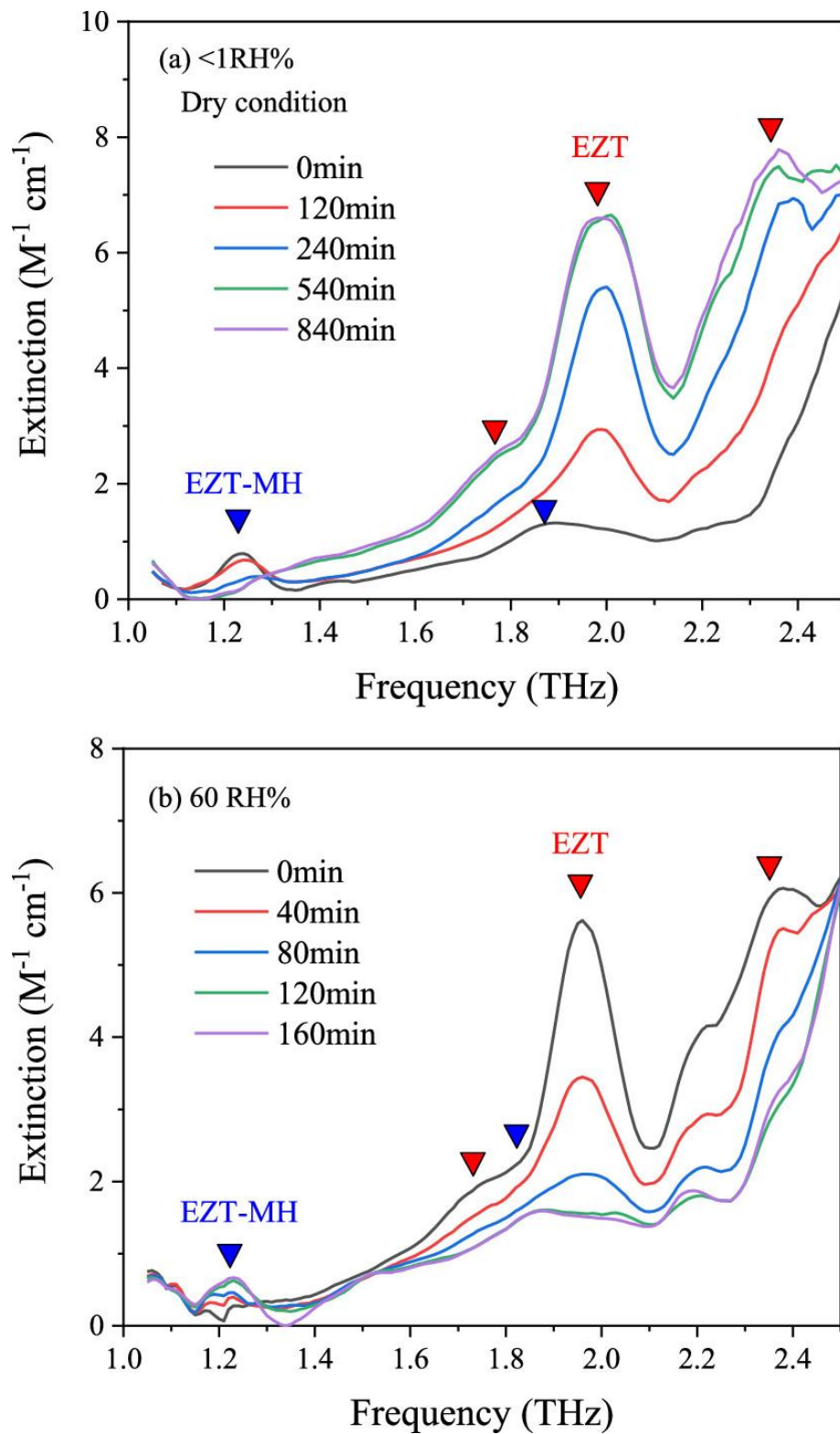
Figure 6-4. Absorption spectra of ezetimibe tablet (thickness = 2.5 mm) kept in a sample chamber at **(a)** <1 RH % and **(b)** 60 RH %.

Figure 6-5a shows the absorption spectra of the formulation and placebo tablets under dry conditions. Before starting the measurement, the tablet containing the ezetimibe was kept at a RH of <1% overnight, which means that all the ezetimibe in the tablet was initially in the anhydrate form. There was an extinction difference around 1.98 THz of the spectra of the EZT tablet and the placebo tablet, corresponding to the absorption peak of EZT. Strong absorption peaks of lactose at 1.20, 1.38, 1.82, and 2.20 THz appeared in both spectra. In the high-frequency region, the extinction became large due to the absorption and scattering of cellulose in the tablets. Absorption spectra were repeatedly measured at room temperature and at a RH of approximately 60%. To make the change in the absorption peaks of EZT more apparent, interference from the strong absorption peaks of lactose was reduced by subtracting the placebo's spectrum from the spectra of the formulation tablet, as shown in **Figure 6-5b**. The extinction changes at 1.98 THz, corresponding to the absorption peak of EZT, showed a positive peak at 0 min but decreased over time. After 5 days, hydration of EZT was completed. In comparison with the hydration of the pure EZT tablet, the formulation tablet hydration rate was less than one-fiftieth of that of the pure EZT tablet due to the presence of the lactose and cellulose excipients, as shown in **Figure 6.** Using our FD-THz spectrometer with the humidity-controlled measurement chamber, the hydration and dehydration processes of APIs in formulation tablets could be monitored successfully including tablets with and without excipients.
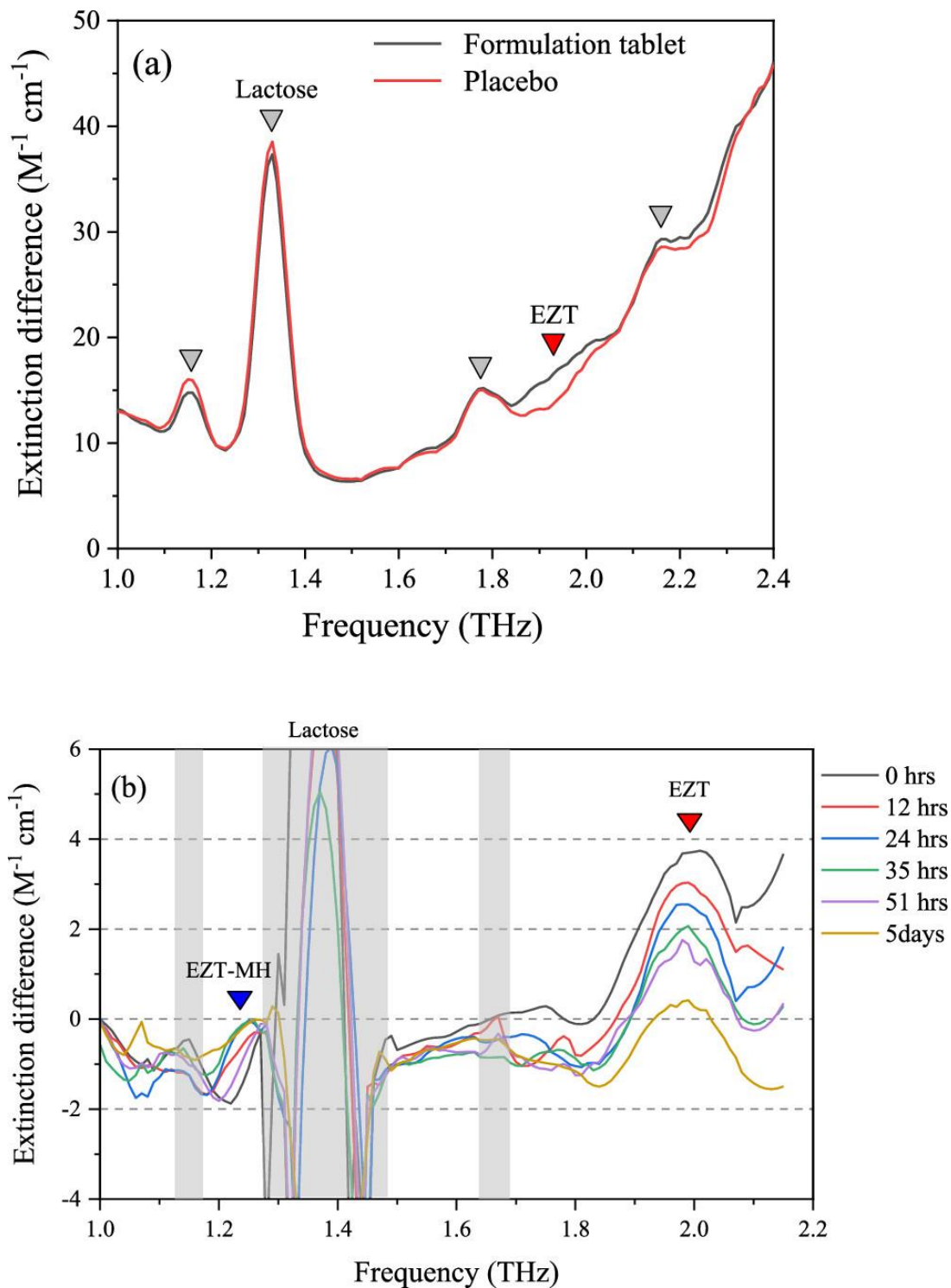
Figure 6-5. Observation of hydration of ezetimibe in a formulation tablet; **(a)** THz absorption spectra of the formulation and placebo tablets measured under dry conditions and **(b)** their difference from spectra of the placebo tablet which were repeatedly measured at a RH of approximately 60%.
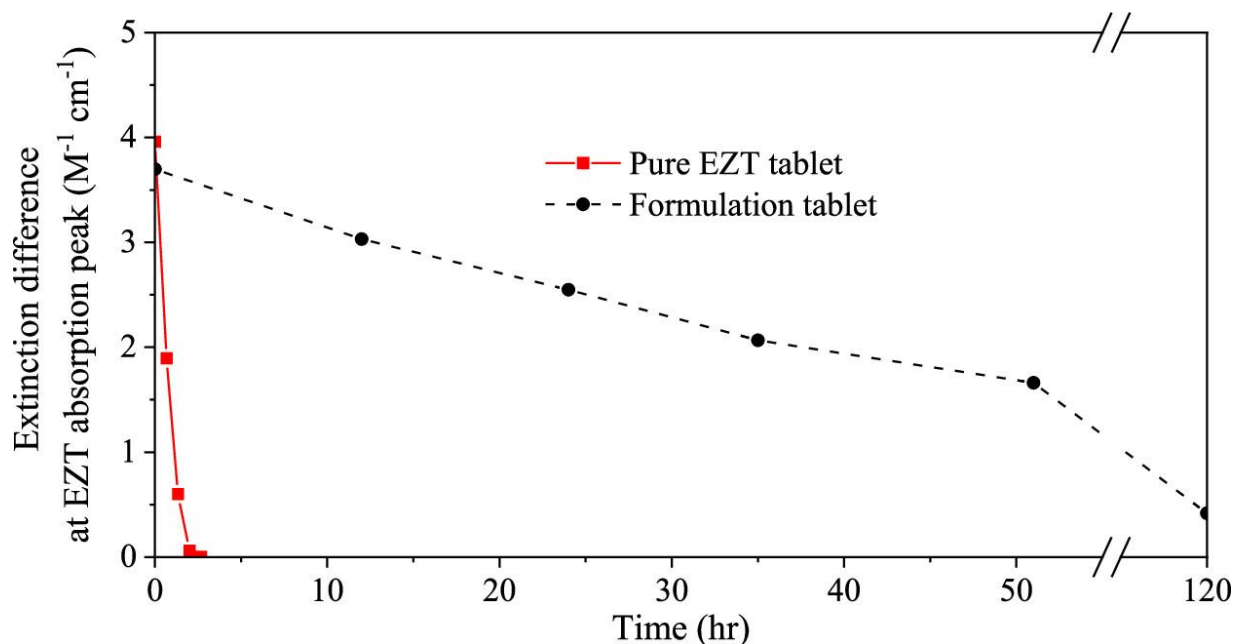
Figure 6-6. Time-dependent extinction changes at 1.98 THz, corresponding to an EZT absorption peak, in a non-dry environment (60% RH). Hydration of EZT in both pure and formulation tablets was observed.

6.3.2 Polymorph Differences and Optimized Structures

6.3.2.1 Evaluation of the ss-DFT Optimized Structures

The accuracy of the optimized crystal structures is paramount when simulating low-frequency vibrational spectra and evaluating energy factors in the solids. The ss-DFT fully optimized structures of EZT and EZT-MH matched well with the experimental data, as summarized in **Table 6-2**. The highest percent error in the fully optimized EZT unit cell dimensions was −0.93% on the *c*-axis, with the average absolute error in the calculated unit cell dimensions being 0.62%. Although the lattice parameters were compared to the powder X-ray structure, the internal structure was compared to single-crystal X-ray structure because while the single-crystal structure has the wrong chirality, all the atomic level values are comparable. Root-mean-square deviation (rmsd) values were good and yielded 0.02 Å for bond lengths, 0.82° for

bond angles, and 2.15° for dihedral angles (only non-hydrogen atoms were considered for rmsd

values).

Table 6-2. Unit cell dimensions (Å) of EZT from experiment (CSD structure QUWYIR[38]), after ss-DFT optimization, and the percent error between the two.

Lattice Parameter	Experimental	Calculated	Percent Error
a	5.94606	5.900256	-0.77%
b	15.8898	15.91676	0.17%
c	21.3765	21.17691	-0.93%
volume (Å3)	2019.6882	1988.78539	-1.53%

The quality of the internal structure of the simulations can also be analyzed by looking at the

hydrogen bonds present in the system. EZT contains two hydrogen bonds, and **Table 6-3** shows

the heavy atom distances and angles for the single-crystal experimental structure and the fully

optimized simulations.

Table 6-3. Two O-H•••O bonds present in EZT heavy atom distances and angles for the experimental structure (CSD structure QUWYIR01[25]) and the fully-optimized structure.

Hydrogen Bond	O•••O (Exp.) (Å)	O•••O (Comp.) (Å)	O-H•••O (Exp.) (°)	O-H•••O (Comp.) (°)
O3-H3•••O1	2.775	2.662	155.0	171.4
O1-H1•••O2	2.743	2.670	143.0	146.8

As listed in **Table 6-4**, the largest error in the fully optimized ss-DFT structure of EZT-MH was

−1.62% on the *a*-axis, with the average absolute error in the calculated unit cell dimensions

being 0.94%. Rmsd assessment of the molecular structures revealed very good agreement with

the experiment, yielding 0.02 Å for bond lengths, 0.44° for bond angles, and 2.06° for dihedral angles (considering only non-hydrogen atoms).

Table 6-4. Unit cell dimensions (Å) of EZT-MH from experiment (CSD structure QATNEF01[22]), after ss-DFT optimization, and the percent error between the two.

Lattice Parameter	Experimental	Calculated	Percent Error
a	6.2411	6.13980	-1.62%
b	15.4844	15.40386	-0.52%
c	22.3655	22.21187	-0.69%
volume ($Å^3$)	2161.3950	2100.72445	-2.81%

EZT-MH has four O−H···O hydrogen bonds, and **Table 6-5** lists these along with their heavy atom distances and angles. The hydrogen bonds present in EZT-MH were on an average slightly shorter and closer to linear than those present in EZT. As with the fully optimized structures, the molecules of the fixed-lattice simulations were also evaluated using rmsd values. No significant differences were found between the two types of simulations, indicating that temperature-dependent unit cell changes have a negligible influence on the intramolecular structure of ezetimibe. This emphasizes that the structural differences between the fully optimized (0 K) and fixed-lattice (room temperature) simulations are intermolecular in nature, a finding that is relevant to the interpretation of the THz spectra of these solids.

Table 6-5. Four O-H•••O bonds present in EZT-MH heavy atom distances and angles for the experimental structure (CSD structure QATNEF01[22]) and the fully-optimized structure.

Hydrogen Bond	O•••O (Exp.) (Å)	O•••O (Comp.) (Å)	O-H•••O (Exp.) (°)	O-H•••O (Comp.) (°)
O3-H3•••O4	2.795	2.726	164.4	168.2
O4-H4•••O1	2.745	2.677	174.2	174.9
O4-H5•••O2	2.693	2.657	161.4	160.0
O1-H1•••O4	2.701	2.659	167.7	173.3

6.3.3 Simulated Terahertz Vibrational Spectra

Vibrational frequency analyses of the EZT and EZT-MH crystals yielded no negative vibrational modes, demonstrating that both ss-DFT fully optimized and fixed-lattice structures were energetic minima on their respective potential energy surfaces. **Figure 6-7** shows the experimental THz vibrational spectrum along with the ss-DFT simulated spectra for the fully optimized and the fixed-lattice structures of EZT. The simulations produced very similar results and provided a good match with the experimental spectrum. In the fully optimized structure simulation (**Figure 6-7** middle, blue), some peaks shifted to slightly higher frequencies, as expected from the reduced unit cell volume of a 0 K simulation. The experimental feature at 1.98 THz was reproduced as two major peaks at 1.98 and 2.01 THz in the simulated spectrum. The experimental peak at 2.42 THz was found to have shifted higher in the simulation at 2.65 THz. Comparing the fixed-lattice and fully optimized simulations (**Figure 6-7** bottom, red) shows that the frequencies derived from the fixed-lattice structure were shifted to slightly lower energies, with the 1.98, 2.01, and 2.65 THz modes moving to 1.94, 1.96, and 2.61 THz, respectively.
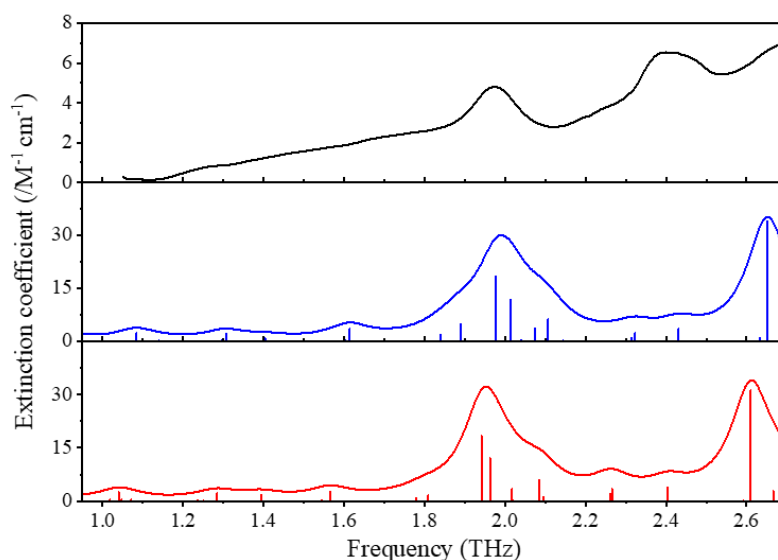
Figure 6-7. Experimental THz spectrum for EZT (top, black), the ss-DFT fully-optimized simulation (middle, blue), and the ss-DFT fixed-lattice simulation (bottom, red).
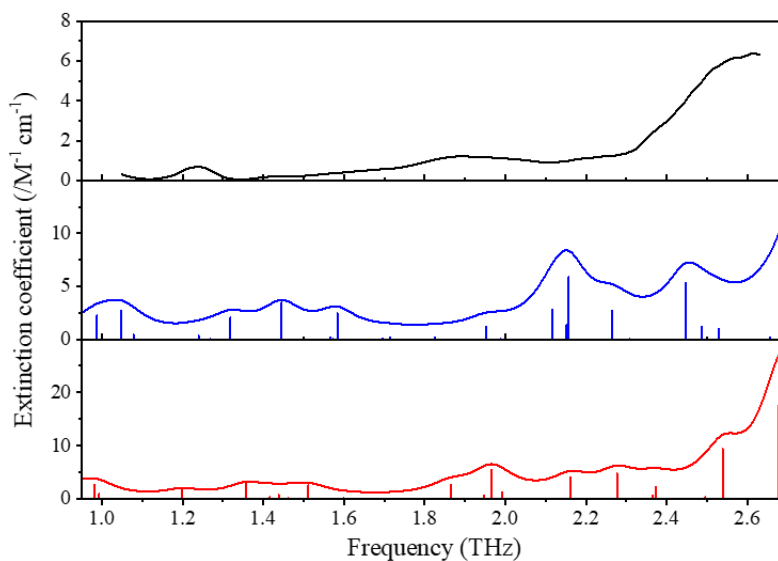
Figure 6-8. Experimental THz spectrum for EZT-MH (top, black) the ss-DFT fully-optimized simulation (middle, blue), and the ss-DFT fixed-lattice simulation (bottom, red).

The experimental spectrum and the ss-DFT simulated spectra for the fully optimized and the fixed-lattice structures of EZT-MH are shown in **Figure 6-8**. Unlike in **Figure 6-7**, these spectra were significantly different. Most of these differences were observed in the frequency

positions of the predicted features, but there were also some changes in the calculated intensities for the lattice vibrations. In the fully optimized simulation (**Figure 6-8** middle, blue), the experimental features at 1.24 and 1.88 THz were reproduced in the simulation slightly higher at 1.45 and 2.16 THz, respectively. The peak at the end of the experimental spectrum (2.6 THz) was reproduced in the simulation at 2.84 THz. In the fixed-lattice simulation (**Figure 6-8** bottom, red), the experimental features at 1.24 and 1.88 THz were reproduced in the simulation slightly higher at 1.36 and 1.97 THz, respectively. The peak at the end of the experimental spectrum (2.6 THz) was reproduced in the simulation as either a lower feature at 2.54 THz or a higher, more intense feature at 2.68 THz. Also, the strong feature seen in the fully optimized simulation at 1.05 THz shifted lower in the fixed-lattice simulation to 0.98 THz. **Table 6-6** lists the frequency positions of the five most intense peaks in the fully optimized simulations of EZT and EZT-MH with where these peaks shift in the fixed-lattice simulation. In the EZT simulations, there was a minimal shift between 0.03 and 0.05 THz. However, in EZT-MH, there was much more dramatic shifting (between 0.07 and 0.19 THz) along with changes in the intensity distribution. ss-DFT also allows for the assignment of vibrational modes to specific motions, and the general mode types are provided in **Table 6-6**. The differences between the fully optimized and the fixed-lattice spectral simulations may come from anharmonicity in the potential energy surfaces that govern the frequency positions of the peaks. The calculations yield harmonic frequencies, but the changes in the lattice dimensions between 0 K and room temperature are driven by anharmonic factors that are at least partially captured in these comparative simulations. This is indicated by comparing the volumes of the fixed-lattice (room temperature) and full-optimized (0 K) unit cells, where EZT shows a unit cell contraction of 1.53%, but EZT-MH contracts by 2.8% over the same temperature range, suggesting that EZT has lesser anharmonic character, whereas EZT-

MH has significantly more. Given the differences in the unit cell dimension changes, the

anhydrous EZT peaks only slightly shifted between the fixed and full structural optimizations,

whereas the EZT-MH spectral peaks moved considerably.

Table 6. Five most intense peaks in the EZT and EZT-MH fully-optimized simulated spectra
between 1.0 and 2.8 THz and 1.0 and 2.62 THz, respectively, along with their frequency in the
fixed-lattice simulations and the general motion type.

EZT		
Fully-Optimized Frequency (THz)	Fixed-Lattice Frequency (THz)	Mode Type
1.98	1.94	Torsion
2.01	1.96	Rotation
2.11	2.08	Torsion
2.65	2.61	Torsion
2.80	2.75	Torsion
EZT-MH		
Fully-Optimized Frequency (THz)	Fixed-Lattice Frequency (THz)	Mode Type
1.05	0.98	Rotation
1.45	1.36	Rotation
2.12	1.95	Rotation
2.16	1.97	Torsion
2.45	2.28	Rotation

6.3.4 Analysis of the Energy Factors in Ezetimibe Crystals

The very good simulations of the structures and THz spectra of these solids indicate that

the simulations accurately modeled the internal and external forces present in crystalline EZT

and EZT-MH. This accuracy allows for a reliable evaluation of the intramolecular and intermolecular energies involved in these solid-state materials. One energetic factor that can be compared between EZT and EZT-MH is the conformational energy of the ezetimibe molecule. The conformational energy of the ezetimibe molecule within EZT-MH was lower in energy than that in EZT by 5.47 kJ/mol (within the fully optimized structures). This was very similar to the value found in the fixed-lattice structures, 5.62 kJ/mol. The conformational difference between the ezetimibe molecules in the anhydrous and hydrated solids could be one factor in why EZT-MH is able to form over the parent species (water and ezetimibe). Cohesive energy is another important factor in the stability of solids. To make the cohesion comparable between the different EZT crystals, the cohesive energy per atom in the unit cell was calculated. EZT-MH had a greater cohesion magnitude of −6.18 kJ/mol than anhydrous EZT with −4.77 kJ/mol. These results show that the EZT-MH solid has both preferred intramolecular and intermolecular interaction energies.

To more fully understand the stability of EZT-MH, its Gibbs free energy can be compared to that of its individual parent species (ezetimibe and water). From the frequency analyses of EZT and EZT-MH, temperature-dependent Gibbs free-energy curves can be calculated. Along with Gibbs free-energy curves for EZT and EZT-MH, a Gibbs free-energy curve can be calculated for an isolated water molecule to model the free energy of a gas-phase molecule as would be released from a dehydrating solid. This can then be used to compare the free energies between EZT-MH and a linear combination of the Gibbs free energies of EZT and water (referred to as EZT + H_2O). **Figure 6-9** illustrates the Gibbs free-energy curves based on the fully optimized structures of EZT-MH and EZT, specifically including the EZT + H_2O result. EZT-MH was lower in energy (more stable) until the curves crossed at 509 K, well above the

melting point of EZT (164 °C).[38] To note the relevant temperature points, EZT-MH was lower in energy than a combination of its parent species at 0 K (−76.78 kJ/ mol) and 298 K (−34.13 kJ/mol). The same Gibbs free-energy analysis was applied to the fixed-lattice calculations, but little change was found, with the energy ranking preserved, and the curve crossing point modestly increased to 528 K. It should be mentioned that these energy calculations do not take into account vibrational anharmonicity, which we have identified as being important to the EZT-MH system; however, this is unlikely to alter the energy rankings in the temperature range of most interest.
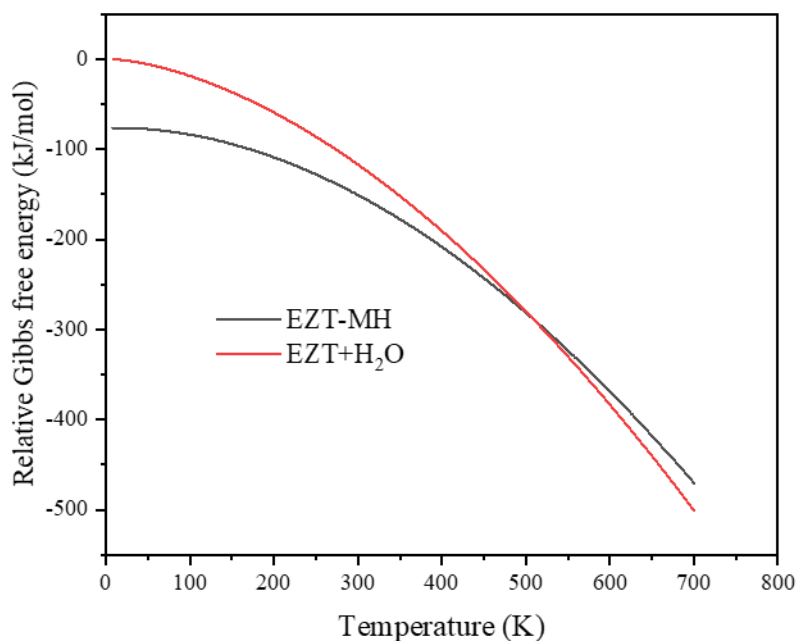
Figure 6-9. Relative Gibbs free energy curve for EZT+H_2O (red) and EZT-MH (black). All energies are per crystallographic asymmetric unit (1 EZT, 1 H_2O). For clarity, the energy values have been set relative to a common zero.

6.4 Conclusion

In this work, the powerful combination of THz spectroscopy and ss-DFT allowed for the analysis of the EZT and EZT-MH, which have similar crystalline morphologies and belong to the same space group. The good agreement between the simulations of the structures and THz spectra of these solids indicated that the simulations accurately modeled the internal and external forces present in crystalline EZT and EZT-MH. It was also discovered that the EZT-MH lattice vibrations exhibited greater anharmonic character than anhydrous EZT, which may be related to the greater number of hydrogen bonds in the hydrated sample. Using a THz spectrometer based on is-TPG with a humidity-controlled sample chamber, the hydration of ezetimibe in formulation tablets could be monitored in real time. The effect of excipients in the formulation was also successfully observed, showing that the rate of the solid-state transition of APIs was delayed in comparison with samples without excipients. These results indicate that the combination of THz-FDS experiments and ss-DFT simulations could be a very useful tool for monitoring and analyzing the solid-state transitions of in situ APIs and for quality control of solid formulations in pharmaceutical manufacturing.

6.5 Supporting Information (Appendix C)

Powder X-ray diffraction (PXRD) pattern of EZT-MH.

6.6 Acknowledgments

6.7 References

(1) Threlfall, T. L. Analysis of organic polymorphs. A review. *Analyst* **1995**, *120*, 2435−2460.

(2) Morris, K. R.; Griesser, U. J.; Eckhardt, C. J.; Stowell, J. G. Theoretical Approaches to Physical Transformations of Active Pharmaceutical Ingredients during Manufacturing Processes. *Adv. Drug Delivery Rev.* **2001**, *48*, 91−114.

(3) Krzyzaniak, J. F.; Williams, G. R.; Ni, N. Identification of Phase Boundaries in Anhydrate/Hydrate Systems. *J. Pharm. Sci.* **2007**, *96*, 1270−1281.

(4) Sanii, R.; Patyk-Kaźmierczak, E.; Hua, C.; Darwish, S.; Pham, T.; Forrest, K. A.; Zaworotko, M. J.; Zaworotko, M. Toward an Understanding of the Propensity for Crystalline Hydrate Formation by Molecular Compounds. Part 2. *Cryst. Growth Des.* **2021,** *21*, 4927.

(5) Pudipeddi, M.; Serajuddin, A. T. M. Trends in Solubility of Polymorphs. *J. Pharm. Sci.* **2005**, *94*, 929.

(6) Airaksinen, S.; Karjalainen, M.; Kivikero, N.; Westermarck, S.; Shevchenko, A.; Rantanen, J.; Yliruusi, J. Excipient Selection Can Significantly Affect Solid-State Phase Transformation in Formula Wet Granulation. *AAPS PharmSciTech* **2005**, *6*, No. E311.

(7) Miroshnyk, I.; Khriachtchev, L.; Mirza, S.; Rantanen, J.; Heinämäki, J.; Yliruusi, J. Insight into Thermally Induced Phase Transformations of Erythromycin A Dihydrate. *Cryst. Growth Des.* **2005**, *6,* 369−374.

(8) Fujii, K.; Aoki, M.; Uekusa, H. Solid-State Hydration/ Dehydration of Erythromycin A Investigated by Ab Initio Powder X-Ray Diffraction Analysis: Stoichiometric and Nonstoichiometric Dehydrated Hydrate. *Cryst. Growth Des.* **2013**, *13*, 2060−2066.

(9) Kim, Y.-s.; Rousseau, R. W. Characterization and Solid-State Transformations of the Pseudopolymorphic Forms of Sodium Naproxen. *Cryst. Growth Des*. **2004**, *4*, 1211−1216.

(10) Amado, A. M.; Nolasco, M. M.; Ribeiro-Claro, P. J. A. Probing Pseudopolymorphic Transitions in Pharmaceutical Solids Using Raman Spectroscopy: Hydration and Dehydration of Theophylline. *J. Pharm. Sci.* **2007**, *96*, 1366.

(11) Paiva, E. M.; Li, Q.; Zaczek, A. J.; Rohwedder, J. J. R.; Zeitler, J. A.; Axel Zeitler, J. Understanding the Metastability of Theophylline FIII by Means of Low-Frequency Vibrational Spectroscopy. *Mol. Pharm.* **2021**, *18,* 3578−3587.

(12) King, M. D.; Davis, E. A.; Smith, T. M.; Korter, T. M. Importance of Accurate Spectral Simulations for the Analysis of Terahertz Spectra: Citric Acid Anhydrate and Monohydrate. *J. Phys. Chem. A* **2011***, 115*, 11039−11044.

(13) Zeitler, J.; Kogermann, K.; Rantanen, J.; Rades, T.; Taday, P.; Pepper, M.; Aaltonen, J.; Strachan, C. Drug Hydrate Systems and Dehydration Processes Studied by Terahertz Pulsed Spectroscopy. *Int. J. Pharm.* **2007,** *334*, 78−84.

(14) Kogermann, K.; Zeitler, J. A.; Rantanen, J.; Rades, T.; Taday, P. F.; Pepper, M.; Heinämäki, J.; Strachan, C. J. Investigating Dehydration from Compacts Using Terahertz Pulsed, Raman, and near-Infrared Spectroscopy. *Appl. Spectrosc.* **2007**, *61,* 1265.

(15) King, M. D.; Korter, T. M. Effect of Waters of Crystallization on Terahertz Spectra: Anhydrous Oxalic Acid and Its Dihydrate. *J. Phys. Chem. A* **2010**, *114,* 7127−7138.

(16) Kawase, K.; Shikata, J.-i.; Imai, K.; Ito, H. Transform-Limited, Narrow-Linewidth, Terahertz-Wave Parametric Generator. *Appl. Phys. Lett.* **2001**, *78*, 2819−2821.

(17) Murate, K.; Taira, Y.; Tripathi, S. R.; Hayashi, S. i.; Nawata, K.; Minamide, H.; Kawase, K. A High Dynamic Range and Spectrally Flat Terahertz Spectrometer Based on Optical Parametric Processes in LiNbO3. *IEEE Trans. Terahertz Sci. Technol* **2014**, *4*, 523−526.

(18) Murate, K.; Kawase, K. Perspective: Terahertz Wave Parametric Generator and Its Applications. *J. Appl. Phys.* **2018**, *124*, 160901.

(19) Mohara, M.; Shimura, K.; Aiko, K.; Kawase, K. Terahertz Spectroscopy Using an Injection-Seeded Terahertz Parametric Generator for Quantitative Analysis and Inspection of over-the-Counter Medicine Tablets. *In Proceedings of SPIE-The International Society for Optical Engineering*; Sadwick, L. P., Yang, T., Eds.; SPIE, 2018; Vol. *10531*, p 75.

(20) Lindenberg, M.; Kopp, S.; Dressman, J. B. Classification of Orally Administered Drugs on the World Health Organization Model List of Essential Medicines According to the Biopharmaceutics Classification System. *Eur. J. Pharm. Biopharm.* **2004**, *58*, 265.

(21) Farias, M. A. d. S.; Soares, F. L. F.; Carneiro, R. L. Crystalline Phase Transition of Ezetimibe in Final Product, after Packing, Promoted by the Humidity of Excipients: Monitoring and Quantification by Raman Spectroscopy. *J. Pharm. Biomed. Anal.* **2016**, *121*, 209−214.

(22) Brüning, J.; Alig, E.; Schmidt, M. U. Ezetimibe Anhydrate, Determined from Laboratory Powder Diffraction Data. *Acta Crystallogr., Sect. C: Cryst. Struct. Commun.* **2010,** *66*, o341.

(23) Ś niezek, M.; Stecko, S.; Panfil, I.; Furman, B.; Chmielewski, M.˙ Total Synthesis of Ezetimibe, a Cholesterol Absorption Inhibitor. *J. Org. Chem.* **2013***, 78*, 7048.

(24) Sugandha, K.; Kaity, S.; Mukherjee, S.; Isaac, J.; Ghosh, A. Solubility Enhancement of Ezetimibe by a Cocrystal Engineering Technique. *Cryst. Growth Des.* **2014**, *14*, 4475−4486.

(25) Shimpi, M. R.; Childs, S. L.; Boström, D.; Velaga, S. P. New Cocrystals of Ezetimibe with L-Proline and Imidazole. *CrystEngComm* **2014**, *16*, 8984.

(26) Baron, P.; Mendrok, J.; Kasai, Y.; Ochiai, S.; Seta, T.; Sagi, K.; Suzuki, K.; Sagawa, H.; Urban, J. AMATERASU: Model for Atmospheric TeraHertz Radiation Analysis and Simulation. *J. Natl. Inst. Inf. Commun. Technol.* **2008**, *55,* 109−121.

(27) Hoshina, H.; Seta, T.; Iwamoto, T.; Hosako, I.; Otani, C.; Kasai, Y. Precise Measurement of Pressure Broadening Parameters for Water Vapor with a Terahertz Time-Domain Spectrometer. *J. Quant. Spectrosc. Radiat. Transfer* **2008**, *109*, 2303.

(28) Dovesi, R.; Erba, A.; Orlando, R.; Zicovich-Wilson, C. M.; Civalleri, B.; Maschio, L.; Rérat, M.; Casassa, S.; Baima, J.; Salustro, S.; et al. Quantum-Mechanical Condensed Matter Simulations with CRYSTAL. *Wiley Interdiscip. Rev.: Comput. Mol. Sci.* **2018**, *8*, No. e1360.

(29) Schäfer, A.; Horn, H.; Ahlrichs, R. Fully Optimized Contracted Gaussian Basis Sets for Atoms Li to Kr. *J. Chem. Phys.* **1992***, 97*, 2571.

(30) Perdew, J. P.; Burke, K.; Ernzerhof, M. Erratum: Generalized Gradient Approximation Made Simple (Physical Review Letters (1996) 77 (3865)). *Phys. Rev. Lett.* **1997**, *78,* 1396.

(31) Grimme, S.; Antony, J.; Ehrlich, S.; Krieg, H. A Consistent and Accurate Ab Initio Parametrization of Density Functional Dispersion Correction (DFT-D) for the 94 Elements H-Pu. *J. Chem. Phys***. 2010,** *132,* 154104.

(32) Grimme, S.; Ehrlich, S.; Goerigk, L. Effect of the Damping Function in Dispersion Corrected Density Functional Theory. *J. Comput. Chem.* **2011**, *32*, 1456−1465.

(33) Grimme, S.; Hansen, A.; Brandenburg, J. G.; Bannwarth, C. Dispersion-Corrected Mean-Field Electronic Structure Methods. *Chem. Rev.* **2016**, *116*, 5105.

(34) Dona, L.; Brandenburg, J. G.; Bush, I. J.; Civalleri, B. Cost-` Effective Composite Methods for Large-Scale Solid-State Calculations. *Faraday Discuss.* **2020**, *224, 292.*

(35) Groom, C. R.; Bruno, I. J.; Lightfoot, M. P.; Ward, S. C. The Cambridge Structural Database. *Acta Crystallogr., Sect. B: Struct. Sci., Cryst. Eng. Mater.* **2016**, *72*, 171−179.

(36) Pascale, F.; Zicovich-Wilson, C. M.; López Gejo, F.; Civalleri, B.; Orlando, R.; Dovesi, R. The Calculation of the Vibrational Frequencies of Crystalline Compounds and Its Implementation in the CRYSTAL Code. *J. Comput. Chem.* **2004***, 25*, 888−897.

(37) Noel, Y.; Zicovich-Wilson, C. M.; Civalleri, B.; D'Arco, P.; Dovesi, R. Polarization Properties of ZnO and BeO: An Ab Initio Study through the Berry Phase and Wannier Functions Approaches. *Phys. Rev. B: Condens. Matter Mater. Phys.* **2002**, *65*, 014111.

(38) Ezetimibe. The Merck Index Online 15th Edition, Monograph ID: M5228. https://www.rsc.org/Merck-Index/monograph/m5228/ ezetimibe?q=unauthorize (accessed Dec 12, 2021).

Chapter 7: The Quantum Mechanic Study of Ofloxacin and Related Levofloxacin Systems

7.1 Introduction

Fluoroquinolones have a bicyclic core and are related to 4-quinolone and are is a class of medicines that are used to treat a wide variety of bacterial infections.[1] Ofloxacin and levofloxacin are both fluoroquinolone antibiotics with levofloxacin being the pure (S)-enantiomer of ofloxacin.[2] Solid levofloxacin exists in a number of anhydrous polymorphic forms as well as hydrated forms, but fewer structures have been reported for ofloxacin. **Figure 7-1** shows the crystallographic unit cell of ofloxacin anhydrous[1, 3], **Figure 7-2** shows the polymorphs, gamma[2] and alpha[4], of levofloxacin. **Figure 7-3** shows levofloxacin hemihydrate[5, 6] and levofloxacin monohydrate[5].
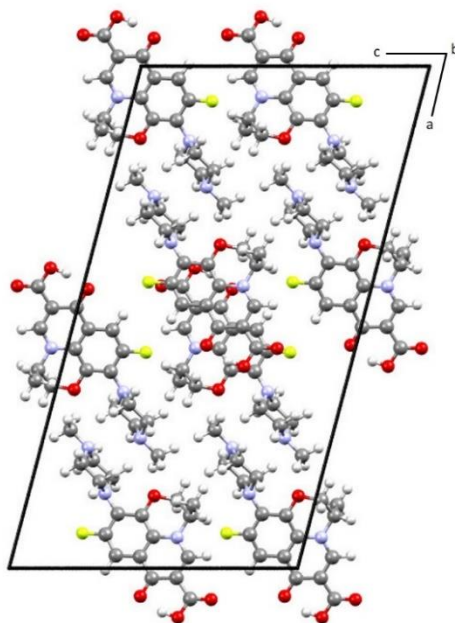
Figure 7-1. Crystallographic unit cell for ofloxacin anhydrous.
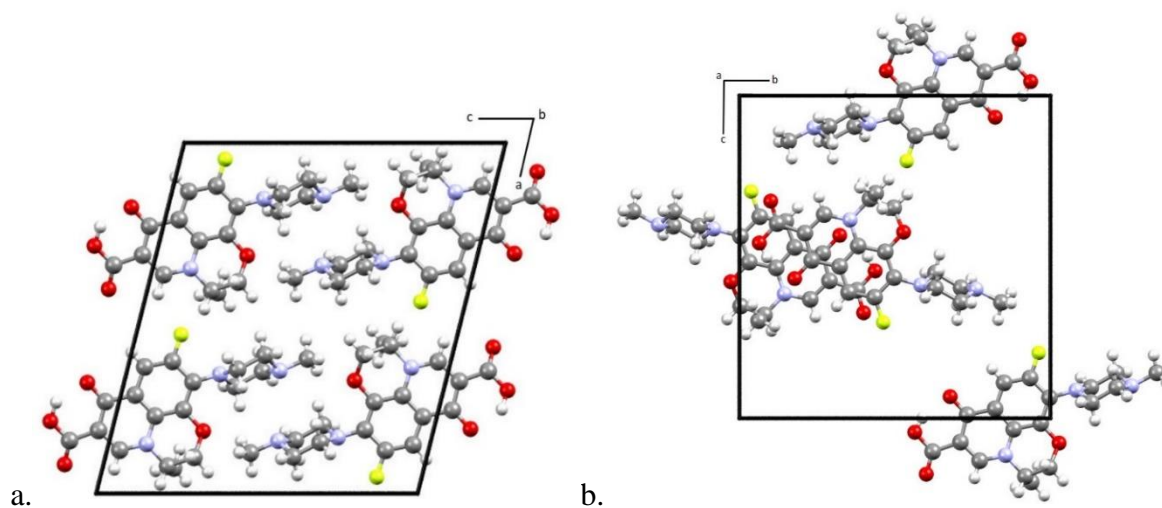
Figure 7-2. Crystallographic unit cells for **a.** the gamma polymorph of levofloxacin and **b.** the alpha polymorph of levofloxacin.
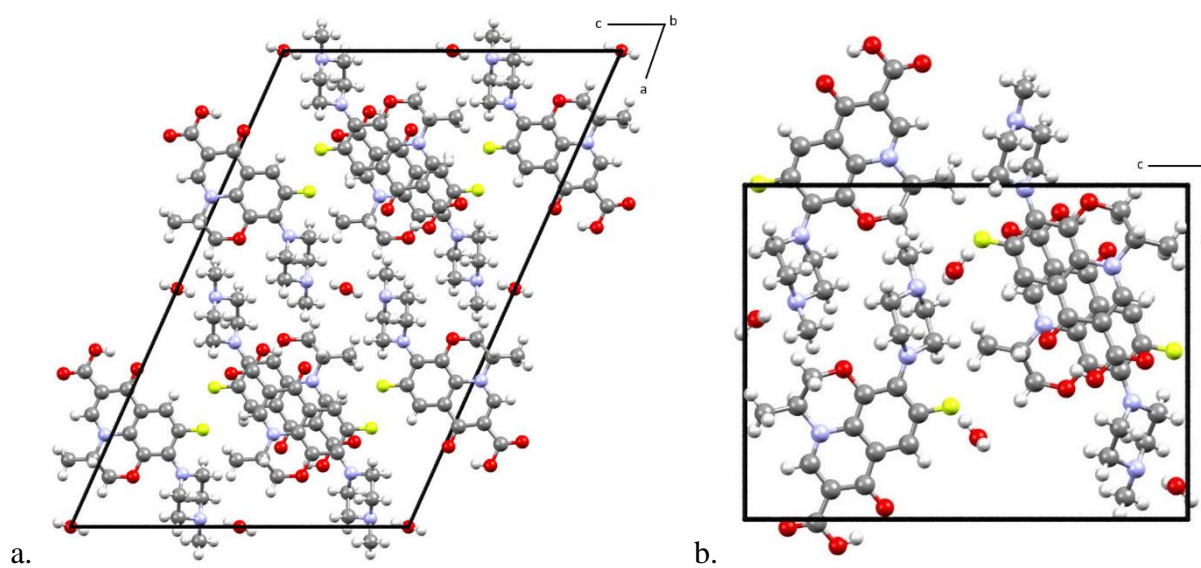
Figure 7-3. Crystallographic unit cells for **a.** levofloxacin hemihydrate and **b.** levofloxacin monohydrate.

The study and understanding of these pharmaceutical polymorphs and hydrates is critical in ensuring that the drug is stable and effective for patients. In practice, the hemihydrate form of levofloxacin is what is prescribed due to its stability despite the fact that it has relatively low solubility.[4]

Solid-state density functional theory (ss-DFT) allows us to simulate low-frequency vibrational spectra which can give additional understanding of the motions involved in the low-frequency modes.[7-10] These low-frequency modes are of special interest to us because the modes in this region come from difference in packing arrangements and intermolecular forces. Since polymorphs differ in crystal packing and the addition of water can increase the amount of hydrogen bonds, the low-frequency region gives unique spectra for a variety of solids.[11-17] These low-frequency modes can be explored through IR or Raman spectroscopy which are governed by different selections rules. Here, the IR-active modes are focused on and experimentally these low-frequency IR-active modes can be explored using terahertz (THz) spectroscopy. THz spectroscopy has a long history of being used to investigate a large range of pharmaceuticals and biomolecules.[18-20] In the future, this computational work will be complemented with experimental work from Hitachi High-Tech and this collaboration was the genesis of this project.

The energetics involved in related systems like polymorphs and hydrates can also be investigated using ss-DFT and this can give insights into why one solid-state structure may be more stable than another. Here, the directly comparable systems of ofloxacin, the alpha polymorph of levofloxacin, and the gamma polymorph of levofloxacin are explored using a 0 K energy analysis as well as using Gibbs free energy which takes into account temperature effects.

7.2 Methods

7.2.1 Theoretical Methods

The quantum mechanical simulations shown here, including geometry optimizations, frequency analyses, and energetic analyses, were performed using CRYSTAL17.[21] The Cambridge Structural Database[22] was used to obtain the starting experimental crystal structures for all the systems studied here. All calculations were done using Ahlrichs' VTZ basis set with

additional polarization functions[23] and the PBE functional.[24] The calculations also include

Grimme's D3 correction term with Becke-Johnson damping[25-27] and the Axilrod-Teller-Muto

type three-body term (keyword ABC).[28-30] The overlap-based truncation criteria for the

bielectronic integrals (Coulomb and exchange) (TOLINTEG) were set to 10^{-10}, 10^{-10}, 10^{-10}, 10^{-10},

and 10^{-20} for all calculations and the maximum order of the multipolar expansion was set to 6

(keyword POLEORDR). For geometry optimizations, the energy convergence criteria was set to

$\Delta E < 10^{-8}$ hartree. For ofloxacin, the alpha polymorph of levofloxacin, and levofloxacin

hemihydrate, fixed-lattice and full optimizations were performed while for the gamma

polymorph of levofloxacin and levofloxacin monohydrate only full optimizations were done. A

fixed-lattice optimization is when the unit cell parameters are fixed at the X-ray structure values

and the atomic positions are allowed to optimize. This type of optimization can be useful in more

accurately reproducing room-temperature spectra and was only performed on the molecules that

had published room-temperature X-ray structures. Full optimizations allow the lattice

dimensions as well as the atomic positions to optimize and, generally, better reproduces low-

temperature spectra.

The energy convergence was increased to $\Delta E < 10^{-10}$ hartree for the vibrational frequency

calculations as well as for the energy calculations. Frequency analyses was done on all of the

systems including for both the fixed-lattice and the fully optimized structures, if applicable. For

ofloxacin, the 1-point numerical derivative approach was used where each atom is displaced

once along each Cartesian axis and the difference quotient formula is used. For all other systems,

a 2-point numerical derivative was used where each atom is displaced twice along each Cartesian

axis and the central-difference formula is used. In this case, only the IR intensities were

calculated and they were calculated using the Berry phase method.[31, 32]

The energetics of all of these systems can also be investigated. The total electronic energy can be determined by performing a single point energy calculation and then this value can be broken down into the cohesive and conformational energies. The conformational energy is the energy of the individual molecule and can be calculated by using the MOLECULE keyword which extracts a single molecule from the unit cell and performs a single point energy calculation on that isolated molecule. This can then be subtracted from the total energy of the unit cell (accounting for the Z value) and the cohesive energy can be determined. The cohesive energy represents the forces that hold the molecules together in the solid-state. Gibbs free energy versus temperature curves can also be constructed from the vibrational frequency analyses.

7.3 Results and Discussion

7.3.1 Optimized Structures

The ss-DFT optimized structure of ofloxacin anhydrous produces small errors in all the lattice parameters demonstrating a well simulated structure. **Table 7-1** shows the experimental lattice parameters for ofloxacin anhydrous along with the ss-DFT calculated parameters and the percent errors. The average unsigned percent error in the axes was 1.14%, with the largest error being on the *b* axis at 1.30%. The ss-DFT optimized structure of ofloxacin anhydrous exhibited root-mean-square deviation (rmsd) values of 0.01 Å for the bond lengths, 0.57° for the bond angles, and 4.79° for the torsions, taking into account only nonhydrogen atoms. The hydrogen bonding within the crystal is also important to evaluate. Ofloxacin anhydrous has one hydrogen bond. The percent error in the hydrogen bond length was -0.44% and the hydrogen bond angle was -1.00%.

Table 7-1. Lattice parameters of ofloxacin anhydrous from experiment (CSD structure CUYCEF01), after ss-DFT optimization, and the percent error between the two.

Ofloxacin anhydrous (space group C2/c)			
Lattice Parameter	Experimental	Calculated	Percent Error
a	30.073 Å	29.7194 Å	-1.18%
b	6.7129 Å	6.80005 Å	1.30%
c	16.722 Å	16.8820 Å	0.96%
β	104.76°	104.403°	-0.34%
Volume	3264.39 Å^3	3304.519 Å^3	1.23%

The ss-DFT optimized structure of the gamma polymorph of levofloxacin produced higher percent errors than the ss-DFT optimized structure of ofloxacin anhydrous. **Table 7-2** summarizes the calculated lattice parameters and the percent errors. The average unsigned percent error in the axes was 5.12%, with the largest error being on the a axis at 7.67%. The ss-DFT optimized structure of gamma polymorph of levofloxacin exhibited rmsd values of 0.02 Å for the bond lengths, 1.54° for the bond angles, and 22.4° for the torsions, taking into account only nonhydrogen atoms. The gamma polymorph of levofloxacin also has one hydrogen bond and the percent error in the hydrogen bond length was -1.83% and the hydrogen bond angle was 20.30%. The only published experimental structure for the gamma polymorph of levofloxacin is a high temperature (423 K) powder X-ray diffraction so while the ss-DFT structure has high errors these may not be surprising since the simulated structure is at 0 K.

Table 7-2. Lattice parameters of the gamma polymorph of levofloxacin from experiment (CSD structure LICWOM), after ss-DFT optimization, and the percent error between the two.

Levofloxacin anhydrous gamma polymorph (space group C2)			
Lattice Parameter	Experimental	Calculated	Percent Error
a	17.2739 Å	18.59817 Å	7.67%
b	7.0307 Å	7.17927 Å	2.11%
c	15.4605 Å	14.57112 Å	-5.75%
β	104.204°	112.4267°	7.89%
Volume	1820.24 Å^3	1798.41 Å^3	-1.20%

Levofloxacin also crystallizes in an alpha form. The ss-DFT optimization of alpha

polymorph produced smaller errors than the gamma polymorph. This is possibly because the

alpha polymorph structure is a single crystal structure while the gamma polymorph structure is

from a powder X-ray diffraction pattern. The 2018 paper that the gamma polymorph structure

comes from also has a powder X-ray diffraction structure for the alpha polymorph

(LICWOM01). This powder X-ray structure was also ss-DFT optimized and produced much

higher errors, average unsigned error in the unit cell dimensions 5.52% versus 0.62%, than the

optimization with single crystal structure indicating that the single crystal structure is more

accurate. **Table 7-3** shows the lattice cell parameters of the experimental and the calculated

structures and the error between the two. The ss-DFT optimized structure of alpha polymorph of

levofloxacin exhibited rmsd values of 0.01 Å for the bond lengths, 0.78° for the bond angles, and

7.70° for the torsions, taking into account only nonhydrogen atoms. The percent error in the

hydrogen bond length was -1.37% and the hydrogen bond angle was 1.94%.

Table 7-3. Lattice parameters of the alpha polymorph of levofloxacin from experiment (CSD
structure CUYCEF02), after ss-DFT optimization, and the percent error between the two.

Levofloxacin anhydrous alpha polymorph (space group $P2_12_12_1$)			
Lattice Parameter	Experimental	Calculated	Percent Error
a	6.6213 Å	6.59719 Å	-0.36%
b	15.810 Å	15.6779 Å	-0.84%
c	16.409 Å	16.3031 Å	-0.65%
Volume	1717.74 Å^3	1686.23 Å^3	-1.83%

Levofloxacin also crystallizes in two hydrates, a hemihydrate and a monohydrate. The

dehydration of the hemihydrate leads to the gamma polymorph while the dehydration of the

monohydrate leads to the alpha polymorph.[4] The optimization of the monohydrate produced low

error with an average unsigned error in the axes of 0.29% (**Table 7-4**). The ss-DFT optimized

structure of levofloxacin monohydrate exhibited rmsd values of 0.01 Å for the bond lengths,

0.87° for the bond angles, and 2.62° for the torsions, taking into account only nonhydrogen

atoms. The levofloxacin monohydrate has six hydrogen bonds. The percent error in the hydrogen

bond lengths was -1.05% and the hydrogen bond angles was 5.03%.

Table 7-4. Lattice parameters of levofloxacin monohydrate from experiment (CSD structure
YUJPAU01), after ss-DFT optimization, and the percent error between the two.

Levofloxacin monohydrate (space group P2₁)			
Lattice Parameter	Experimental	Calculated	Percent Error
a	6.745 Å	6.7925 Å	0.70%
b	13.836 Å	13.8308 Å	-0.04%
c	18.393 Å	18.4147 Å	0.12%
β	95.380°	96.8970°	1.59%
Volume	1708.94 Å³	1717.47 Å³	0.50%

The ss-DFT optimization of the hemihydrate produced low unit cell parameter errors with

an average unsigned error in the axes of 0.88% (**Table 7-5**). The ss-DFT optimized structure of

levofloxacin hemihydrate exhibited rmsd values of 0.01 Å for the bond lengths, 0.65° for the

bond angles, and 3.72° for the torsions, taking into account only nonhydrogen atoms. The

levofloxacin hemihydrate has four hydrogen bonds. The percent error in the hydrogen bond

lengths was -1.84% and the hydrogen bond angles was 3.12%.

Table 7-5. Lattice parameters of levofloxacin hemihydrate from experiment (CSD structure
YUJNUM02), after ss-DFT optimization, and the percent error between the two.

Levofloxacin hemihydrate (space group C2)			
Lattice Parameter	Experimental	Calculated	Percent Error
a	29.127 Å	28.7558 Å	-1.27%
b	6.8850 Å	6.8239 Å	-0.89%
c	18.8490 Å	18.7580 Å	-0.48%
β	114.089°	114.3215°	0.20%
Volume	3450.78 Å³	3354.16 Å³	-2.80%

7.3.2 Simulated Spectra

Below are the simulated spectra of all of the solids mentioned above. **Figure 7-4.** shows the comparison of the fully-optimized and fixed-lattice simulations for ofloxacin anhydrous. **Figure 7-5.** shows the fully-optimized simulated spectrum for the gamma polymorph of levofloxacin. **Figure 7-6.** shows the comparison of the fully-optimized and fixed-lattice simulations for the alpha polymorph of levofloxacin. **Figure 7-7.** shows the comparison of the fully-optimized and fixed-lattice simulations for levofloxacin hemihydrate. **Figure 7-8.** shows the fully-optimized simulated spectrum for levofloxacin monohydrate. A complete list of simulated IR-active vibrational modes for all simulations can be found in the **Supporting Information**.
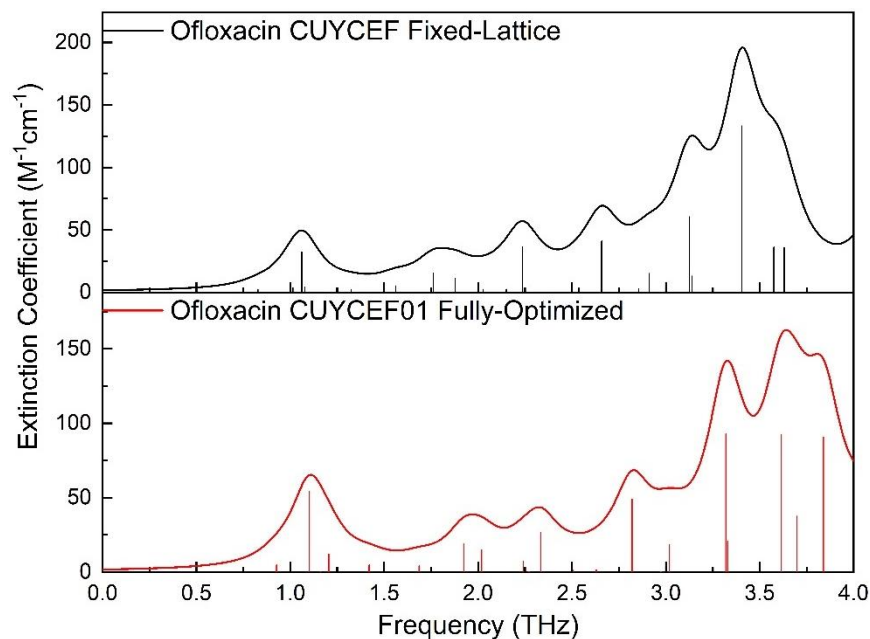
Figure 7-4. The simulated THz spectrum of the fixed-lattice ofloxacin anhydrous structure (top, black) (4.0 cm^{-1} Lorentzian line shape) and the fully-optimized ofloxacin anhydrous structure (bottom, red) (4.0 cm^{-1} Lorentzian line shape).
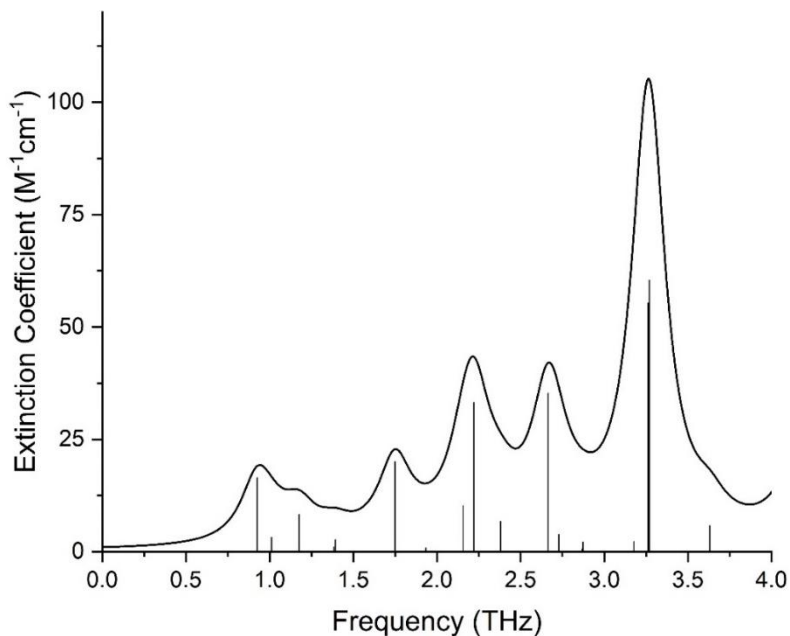
Figure 7-5. The simulated THz spectrum of the gamma polymorph of levofloxacin (4.0 cm^{-1} Lorentzian line shape).
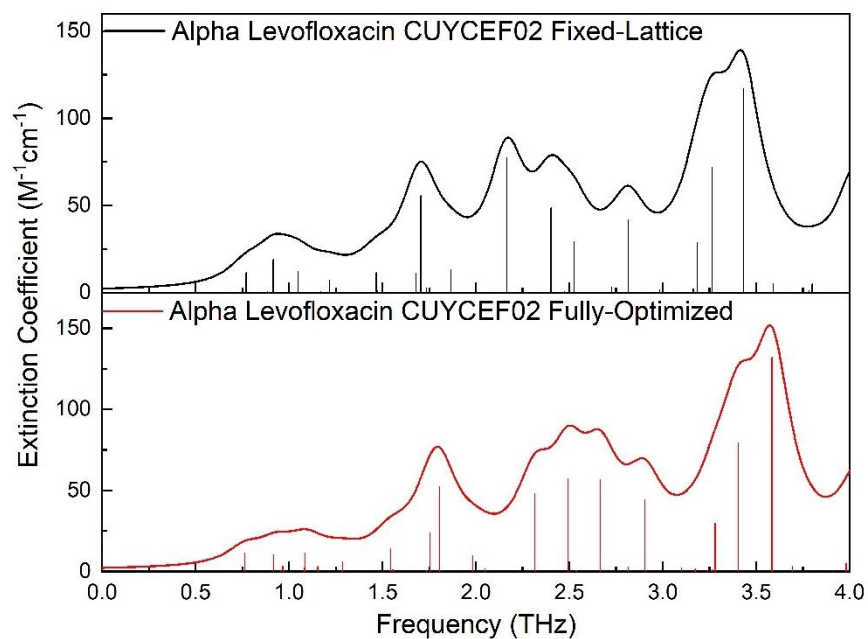
Figure 7-6. The simulated THz spectrum of the fixed-lattice alpha polymorph of levofloxacin structure (top, black) (4.0 cm^{-1} Lorentzian line shape) and the fully-optimized alpha polymorph of levofloxacin structure (bottom, red) (4.0 cm^{-1} Lorentzian line shape).
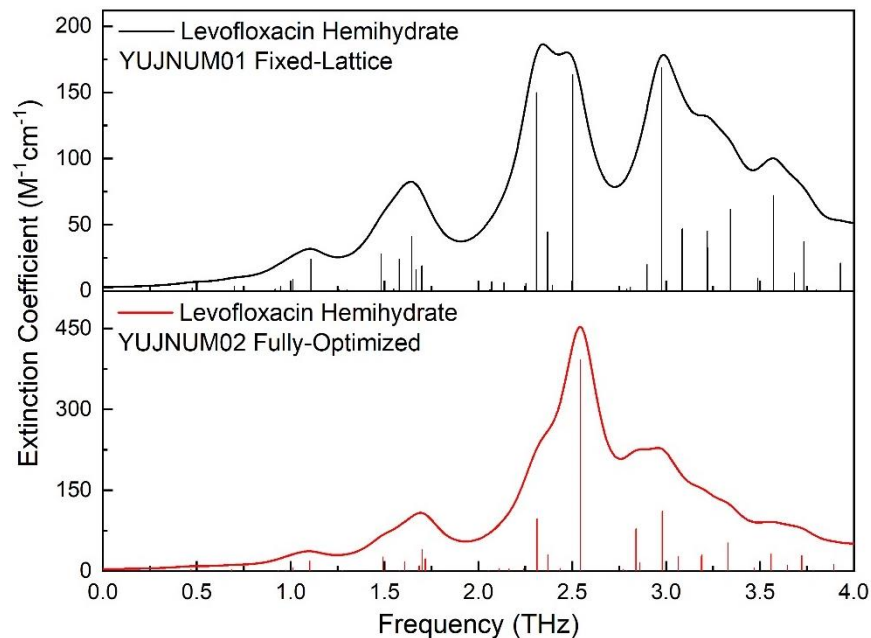
Figure 7-7. The simulated THz spectrum of the fixed-lattice hemihydrate levofloxacin structure (top, black) (4.0 cm^{-1} Lorentzian line shape) and the fully-optimized hemihydrate levofloxacin structure (bottom, red) (4.0 cm^{-1} Lorentzian line shape).
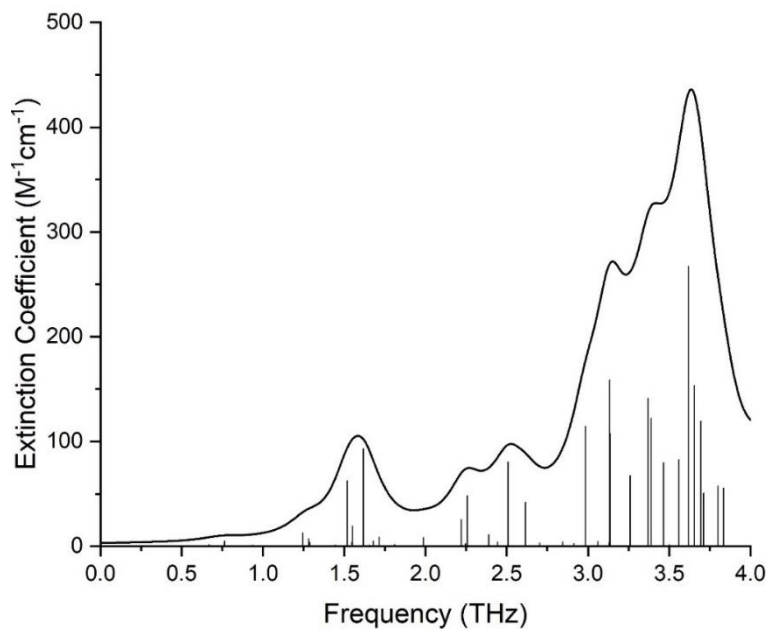
Figure 7-8. The simulated THz spectrum of levofloxacin monohydrate (4.0 cm^{-1} Lorentzian line shape).

7.3.3 Energetic Analysis

The ss-DFT simulations allow for the energetics of the different systems to be explored. Ofloxacin and the polymorphs of levofloxacin can be directly compared to each other because they are the same molecule. Ofloxacin is a racemic mixture while levofloxacin is the S-(-) enantiomer. A variety of energetic values can be examined including electronic energy which can then be broken down into conformational energy and cohesive energy. **Table 7-6** shows the relative values for the electronic energy and conformational energy as well as the cohesive energy per formula unit for the three comparable systems. Ofloxacin has the lowest electronic energy and cohesive energy while the gamma polymorph of levofloxacin has the lowest conformational energy.

Table 7-6. Relative electronic energy, relative conformational energy and cohesive energy per formula unit in kJ/mol for the full ss-DFT optimizations of ofloxacin, the alpha polymorphs of levofloxacin, and the gamma polymorph of levofloxacin.

	Relative Electronic Energy per Formula Unit (kJ/mol)	Relative Conformational Energy per Formula Unit (kJ/mol)	Cohesive Energy per Formula Unit (kJ/mol)
Ofloxacin	0	4.22	-195.22
Levofloxacin Alpha	11.73	1.85	-181.13
Levofloxacin Gamma	16.09	0	-174.91

Gibbs free energy versus temperature curves can be constructed from the frequency analyses and give additional energetic information by including vibrational contributions and entropy. The Gibbs free energy versus temperature curves for ofloxacin, the alpha polymorphs of levofloxacin, and the gamma polymorph of levofloxacin are consistent with the energetic ranking from the cohesive energy analysis (**Figure 7-9**). Ofloxacin is the most stable over the entire energy range with the alpha polymorphs of levofloxacin being the next most stable and the gamma polymorph of levofloxacin is the least stable according to the Gibbs free energy curves.
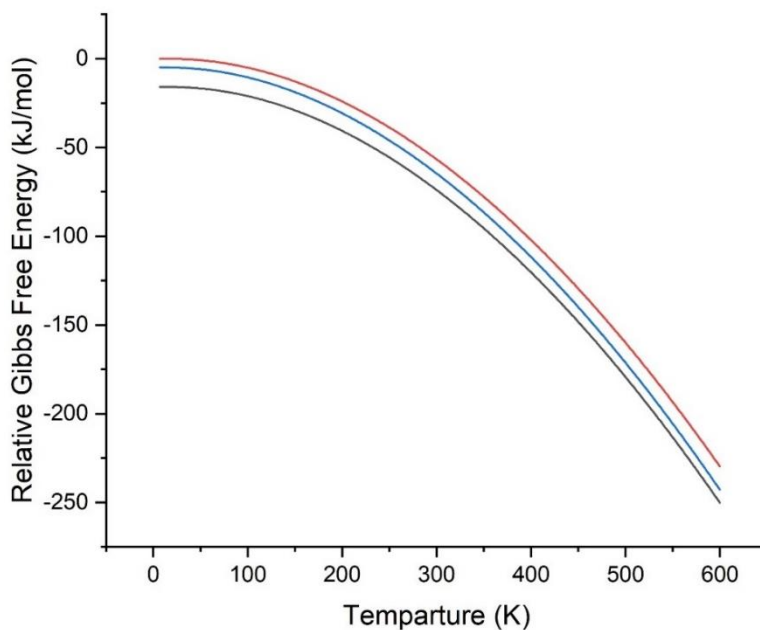
Figure 7-9. Relative Gibbs Free Energies of ofloxacin (black), the alpha polymorph of levofloxacin (blue), and the gamma polymorph of levofloxacin (red).

7.4 Conclusion

By studying ofloxacin and the related levofloxacin systems using ss-DFT, we demonstrate that these computational techniques can be used to simulate large pharmaceutical compounds that have polymorphs as well as hydrates. The energetic analysis shows that the racemic ofloxacin solid is the most stable with the levofloxacin polymorphs being less stable. In the future, these results will be combined with experimental terahertz data from Hitachi High-Tech to gain further insights into the hydration and dehydration of levofloxacin.

7.5 Supporting Information (see Appendix D)

List of solid-state DFT IR-active frequencies, intensities, and mode symmetries for fully-optimized ofloxacin anhydrous, fixed-lattice ofloxacin anhydrous, fully-optimized gamma polymorph of levofloxacin, fully-optimized alpha polymorph of levofloxacin, fixed-lattice alpha polymorph of levofloxacin, fully-optimized levofloxacin hemihydrate, fixed-lattice simulation of levofloxacin hemihydrate, and fully-optimized levofloxacin monohydrate.

7.6 Acknowledgements

7.7 References

1.   Holstein, J. J.; Hübschle, C. B.; Dittrich, B., Electrostatic Properties of Nine Fluoroquinolone Antibiotics Derived Directly from Their Crystal Structure Refinements. *CrystEngComm* **2012,** *14* (7), 2520-2531.

2.   Freitas, J. T.; de Melo, C. C.; Viana, O. M.; Ferreira, F. F.; Doriguetto, A. C., Crystal Structure of Levofloxacin Anhydrates: A High-Temperature Powder X-Ray Diffraction Study Versus Crystal Structure Prediction. *Crystal Growth & Design* **2018,** *18* (6), 3558-3568.

3.   Mahapatra, S.; Venugopala, K.; Guru Row, T. N., A Device to Crystallize Organic Solids: Structure of Ciprofloxacin, Midazolam, and Ofloxacin as Targets. *Crystal growth & design* **2010,** *10* (4), 1866-1870.

4.   Wei, N.; Jia, L.; Shang, Z.; Gong, J.; Wu, S.; Wang, J.; Tang, W., Polymorphism of Levofloxacin: Structure, Properties and Phase Transformation. *CrystEngComm* **2019,** *21* (41), 6196-6207.

5.   Singh, S. S.; Thakur, T. S., New Crystalline Salt Forms of Levofloxacin: Conformational Analysis and Attempts Towards the Crystal Structure Prediction of the Anhydrous Form. *CrystEngComm* **2014,** *16* (20), 4215-4230.

6.   Gorman, E. M.; Samas, B.; Munson, E. J., Understanding the Dehydration of Levofloxacin Hemihydrate. *Journal of pharmaceutical sciences* **2012,** *101* (9), 3319-3330.

7.   Davis, M. P.; Mohara, M.; Shimura, K.; Korter, T. M., Simulation and Assignment of the Terahertz Vibrational Spectra of Enalapril Maleate Cocrystal Polymorphs. *The Journal of Physical Chemistry A* **2020,** *124* (47), 9793-9800.

8.   Ruggiero, M. T.; Bardon, T.; Strlic, M.; Taday, P. F.; Korter, T. M., Assignment of the Terahertz Spectra of Crystalline Copper Sulfate and Its Hydrates Via Solid-State Density Functional Theory. *The Journal of Physical Chemistry A* **2014,** *118* (43), 10101-10108.

9.   Zaczek, A. J.; Catalano, L.; Naumov, P.; Korter, T. M., Mapping the Polymorphic Transformation Gateway Vibration in Crystalline 1, 2, 4, 5-Tetrabromobenzene. *Chemical science* **2019,** *10* (5), 1332-1341.

10.   Dampf, S. J.; Korter, T. M., Anomalous Temperature Dependence of the Lowest-Frequency Lattice Vibration in Crystalline Γ-Aminobutyric Acid. *The Journal of Physical Chemistry A* **2019,** *123* (10), 2058-2064.

11.   Delaney, S. P.; Pan, D.; Galella, M.; Yin, S. X.; Korter, T. M., Understanding the Origins of Conformational Disorder in the Crystalline Polymorphs of Irbesartan. *Crystal growth & design* **2012,** *12* (10), 5017-5024.

12.   Delaney, S. P.; Pan, D.; Yin, S. X.; Smith, T. M.; Korter, T. M., Evaluating the Roles of Conformational Strain and Cohesive Binding in Crystalline Polymorphs of Aripiprazole. *Crystal growth & design* **2013,** *13* (7), 2943-2952.

13.   Ruggiero, M. T.; Sibik, J.; Zeitler, J. A.; Korter, T. M., Examination of L-Glutamic Acid Polymorphs by Solid-State Density Functional Theory and Terahertz Spectroscopy. *The Journal of Physical Chemistry A* **2016,** *120* (38), 7490-7495.

14.   Ruggiero, M. T.; Sutton, J. J.; Fraser-Miller, S. J.; Zaczek, A. J.; Korter, T. M.; Gordon, K. C.; Zeitler, J. A., Revisiting the Thermodynamic Stability of Indomethacin Polymorphs with Low-Frequency Vibrational Spectroscopy and Quantum Mechanical Simulations. *Crystal Growth & Design* **2018,** *18* (11), 6513-6520.

15.   Dierks, T. M.; Korter, T. M., Comparison of Intermolecular Forces in Anhydrous Sorbitol and Solvent Cocrystals. *The Journal of Physical Chemistry A* **2017,** *121* (30), 5720-5727.

16.   Squires, A.; Lewis, R.; Zaczek, A. J.; Korter, T. M., Distinguishing Quinacridone Pigments Via Terahertz Spectroscopy: Absorption Experiments and Solid-State Density Functional Theory Simulations. *The Journal of Physical Chemistry A* **2017,** *121* (18), 3423-3429.

17.   Davis, M. P.; Korter, T. M., Evaluating Hydrogen Bonding in Organic Cocrystals Using Low-Frequency Raman Vibrational Spectroscopy and Quantum Mechanical Simulations. *Crystal Growth & Design* **2022,** *22* (3), 1922-1932.

18.   Zeitler, J. A. R., Thomas; Taday, Philip F. , Pharmaceutical and Security Applications of Terahertz Spectroscopy. In *Terahertz Spectroscopy: Principles and Applications*, Dexheimer, S. L., Ed. CRC press: 2008; pp 299-320.

19.   Zeitler, J. A.; Taday, P. F.; Newnham, D. A.; Pepper, M.; Gordon, K. C.; Rades, T., Terahertz Pulsed Spectroscopy and Imaging in the Pharmaceutical Setting-a Review. *Journal of Pharmacy and Pharmacology* **2007,** *59* (2), 209-223.

20.   Neu, J.; Schmuttenmaer, C. A., Tutorial: An Introduction to Terahertz Time Domain Spectroscopy (Thz-Tds). *Journal of Applied Physics* **2018,** *124* (23), 231101.

21.   Dovesi, R.; Erba, A.; Orlando, R.; Zicovich-Wilson, C. M.; Civalleri, B.; Maschio, L.; Rérat, M.; Casassa, S.; Baima, J.; Salustro, S., Quantum-Mechanical Condensed Matter Simulations with Crystal. *Wiley Interdisciplinary Reviews: Computational Molecular Science* **2018**, e1360.

22.   Groom, C. R.; Bruno, I. J.; Lightfoot, M. P.; Ward, S. C., The Cambridge Structural Database. *Acta Crystallographica Section B: Structural Science, Crystal Engineering and Materials* **2016,** *72* (2), 171-179.

23.   Schäfer, A.; Horn, H.; Ahlrichs, R., Fully Optimized Contracted Gaussian Basis Sets for Atoms Li to Kr. *The Journal of Chemical Physics* **1992,** *97* (4), 2571-2577.

24.   Perdew, J. P.; Burke, K.; Ernzerhof, M., Generalized Gradient Approximation Made Simple. *Physical Review Letters* **1996,** *77* (18), 3865.

25.   Grimme, S.; Antony, J.; Ehrlich, S.; Krieg, H., A Consistent and Accurate Ab Initio Parametrization of Density Functional Dispersion Correction (Dft-D) for the 94 Elements H-Pu. *The Journal of Chemical Physics* **2010,** *132* (15), 154104.

26.   Grimme, S.; Ehrlich, S.; Goerigk, L., Effect of the Damping Function in Dispersion Corrected Density Functional Theory. *Journal of computational chemistry* **2011,** *32* (7), 1456-1465.

27.   Grimme, S.; Hansen, A.; Brandenburg, J. G.; Bannwarth, C., Dispersion-Corrected Mean-Field Electronic Structure Methods. *Chemical Reviews* **2016,** *116* (9), 5105-5154.

28.   Axilrod, B.; Teller, E., Interaction of the Van Der Waals Type between Three Atoms. *The Journal of Chemical Physics* **1943,** *11* (6), 299-300.

29.   Muto, Y., Force between Nonpolar Molecules. *J. Phys. Math. Soc. Jpn* **1943,** *17*, 629-631.

30.   Donà, L.; Brandenburg, J. G.; Bush, I. J.; Civalleri, B., Cost-Effective Composite Methods for Large Scale Solid-State Calculations. *Faraday Discussions* **2020**.

31.   Pascale, F.; Zicovich-Wilson, C. M.; López Gejo, F.; Civalleri, B.; Orlando, R.; Dovesi, R., The Calculation of the Vibrational Frequencies of Crystalline Compounds and Its Implementation in the Crystal Code. *Journal of computational chemistry* **2004,** *25* (6), 888-897.

32.   Noel, Y.; Zicovich-Wilson, C.; Civalleri, B.; D'arco, P.; Dovesi, R., Polarization Properties of Zno and Beo: An Ab Initio Study through the Berry Phase and Wannier Functions Approaches. *Physical Review B* **2001,** *65* (1), 014111.

Chapter 8: Low-Frequency Vibrational Spectroscopy and Quantum Mechanical Simulations of the Crystalline Polymorphs of the Antiviral Ribavirin

Margaret P. Davis and Timothy M. Korter*

Department of Chemistry, Syracuse University, 1-014 Center for Science and Technology, Syracuse, New York 13244-4100, United States
* Email: tmkorter@syr.edu

Abstract

Crystal polymorphism is a common phenomenon in pharmaceutical solids and a critical factor when considering the formulation of therapeutics since multiple polymorphs may form during drug manufacturing. Low-frequency vibrational spectroscopy is sensitive to polymorphic content and in this work, terahertz time-domain spectroscopy (THz-TDS) and low-frequency Raman spectroscopy (LFRS) were applied to the study of crystalline ribavirin, a widely applicable antiviral. Characteristic spectra with numerous peaks in the sub-200 cm^{-1} region were obtained of the more common polymorph of ribavirin (Form II). Solid-state density functional theory (ss-DFT) simulations were then used to optimize the crystal structure of this polymorph and calculate the frequencies and spectral intensities of the lattice vibrations in the low-frequency region. Excellent agreement between experiment and theory enabled the observed spectral peaks to be assigned to specific atomic motions in the solid. Of particular interest are the torsional vibrations of ribavirin involving the triazole and ribofuranosyl rings that appear between 105 and 140 cm^{-1} and these vibrations provided insight into the potential energy surface that is most important for the overall conformation of ribavirin. The Form I and Form II polymorphs of ribavirin were both evaluated with ss-DFT analyses which offered insights into the factors governing the relative stabilities of the two polymorphs. The simulations revealed that Form II is more stable under ambient conditions due to a stronger cohesive energy than Form I,

however ribavirin in Form I has a significantly lower conformational energy. These findings are consistent with Form II being thermodynamically favorable and Form I being kinetically formed from solution. Overall, these results demonstrate that ss-DFT can be used to accurately simulate and assign the low-frequency vibrational spectra of complex pharmaceutical solids, predict the spectral profiles of unstable or difficult to isolate polymorphs, and improve understanding of the energy factors influencing crystal growth.

8.1 Introduction

The polymorphic behavior of solid-state pharmaceutical molecules is of great importance in the formulation and application of medications.[1, 2] Polymorphism can be defined as when a crystalline solid has more than one three-dimensional arrangement of its components, with distinct differences often found in both molecular shape and intermolecular contacts. Polymorphs can have vastly different physical and chemical properties such as changes in aqueous solubility, which in the case of pharmaceuticals can modify the ability of the drug to perform its medical function.[3-5] Due to the ramifications of polymorphism on drug efficacy, it is important to identify, differentiate, and study polymorphs to improve drug design and production.[6]

Vibrational spectroscopy techniques operating in the sub-200 cm^{-1} spectral region, including terahertz time-domain spectroscopy (THz-TDS) and low-frequency Raman spectroscopy (LFRS), are particularly useful for examining crystalline polymorphs.[7-10] The vibrations present in this region involve large-amplitude motions of all components within the crystal and therefore offer new insights into internal torsional coordinates, external intermolecular motions, and the three-dimensional packing of the unit cell contents.[7, 9, 11] Experimental low-frequency vibrational spectroscopy can be combined with solid-state density functional theory (ss-DFT) to further explore these spectra and the energetics involved in polymorphism.[12, 13] Given the unique material-specific character of sub-200 cm^{-1} vibrations, ss-DFT is valuable because it enables unambiguous spectral assignments and reveals the molecular origins of the measured spectra. In addition to assigning observed spectra to specific atomic-level motions, ss-DFT also allows for detailed investigations of the energetic factors involved in polymorph structures. This permits elucidation of the reasons underlying the differing stabilities of various solid forms.[12, 14, 15]

In this study, we apply these techniques in the research of crystalline ribavirin ($C_8H_{12}N_4O_5$). The antiviral properties of ribavirin were discovered in 1972 and since then it has been primarily used to treat respiratory infections and in combination with other medicines for hepatitis C.[16-18] More recently, ribavirin has attracted interest as a possible therapeutic against SARS-CoV-2.[19] In the solid state, it can be found in two crystalline polymorphs (known as Form I and Form II, **Figure 8-1**).[20] Ribavirin Form II (R-II) is considered the thermodynamically stable polymorph and is found in commercial products.[16] However, previous experiments have demonstrated that mechanical processing can cause conversion between the two polymorphs which could present a risk during manufacturing and storage of ribavirin.[21] The relationship between these two polymorphs is also interesting because the stability ranking violates the typical density rule.[3] While this rule does not always hold, these polymorphs exhibit atypical behavior where R-II is more stable, but also less dense than ribavirin Form I (R-I).[21]

One important factor that directly affects the crystalline polymorphism of drug molecules is conformational flexibility or the ability of the molecules to achieve multiple three-dimensional shapes. The conformational flexibility of pharmaceutical compounds has long been a subject of study and the basis for designing and understanding drug function, generally represented as the structure-activity relationship.[22, 23] The conformations of several antivirals have been studied in this context, including acyclovir[24], peramivir[25], and ritonavir[26, 27], to name a few. The conformation of ribavirin has been the subject of computational conformational analyses before, using both semi-empirical[28, 29] and density functional theory methods[30]. The potential energy surface governing torsion of the O1-C1-N1-C6 dihedral angle (**Figure 8-1**) has been a focus, as this is the coordinate primarily responsible for the conformation of the molecule in the solid state and also for its successful drug binding capability.[28] The shape of the molecule is also strongly

affected by intermolecular forces as it interacts with its environment and this is exemplified by the fact that the conformation of a bound drug in an active site is typically different than that in solution.[31] Therefore, the conformational energy associated with the shape of ribavirin is of particular interest here as it can provide insights into the crystallization mechanism from solution, but also is important for understanding the drug action of the molecule.

In the current work, the more stable R-II polymorph is investigated using THz-TDS and LFRS, and then ss-DFT is applied in the analysis of both ribavirin solid forms. These vibrational spectra and simulations provide uniquely identifying spectral features for ribavirin polymorphs that may be used for analytical purposes. More important for the central interest here is that the observed vibrations represent intermolecular motions that yield insight into the crystal packing and intramolecular torsions that are linked to the three-dimensional shape of ribavirin. The exact natures of the peaks in the measured spectra have been determined with ss-DFT, enabling identification of the key torsional vibrations and how conformational and cohesive energies combine to dictate polymorph stability.
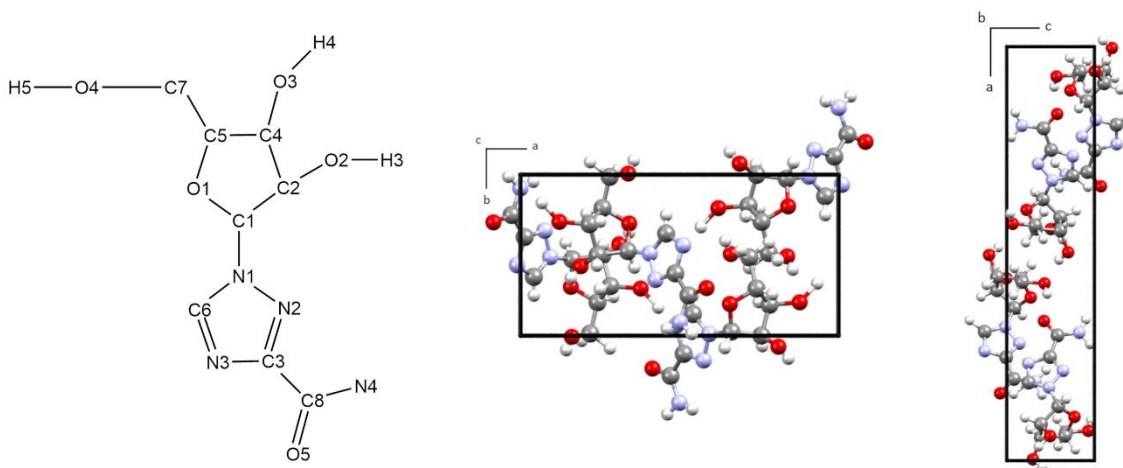
Figure 8-1. Two-dimensional representation of ribavirin with relevant hydrogens labeled (left), crystallographic unit cells for R-I (middle), and R-II (right).

8.2 Methods

8.2.1 Sample Preparation

Ribavirin was purchased from TCI America and used without further purification. Room-temperature powder X-ray diffraction (PXRD) was done on the ribavirin sample with a Bruker D2 Phaser diffractometer (Cu Kα radiation, λ=1.54060 Å, 5° to 70° with 0.5 s per step). PXRD data was compared to data from the Cambridge Structural Database (CSD)[32] and the ribavirin sample was confirmed to be R-II (P$2_12_12_1$, Z=4).[20] The PXRD comparison can be found in the **Supporting Information**. Numerous attempts to grow significant quantities of R-I were unsuccessful and these results are provided in the **Supporting Information**.

8.2.2 Terahertz Time-Domain Spectroscopy (THz-TDS)

THz-TDS data was collected at the University of Vermont in the research group of Prof. Michael Ruggiero. R-II was first ground and mixed with polytetrafluoroethylene (PTFE) and then pressed into 13 mm diameter x 3.04 mm thick pellets (2.2% w/w). A blank reference pellet of pure PTFE was used to ratio out any matrix absorption by the PTFE in preparation of the final terahertz data shown here. Room-temperature (295 K) and 20 K (closed-cycle helium cryostat) THz-TDS data were collected using a Toptica Photonics TeraFlash spectrometer (Munich, Germany). The instrument is based on a λ=1.5 μm femtosecond fiber laser used to illuminate photoconductive switch elements, with an InGaAs 25 μm strip-line photoconductive antenna for THz generation, and a 25 μm InGaAs dipole photoconductive antenna for THz detection. The final THz-TDS spectra had a spectral range of 150.0 cm^{-1} and a spectral resolution of 1.1 cm^{-1}. The data was zero-padded so there was an equal number of points 30 ps before and after the pulse. This smooths the spectra without changing the information obtained from the spectra. The

zero-padded sample and blank waveforms were then ratioed and Fourier-transformed using the Blackman window. The absorption spectra are expressed in units of molar extinction coefficient (M^{-1} cm^{-1}) where concentration is based on the concentration of the crystallographic unit cells in the sample.

8.2.3 Low-Frequency Raman Spectroscopy (LFRS)

A Coherent (Ondax) THz-Raman system (Santa Clara, CA) was used to take both room-temperature (295 K) and 78 K (liquid nitrogen) data using a laser centered at 784.7 nm and an Andor Shamrock DR-750 spectrograph with an iDus 416 CCD detector. For all measurements, finely ground powder was placed in a cryostat-mounted cuvette system with glass windows that allowed the sample to be cooled via liquid nitrogen as needed. At both 295 K and 78 K, 225 acquisitions were taken with 3 second exposure times. The Raman spectra had a spectral range of 10 to 300 cm^{-1} and a spectral resolution of 0.6 cm^{-1}.

8.2.4 Theoretical Methods

CRYSTAL17[33] was used to complete quantum mechanical simulations of R-I and R-II. For all of the calculations, the def2-TZVP[34] basis set was used along with the Perdew-Burke-Ernzerhof (PBE)[35] density functional augmented with Grimme's London dispersion correction (D3) utilizing the Becke-Johnson damping correction[36-38] and three-body repulsion Axilrod-Teller-Muto repulsion contributions (program keyword "ABC")[39-41]. A pruned integration grid of 99 radial points and 1454 angular points was used for all calculations. For both R-I and R-II, 125 k-points were used in the irreducible Brillouin zone (SHRINK 9 9). For optimizations, vibrational frequencies, and energy calculations, the overlap-based truncation criteria for the

bielectronic integrals (Coulomb and exchange, TOLINTEG) were set to 10^{-10}, 10^{-10}, 10^{-10}, 10^{-10}, and 10^{-20}.

The Cambridge Structural Database (CSD)[32] was used to obtain the starting experimental structures for the optimizations, reference codes VIRAZL for R-I and VIRAZL01 for R-II (both reported at room temperature).[20] For optimizations, an energy convergence of $\Delta E < 10^{-8}$ hartree was used. Two types of optimizations were done for R-II, to better simulate both the cold and room-temperature structures and resulting vibrational spectra. Fixed-lattice simulations were done to better approximate the room-temperature spectra and can be seen in the **Supporting Information**. These were performed by setting the lattice dimensions to the measured room-temperature XRD values and allowing only the atom positions to optimize within these constraints. Full optimizations were done by allowing the lattice dimensions and the atom positions to simultaneously optimize and being a 0 K simulation, are more representative of low-temperature structures and spectra.

Vibrational frequency analyses were done for both the fixed-lattice and fully-optimized structures for R-II and for only the fully-optimized structure of R-I. For the normal mode vibrational frequency and energy calculations, an energy convergence of $\Delta E < 10^{-10}$ hartree was used. For the frequency calculations, each atom was displaced twice along each Cartesian axis and determination of the numerical derivatives of the Hessian matrix was done with the central difference formula. The IR and Raman intensities were both calculated using the Coupled-Perturbed Hartree-Fock/Kohn-Sham (CPHF) approach.[42-44] For the Raman intensities, parameters for the experimental temperature and laser wavelength were accounted for. Simulated spectra were also convolved with Lorentzian line shapes to facilitate comparison with experiment using empirical full-width-at-half-maximum (FWHM) values.

Energy analyses were also done on both polymorphs. The total electronic energy of the crystallographic unit cell can be broken down into conformational and cohesive energies. The conformational energy was found by extracting an individual ribavirin molecule (the asymmetric unit of both polymorphs is one ribavirin molecule) from the ss-DFT optimized crystal and the energy of the fixed conformation was calculated. To determine the cohesive energy, the conformational energies of all the individual molecules in the unit cell were subtracted from the total electronic energy. Finally, the vibrational calculations were used to construct Gibbs free energy vs. temperature curves from 0 to 500 K for each polymorph.

Isolated molecule DFT simulations were also performed on single ribavirin molecules using Gaussian 16W (Revision C.01).[45] This software was used to scan the potential energy surface around the O1-C1-N1-C6 dihedral angle and perform gas-phase geometry optimizations. The Gaussian calculations were set up to be as close to the CRYSTAL17 parameters as possible, using the same density functional, noncovalent corrections, and basis set, but with the DFT integration grid increased to a larger grid than the software default (integral=grid=superfine).

8.3 Results and Discussion

8.3.1   Structural Differences and Optimization

The R-I and R-II crystals crystals were ss-DFT optimized and subsequent frequency analyses (vide infra) indicated the structures corresponded to minima on their respective potential energy surfaces. The fully-optimized ss-DFT structure of R-I had an average unsigned overall percent error in the unit cell dimensions of 0.42% with the largest error being 0.69% on the *c* axis and a volume error of 0.01%. The root-mean-squared deviation (rmsd) in the internal structure also showed low errors with an rmsd for the bond lengths of 0.01 Å, the bond angles of

1.05°, and the torsions of 1.30°. The rmsd for the intermolecular heavy-atom hydrogen bond lengths of R-I was 0.06 Å. The fully-optimized ss-DFT structure of R-II had an average unsigned overall percent error in the unit cell dimensions of 0.71% with the largest error being 1.50% on the *a* axis and a volume error of -1.31%. The R-II structure had an rmsd of 0.01 Å for the bond lengths, 0.80° for the bond angles, and 1.41° for the torsions. The rmsd for the intermolecular heavy-atom hydrogen bond lengths of R-II was 0.05 Å. Crystallographic information files (CIF) for both fully-optimized polymorphs are provided in the **Supporting Information.**

8.3.2   Experimental and Simulated Terahertz Spectra

The experimental THz spectra of R-II recorded at ambient and low temperatures are shown in **Figure 8-2**. The spectra show distinct absorption features at both temperatures, but the features narrow and shift to higher energy with cooling as is typical.[46] It is worth noting that in the case of R-II, the THz peaks are reasonably well resolved at 295 K and there are only modest changes at 78 K. This is indicative of the R-II crystal lattice vibrations being more harmonic in character as compared to other solids where much larger temperature effects have been observed that reveal their anharmonic natures.[47] The apparent near-harmonic behavior of the R-II crystal is also consistent with the comparison of the full geometry optimization that deviated from the room-temperature unit cell volume by only 0.01%.
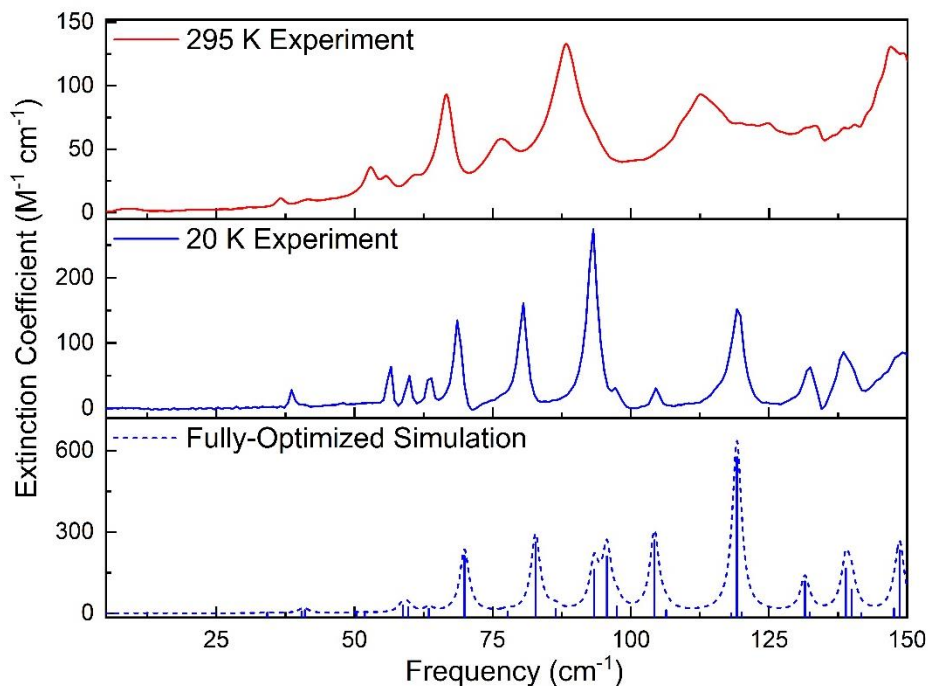
Figure 8-2. Experimental 295 K (solid red line) and 20 K (solid blue line) THz spectra for R-II from 5 to 120 cm^{-1}. Simulated THz spectra are shown based on the full-optimization (dashed blue line, 1.0 cm^{-1} FWHM) calculations.

The experimental 20 K THz spectrum of R-II is shown in **Figure 8-2** along with the fully-optimized ss-DFT simulation. The fully-optimized simulation shows good agreement with the 20 K THz spectrum demonstrating that by using different types of ss-DFT optimizations a reasonable representation of both the 295 K and 20 K THz spectra can be achieved. A complete list of simulated IR-active vibrational modes for both the fixed-lattice and the fully-optimized simulations can be found in the **Supporting Information**.

Four major features can be identified in the 20 K THz-TDS spectrum at 69, 81, 93, and 119 cm^{-1}. There are also a series of four smaller peaks between 35 and 65 cm^{-1} and two smaller peaks between 95 and 105 cm^{-1}. The fully-optimized simulation reproduces the four most intense peaks well, with peaks at 69.9, 82.8, and 119.2 cm^{-1} corresponding to the experimental peaks at 69, 81, and 119 cm^{-1}, respectively. The most intense feature at 93 cm^{-1} in the experimental

spectrum originates from the two features in the simulation at 93.4 and 95.7 cm^{-1} that are split by a greater magnitude than what is measured.

8.3.3   Experimental and Simulated Low-Frequency Raman Vibrational Spectra

The 295 K and 78 K LFRS data for R-II are shown in **Figure 8-3**. The spectra both offer distinct spectral signatures for the R-II polymorph with several strong features being observed in each. As described for the THz-TDS data, the changes in the Raman spectrum with sample cooling are relatively small and support the harmonic nature of the ribavirin crystal. LFRS simulations also demonstrate that the ss-DFT model used here for ribavirin offers an accurate reproduction of the low-frequency vibrations in the R-II crystal.
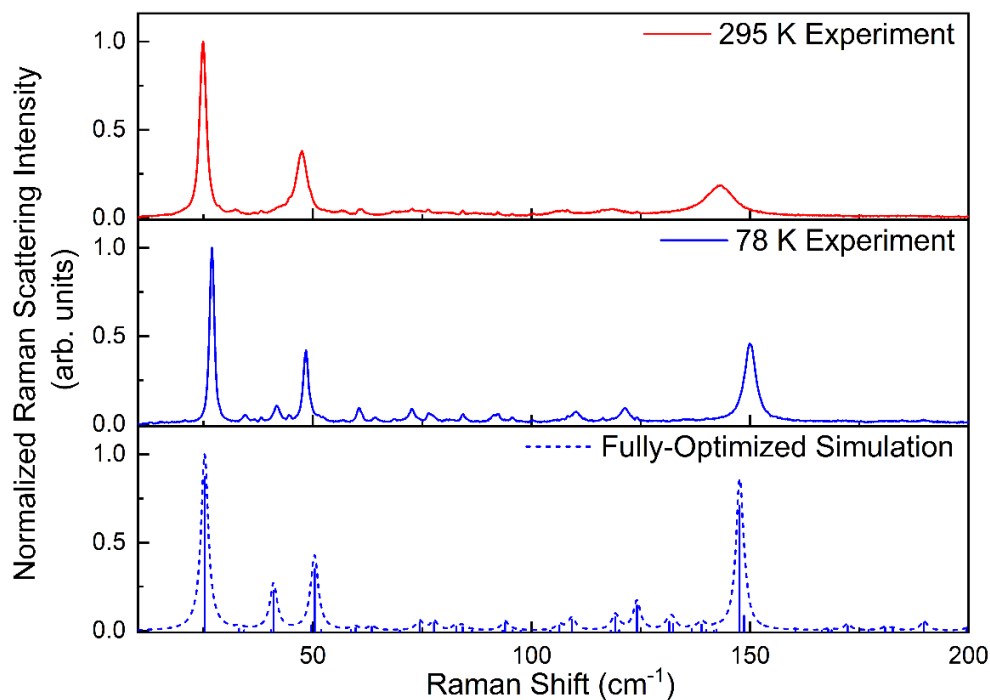
Figure 8-3. Experimental 295 K (solid red line) and 78 K (solid blue line) Raman spectra for R-II from 10 to 200 cm^{-1}. Simulated Raman spectra are shown based the full-optimization (dashed blue line, 1.0 cm^{-1} FWHM) calculations.

Figure 8-3 shows the 78 K Raman spectrum for R-II along with the fully-optimized ss-DFT simulation. As was seen with the THz-TDS data, the fully-optimized ss-DFT simulation does well at reproducing the lower temperature Raman spectrum. A complete list of simulated Raman-active vibrational modes for both the fixed lattice and the fully-optimized simulations can be found in the **Supporting Information**.

Within the 78 K Raman spectrum, three prominent peaks can be identified. The most intense peak is at 27 cm^{-1} in the experimental data and there are two other peaks at 48 and 150 cm^{-1} with several much weaker peaks between 50 and 145 cm^{-1}. The simulation also shows three main peaks that are in good agreement with the experimental spectrum, at 25.2, 50.4, and 147.6 cm^{-1}. The frequency positions of the predicted Raman peaks are very good, but the simulated intensities tend to be overestimated for some vibrations, including the simulated peaks at 41.0 cm^{-1} and 147.6 cm^{-1}, and the minor features above 150 cm^{-1}.

8.3.4   Types of Vibrations in the sub-200 cm^{-1} Region

ss-DFT simulations also allow for the motion of the different vibrational modes to be determined and visualized. Lower frequency modes generally represent vibrations with more collective motion that involve external coordinates (e.g. translations) while higher frequency modes become more localized. This can be seen in the THz-TDS data with the simulated mode at 41.0 cm^{-1} in the fully-optimized simulation (corresponding to a 20 K experimental mode at 39 cm^{-1}) and in the LFRS data at 25.2 cm^{-1} in the fully-optimized simulation (corresponding to 27 cm^{-1} in the 78 K spectrum) where both modes represent different rotational motions. At higher frequency, modes such as that at 93.4 cm^{-1} in the THz-TDS fully-optimized simulation (93 cm^{-1}

in the 20 K data) and 147.6 cm^{-1} in the LFRS fully-optimized simulation (150 cm^{-1} in the 78 K data) the motion becomes more localized torsions in specific parts of the molecules.

8.3.5   Dihedral Angle Analysis

A critical dihedral angle in ribavirin is the O1-C1-N1-C6 coordinate (**Figure 8-1**) connecting the two rings which has been studied earlier for its relevance to drug binding.[28] The experimental value for this dihedral angle in R-I is 10.406° and 119.019° in R-II as determined by single-crystal XRD. After the ss-DFT full optimization, the dihedral angle was 9.992° and 120.509°, respectively, showing the ss-DFT optimizations to be in excellent agreement with experiment. In terms of conformational energy, the conformation of ribavirin in the R-I polymorph is 15.95 kJ/mol lower in energy than in R-II, indicating the R-I conformation to be significantly more favorable. To further investigate this dihedral angle and the energy differences between the different conformations, single-molecule calculations were used to scan the dihedral angle potential energy surface and perform gas-phase geometry optimizations of the ribavirin molecules found in each solid-state polymorph.

First, a single ribavirin was extracted from both the R-I and R-II fully-optimized crystals and all other dihedral angles and geometry parameters in the molecules were fixed at the ss-DFT values for both polymorphs. Then, rigid scans consisting of 36 steps in 10° increments were done of the O1-C1-N1-C6 dihedral in the R-I and R-II molecules to obtain the ring-ring potential energy surface for the ss-DFT optimized molecules. Once minima were found, finer dihedral scans with 1° increments were done near these positions.

In the R-I rigid dihedral scan, the starting dihedral angle of 9.992° was close to the lowest energy dihedral angle found in the gas-phase potential energy surface scan at 17°. The energy

difference between the R-I starting structure and the dihedral angle minimum was 0.34 kJ/mol. The R-II rigid dihedral scan produced a very different result as the starting dihedral angle was not near the minima of the gas-phase potential energy surface. The lowest energy dihedral angle found in the scan was 271° and was lower in energy than the starting angle by 9.74 kJ/mol (though still higher in energy than scanned R-I by 6.48 kJ/mol). This indicates that the conformation of ribavirin in the R-II crystal is imposed by intermolecular forces and solid-state packing to a greater extent than in the R-I crystal. Plots of the energy versus dihedral angle are provided in the **Supporting Information**.

To further investigate the conformations of the two polymorphs, gas-phase full optimizations were done using the ss-DFT optimized structures as starting points. After gas-phase optimizations, the energy ranking was unchanged, but the R-I molecule was only 5.17 kJ/mol lower in energy than the R-II molecule. The dihedral angle changed significantly in both and became 26.607° in R-I and 11.588° in R-II. Normal mode analyses of both gas-phase optimized ribavirin structures showed them to be at potential energy surface minima. Complete optimizations of the R-I and R-II structures would ideally yield the same final geometry for the energetic minimum, however the positioning of substituents on the ribosyl ring leads to differing local minima. The main difference in these two optimized structures is the position of the O4-H5 hydroxyl group attached to C7 (**Figure 8-1**). In R-I, the ss-DFT torsional angle of C5-C7-O4-H5 was 170.898° and in R-II it was -56.410. However, a lower energy conformation can be achieved by two manual alterations of the optimized R-I molecule with subsequent geometry optimization in software. First, rotation of the O1-C1-N1-C6 dihedral angle to approximately -140° positions the hydroxylmethyl group near the triazole ring to permit intramolecular hydrogen bonding from the hydroxyl to a ring nitrogen. Second, rotation of the N2-C3-C8-O5 dihedral angle from ~0° to

~180° moves the amide group to an energetically preferred orientation for isolated ribavirin. This amide orientation is the same as that of ribavirin in some co-crystalline solids[48] and in crystals of 1H-1,2,4-triazole-3-carboxamide[49]. Subsequent optimization of this manually prepared structure resulted in the lowest energy conformation found in this study (25.20 kJ/mol lower than gas-phase fully optimized R-I), with an O1-C1-N1-C6 dihedral angle of -127.772°. This final structure (coordinates are provided in the **Supporting Information**) is lower in energy and yielded no negative vibrational modes, but it cannot be defined as the global minimum energy conformation for ribavirin as only a small portion of conformational space was considered. The structure is different than what has been previously reported, but also similar in the sense that the lowest energy conformers contained an intramolecular bond.[30] It is expected that structures found through solid-state and gas-phase simulations (and experiments) will differ from solution-phase conformations in much the same way that drug structures differ in their solution and bound states.[30]

8.3.6   Torsional Vibrations Involving the Ring-Ring Dihedral Angle

The ss-DFT frequency analyses also generate eigenvectors as part of the vibrational simulations, and this allows for the atomic motions associated with a vibration (Raman or IR active) to be investigated. Due to the importance of the O1-C1-N1-C6 dihedral angle, specific vibrations that involve this torsion can be identified and the correlation of theory and experimental vibrational frequencies serves as a benchmark for the quality of the predicted ring-ring potential energy surface. Three ss-DFT calculated vibrations under 150 cm^{-1} that involve a large degree of motion in this dihedral can be found in each polymorph. These modes are 117.2, 123.1, and 127.5 cm^{-1} in R-I and 106.4, 109.3, and 138.9 cm^{-1} in R-II. Focusing on R-II for comparison to the experiments, the modes at 106.4 cm^{-1} and 138.9 cm^{-1} are IR-active and all

three modes are Raman-active. Based on the theoretical intensity values, the peak at 106.4 cm^{-1}

should be very weak in the IR spectrum and in fact was not observed experimentally. The mode

at 138.9 cm^{-1} is significantly stronger and can be seen in the experimental spectrum at

approximately 139 cm^{-1}, in very good agreement (**Figure 8-4**).
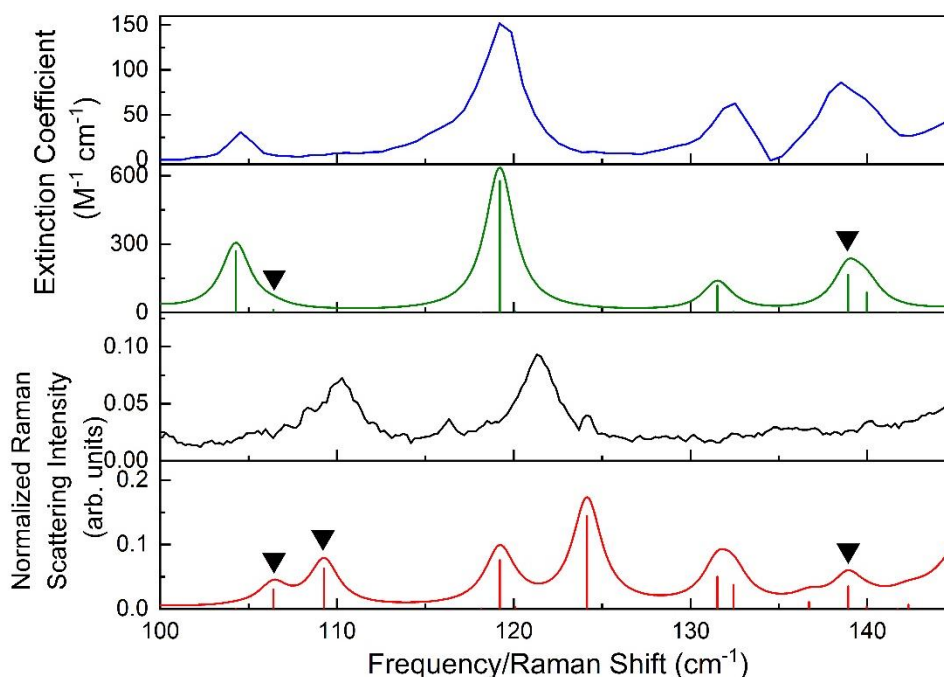
Figure 8-4. Experimental 20 K THz spectrum of R-II (blue), the fully-optimized ss-DFT simulated THz spectrum (1.0 cm^{-1} Lorentzian line shape) (green), experimental 78 K Raman spectrum of R-II (black), and the fully-optimized ss-DFT simulated Raman spectrum (1.0 cm^{-1} Lorentzian line shape) (red). Black triangles above the torsional modes.

When considering the experimental Raman spectrum, the predicted vibrations at 106.4 cm^{-1}

and 109.3 cm^{-1} are represented by a somewhat broad asymmetric peak with a maximum at 110.3

cm^{-1} that is very close to the 109.3 cm^{-1} vibration, calculated to be the more intense of the pair

(**Figure 8-4**). The predicted mode at 138.9 cm^{-1} cannot be unambiguously located in the

experimental spectrum due to the weak Raman scattering intensity of the vibrations in this

region. Despite the limited experimental opportunities for locating torsional vibrations of

crystalline ribavirin, those that have been identified match well with the simulated frequencies and demonstrate that the ring-ring torsional potential energy is being well modeled.

8.3.7   Analysis of Energy Factors in Crystallization

Due to the good accuracy of the structural and vibrational simulations as compared to the experimental structural and vibrational data, the ss-DFT simulations can be expected to provide meaningful analyses of the energetic factors driving formation of the two polymorphs of ribavirin. For this purpose, only the fully-optimized ss-DFT simulations are considered. After full optimizations, the total electronic energy of R-II is lower than R-I by 8.87 kJ/mol per asymmetric unit. These results are consistent with evidence indicating that R-II is thermodynamically stable, while R-I is metastable and kinetically formed.[21] The total electronic energy of both polymorphs can be further broken down into conformational and cohesive energies. These calculations show that R-II has a stronger cohesive energy by -24.82 kJ/mol per asymmetric unit, while R-I has a preferred conformational energy by -15.95 kJ/mol. The cohesion energy difference is likely the driving factor for why R-II is the more stable polymorph at ambient conditions. Ribavirin molecules possessing lower conformational energy in metastable R-I is consistent with Ostwald's step rule which suggests that the molecular conformations will more closely resemble those in solution in the polymorph formed first upon initial crystallization.[3]

In addition to examining ribavirin cohesion and conformation in the solid-state, ss-DFT can also be used to calculate Gibbs free energy curves of the polymorphs. The free energy calculations include the additional factors of vibrational energy and entropy to better understand the stability ranking of R-I and R-II. **Figure 8-5** shows the Gibbs free energy versus temperature

curves for R-I and R-II. These curves demonstrate that the two polymorphs have a monotropic relationship and that R-II is the thermodynamically stable form of crystalline ribavirin over the entire temperature range.
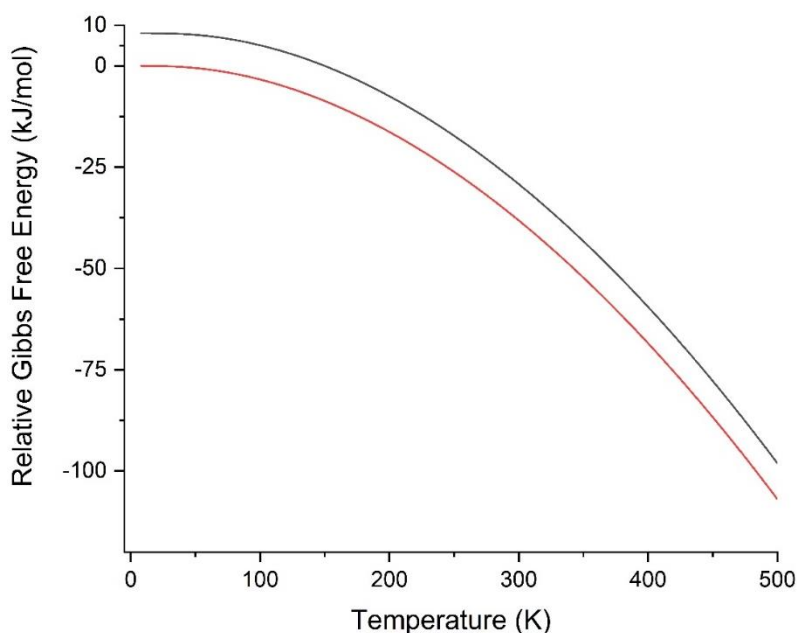
Figure 8-5. Relative Gibbs free energy curve for R-II (red) and R-I (black). All energies are per asymmetric unit (one ribavirin molecule). For clarity, the energy values have been set relative to a common zero.

8.4 Conclusion

Crystalline ribavirin exhibits strong and distinct low-frequency vibrational spectra that could be utilized for monitoring pharmaceutical manufacturing processes. Leveraging infrared and Raman spectroscopies of lattice vibrations in polymorphic solids with support from quantum mechanical stimulations enables new insights to be achieved. The exploration of the low-frequency vibrational spectra of the R-II polymorph and the energetics involved in the stability of both R-I and R-II demonstrate the strengths of this combined approach. By investigating the conformation of the ribavirin molecules within the R-I and R-II crystals it is apparent how the

conformation of R-II in the solid-state is enforced by intermolecular forces and how the conformation can change dramatically between the solid-state and isolated ribavirin molecules. Further energetic analysis shows that R-II is more stable than R-I in terms of Gibbs free energy over a wide temperature range and this is driven primarily by its stronger cohesive energy. Overall, these findings emphasize the metastability of the R-I polymorph and provide further evidence of a kinetic pathway for growth of this crystal form of ribavirin.

8.5 Supporting Information (see Appendix E)

PXRD patterns for pure R-II sample and mixture of R-II and R-I sample with comparison to database patterns for R-I and R-II. FTIR spectrum of R-II from 80 to 300 cm^{-1}. Experimental 295 K and 20 K THz spectra for R-II with simulated THz spectra based on fixed-lattice and full-optimization calculations. Experimental 295 K and 78 K Raman spectra for R-II with simulated THz spectra based on fixed-lattice and full-optimization calculations. List of solid-state DFT IR- and Raman-active modes for R-I and R-II full optimization and R-II fixed-lattice optimization. Energy versus dihedral angle curves for R-I and R-II. Coordinates for R-I final confirmation from Gaussian. CIFs of the R-I and R-II full optimizations.

8.6 Acknowledgements

8.7 References

1.   Maheshwari, R.; Chourasiya, Y.; Bandopadhyay, S.; Katiyar, P. K.; Sharma, P.; Deb, P. K.; Tekade, R. K., Chapter 1 - Levels of Solid State Properties: Role of Different Levels During Pharmaceutical Product Development. In *Dosage Form Design Parameters*, Tekade, R. K., Ed. Academic Press: 2018; pp 1-30.

2.   Chieng, N.; Rades, T.; Aaltonen, J., An Overview of Recent Studies on the Analysis of Pharmaceutical Polymorphs. *Journal of pharmaceutical and biomedical analysis* **2011,** *55* (4), 618-644.

3.   Lee, E. H., A Practical Guide to Pharmaceutical Polymorph Screening & Selection. *Asian Journal of Pharmaceutical Sciences* **2014,** *9* (4), 163-175.

4.   Llinàs, A.; Goodman, J. M., Polymorph Control: Past, Present and Future. *Drug Discovery Today* **2008,** *13* (5-6), 198-210.

5.   Bhatia, A.; Chopra, S.; Nagpal, K.; Deb, P. K.; Tekade, M.; Tekade, R. K., Chapter 2 - Polymorphism and Its Implications in Pharmaceutical Product Development. In *Dosage Form Design Parameters*, Tekade, R. K., Ed. Academic Press: 2018; pp 31-65.

6.   Parrott, E. P. J.; Zeitler, J. A., Terahertz Time-Domain and Low-Frequency Raman Spectroscopy of Organic Materials. *Applied Spectroscopy* **2015,** *69* (1), 1-25.

7.   Zeitler, J. A.; Taday, P. F.; Newnham, D. A.; Pepper, M.; Gordon, K. C.; Rades, T., Terahertz Pulsed Spectroscopy and Imaging in the Pharmaceutical Setting-a Review. *Journal of Pharmacy and Pharmacology* **2007,** *59* (2), 209-223.

8.   Zaczek, A. J.; Catalano, L.; Naumov, P.; Korter, T. M., Mapping the Polymorphic Transformation Gateway Vibration in Crystalline 1, 2, 4, 5-Tetrabromobenzene. *Chemical science* **2019,** *10* (5), 1332-1341.

9.   Larkin, P. J.; Dabros, M.; Sarsfield, B.; Chan, E.; Carriere, J. T.; Smith, B. C., Polymorph Characterization of Active Pharmaceutical Ingredients (Apis) Using Low-Frequency Raman Spectroscopy. *Applied spectroscopy* **2014,** *68* (7), 758-776.

10.   Bērziņš, K.; Fraser-Miller, S. J.; Gordon, K. C., Recent Advances in Low-Frequency Raman Spectroscopy for Pharmaceutical Applications. *International Journal of Pharmaceutics* **2021,** *592*, 120034.

11.   Inoue, M.; Hisada, H.; Koide, T.; Fukami, T.; Roy, A.; Carriere, J.; Heyler, R., Transmission Low-Frequency Raman Spectroscopy for Quantification of Crystalline Polymorphs in Pharmaceutical Tablets. *Analytical chemistry* **2019,** *91* (3), 1997-2003.

12.   Ruggiero, M. T.; Sutton, J. J.; Fraser-Miller, S. J.; Zaczek, A. J.; Korter, T. M.; Gordon, K. C.; Zeitler, J. A., Revisiting the Thermodynamic Stability of Indomethacin Polymorphs with Low-Frequency Vibrational Spectroscopy and Quantum Mechanical Simulations. *Crystal Growth & Design* **2018,** *18* (11), 6513-6520.

13.   Neu, J.; Nikonow, H.; Schmuttenmaer, C. A., Terahertz Spectroscopy and Density Functional Theory Calculations of Dl-Norleucine and Dl-Methionine. *The Journal of Physical Chemistry A* **2018,** *122* (28), 5978-5982.

14.   Dierks, T. M.; Korter, T. M., Comparison of Intermolecular Forces in Anhydrous Sorbitol and Solvent Cocrystals. *The Journal of Physical Chemistry A* **2017,** *121* (30), 5720-5727.

15.   Zaczek, A. J.; Korter, T. M., Polymorphism in Cis–Trans Muconic Acid Crystals and the Role of C–H··· O Hydrogen Bonds. *Crystal Growth & Design* **2017,** *17* (8), 4458-4466.

16.   Tong, H. H.; Shekunov, B. Y.; Chan, J. P.; Mok, C. K.; Hung, H. C.; Chow, A. H., An Improved Thermoanalytical Approach to Quantifying Trace Levels of Polymorphic Impurity in Drug Powders. *International journal of pharmaceutics* **2005,** *295* (1-2), 191-199.

17.   Goodarzi, N.; Morgani, A. B.; Abrahamsson, B.; Cristofoletti, R.; Groot, D.; Langguth, P.; Mehta, M. U.; Polli, J. E.; Shah, V. P.; Dressman, J. B., Biowaiver Monographs for Immediate Release Solid Oral Dosage Forms: Ribavirin. *Journal of Pharmaceutical Sciences* **2016,** *105* (4), 1362-1369.

18.   Witkowski, J.; Robins, R. K.; Sidwell, R. W.; Simon, L. N., Design, Synthesis, and Broad Spectrum Antiviral Activity of 1-. Beta.-D-Ribofuranosyl-1, 2, 4-Triazole-3-Carboxamide and Related Nucleosides. *Journal of medicinal chemistry* **1972,** *15* (11), 1150-1154.

19.   Unal, M. A.; Bitirim, C. V.; Summak, G. Y.; Bereketoglu, S.; Cevher Zeytin, I.; Besbinar, O.; Gurcan, C.; Aydos, D.; Goksoy, E.; Kocakaya, E., Ribavirin Shows Antiviral Activity against Sars-Cov-2 and Downregulates the Activity of Tmprss2 and the Expression of Ace2 in Vitro. *Canadian journal of physiology and pharmacology* **2021,** *99* (5), 449-460.

20.   Prusiner, P.; Sundaralingam, M., The Crystal and Molecular Structures of Two Polymorphic Crystalline Forms of Virazole (1-B-D-Ribofuranosyl-1, 2, 4-Triazole-3-Carboxamide). A New Synthetic Broad Sprectrum Antiviral Agent. *Acta Crystallographica Section B: Structural Crystallography and Crystal Chemistry* **1976,** *32* (2), 419-426.

21.   Vasa, D. M.; Wildfong, P. L., Solid-State Transformations of Ribavirin as a Result of High-Shear Mechanical Processing. *International Journal of Pharmaceutics* **2017,** *524* (1-2), 339-350.

22.   Foloppe, N.; Chen, I.-J., Conformational Sampling and Energetics of Drug-Like Molecules. *Current medicinal chemistry* **2009,** *16* (26), 3381-3413.

23.   Veale, C. G., Into the Fray! A Beginner's Guide to Medicinal Chemistry. *ChemMedChem* **2021,** *16* (8), 1199-1225.

24.   Alvarez-Ros, M. C.; Palafox, M. A., Conformational Analysis, Molecular Structure and Solid State Simulation of the Antiviral Drug Acyclovir (Zovirax) Using Density Functional Theory Methods. *Pharmaceuticals* **2014,** *7* (6), 695-722.

25.   Richards, M. R.; Brant, M. G.; Boulanger, M. J.; Cairo, C. W.; Wulff, J. E., Conformational Analysis of Peramivir Reveals Critical Differences between Free and Enzyme-Bound States. *MedChemComm* **2014,** *5* (10), 1483-1488.

26.   Chakraborty, D.; Sengupta, N.; Wales, D. J., Conformational Energy Landscape of the Ritonavir Molecule. *The Journal of Physical Chemistry B* **2016,** *120* (19), 4331-4340.

27.   Wang, C.; Rosbottom, I.; Turner, T. D.; Laing, S.; Maloney, A. G.; Sheikh, A. Y.; Docherty, R.; Yin, Q.; Roberts, K. J., Molecular, Solid-State and Surface Structures of the Conformational Polymorphic Forms of Ritonavir in Relation to Their Physicochemical Properties. *Pharmaceutical research* **2021,** *38* (6), 971-990.

28.   Miles, D. L.; Miles, D. W.; Redington, P.; Eyring, H., Theoretical Studies of the Conformational Properties of Ribavirin. *Proceedings of the National Academy of Sciences* **1976,** *73* (12), 4257-4260.

29.   Vijan, L. E.; Topală, C. M., Study of Ribavirin–Nucleic Acids Interaction. *Chemical Engineering Communications* **2016,** *203* (12), 1562-1571.

30.   Ladetto, M.; Márquez, M.; Romani, D.; Brandán, S., Structural and Vibrational Studies on Isomers of Antiviral Ribavirin Drug in Gas and Aqueous Environmental by Using the Sqm Approach. *J Adv Chem* **2019,** *16*, 6325-6353.

31.   Gao, C.; Park, M.-S.; Stern, H. A., Accounting for Ligand Conformational Restriction in Calculations of Protein-Ligand Binding Affinities. *Biophysical journal* **2010,** *98* (5), 901-910.

32.   Groom, C. R.; Bruno, I. J.; Lightfoot, M. P.; Ward, S. C., The Cambridge Structural Database. *Acta Crystallographica Section B: Structural Science, Crystal Engineering and Materials* **2016,** *72* (2), 171-179.

33.   Dovesi, R.; Erba, A.; Orlando, R.; Zicovich-Wilson, C. M.; Civalleri, B.; Maschio, L.; Rérat, M.; Casassa, S.; Baima, J.; Salustro, S., Quantum-Mechanical Condensed Matter Simulations with Crystal. *Wiley Interdisciplinary Reviews: Computational Molecular Science* **2018**, e1360.

34.   Weigend, F.; Ahlrichs, R., Balanced Basis Sets of Split Valence, Triple Zeta Valence and Quadruple Zeta Valence Quality for H to Rn: Design and Assessment of Accuracy. *Physical Chemistry Chemical Physics* **2005,** *7* (18), 3297-3305.

35.   Perdew, J. P.; Burke, K.; Ernzerhof, M., Generalized Gradient Approximation Made Simple. *Physical Review Letters* **1996,** *77* (18), 3865.

36.   Grimme, S.; Antony, J.; Ehrlich, S.; Krieg, H., A Consistent and Accurate Ab Initio Parametrization of Density Functional Dispersion Correction (Dft-D) for the 94 Elements H-Pu. *The Journal of Chemical Physics* **2010,** *132* (15), 154104.

37.   Grimme, S.; Ehrlich, S.; Goerigk, L., Effect of the Damping Function in Dispersion Corrected Density Functional Theory. *Journal of Computational Chemistry* **2011,** *32* (7), 1456-1465.

38.   Grimme, S.; Hansen, A.; Brandenburg, J. G.; Bannwarth, C., Dispersion-Corrected Mean-Field Electronic Structure Methods. *Chemical Reviews* **2016,** *116* (9), 5105-5154.

39.   Donà, L.; Brandenburg, J. G.; Bush, I. J.; Civalleri, B., Cost-Effective Composite

Methods for Large Scale Solid-State Calculations. *Faraday Discussions* **2020**.

40.   Axilrod, B.; Teller, E., Interaction of the Van Der Waals Type between Three Atoms. *The*

Journal of Chemical Physics **1943,** *11* (6), 299-300.

41.   Muto, Y., Force between Nonpolar Molecules. *J. Phys. Math. Soc. Jpn* **1943,** *17*, 629-

631.

42.   Ferrero, M.; Rérat, M.; Kirtman, B.; Dovesi, R., Calculation of First and Second Static

Hyperpolarizabilities of One-to Three-Dimensional Periodic Compounds. Implementation in the

Crystal Code. *The Journal of chemical physics* **2008,** *129* (24), 244110.

43.   Ferrero, M.; Rérat, M.; Orlando, R.; Dovesi, R., Coupled Perturbed Hartree-Fock for

Periodic Systems: The Role of Symmetry and Related Computational Aspects. *The Journal of*

chemical physics **2008,** *128* (1), 014110.

44.   Ferrero, M.; Rérat, M.; Orlando, R.; Dovesi, R., The Calculation of Static Polarizabilities

of 1-3d Periodic Compounds. The Implementation in the Crystal Code. *Journal of computational*

chemistry **2008,** *29* (9), 1450-1459.

45.   Frisch, M. J.; Trucks, G. W.; Schlegel, H. B.; Scuseria, G. E.; Robb, M. A.; Cheeseman,

J. R.; Scalmani, G.; Barone, V.; Petersson, G. A.; Nakatsuji, H.; Li, X.; Caricato, M.; Marenich,

A. V.; Bloino, J.; Janesko, B. G.; Gomperts, R.; Mennucci, B.; Hratchian, H. P.; Ortiz, J. V.;

Izmaylov, A. F.; Sonnenberg, J. L.; Williams; Ding, F.; Lipparini, F.; Egidi, F.; Goings, J.; Peng,

B.; Petrone, A.; Henderson, T.; Ranasinghe, D.; Zakrzewski, V. G.; Gao, J.; Rega, N.; Zheng, G.;

Liang, W.; Hada, M.; Ehara, M.; Toyota, K.; Fukuda, R.; Hasegawa, J.; Ishida, M.; Nakajima,

T.; Honda, Y.; Kitao, O.; Nakai, H.; Vreven, T.; Throssell, K.; Montgomery Jr., J. A.; Peralta, J.

E.; Ogliaro, F.; Bearpark, M. J.; Heyd, J. J.; Brothers, E. N.; Kudin, K. N.; Staroverov, V. N.;

Keith, T. A.; Kobayashi, R.; Normand, J.; Raghavachari, K.; Rendell, A. P.; Burant, J. C.; Iyengar, S. S.; Tomasi, J.; Cossi, M.; Millam, J. M.; Klene, M.; Adamo, C.; Cammi, R.; Ochterski, J. W.; Martin, R. L.; Morokuma, K.; Farkas, O.; Foresman, J. B.; Fox, D. J. *Gaussian 16 Rev. C.01*, Wallingford, CT, 2016.

46.   Fan, W.; Burnett, A.; Upadhya, P.; Cunningham, J.; Linfield, E.; Davies, A., Far-Infrared Spectroscopic Characterization of Explosives for Security Applications Using Broadband Terahertz Time-Domain Spectroscopy. *Applied spectroscopy* **2007,** *61* (6), 638-643.

47.   Dampf, S. J.; Korter, T. M., Anomalous Temperature Dependence of the Lowest-Frequency Lattice Vibration in Crystalline Γ-Aminobutyric Acid. *The Journal of Physical Chemistry A* **2019,** *123* (10), 2058-2064.

48.   Chen, J.-M.; Li, S.; Lu, T.-B., Pharmaceutical Cocrystals of Ribavirin with Reduced Release Rates. *Crystal growth & design* **2014,** *14* (12), 6399-6408.

49.   Xie, Q.-R., 1h-1, 2, 4-Triazole-3-Carboxamide. *Acta Crystallographica Section E: Structure Reports Online* **2008,** *64* (6), o1110-o1110.

Chapter 9: Investigating Anhydrous and Hydrated Ampicillin and Amoxicillin Crystals through Low-Frequency Vibrational Spectroscopy and Quantum Mechanical Simulations

9.1 Introduction

Ampicillin and amoxicillin are both popular antibiotics that are part of the penicillin family.[1, 2] Amoxicillin is the most prescribed antibiotic in the United State according to the CDC and one of the most prescribed drugs overall.[3] Amoxicillin and ampicillin are both administered in their trihydrate forms which have very similar structures.[4, 5] Despite being very similar molecules, the only difference being an aromatic hydroxyl group on amoxicillin, only the anhydrous form of ampicillin has been crystallized while amoxicillin anhydrous has never been identified (**Figure 9-1**).[6]
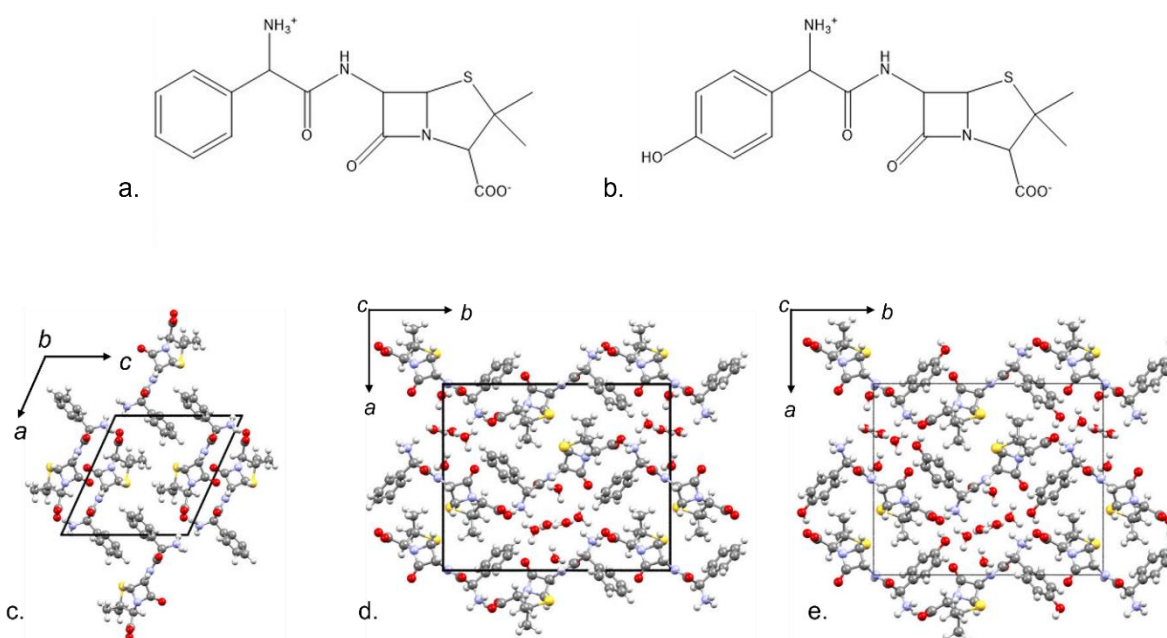
Figure 9-1. The 2D structures of **a.** ampicillin and **b.** amoxicillin. The crystallographic unit cells of **c.** ampicillin anhydrous, **d.** ampicillin trihydrate, and **c.** amoxicillin trihydrate.

Due to the similarities between the trihydrate crystal structures, any slight differences in intermolecular forces or crystal packing are important. For this reason, the low-frequency vibrational modes, which involve motion of the entire unit cell and can highlight intermolecular

forces and three-dimensional crystal packing, are investigated here through low-frequency Raman spectroscopy (LFRS). Low-frequency vibrational spectroscopy is also useful because this region can provide a fingerprint spectrum for identifying different molecules[7-16] and, therefore, Raman spectroscopy can be used to differentiate between the nearly identical ampicillin trihydrate and amoxicillin trihydrate crystals.

In combination with LFRS, solid-state density functional theory (ss-DFT) is used to further explore the structural and energetic differences between ampicillin and amoxicillin and why amoxicillin anhydrous may not form experimentally. Experimental structural information as well as the low-frequency vibrational spectra can be used to benchmark the computational simulations and judge their accuracy.[17-19] Once an accurate computational method has been determined, the energetics of the existing systems can be explored, and predictions can be made about a hypothetical amoxicillin anhydrous structure.[20-23]

9.2 Experimental Methods

9.2.1 Sample Preparation

Ampicillin and amoxicillin were bought from Sigma-Aldrich. Powder X-ray diffraction (PXRD) was done on both purchased samples using a Bruker D2 Phaser diffractometer (Cu Kα radiation, λ=1.54060 Å, 5° to 70° with 0.5 s per step). The ampicillin sample was determined to be in its anhydrous form (P2$_1$, Z=2)[24] and the amoxicillin sample was in its trihydrate form (P2$_1$2$_1$2$_1$, Z=4)[25]. Ampicillin trihydrate (P2$_1$2$_1$2$_1$, Z=4)[26] was crystallized by dissolving ampicillin in water and allowing it to slowly evaporate at ambient conditions and then confirming the structure via PXRD. The PXRD patterns can be found in the **Supporting Information**. All samples were ground into a fine powder using a mortar and pestle before LFRS was performed.

9.2.2 Low-Frequency Raman Spectroscopy (LFRS)

LFRS data was taken at both room (295 K) and low-temperature (78 K, via liquid nitrogen) using a Coherent (Ondax) THz-Raman system (Santa Clara, CA). This system uses an Andor Shamrock DR-750 spectrograph with an iDus 416 CCD detector and a laser centered at 784.7 nm. The finely ground sample were positioned in a cryostat-mounted cuvette system with glass windows and spectra were taken at room-temperature. Liquid nitrogen was also used to cool the cryostat so that spectra could be taken at 78 K. A 3 second exposure time with 225 acquisitions was used for all samples and the resulting Raman spectrum has a spectral range of 10 to 300 cm^{-1} with a resolution of 0.6 cm^{-1}.

9.3 Theoretical Methods

All calculations were done using CRYSTAL17[27] and used the Ahlrichs' VTZ basis set with additional polarization functions[28] and the PBE functional[29]. All calculations also included the Grimme's D3 dispersion correction term with Becke-Johnson damping[30-32] and a three-body Axilrod-Teller-Muto type term[33, 34]. The overlap-based truncation criteria for the bielectronic integrals (Coulomb and exchange) (TOLINTEG) were set to 10^{-10}, 10^{-10}, 10^{-10}, 10^{-10}, and 10^{-20} for all calculations. The starting structures for the geometry optimizations were obtained from the Cambridge Structural Database[35]. Single point energy calculations were used to determine the number of k-points in the irreducible Brillouin zone and both trihydrates had 64 k-points in the irreducible Brillouin zone (SHRINK=7) and ampicillin anhydrous had 170 k-points in the irreducible Brillouin zone (SHRINK=8). An energy convergence of $\Delta E < 10^{-8}$ hartree was used for the geometry optimizations and energy calculations and one of $\Delta E < 10^{-10}$ hartree was used for the vibrational frequency calculations.

For all frequency calculations, a 2-point numerical derivative was used and IR and Raman intensities were calculated. The 2-point numerical derivative uses the central-difference formula and each atom is displaced twice along each Cartesian axis. The IR and Raman intensities were calculated using the Coupled-Perturbed Hartree-Fock/Kohn-Sham (CPHF) approach[36-38] and for the Raman intensities, temperature and laser wavelength parameters were used. Once the calculation finished, the simulated Raman frequencies and intensities were convolved with a Lorentzian line shape using an empirical full-width-at-half-maximum (FWHM) value.

CRYSTAL17 was also used to do energy calculations including calculating the total electronic, conformational, cohesive, and Gibbs free energies. Gibbs free energy versus temperature curves can be obtained from the frequency calculations. The conformational energy is calculated by extracting an individual molecule from the unit cell and converging the energy of that individual molecule (keyword MOLECULE). The conformational energy multiplied by the Z value can be subtracted from the total electronic energy of the unit cell to calculate the cohesive energy. Calculating conformational and cohesive energies becomes more difficult due to the zwitterionic nature of ampicillin and amoxicillin. To perform these calculations, the PBE0 functional[39] was used and the overlap-based truncation criteria for the bielectronic integrals (Coulomb and exchange) (TOLINTEG) were increased to 10^{-15}, 10^{-15}, 10^{-15}, 10^{-30}, and 10^{-60}. These changes allow for successful electronic convergence in the single point and MOLECULE calculations that are necessary to calculate conformational and cohesive energies.

9.4 Results and Discussion

9.4.1 Optimized Structures

Ampicillin anhydrous, ampicillin trihydrate, and amoxicillin trihydrate were all

optimized using ss-DFT and produced low errors. Ampicillin anhydrous had an average unsigned percent error on the lattice dimensions of 1.06% and a percent error on the volume of -1.81%. The root-mean-square deviation (rmsd) of the heavy atom bond lengths was 0.02 Å, the rmsd of the bond angles was 1.25°, and the rmsd of the dihedral angles was 3.22° in ampicillin anhydrous. Ampicillin anhydrous has four hydrogen bonds and the errors in the hydrogen bond heavy atom length is low with an rmsd value of 0.07 Å. The rmsd of the bond angles is large, 20.31°, most likely because two of the hydrogen bonds are far from linear, 130.6° and 132.7°, which tend to be more difficult to simulate.[40]

The ss-DFT optimization of ampicillin trihydrate also produced low errors with an average unsigned percent error on the lattice dimensions of 0.78% and a percent error in the volume of -2.32%. The rmsd value of the bond lengths was 0.02 Å, of the bond angles was 1.06°, and of the dihedral angles was 2.04°. Both trihydrates have ten hydrogen bonds and the rmsd value of the heavy atom hydrogen bond lengths in ampicillin trihydrate was 0.09 Å and the rmsd value of the hydrogen bond angles was 10.74°. Amoxicillin trihydrate had an average unsigned percent error on the lattice dimensions of 0.15% and a percent error in the volume of 0.37%. The rmsd values were also low with an rmsd value of 0.02 Å on the bond lengths, of 1.17° on the bond angles, and of 1.50° on the dihedral angles. The rmsd value of the heavy atom hydrogen bond lengths was 0.16 Å and of hydrogen bond angles was 13.38°.

9.4.2 Low-Frequency Raman Spectroscopy

LFRS can provide unique spectra for anhydrous versus hydrates species as well as for samples that have very similar crystal structures. **Figure 9-2.a.** demonstrates how ampicillin anhydrous and ampicillin trihydrate have unique spectra and can be clearly differentiated from

each other. **Figure 9-2.b.** explores a similar idea with ampicillin trihydrate and amoxicillin

trihydrate which have very similar crystal structures, but distinctly characteristic spectra.

a.   b.
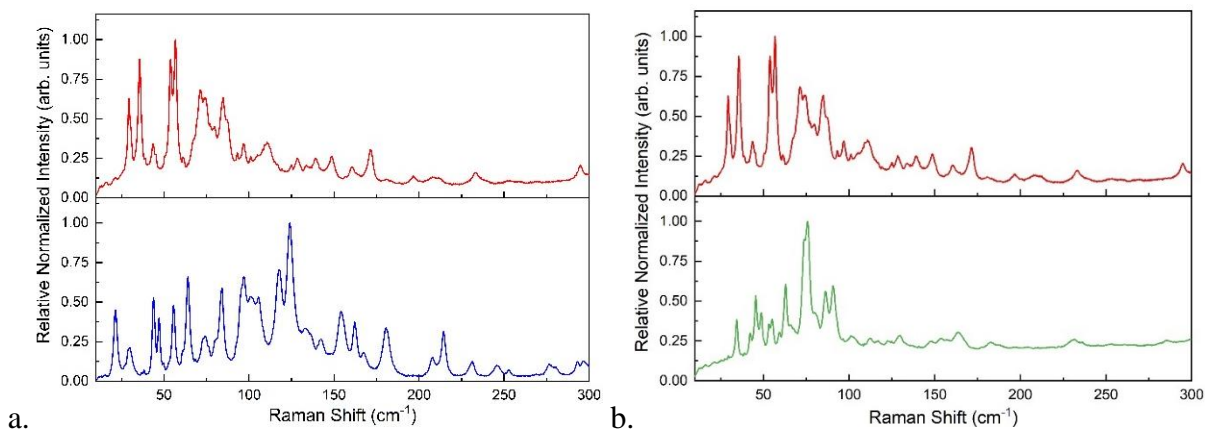
Figure 9-2. a. The experimental Raman spectra of ampicillin trihydrate (red, top) and
ampicillin anhydrous (blue, bottom) at 78 K. **b.** The experimental Raman spectra of ampicillin
trihydrate (red, top) and amoxicillin trihydrate (green, bottom) at 78 K.

The optimized structures of the three systems discussed above were used to run

vibrational frequency analyses and simulate the LFRS data. The frequency analyses confirmed

that all three optimized structures were minima on their respective potential energy surfaces. The

LFRS data of all three samples is complex, but ss-DFT does a good job of reproducing the

frequency positions and general intensities. **Figure 9-3** shows the experimental Raman spectrum

of ampicillin anhydrous at 78 K along with the simulated spectrum and illustrates the good

match between the experimental data and the simulation.
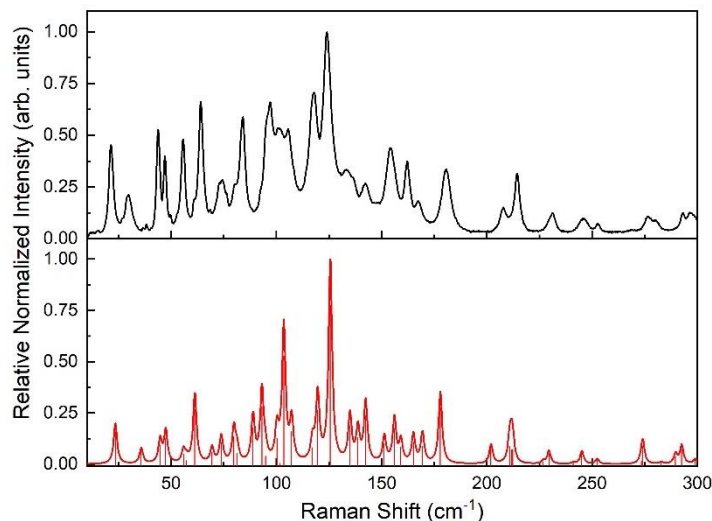
Figure 9-3. The experimental Raman spectrum of ampicillin anhydrous (black, top) at 78 K and the ss-DFT simulation (1.0 cm^{-1} FWHM Lorentzian line shape) (bottom, red).

Figure 9-4 demonstrates the same findings for the simulations of ampicillin trihydrate and amoxicillin trihydrate, adding to our confidence in the selected computational model to accurately simulate these larger pharmaceutical systems.

a.   b.
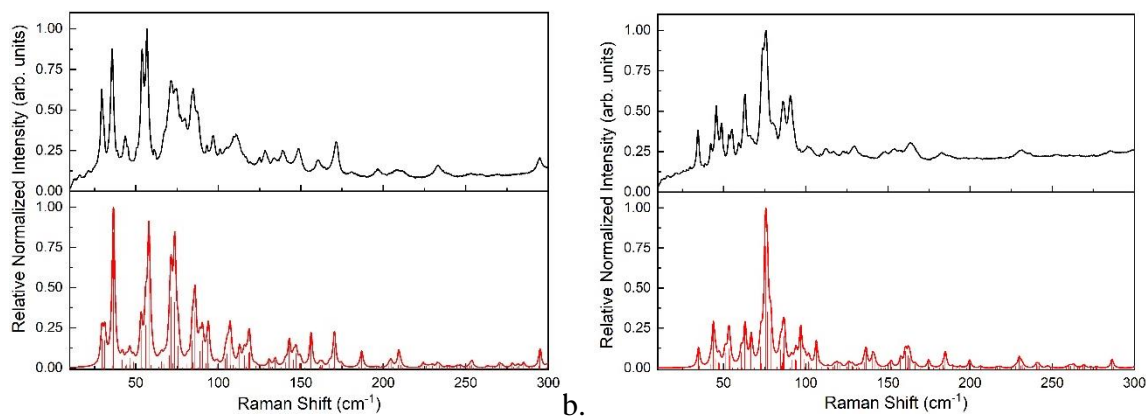
Figure 9-4. a. The experimental Raman spectrum of ampicillin trihydrate (black, top) at 78 K and the ss-DFT simulation (1.0 cm^{-1} FWHM Lorentzian line shape) (bottom, red) and **b.** the experimental Raman spectrum of amoxicillin trihydrate (black, top) and the ss-DFT simulation (1.0 cm^{-1} FWHM Lorentzian line shape) (bottom, red).

9.4.3 Cohesive Energies of Ampicillin Trihydrate and Amoxicillin Trihydrate

As well as simulating the vibrational spectra, ss-DFT also provides insights into the energetic differences between the two hydrates. The cohesive energy of ampicillin trihydrate and amoxicillin trihydrate can be compared on per atom basis. While the cohesive energy of amoxicillin trihydrate is slightly lower than that of ampicillin trihydrate, by 0.18 kJ/mol per atom, the cohesive energies of these two systems are remarkably close. This is not entirely surprising since the structures of the two trihydrates are isomorphic, but amoxicillin does possess an additional hydroxyl group compared to ampicillin which could enhance the cohesion through greater dipole-dipole interactions.

9.4.4 Hypothetical Amoxicillin Anhydrous

Since the computational model chosen here does a good job of simulating the structural parameters and vibrational frequencies for ampicillin anhydrous, ampicillin trihydrate, and amoxicillin trihydrate, this computational model can be used to make predictions about a hypothetical amoxicillin anhydrous structure. There are a number of ways to predict the amoxicillin anhydrous structure and here we take a couple of different approaches to produce a hypothetical amoxicillin anhydrous structure. Due to the similarities between the trihydrate structures, it was assumed that the anhydrous structures may be very similar as well and, therefore, the ampicillin anhydrous structure was modified to be an amoxicillin anhydrous structure by simply adding a hydroxyl group to the para position on the benzyl ring. This structure was then initially optimized in the $P2_1$ space group and then reduced to P1 and re-optimized. The P1 re-optimization only took one step to converge and, therefore, the $P2_1$ setting is an appropriate space group setting for this structure. This structure will be called the

hypothetical amoxicillin anhydrous structure. A frequency analysis was done on this structure, and it was determined to be a minima on its potential energy surface.

Another path to determining an amoxicillin anhydrous structure was to delete the waters from the amoxicillin trihydrate structure and then reduce the structure to P1 and allow it to relax and fully optimize without symmetry constraints. Once this structure was optimized in P1, ISOCIF[41] was used and the $P2_1$ space group was found. A re-optimization in $P2_1$ was done, converging in 20 steps, and then a frequency analysis was done to confirm this structure to be a minimum on its potential energy surface. This structure will be called the hypothetical dehydrated amoxicillin structure. **Table 1** shows the lattice cell dimensions of both of these structures along with the experimental lattice dimensions for ampicillin anhydrous, ampicillin trihydrate, and amoxicillin trihydrate.

Following the same dehydration method, the waters in ampicillin trihydrate were deleted and this structure was optimized in $P2_1$, then in P1, and then ISOCIF was used and the $P2_1$ space group was found again. This hypothetical dehydrated ampicillin structure was also determined to be a minimum on its potential energy surface. This structure, however, is not the same as the experimentally known ampicillin anhydrous structure. **Table 1** shows the lattice cell dimensions of this structure as well.

Table 1. Lattice dimensions and volumes of the experimental structures of ampicillin anhydrous[24], ampicillin trihydrate[26], amoxicillin trihydrate[25], and the hypothetical amoxicillin anhydrous, dehydrated amoxicillin, and dehydrated ampicillin structures.

	Exp. Ampicillin Trihydrate[26]	Hypothetical Dehydrated Ampicillin	Exp. Ampicillin Anhydrous[24]	Exp. Amoxicillin Trihydrate	Hypothetical Dehydrated Amoxicillin[25]	Hypothetical Amoxicillin Anhydrous
Space Group	$P2_12_12_1$	$P2_1$	$P2_1$	$P2_12_12_1$	$P2_1$	$P2_1$
a	15.52275 Å	6.1394 Å	12.4 Å	15.622 Å	6.6598 Å	12.3514 Å
b	18.9256 Å	20.4283 Å	6.2 Å	18.785 Å	18.9033 Å	6.1861 Å
c	6.67375 Å	15.1478 Å	12.0 Å	6.645 Å	15.5254 Å	12.1046 Å
β	90°	90.048°	114.5°	90°	90.001°	112.770°
Volume	1960.597 Å^3	1899.7831 Å^3	839.494 Å^3	1950.037 Å^3	1954.5402 Å^3	852.8005 Å^3
Density	1.367 g/cm^3	1.221 g/cm^3	1.388 g/cm^3	1.429 g/cm^3	1.241 g/cm^3	1.422 g/cm^3

The creation of these hypothetical crystal structures did not lead to an obvious solution for the crystal structure of anhydrous amoxicillin, but has revealed structures that likely correspond to dehydrated metastable species that exist for a short period of time before relaxing into formal anhydrous forms or decomposing into an amorphous solid[42]. These hypothetical structures provide potential crystal structures that may be experimentally found under certain circumstances and may be accessible with careful control of sample temperature and humidity and therefore are worthy of future study. They certainly offer some clues as to the potential pathway and existence of amoxicillin anhydrous.

9.5 Conclusions

This work expands our scientific knowledge of the very common antibiotics ampicillin and amoxicillin and for the first time shows the low-frequency Raman spectral signatures of ampicillin anhydrous, ampicillin trihydrate, and amoxicillin trihydrate. Based on the accurate vibrational simulations, the ss-DFT computational model was used to explore possible amoxicillin anhydrous structures that may be used as a basis for future experimental work. In the

future, this work will be complimented by complete energetic analysis of the hypothetical structures proposed and single-molecule simulations of the antibiotic molecules to better understand the conformations of these compounds in solution prior to crystallization.

9.6 Supporting Information (see Appendix F)

PXRD patters for ampicillin anhydrous, ampicillin trihydrate, and amoxicillin trihydrate along with the CSD generated patterns.

9.7 Acknowledgements

M.P.D. and T.M.K. thank Syracuse University for providing computational resources.

9.8 References

1. Bebu, A.; Szabó, L.; Leopold, N.; Berindean, C.; David, L., Ir, Raman, Sers and Dft Study of Amoxicillin. *Journal of Molecular Structure* **2011,** *993* (1-3), 52-56.

2. Baraldi, C.; Tinti, A.; Ottani, S.; Gamberini, M. C., Characterization of Polymorphic Ampicillin Forms. *Journal of pharmaceutical and biomedical analysis* **2014,** *100*, 329-340.

3. Prevention, C. f. D. C. Outpatient Antibiotic Prescriptions—United States, 2015. https://www.cdc.gov/antibiotic-use/data/report-2015.html.

4. Brittain, H. G., Solid-State Fluorescence of the Trihydrate Phases of Ampicillin and Amoxicillin. *AAPS PharmSciTech* **2005,** *6* (3), E444-E448.

5. Healy, A. M.; Worku, Z. A.; Kumar, D.; Madi, A. M., Pharmaceutical Solvates, Hydrates and Amorphous Forms: A Special Emphasis on Cocrystals. *Advanced drug delivery reviews* **2017,** *117*, 25-46.

6. Han, J.; Suryanarayanan, R., A Method for the Rapid Evaluation of the Physical Stability of Pharmaceutical Hydrates. *Thermochimica acta* **1999,** *329* (2), 163-170.

7.   Larkin, P. J.; Dabros, M.; Sarsfield, B.; Chan, E.; Carriere, J. T.; Smith, B. C., Polymorph Characterization of Active Pharmaceutical Ingredients (Apis) Using Low-Frequency Raman Spectroscopy. *Applied spectroscopy* **2014,** *68* (7), 758-776.

8.   Liu, H.-B.; Chen, Y.; Zhang, X.-C., Characterization of Anhydrous and Hydrated Pharmaceutical Materials with Thz Time-Domain Spectroscopy. *Journal of pharmaceutical sciences* **2007,** *96* (4), 927-934.

9.   Strachan, C. J.; Taday, P. F.; Newnham, D. A.; Gordon, K. C.; Zeitler, J. A.; Pepper, M.; Rades, T., Using Terahertz Pulsed Spectroscopy to Quantify Pharmaceutical Polymorphism and Crystallinity. *Journal of Pharmaceutical Sciences* **2005,** *94* (4), 837-846.

10.   Strachan, C. J.; Rades, T.; Newnham, D. A.; Gordon, K. C.; Pepper, M.; Taday, P. F., Using Terahertz Pulsed Spectroscopy to Study Crystallinity of Pharmaceutical Materials. *Chemical Physics Letters* **2004,** *390* (1-3), 20-24.

11.   Zeitler, J. A.; Taday, P. F.; Newnham, D. A.; Pepper, M.; Gordon, K. C.; Rades, T., Terahertz Pulsed Spectroscopy and Imaging in the Pharmaceutical Setting-a Review. *Journal of Pharmacy and Pharmacology* **2007,** *59* (2), 209-223.

12.   Zeitler, J. A. R., Thomas; Taday, Philip F. , Pharmaceutical and Security Applications of Terahertz Spectroscopy. In *Terahertz Spectroscopy: Principles and Applications*, Dexheimer, S. L., Ed. CRC press: 2008; pp 299-320.

13.   Bērziņš, K.; Fraser-Miller, S. J.; Gordon, K. C., Recent Advances in Low-Frequency Raman Spectroscopy for Pharmaceutical Applications. *International Journal of Pharmaceutics* **2021,** *592*, 120034.

14. Remoto, P. I. J.; Bērziņš, K. r.; Fraser-Miller, S. J.; Korter, T. M.; Rades, T.; Rantanen, J.; Gordon, K. C., Elucidating the Dehydration Mechanism of Nitrofurantoin Monohydrate Ii Using Low-Frequency Raman Spectroscopy. *Crystal Growth & Design* **2022,** *22* (4), 2733-2741.

15. Robert, C.; Fraser-Miller, S. J.; Berzins, K.; Okeyo, P. O.; Rantanen, J.; Rades, T.; Gordon, K. C., Monitoring the Isothermal Dehydration of Crystalline Hydrates Using Low-Frequency Raman Spectroscopy. *Molecular Pharmaceutics* **2021,** *18* (3), 1264-1276.

16. Hisada, H.; Inoue, M.; Koide, T.; Carriere, J.; Heyler, R.; Fukami, T., Direct High-Resolution Imaging of Crystalline Components in Pharmaceutical Dosage Forms Using Low-Frequency Raman Spectroscopy. *Organic Process Research & Development* **2015,** *19* (11), 1796-1798.

17. Delaney, S. P.; Korter, T. M., Terahertz Spectroscopy and Computational Investigation of the Flufenamic Acid/Nicotinamide Cocrystal. *The Journal of Physical Chemistry A* **2015,** *119* (13), 3269-3276.

18. Mazurek, A. H.; Szeleszczuk, Ł.; Pisklak, D. M., Periodic Dft Calculations—Review of Applications in the Pharmaceutical Sciences. *Pharmaceutics* **2020,** *12* (5), 415.

19. Dampf, S. J.; Korter, T. M., Crystalline Molecular Standards for Low-Frequency Vibrational Spectroscopies. *Journal of Infrared, Millimeter, and Terahertz Waves* **2020,** *41* (11), 1284-1300.

20. Dierks, T. M.; Korter, T. M., Origins of the Relative Stabilities of Anhydrous and Hydrated D-Mannitol Crystals. *The Journal of Physical Chemistry A* **2016,** *120* (33), 6629-6636.

21. Delaney, S. P.; Pan, D.; Yin, S. X.; Smith, T. M.; Korter, T. M., Evaluating the Roles of Conformational Strain and Cohesive Binding in Crystalline Polymorphs of Aripiprazole. *Crystal growth & design* **2013,** *13* (7), 2943-2952.

22.   Mohara, M.; Davis, M. P.; Korter, T. M.; Shimura, K.; Ono, T.; Aiko, K., Study on Hydration and Dehydration of Ezetimibe by Terahertz Spectroscopy with Humidity-Controlled Measurements and Theoretical Analysis. *The Journal of Physical Chemistry A* **2022**.

23.   Zaczek, A. J.; Korter, T. M., Polymorphism in Cis–Trans Muconic Acid Crystals and the Role of C–H··· O Hydrogen Bonds. *Crystal Growth & Design* **2017,** *17* (8), 4458-4466.

24.   Boles, M.; Girven, R., The Structures of Ampicillin: A Comparison of the Anhydrate and Trihydrate Forms. *Acta Crystallographica Section B: Structural Crystallography and Crystal Chemistry* **1976,** *32* (8), 2279-2284.

25.   Boles, M.; Girven, R.; Gane, P., The Structure of Amoxycillin Trihydrate and a Comparison with the Structures of Ampicillin. *Acta Crystallographica Section B: Structural Crystallography and Crystal Chemistry* **1978,** *34* (2), 461-466.

26.   Burley, J. C.; Streek, J.; Stephens, P. W., Ampicillin Trihydrate from Synchrotron Powder Diffraction Data. *Acta Crystallographica Section E: Structure Reports Online* **2006,** *62* (2), o797-o799.

27.   Dovesi, R.; Erba, A.; Orlando, R.; Zicovich-Wilson, C. M.; Civalleri, B.; Maschio, L.; Rérat, M.; Casassa, S.; Baima, J.; Salustro, S., Quantum-Mechanical Condensed Matter Simulations with Crystal. *Wiley Interdisciplinary Reviews: Computational Molecular Science* **2018**, e1360.

28.   Schäfer, A.; Horn, H.; Ahlrichs, R., Fully Optimized Contracted Gaussian Basis Sets for Atoms Li to Kr. *The Journal of Chemical Physics* **1992,** *97* (4), 2571-2577.

29.   Perdew, J. P.; Burke, K.; Ernzerhof, M., Generalized Gradient Approximation Made Simple. *Physical Review Letters* **1996,** *77* (18), 3865.

30.	Grimme, S.; Antony, J.; Ehrlich, S.; Krieg, H., A Consistent and Accurate Ab Initio Parametrization of Density Functional Dispersion Correction (Dft-D) for the 94 Elements H-Pu. *The Journal of Chemical Physics* **2010,** *132* (15), 154104.

31.	Grimme, S.; Ehrlich, S.; Goerigk, L., Effect of the Damping Function in Dispersion Corrected Density Functional Theory. *Journal of computational chemistry* **2011,** *32* (7), 1456-1465.

32.	Grimme, S.; Hansen, A.; Brandenburg, J. G.; Bannwarth, C., Dispersion-Corrected Mean-Field Electronic Structure Methods. *Chemical Reviews* **2016,** *116* (9), 5105-5154.

33.	Axilrod, B.; Teller, E., Interaction of the Van Der Waals Type between Three Atoms. *The Journal of Chemical Physics* **1943,** *11* (6), 299-300.

34.	Muto, Y., Force between Nonpolar Molecules. *J. Phys. Math. Soc. Jpn* **1943,** *17*, 629-631.

35.	Macrae, C. F.; Sovago, I.; Cottrell, S. J.; Galek, P. T.; McCabe, P.; Pidcock, E.; Platings, M.; Shields, G. P.; Stevens, J. S.; Towler, M., Mercury 4.0: From Visualization to Analysis, Design and Prediction. *Journal of applied crystallography* **2020,** *53* (1), 226-235.

36.	Ferrero, M.; Rérat, M.; Kirtman, B.; Dovesi, R., Calculation of First and Second Static Hyperpolarizabilities of One-to Three-Dimensional Periodic Compounds. Implementation in the Crystal Code. *The Journal of chemical physics* **2008,** *129* (24), 244110.

37.	Ferrero, M.; Rérat, M.; Orlando, R.; Dovesi, R., Coupled Perturbed Hartree-Fock for Periodic Systems: The Role of Symmetry and Related Computational Aspects. *The Journal of chemical physics* **2008,** *128* (1), 014110.

38.   Ferrero, M.; Rérat, M.; Orlando, R.; Dovesi, R., The Calculation of Static Polarizabilities of 1-3d Periodic Compounds. The Implementation in the Crystal Code. *Journal of computational chemistry* **2008,** *29* (9), 1450-1459.

39.   Adamo, C.; Barone, V., Toward Reliable Density Functional Methods without Adjustable Parameters: The Pbe0 Model. *The Journal of chemical physics* **1999,** *110* (13), 6158-6170.

40.   Ireta, J.; Neugebauer, J.; Scheffler, M., On the Accuracy of Dft for Describing Hydrogen Bonds: Dependence on the Bond Directionality. *The Journal of Physical Chemistry A* **2004,** *108* (26), 5692-5698.

41.   Stokes, H.; Hatch, D.; Campbell, B., Isocif, Isotropy Software Suite, Iso.Byu.Edu. 2022.

42.   Takahashi, M.; Uekusa, H., Dehydration and Rehydration Mechanisms of Pharmaceutical Crystals: Classification of Hydrates by Activation Energy. *Journal of Pharmaceutical Sciences* **2022,** *111* (3), 618-627.

Chapter 10: Conclusions

Studying the intermolecular and intramolecular forces that contribute to the energetic factors involved in the stability of polymorphs, hydrates, and cocrystals is critical for the understanding and development of future drug formulations. This work demonstrates how low-frequency vibrational spectroscopies and ss-DFT can be used together to gain new insights into polymorphs, hydrates, and cocrystals. Low-frequency vibrational spectroscopies, both THz and LFRS, can be used to identify and differentiate both pure (**Chapter 7 and Chapter 8**) and cocrystal (**Chapter 5**) pharmaceutical polymorphs. It is also useful for differentiating anhydrous and hydrated crystals and tracking hydration under different levels of relative humidity (**Chapter 6**). Low-frequency vibrational spectroscopy also provides a benchmark for computational techniques which is valuable in determining the most accurate computational parameters for different systems. Accurate ss-DFT models allow for the individual motions of different low-frequency modes to be characterized, something that is nearly impossible otherwise. The vibrational identities are valuable because this connects the large-amplitude motions to molecular shape and crystal packing.

Computational methods then provide additional insights into why certain polymorphs are more stable or why cocrystals or hydrates form over their pure components. Through ss-DFT, active pharmaceuticals can be studied, but model cocrystal systems can also be used to learn about hydrogen bonding in related cocrystals. Taking this idea even further, computationally designed hypothetical crystals can be used to explore how modifications of the van der Waals forces can impact stability (**Chapter 4**) as well as predict possible dehydrate crystals (**Chapter 9**). Computational modeling also allows for the calculations of other important energetic factors such as free energy which can give information on stability over a set temperature range.

This work demonstrates how combining low-frequency vibrational spectroscopies and ss-DFT can be instrumental in expanding our knowledge of pharmaceutical polymorphs, cocrystals, and hydrates. Ideas explored here could also be useful in continuing to explore how hydrates form and dehydrate as well as how cocrystals may dissociate in different environments. In the future, this work and extensions of it could be used to screen pharmaceutical compounds for polymorphs, cocrystals, and hydrates and develop more effective crystal engineering techniques.

Appendix A: Supporting Information for Chapter 4

Supporting Information Table of Contents

Table A-11. Solid-state DFT IR-active modes with frequencies (cm-1), intensities (km/mol), and mode symmetries for U:GA-I.

Table A-12. Solid-state DFT Raman-active modes with frequencies (cm^{-1}), relative intensities (normalized to 1000), and mode symmetries for U:GA-I at 78 K.

Table A-13. Solid-state DFT IR-active modes with frequencies (cm-1), intensities (km/mol), and mode symmetries for U:GA-II.

Table A-14. Solid-state DFT Raman-active modes with frequencies (cm^{-1}), relative intensities (normalized to 1000), and mode symmetries for U:GA-II at 78 K.

Table A-15. Solid-state DFT IR-active modes with frequencies (cm-1), intensities (km/mol), and mode symmetries for T:GA.

Table A-16. Solid-state DFT Raman-active modes with frequencies (cm^{-1}), relative intensities (normalized to 1000), and mode symmetries for T:GA at 78 K.

Table A-17. Solid-state DFT IR-active modes with frequencies (cm^{-1}), intensities (km/mol), and mode symmetries for U:TA.

Table A-18. Solid-state DFT Raman-active modes with frequencies (cm^{-1}), relative intensities (normalized to 1000), and mode symmetries for U:TA at 78 K.

Table A-19. Solid-state DFT IR-active modes with frequencies (cm-1), intensities (km/mol), and mode symmetries for thiourea-DL-tartaric acid (T:TA).

Table A-20. Solid-state DFT Raman-active modes with frequencies (cm^{-1}), relative intensities (normalized to 1000), and mode symmetries for T:TA at 78 K.

Figure A-8. Relative Gibbs free energy curves for cocrystallized U:GA-I (green), U:GA-II (black) and the linear combination of relative Gibbs free energies of pure urea and pure glutaric acid (red). For clarity, the energy values have been set relative to a common zero and are per asymmetric unit.

Figure A-9. Relative Gibbs free energy curves for cocrystallized T:GA (purple) and the linear combination of relative Gibbs free energies of pure thiourea and pure glutaric acid (green). For clarity, the energy values have been set relative to a common zero and are per asymmetric unit.

Figure A-10. Relative Gibbs free energy curves for cocrystallized U:TA (purple) and the linear combination of relative Gibbs free energies of pure urea and pure DL-tartaric acid (red). For clarity, the energy values have been set relative to a common zero and are per asymmetric unit.

Figure A-11. Relative Gibbs free energy curve for cocrystallized T:TA (green) and the linear combination of relative Gibbs free energies of pure thiourea and pure DL-tartaric acid (orange). For clarity, the energy values have been set relative to a common zero and are per asymmetric unit.

Supporting Information References

A-R1. Birkedal, H.; Madsen, D.; Mathiesen, R. H.; Knudsen, K.; Weber, H. P.; Pattison, P.; Schwarzenbach, D., The charge density of urea from synchrotron diffraction data. Acta Crystallogr., Sect. A: Found. Crystallogr. 2004, A60 (5), 371-381.

A-R2. Takahashi, I.; Onodera, A.; Shiozaki, Y., Structural changes of thiourea in connection with its phase transitions: reappraisal of rigidity and libration of the molecule. Acta Crystallographica Section B: Structural Science 1990, 46 (5), 661-664.

A-R3. Thalladi, V. R.; Nüsse, M.; Boese, R., The Melting Point Alternation in A, Ω-Alkanedicarboxylic Acids. Journal of the American Chemical Society 2000, 122 (38), 9227-9236.

A-R4. Videnova-Adrabińska, V., Pre-Designed Structural Building Blocks of a (1: 1) Urea–Glutaric Acid Co-Crystal. Journal of Materials Chemistry 1995, 5 (12), 2309-2311

A-R5. Chadwick, K.; Davey, R.; Sadiq, G.; Cross, W.; Pritchard, R., The Utility of a Ternary Phase Diagram in the Discovery of New Co-Crystal Forms. CrystEngComm 2009, 11 (3), 412-414.

A-R6. Thirumurugan, R.; Babu, B.; Anitha, K.; Chandrasekaran, J., Synthesis, Growth, Characterization and Quantum Chemical Investigations of a Promising Organic Nonlinear Optical Material: Thiourea-Glutaric Acid. Journal of Molecular Structure 2018, 1171, 915-925.

A-R7. Falvello, L. R., Experimental Crystal Strucutre Determination. 2016.

A-R8. Kostyanovsky, R. G.; Kostyanovsky, V. R.; Kadorkina, G. K., The enigma of a (±)-tartaric acid–urea cocrystal. Mendeleev Communications 2009, 1 (19), 17-18.
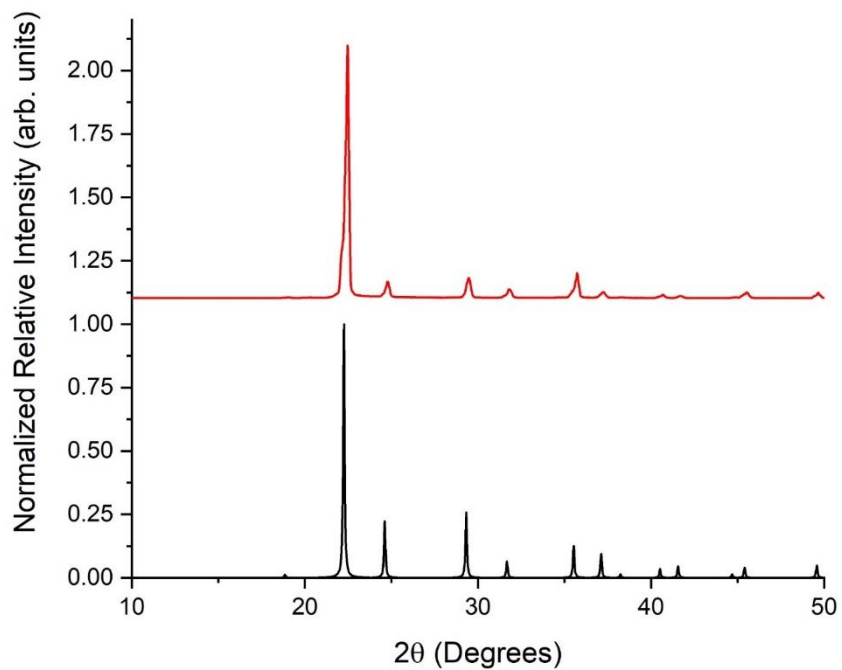
Figure A-1. PXRD patterns of urea sample (red) and CSD published pattern[A-R1] (black) (patterns offset for clarity).
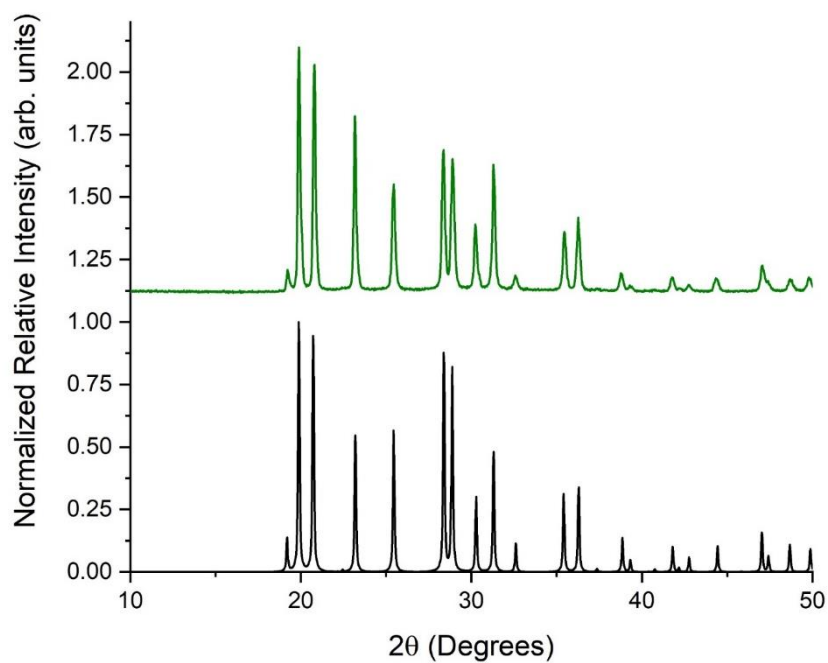
Figure A-2. Room temperature PXRD patterns of thiourea phase V sample (green) and CSD published pattern[A-R2] (black) (patterns offset for clarity).
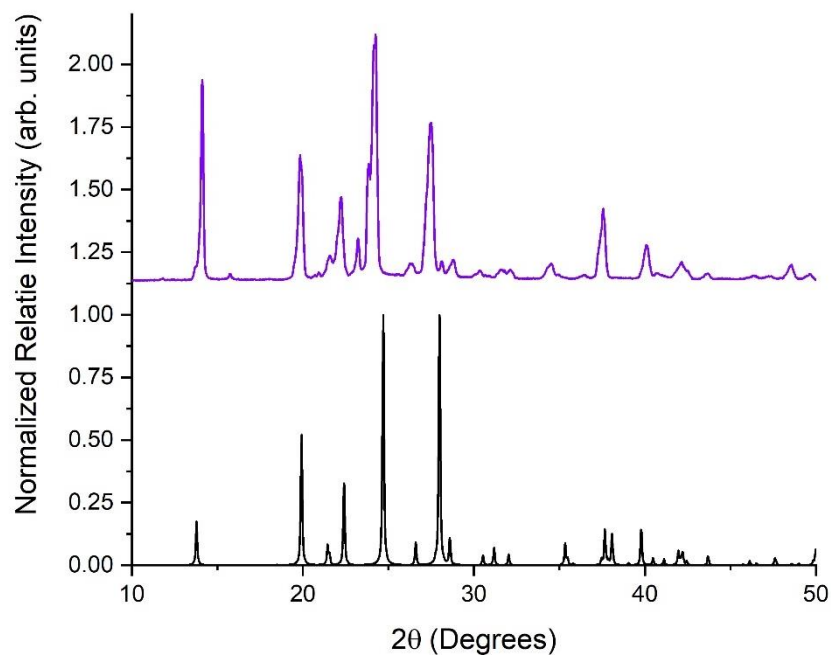
Figure A-3. Room temperature PXRD patterns of glutaric acid sample (purple) and CSD published pattern[A-R3] (black) (patterns offset for clarity).
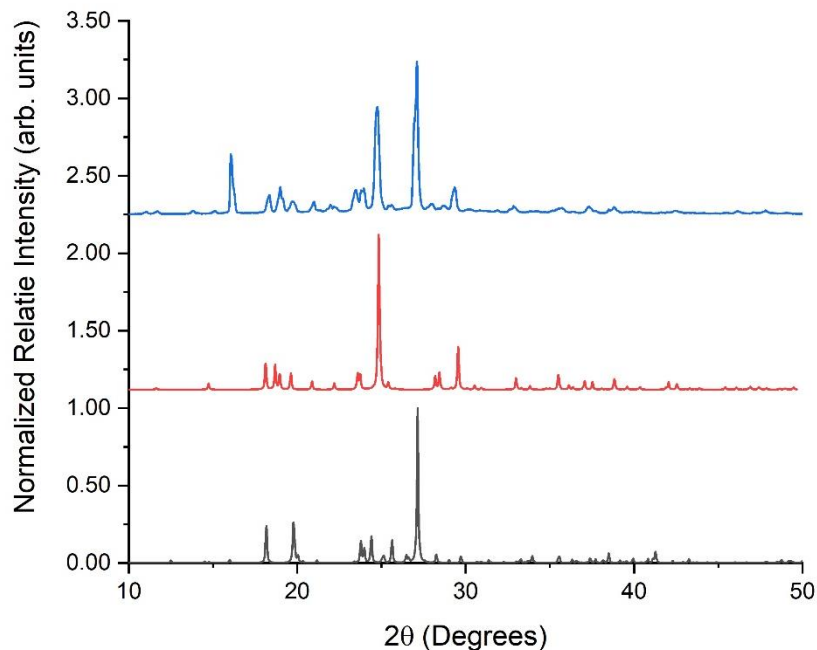
Figure A-4. Room temperature PXRD patterns of urea-glutaric acid sample (blue), CSD published pattern for urea-glutaric acid form 1[A-R4] (U:GA-I) (red), CSD published patter for urea-glutaric acid form 2[A-R5] (U:GA-II) (black) (patterns offset for clarity).
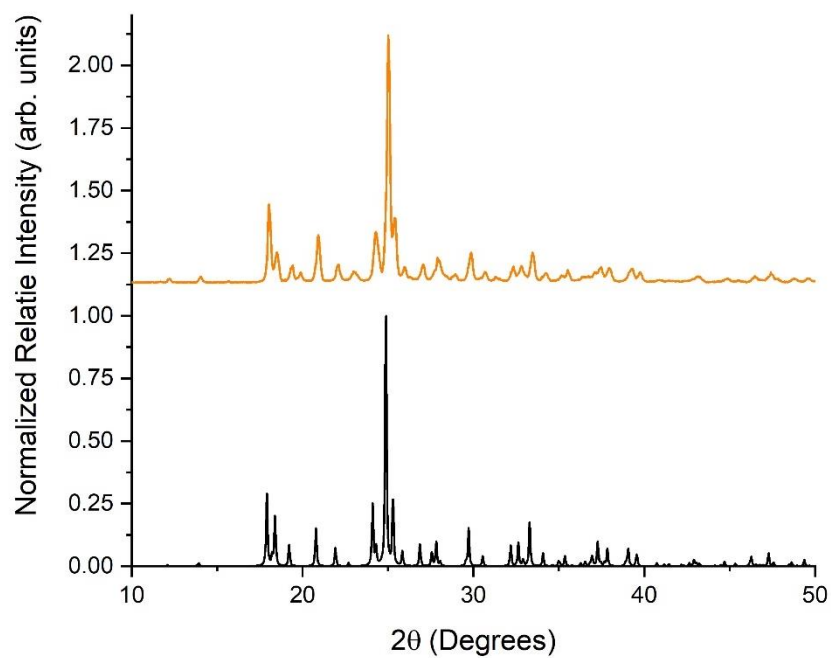
Figure A-5. Room temperature PXRD patterns of thiourea-glutaric acid sample (T:GA) (orange) and CSD published pattern[A-R6] (black) (patterns offset for clarity).
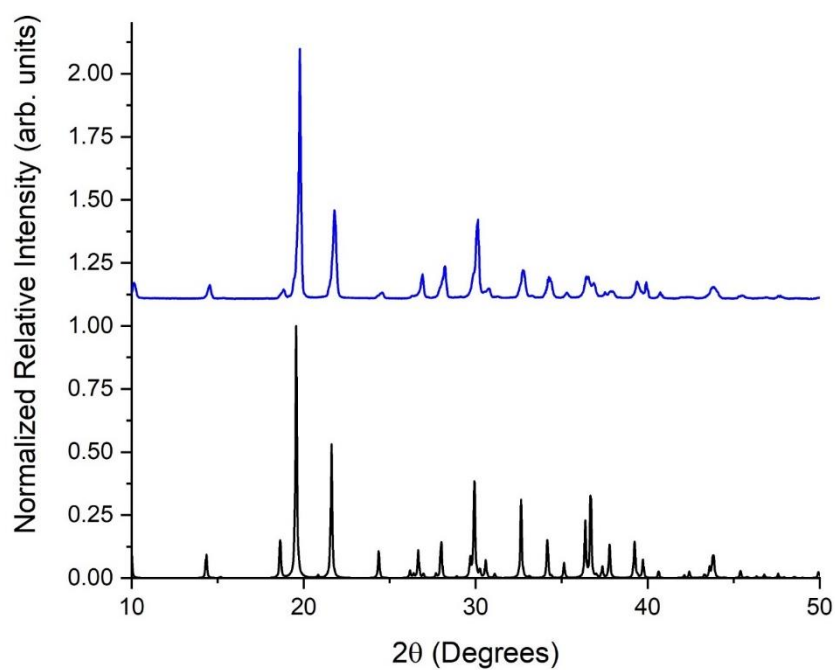
Figure A-6. PXRD patterns of DL-tartaric acid sample (blue) and CSD published pattern[A-R7] (black) (patterns offset for clarity).
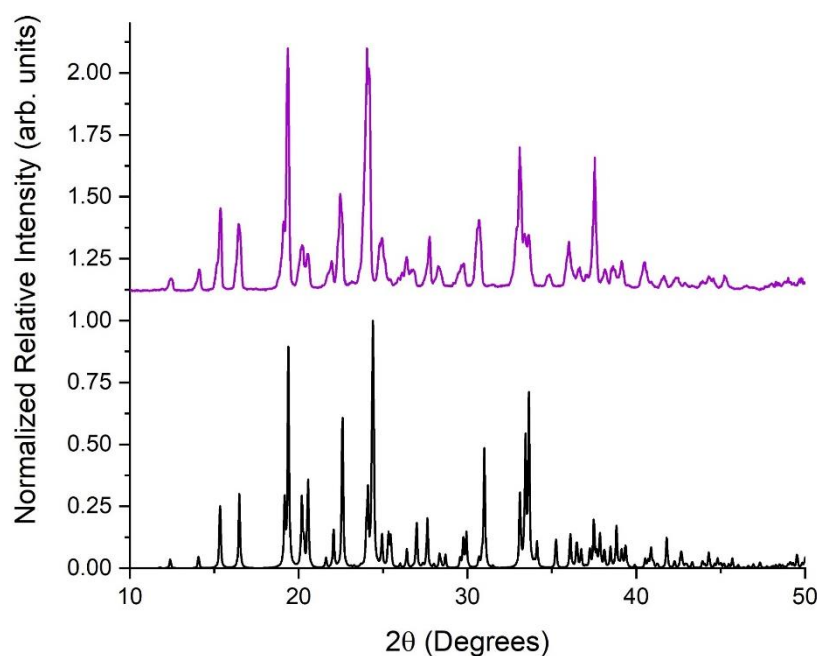
Figure A-7. PXRD patterns of urea-DL-tartaric acid sample (U:TA) (purple) and CSD published pattern[A-R8] (black) (patterns offset for clarity).

Table A-1. Solid-state DFT optimized lattice parameters for U:GA-I.

	Lattice Parameters				
	Space Group	a (Å)	b (Å)	c (Å)	β (°)
U:GA-I	P2$_1$/n	8.5575	11.6660	9.8365	116.4216

Table A-2. Solid-state DFT optimized atomic positions in fractional coordinates for the asymmetric unit cell of U:GA-I.

Atom (Atomic Number)	X/A	Y/B	Z/C
8	2.31693E-01	6.44474E-02	8.02014E-02
8	2.31333E-01	4.37418E-01	7.95047E-02
8	4.73748E-01	-4.44341E-02	1.61368E-01
8	4.73474E-01	-4.53739E-01	1.61189E-01
6	3.13156E-01	-3.56102E-02	1.05571E-01
6	3.12863E-01	-4.62535E-01	1.05215E-01
6	1.94336E-01	-1.38649E-01	5.96176E-02
6	1.94147E-01	-3.59441E-01	5.94710E-02
6	2.99192E-01	-2.49083E-01	1.10657E-01
1	3.17898E-01	1.31901E-01	1.08092E-01

1	3.17555E-01	3.69995E-01	1.07507E-01
1	9.82814E-02	-1.29039E-01	1.04681E-01
1	1.17178E-01	-3.63290E-01	-6.49341E-02
1	1.17438E-01	-1.34702E-01	-6.47970E-02
1	9.81706E-02	-3.69076E-01	1.04620E-01
1	3.97941E-01	-2.49097E-01	6.79685E-02
1	3.71652E-01	-2.49143E-01	2.35295E-01
8	4.28212E-01	2.50917E-01	1.47307E-01
7	-3.15443E-01	1.51803E-01	2.41875E-01
7	-3.15594E-01	3.50148E-01	2.40935E-01
6	-4.03807E-01	2.50955E-01	2.09538E-01
1	-3.86279E-01	7.69536E-02	2.16975E-01
1	-3.86554E-01	4.24948E-01	2.15999E-01
1	-1.82666E-01	1.47811E-01	2.92481E-01
1	-1.82816E-01	3.54237E-01	2.91884E-01

Table A-3. Solid-state DFT optimized lattice parameters for U:GA-II.

	Lattice Parameters			
	Space Group	a (Å)	b (Å)	c (Å)
U:GA-II	Pnma	15.2261	11.6669	4.9532

Table A-4. Solid-state DFT optimized atomic positions in fractional coordinates for the asymmetric unit cell of U:GA-II.

Atom (Atomic Number)	X/A	Y/B	Z/C
6	4.52981E-01	2.50000E-01	-1.93070E-01
7	4.82500E-01	3.49167E-01	-9.03495E-02
8	3.98763E-01	2.50000E-01	-3.92469E-01
1	-4.77407E-01	3.52887E-01	7.41319E-02
1	4.54818E-01	4.23749E-01	-1.61441E-01
6	-3.39655E-01	2.50000E-01	4.89189E-01
6	-3.08176E-01	3.60111E-01	-3.77166E-01
6	-3.51796E-01	4.63462E-01	4.99356E-01
8	-3.33243E-01	-4.37985E-01	-3.80060E-01
8	-4.00592E-01	4.56261E-01	3.00657E-01
1	-3.19097E-01	2.50000E-01	2.76333E-01
1	-4.11773E-01	2.50000E-01	4.87578E-01
1	-3.62735E-01	-3.70102E-01	-4.76249E-01
1	-2.36759E-01	3.71552E-01	-3.99499E-01
1	-3.21454E-01	3.61535E-01	-1.58680E-01

Table A-5. Solid-state DFT optimized lattice parameters for modified T:GA structure.

	Lattice Parameters			
	Space Group	a (Å)	b (Å)	c (Å)
T:GA	Pc2$_1$n	5.2423	12.7083	14.2058

Table A-6. Solid-state DFT optimized atomic positions in fractional coordinates for the asymmetric unit cell of the modified T:GA.

Atom (Atomic Number)	X/A	Y/B	Z/C
16	-4.86916E-01	2.27013E-01	-3.98232E-01
7	-9.04339E-02	1.35594E-01	-4.80585E-01
1	8.03389E-02	1.29697E-01	4.84789E-01
1	-1.75111E-01	6.64413E-02	-4.59837E-01
7	-9.04270E-02	3.18423E-01	-4.80593E-01
1	8.03544E-02	3.24310E-01	4.84786E-01
1	-1.75094E-01	3.87579E-01	-4.59851E-01
6	-1.98668E-01	2.27010E-01	-4.57152E-01
8	2.96467E-01	2.14719E-02	4.12110E-01
6	4.59598E-01	4.26324E-01	3.49758E-01
8	-4.13244E-01	-4.91178E-01	3.16636E-01
8	2.96483E-01	4.32567E-01	4.12083E-01
8	-4.13207E-01	-5.47822E-02	3.16686E-01
6	-4.56469E-01	3.25745E-01	3.03218E-01
1	-2.48687E-01	3.20285E-01	3.14104E-01
1	-4.80634E-01	3.36294E-01	2.26800E-01
6	4.10626E-01	2.27015E-01	3.38771E-01
1	4.12721E-01	2.27017E-01	4.16204E-01
1	2.09199E-01	2.27021E-01	3.16679E-01
6	-4.56504E-01	1.28271E-01	3.03223E-01
1	-4.80727E-01	1.17704E-01	2.26809E-01
1	-2.48714E-01	1.33731E-01	3.14086E-01
6	4.59590E-01	2.77123E-02	3.49788E-01
1	-4.67890E-01	-1.22277E-01	3.49625E-01
1	-4.67925E-01	-4.23685E-01	3.49580E-01

Table A-7. Solid-state DFT optimized lattice parameters for U:TA.

	Lattice Parameters				
	Space Group	a (Å)	b (Å)	c (Å)	β (°)
U:TA	P2$_1$	4.71973	23.55862	7.61222	100.01252

Table A-8. Solid-state DFT optimized atomic positions in fractional coordinates for the asymmetric unit cell of U:TA.

Atom (Atomic Number)	X/A	Y/B	Z/C
8	6.83536E-02	3.28010E-01	-2.04728E-01
6	9.58235E-02	3.44513E-01	-4.83944E-02
8	2.68727E-01	3.84292E-01	2.43632E-02
1	3.91608E-01	3.98167E-01	-6.61812E-02
6	-6.77805E-02	3.16709E-01	8.11992E-02
1	-1.43963E-01	3.50270E-01	1.61521E-01
8	-3.00903E-01	2.85677E-01	-7.62494E-03
1	-2.88442E-01	2.76280E-01	-1.33867E-01
6	1.37310E-01	2.77891E-01	2.08470E-01
1	2.94137E-01	3.05415E-01	2.90721E-01
8	2.65530E-01	2.36626E-01	1.14915E-01
1	4.38243E-01	2.53746E-01	8.23332E-02
6	-2.64198E-02	2.47847E-01	3.35961E-01
8	-2.88448E-02	1.95682E-01	3.48924E-01
8	-1.59086E-01	2.83252E-01	4.25341E-01
1	-2.61505E-01	2.62404E-01	-4.78976E-01
8	-3.91597E-01	-4.43924E-01	2.25957E-01
6	-3.56525E-01	-4.94832E-01	2.58777E-01
8	-2.02082E-01	4.71223E-01	1.78227E-01
1	-1.30816E-01	4.92764E-01	7.43384E-02
6	4.98547E-01	4.74963E-01	3.95888E-01
1	3.35870E-01	4.47627E-01	3.17440E-01
8	3.75643E-01	-4.83890E-01	4.93822E-01
1	2.06750E-01	4.98807E-01	-4.67705E-01
6	-2.92965E-01	4.35602E-01	-4.81506E-01
1	-2.17053E-01	4.03153E-01	4.34192E-01
8	-5.84306E-02	4.65052E-01	-3.88442E-01
1	-9.16419E-02	4.80956E-01	-2.70447E-01
6	-4.55495E-01	4.05486E-01	-3.54584E-01
8	-4.17411E-01	4.18026E-01	-1.94573E-01
8	3.62412E-01	3.68079E-01	-4.32998E-01
1	2.48857E-01	3.51276E-01	-3.42356E-01
7	3.25391E-01	1.77671E-01	-2.23380E-01
1	2.42018E-01	2.08740E-01	-1.55976E-01
1	2.64547E-01	1.36833E-01	-2.08721E-01
7	-3.78503E-01	1.49317E-01	-4.16130E-01
1	-2.32682E-01	1.60413E-01	-4.93474E-01

1	-4.16763E-01	1.07670E-01	-3.91252E-01
6	-4.87260E-01	1.91056E-01	-3.28898E-01
8	-4.15754E-01	2.42973E-01	-3.43638E-01
7	-1.08131E-01	1.10660E-01	1.93201E-02
1	-2.84978E-01	9.45775E-02	-5.72614E-02
1	-1.13401E-01	1.51165E-01	6.52992E-02
7	2.62762E-01	9.26121E-02	2.48654E-01
1	3.89454E-01	6.42451E-02	3.26721E-01
1	2.56628E-01	1.33877E-01	2.88746E-01
6	6.34125E-02	7.28150E-02	1.18075E-01
8	3.81753E-02	1.96786E-02	8.46801E-02

Table A-9. Solid-state DFT optimized lattice parameters for T:TA.

	Lattice Parameters				
	Space Group	a (Å)	b (Å)	c (Å)	β (°)
U:TA	P2$_1$	4.85260	24.36528	7.99792	99.85418

Table A-10. Solid-state DFT optimized atomic positions in fractional coordinates for the asymmetric unit cell of T:TA.

Atom (Atomic Number)	X/A	Y/B	Z/C
8	1.06172E-01	3.33552E-01	-1.44010E-01
6	1.47421E-01	3.46930E-01	7.20562E-03
8	3.24955E-01	3.84362E-01	7.76217E-02
1	4.40797E-01	3.99152E-01	-9.36594E-03
6	-5.18533E-03	3.18392E-01	1.33237E-01
1	-7.20355E-02	3.49736E-01	2.16790E-01
8	-2.46009E-01	2.90626E-01	5.07988E-02
1	-2.19816E-01	2.76342E-01	-6.17508E-02
6	1.98022E-01	2.78185E-01	2.44944E-01
1	3.64028E-01	3.02620E-01	3.22786E-01
8	3.06959E-01	2.37857E-01	1.48132E-01
1	4.74850E-01	2.53941E-01	1.12045E-01
6	3.17557E-02	2.50175E-01	3.66270E-01
8	-2.63016E-03	2.00156E-01	3.69881E-01
8	-7.60354E-02	2.86196E-01	4.59535E-01
1	-1.89255E-01	2.66065E-01	-4.59479E-01
8	-2.35813E-01	-4.48829E-01	3.67337E-01
6	-2.88396E-01	-4.97839E-01	3.51810E-01
8	-2.10088E-01	4.69591E-01	2.35834E-01

1	-1.16653E-01	4.92435E-01	1.54176E-01
6	-4.50734E-01	4.72146E-01	4.71197E-01
1	3.87607E-01	4.46799E-01	3.93248E-01
8	4.30932E-01	-4.88001E-01	-4.33757E-01
1	2.61595E-01	4.95657E-01	-3.98778E-01
6	-2.47259E-01	4.32850E-01	-4.13280E-01
1	-1.80232E-01	4.00605E-01	-4.94137E-01
8	-6.73499E-03	4.60096E-01	-3.29669E-01
1	-3.17352E-02	4.76929E-01	-2.18489E-01
6	-4.09208E-01	4.05820E-01	-2.88554E-01
8	-3.73062E-01	4.19909E-01	-1.38134E-01
8	4.10299E-01	3.69145E-01	-3.60368E-01
1	2.91781E-01	3.54624E-01	-2.74583E-01
7	3.30382E-01	1.52481E-01	-2.21562E-01
1	2.15647E-01	1.78934E-01	-1.62925E-01
1	2.54767E-01	1.13373E-01	-2.46842E-01
7	-3.82342E-01	1.42123E-01	-4.23112E-01
1	-2.42917E-01	1.58952E-01	-4.91396E-01
1	-4.28653E-01	1.01105E-01	-4.32857E-01
6	-4.99035E-01	1.74660E-01	-3.20439E-01
16	-4.34191E-01	2.43555E-01	-3.05240E-01
7	-1.27837E-01	1.37923E-01	4.37281E-02
1	-3.21473E-01	1.36311E-01	-2.96145E-02
1	-7.11733E-02	1.72434E-01	1.13971E-01
7	2.36251E-01	9.37291E-02	2.08708E-01
1	3.37283E-01	5.92381E-02	2.60060E-01
1	2.84112E-01	1.30218E-01	2.69639E-01
6	3.60308E-03	9.05501E-02	9.22150E-02
16	-1.30545E-01	2.96383E-02	4.77918E-03

Table A-11. Solid-state DFT IR-active modes with frequencies (cm-1), intensities (km/mol), and mode symmetries for U:GA-I.

Mode Label (ν)	Frequency (cm^{-1})	Intensity (km/mol)	Mode Symmetry	Mode Label (ν)	Frequency (cm^{-1})	Intensity (km/mol)	Mode Symmetry
5	27.94	0.05	Au	80	456.20	0.00	Au
6	32.57	0.00	Bu	81	497.27	0.74	Bu
10	50.65	0.01	Au	83	521.75	3.45	Au
13	58.27	0.06	Bu	84	523.47	1.61	Au
14	60.21	2.04	Bu	88	533.32	0.00	Au
16	66.30	1.82	Au	89	535.68	0.07	Bu
21	79.93	0.00	Au	91	548.12	1127.23	Bu
23	88.63	0.00	Bu	92	558.43	8.23	Au
24	88.76	0.00	Au	94	558.69	15.20	Au
25	92.05	0.01	Au	98	561.23	0.18	Bu
27	101.27	72.71	Au	100	564.62	109.13	Bu
29	101.85	49.51	Bu	103	573.42	0.01	Au
31	105.61	0.22	Bu	104	577.39	1473.45	Bu
32	108.57	9.49	Au	106	622.42	105.67	Au
33	109.08	129.40	Au	108	623.12	0.02	Bu
35	113.90	0.01	Bu	110	657.04	0.00	Bu
36	115.20	14.29	Bu	112	658.82	241.91	Au
39	122.17	14.68	Bu	113	660.13	0.00	Bu
42	137.21	0.00	Au	115	671.63	16.38	Au
45	143.32	0.00	Au	119	678.06	0.00	Au
48	160.18	17.64	Bu	120	679.35	50.26	Bu
51	164.55	0.06	Au	121	724.97	0.00	Au
53	166.44	56.31	Au	124	728.35	58.23	Bu
54	169.43	34.71	Bu	125	746.80	0.00	Au
56	172.53	0.35	Bu	128	754.26	73.42	Bu
57	183.84	0.03	Bu	129	805.57	0.01	Au
60	194.54	0.97	Au	131	810.74	156.64	Bu
62	200.82	0.03	Au	133	835.55	0.00	Bu
64	215.98	13.10	Bu	136	839.95	3.24	Au
65	231.81	0.00	Bu	137	884.96	0.03	Bu
67	237.83	259.64	Au	138	885.36	181.05	Au
70	309.23	12.75	Bu	141	917.55	32.01	Bu
72	311.30	0.11	Au	142	918.65	0.00	Au
75	320.52	0.00	Bu	145	1001.59	6.48	Bu
76	321.16	619.69	Au	147	1003.58	0.72	Au
78	452.42	143.91	Bu	149	1010.45	1149.82	Bu

151	1014.98	0.00	Au	233	1535.54	0.04	Bu
154	1024.84	184.10	Bu	235	1546.43	493.88	Au
156	1026.73	0.00	Au	237	1602.28	2689.73	Au
158	1042.94	0.00	Au	239	1638.80	7174.08	Bu
160	1050.80	22.55	Bu	240	1641.15	51.88	Bu
161	1057.03	124.29	Bu	243	1649.07	0.38	Au
163	1058.06	0.01	Au	245	1661.92	1366.68	Bu
165	1061.09	0.03	Bu	246	1664.69	0.01	Au
167	1067.75	62.85	Au	248	1668.83	1.24	Bu
170	1070.61	0.02	Bu	252	1700.65	0.00	Au
171	1077.91	49.43	Au	253	2640.05	18163.85	Au
173	1134.47	0.00	Au	255	2646.79	1.46	Bu
175	1137.31	0.92	Au	257	2776.30	3.73	Au
178	1141.18	0.04	Bu	260	2788.76	4812.05	Bu
180	1153.56	807.16	Bu	261	2977.24	68.03	Bu
182	1185.29	0.00	Bu	263	2979.59	0.03	Au
183	1188.20	844.90	Au	265	2984.39	17.36	Au
186	1228.73	0.02	Au	266	2984.57	0.07	Bu
189	1241.33	5.74	Bu	269	2995.70	0.00	Au
191	1247.11	68.20	Bu	271	2996.80	89.51	Bu
192	1248.69	0.00	Au	273	3019.74	30.72	Bu
194	1281.09	0.00	Bu	275	3020.17	0.00	Au
196	1286.27	1074.19	Au	277	3031.73	17.28	Au
198	1292.71	2003.94	Au	279	3032.11	0.02	Bu
200	1298.47	0.01	Bu	282	3046.47	0.00	Au
203	1350.72	0.12	Au	283	3046.74	74.30	Bu
204	1360.45	0.04	Bu	285	3221.22	9684.12	Au
207	1364.03	10.58	Bu	287	3228.65	0.01	Bu
208	1365.25	295.27	Au	291	3259.43	0.02	Au
209	1387.75	71.41	Au	292	3274.25	2097.89	Bu
210	1389.01	538.85	Bu	293	3466.37	4.35	Bu
211	1389.08	0.01	Au	296	3475.11	2.02	Au
213	1389.85	2.06	Bu	297	3476.67	14.37	Au
217	1439.96	12.12	Au	299	3484.40	5655.50	Bu
218	1440.32	698.11	Au				
221	1443.83	218.80	Bu				
224	1446.43	0.06	Bu				
226	1464.83	40.15	Bu				
227	1465.89	0.01	Au				
229	1501.92	398.50	Bu				
231	1517.13	0.00	Au				

Table A-12. Solid-state DFT Raman-active modes with frequencies (cm^{-1}), relative intensities (normalized to 1000), and mode symmetries for U:GA-I at 78 K.

Mode Label (v)	Frequency (cm^{-1})	Relative Intensity	Mode Symmetry	Mode Label (v)	Frequency (cm^{-1})	Relative Intensity	Mode Symmetry
4	14.87	0.17	Ag	73	317.32	9.16	Bg
7	33.61	0.17	Bg	74	319.27	0.02	Ag
8	40.18	9.86	Ag	77	451.91	0.00	Bg
9	49.30	141.77	Bg	79	455.79	93.13	Ag
11	52.95	0.21	Ag	82	499.31	45.52	Bg
12	57.25	0.04	Bg	85	523.94	2.82	Ag
15	62.73	27.35	Ag	86	527.26	0.36	Ag
17	66.48	0.05	Ag	87	529.70	0.02	Ag
18	66.51	89.27	Bg	90	536.17	12.71	Bg
19	67.17	311.20	Bg	93	558.55	0.07	Bg
20	70.26	33.40	Bg	95	559.38	35.01	Ag
22	81.38	0.01	Bg	96	559.84	30.13	Bg
26	92.39	289.23	Ag	97	560.80	0.68	Ag
28	101.81	0.26	Ag	99	561.80	0.29	Bg
30	105.60	229.21	Bg	101	566.62	5.80	Ag
34	110.46	18.61	Ag	102	572.46	0.02	Bg
37	117.97	0.17	Ag	105	621.34	0.00	Ag
38	119.76	0.07	Bg	107	622.87	77.11	Bg
40	125.54	356.18	Ag	109	656.57	0.00	Ag
41	126.35	38.43	Bg	111	657.81	5.55	Bg
43	138.61	49.63	Ag	114	671.02	5.39	Bg
44	142.70	74.32	Ag	116	673.51	0.01	Bg
46	145.06	0.04	Bg	117	675.61	7.91	Ag
47	148.78	54.15	Ag	118	676.46	0.18	Ag
49	163.32	0.04	Bg	122	726.63	20.44	Ag
50	164.54	0.00	Bg	123	727.22	0.00	Bg
52	165.09	0.01	Ag	126	747.47	4.94	Ag
55	170.48	12.17	Bg	127	752.44	0.00	Bg
58	188.25	95.76	Bg	130	810.70	0.01	Bg
59	191.57	25.84	Ag	132	817.24	6.41	Ag
61	194.80	0.14	Ag	134	837.02	0.00	Ag
63	208.07	0.00	Bg	135	838.88	7.39	Bg
66	237.81	0.00	Ag	139	886.14	1.05	Bg
68	239.87	28.17	Bg	140	887.84	0.01	Ag
69	308.59	0.00	Bg	143	920.00	187.34	Ag
71	310.12	110.76	Ag	144	920.80	0.00	Bg

146	1002.91	0.07	Bg	228	1468.39	7.40	Ag
148	1005.20	0.13	Ag	230	1502.67	166.58	Ag
150	1011.49	8.77	Ag	232	1521.68	0.00	Bg
152	1019.06	0.00	Bg	234	1540.54	0.00	Ag
153	1024.82	0.00	Bg	236	1548.91	87.50	Bg
155	1026.57	422.35	Ag	238	1610.47	0.00	Ag
157	1041.29	0.01	Bg	241	1643.44	28.71	Bg
159	1049.76	6.12	Ag	242	1647.39	0.15	Bg
162	1057.73	39.41	Ag	244	1661.78	196.94	Ag
164	1058.23	0.11	Bg	247	1665.62	0.08	Ag
166	1061.73	44.45	Bg	249	1669.75	4.87	Bg
168	1068.93	41.99	Bg	250	1680.16	0.00	Bg
169	1069.46	0.00	Ag	251	1683.71	21.17	Ag
172	1078.63	0.00	Ag	254	2643.80	0.20	Ag
174	1135.13	12.20	Ag	256	2673.13	217.84	Bg
176	1137.73	0.00	Ag	258	2777.30	780.06	Ag
177	1137.93	17.15	Bg	259	2779.09	0.07	Bg
179	1153.54	0.00	Bg	262	2978.61	1000.00	Ag
181	1183.89	10.70	Bg	264	2979.72	0.00	Bg
184	1189.04	0.00	Ag	267	2984.97	0.40	Ag
185	1226.47	33.87	Ag	268	2984.99	0.36	Bg
187	1233.14	0.00	Bg	270	2996.24	0.00	Bg
188	1240.24	2.64	Ag	272	2997.11	31.75	Ag
190	1245.07	0.01	Bg	274	3020.06	0.00	Bg
193	1276.95	41.76	Bg	276	3020.64	409.44	Ag
195	1281.10	0.00	Ag	278	3031.77	0.38	Ag
197	1291.15	0.00	Ag	280	3032.39	0.29	Bg
199	1293.99	51.70	Bg	281	3046.41	0.00	Bg
201	1340.45	29.41	Ag	284	3047.35	39.02	Ag
202	1340.88	0.00	Bg	286	3221.84	0.02	Ag
205	1362.20	0.02	Ag	288	3234.19	74.80	Bg
206	1362.34	2.31	Bg	289	3255.92	426.82	Ag
212	1389.21	1.18	Bg	290	3258.25	0.03	Bg
214	1391.21	237.84	Ag	294	3466.40	123.92	Bg
215	1392.25	0.18	Ag	295	3473.46	297.10	Ag
216	1393.92	0.00	Bg	298	3477.40	4.68	Ag
219	1440.95	0.00	Bg	300	3486.65	0.07	Bg
220	1441.46	20.64	Ag				
222	1445.66	0.01	Ag				
223	1445.67	9.47	Bg				
225	1464.54	0.00	Bg				

Table A-13. Solid-state DFT IR-active modes with frequencies (cm-1), intensities (km/mol), and mode symmetries for U:GA-II.

Mode Label (ν)	Frequency (cm⁻¹)	Intensity (km/mol)	Mode Symmetry	Mode Label (ν)	Frequency (cm⁻¹)	Intensity (km/mol)	Mode Symmetry
6	39.44	2.14	B3u	105	620.64	92.56	B3u
9	47.33	0.82	B2u	108	623.98	924.00	B1u
10	47.91	0.11	B1u	111	658.90	262.87	B3u
17	64.55	0.00	B1u	113	672.29	60.10	B3u
18	72.09	0.84	B2u	116	675.35	26.56	B1u
23	84.09	26.96	B3u	119	679.33	5.99	B2u
26	98.32	29.73	B3u	121	737.58	17.55	B1u
29	99.00	19.99	B1u	123	739.74	32.43	B2u
30	100.59	71.59	B2u	127	753.82	63.42	B2u
31	104.66	5.91	B1u	128	754.99	45.85	B1u
35	113.41	1.60	B2u	129	805.55	148.24	B2u
37	120.99	202.04	B3u	130	807.77	149.68	B1u
45	147.75	0.91	B2u	135	852.96	2.42	B3u
46	149.64	0.07	B1u	139	887.77	136.69	B3u
48	154.19	1.77	B2u	141	920.76	11.39	B2u
49	160.57	1.30	B1u	143	922.57	0.95	B1u
51	164.73	42.69	B3u	146	994.01	12.38	B3u
54	168.64	2.09	B2u	149	1002.24	996.89	B1u
55	171.03	17.91	B1u	151	1003.25	661.21	B2u
57	181.05	11.28	B3u	153	1022.83	66.55	B2u
63	212.85	9.40	B1u	154	1023.91	5.51	B1u
64	214.08	6.86	B2u	158	1049.88	21.80	B2u
66	235.28	230.83	B3u	160	1051.39	1.09	B1u
69	307.60	3.51	B2u	162	1058.17	15.03	B1u
70	307.62	10.75	B1u	163	1058.20	43.93	B2u
75	321.09	615.33	B3u	167	1067.10	48.92	B3u
77	453.35	49.82	B2u	171	1078.37	51.41	B3u
78	454.07	83.30	B1u	174	1133.22	17.49	B3u
84	526.16	15.82	B3u	179	1155.52	366.07	B2u
88	547.59	38.65	B3u	180	1159.84	230.66	B1u
91	553.53	159.18	B1u	184	1184.31	795.15	B3u
92	554.36	167.32	B2u	186	1225.03	87.23	B1u
93	555.17	1.09	B3u	188	1242.34	25.41	B2u
101	563.30	3.45	B2u	190	1244.12	15.19	B1u
102	566.76	70.01	B1u	192	1244.96	5.42	B2u
103	591.86	1658.24	B2u	198	1285.46	138.63	B3u

199	1290.23	2700.04	B3u
202	1339.46	8.41	B1u
207	1356.77	424.07	B3u
208	1360.40	56.18	B2u
212	1394.99	122.30	B1u
213	1396.22	181.45	B2u
215	1396.35	55.53	B3u
217	1440.56	707.40	B3u
220	1442.45	64.19	B1u
224	1444.18	28.52	B2u
227	1464.19	3.17	B2u
228	1464.92	9.99	B1u
229	1503.80	277.14	B2u
230	1504.86	23.39	B1u
234	1542.89	627.22	B3u
237	1602.60	2443.57	B3u
239	1639.98	2607.50	B2u
243	1653.57	1079.60	B1u
244	1654.69	0.27	B3u
246	1666.96	654.45	B2u
250	1671.87	3088.92	B1u
253	2663.58	17800.37	B3u
259	2806.71	2350.48	B2u
260	2815.07	1813.25	B1u
261	2983.27	31.56	B1u
263	2983.55	2.58	B2u
265	2988.58	25.26	B3u
270	3000.08	10.40	B2u
271	3000.15	113.63	B1u
273	3017.81	2.77	B1u
276	3018.04	29.13	B2u
278	3026.69	11.83	B3u
282	3047.95	45.51	B2u
284	3048.28	16.14	B1u
285	3213.78	9947.08	B3u
291	3268.31	1498.07	B2u
292	3268.74	566.09	B1u
297	3472.35	15.24	B3u
299	3480.42	2488.36	B2u
300	3490.19	2707.26	B1u

Table A-14. Solid-state DFT Raman-active modes with frequencies (cm^{-1}), relative intensities (normalized to 1000), and mode symmetries for U:GA-II at 78 K.

Mode Label (v)	Frequency (cm^{-1})	Relative Intensity	Mode Symmetry	Mode Label (v)	Frequency (cm^{-1})	Relative Intensity	Mode Symmetry
7	41.27	14.62	Ag	73	318.93	5.78	B2g
8	46.29	0.44	B3g	74	319.63	3.65	B1g
11	49.40	15.43	B2g	79	454.91	87.78	Ag
12	51.68	17.17	B1g	80	455.21	1.65	B3g
13	53.30	5.06	Ag	81	515.55	3.73	B1g
14	55.52	20.34	B3g	82	516.26	59.81	B2g
15	60.05	120.58	B1g	85	532.41	0.85	B1g
16	60.20	98.80	B2g	86	534.57	12.50	B2g
19	73.07	121.19	B1g	87	544.57	2.02	Ag
20	74.58	420.81	Ag	89	549.45	0.04	B3g
21	74.99	299.51	B2g	90	550.79	4.37	B2g
24	85.92	51.41	B3g	95	556.14	47.20	B1g
25	93.13	121.93	B1g	97	557.10	2.78	B3g
28	98.67	37.86	B2g	98	559.29	30.01	Ag
32	106.74	46.94	Ag	99	560.92	0.10	B3g
34	113.03	2.63	B3g	100	561.25	10.43	Ag
36	116.61	0.23	B1g	106	622.06	26.84	B1g
38	127.27	14.50	B2g	107	622.29	31.71	B2g
39	136.38	190.11	Ag	109	658.16	14.96	B2g
40	138.13	1.33	B3g	112	658.98	0.94	B1g
41	139.66	1.98	B3g	114	673.31	2.10	B2g
42	140.95	33.58	Ag	115	673.44	0.44	B1g
43	143.99	4.54	B3g	118	676.72	8.75	Ag
44	145.36	19.59	Ag	120	679.91	1.30	B3g
47	153.88	10.77	B3g	122	738.26	10.38	Ag
50	161.09	57.04	Ag	124	741.66	0.47	B3g
53	168.17	16.22	B2g	125	746.88	6.68	Ag
56	173.19	12.16	B1g	126	746.97	1.98	B3g
58	184.88	33.68	B2g	131	814.18	2.39	B3g
60	187.58	21.81	B1g	132	814.18	5.19	Ag
61	195.97	24.38	Ag	134	851.51	1.79	B1g
62	196.42	3.38	B3g	136	853.36	0.79	B2g
65	232.13	4.86	B2g	137	887.33	1.12	B2g
67	238.47	14.15	B1g	138	887.63	0.03	B1g
71	308.39	0.38	B3g	142	921.35	9.98	B3g
72	308.71	103.72	Ag	144	922.87	165.60	Ag

147	994.21	0.02	B1g	226	1463.46	11.54	Ag
148	995.35	0.00	B2g	231	1505.47	127.60	Ag
150	1002.86	8.12	Ag	232	1511.57	9.81	B3g
152	1010.60	1.52	B3g	233	1539.94	29.76	B2g
155	1025.67	11.83	B3g	236	1546.07	36.91	B1g
156	1025.81	360.42	Ag	240	1646.66	9.82	B1g
157	1049.71	0.05	B3g	241	1646.82	17.51	B2g
159	1050.64	1.24	Ag	245	1664.07	165.93	Ag
161	1057.43	21.32	Ag	247	1667.28	2.80	B1g
164	1058.34	10.77	B3g	248	1668.64	15.00	B3g
165	1061.36	29.88	B2g	249	1670.56	0.54	B2g
166	1061.66	16.09	B1g	251	1683.01	12.20	Ag
168	1067.31	23.58	B2g	252	1684.26	0.08	B3g
170	1068.22	13.55	B1g	254	2668.43	76.78	B2g
173	1133.14	4.19	B2g	256	2694.31	121.07	B1g
176	1133.70	4.73	B1g	257	2792.97	24.05	B3g
177	1136.64	7.64	Ag	258	2793.80	687.28	Ag
178	1136.75	5.33	B3g	262	2983.41	2.85	B3g
181	1178.20	9.78	B1g	264	2984.31	1000.00	Ag
183	1183.94	2.17	B2g	266	2988.64	1.12	B2g
185	1221.41	19.52	Ag	268	2988.87	0.09	B1g
187	1236.80	0.00	B3g	269	3000.06	13.74	B3g
189	1243.30	5.05	Ag	272	3000.18	49.67	Ag
191	1244.75	0.03	B3g	274	3017.91	307.16	Ag
193	1281.82	16.62	B1g	275	3018.00	0.53	B3g
195	1284.72	28.70	B1g	277	3026.60	0.08	B2g
197	1285.34	32.00	B2g	280	3026.73	0.20	B1g
200	1290.86	5.61	B2g	281	3047.94	1.64	Ag
201	1338.87	23.56	Ag	283	3048.02	1.44	B3g
203	1354.69	9.91	B3g	287	3220.34	20.67	B2g
204	1354.96	0.44	B1g	288	3225.76	45.11	B1g
206	1356.42	1.43	B2g	289	3247.68	358.28	Ag
209	1392.86	23.82	Ag	290	3248.33	17.77	B3g
210	1393.50	2.51	B1g	293	3462.22	48.90	B2g
214	1396.27	0.07	B2g	294	3462.42	54.10	B1g
216	1396.43	124.37	B3g	295	3470.08	159.50	Ag
219	1442.17	8.17	B2g	296	3470.39	75.45	B3g
221	1442.50	11.74	Ag				
222	1442.68	3.37	B1g				
223	1443.98	4.99	B3g				
225	1462.62	0.51	B3g				

Table A-15. Solid-state DFT IR-active modes with frequencies (cm-1), intensities (km/mol), and mode symmetries for T:GA.

Mode Label (ν)	Frequency (cm⁻¹)	Intensity (km/mol)	Mode Symmetry	Mode Label (ν)	Frequency (cm⁻¹)	Intensity (km/mol)	Mode Symmetry
5	42.29	0.00	A1	53	155.15	3.77	A1
6	44.84	0.00	B1	55	157.95	0.00	B2
7	44.95	0.00	B2	57	161.17	12.27	B1
9	48.86	0.82	B1	58	164.26	0.01	B1
10	51.25	0.42	B2	59	168.23	6.51	B2
11	53.98	5.43	A1	60	168.26	0.00	A1
12	54.55	0.30	A1	61	178.70	0.00	A1
13	56.13	0.00	B1	63	193.59	29.71	B2
15	59.37	0.00	B2	64	199.86	10.53	B1
16	60.56	0.00	B2	65	210.72	146.16	A1
19	83.52	0.69	B1	67	212.50	0.00	B2
20	85.54	0.00	A1	68	213.44	0.00	B1
21	90.42	22.57	A1	69	271.07	0.00	B2
23	92.34	0.00	B1	70	271.18	0.00	B1
24	92.68	0.00	A1	71	271.79	531.35	A1
25	95.74	1.10	B2	73	296.09	0.13	B1
26	98.51	58.15	B1	74	297.52	0.37	B2
27	99.37	0.00	B2	76	299.32	0.01	A1
30	101.56	0.01	B1	77	439.19	27.63	A1
31	103.71	75.32	A1	79	439.79	0.00	B2
33	105.63	0.01	A1	80	439.97	0.00	B1
34	108.82	9.64	B1	81	453.83	43.39	B1
35	109.30	8.48	B2	83	456.69	1.38	B2
36	109.36	0.04	A1	84	457.17	0.01	A1
37	110.63	1.32	B2	86	485.83	0.00	A1
38	110.88	0.56	B2	87	487.65	110.54	B2
39	110.96	0.04	B1	88	487.78	0.25	B1
40	114.11	0.00	B1	90	533.27	0.00	B1
42	116.77	0.00	B2	91	534.04	17.37	A1
45	128.52	40.54	A1	92	535.50	0.00	B2
46	128.90	5.36	A1	93	538.99	20.20	A1
47	132.29	32.63	B2	94	539.25	0.00	B2
48	133.73	1.58	B1	96	545.64	0.01	B1
49	144.60	6.15	A1	97	552.48	11.42	B2
51	151.20	0.00	B1	98	552.64	34.97	B1
52	154.02	0.00	B2	99	552.79	0.00	A1

101	573.50	0.00	B2	156	928.39	2.85	B2
102	573.71	0.00	B1	157	1041.98	0.02	B1
103	578.03	126.05	A1	158	1042.01	0.00	B2
105	594.99	0.01	A1	159	1049.37	42.46	A1
107	612.56	1014.54	B1	161	1049.98	100.29	B2
108	617.01	16.81	B2	162	1049.99	0.20	A1
110	619.93	0.00	A1	163	1050.09	32.40	B1
111	622.73	1167.45	B1	165	1061.53	0.00	B2
112	640.58	0.00	B1	166	1061.60	0.00	B1
113	640.67	0.00	B2	167	1061.62	13.06	A1
115	641.06	248.26	A1	169	1069.01	0.00	A1
116	652.50	781.70	B2	170	1069.12	68.46	B2
117	664.90	47.61	B2	171	1070.41	26.07	B1
118	665.99	0.01	A1	173	1100.65	0.02	A1
119	670.71	3.19	B1	175	1102.58	104.10	B1
121	675.12	0.00	B1	176	1104.01	169.72	B2
122	675.17	0.02	B2	178	1139.11	0.00	B1
123	687.77	3.03	A1	179	1139.28	0.00	B2
126	714.88	0.02	A1	180	1139.36	10.01	A1
127	716.74	316.93	B2	182	1164.08	0.00	B1
128	717.59	23.60	B1	183	1175.53	1900.77	A1
129	753.60	0.00	A1	184	1175.86	0.00	B2
130	753.70	35.79	B2	185	1193.46	0.01	A1
131	756.22	46.56	B1	186	1199.77	118.65	B2
134	800.53	0.00	A1	188	1231.79	37.39	B1
135	807.13	372.47	B1	190	1253.96	0.01	B1
136	812.87	39.21	B2	191	1257.28	1.90	A1
137	835.61	335.14	B1	192	1257.42	1.83	B2
138	836.90	574.33	B2	193	1258.05	2670.73	A1
139	838.46	0.26	B1	194	1258.33	0.02	B2
140	840.25	0.00	A1	196	1258.57	0.28	B1
142	843.19	0.03	B2	198	1280.64	0.00	B1
144	844.46	14.54	A1	199	1281.05	0.00	B2
145	851.39	7.03	A1	200	1281.17	0.13	A1
147	855.93	0.02	B2	201	1308.35	41.33	B2
148	858.04	0.00	B1	202	1310.72	0.09	A1
149	876.82	0.01	B1	203	1310.87	146.83	B1
151	878.07	221.22	A1	205	1341.55	11.78	A1
152	878.27	0.02	B2	206	1341.64	0.00	B2
153	927.71	0.01	A1	208	1342.49	0.00	B1
155	928.04	0.50	B1	209	1349.41	0.06	A1

210	1352.42	371.46	B2	265	2980.47	6.89	A1
211	1352.42	31.42	B1	266	2980.50	0.00	B2
213	1385.81	0.05	B1	268	2980.81	0.00	B1
215	1389.94	1.03	B2	270	2986.67	151.61	B2
216	1391.19	109.42	A1	271	2986.75	19.89	B1
217	1391.27	178.33	B2	272	2986.96	0.00	A1
218	1391.34	0.98	A1	273	2999.66	0.71	B2
219	1394.56	177.60	B1	275	2999.83	4.11	B1
221	1402.65	914.17	A1	276	2999.87	0.00	A1
222	1403.02	0.17	B2	278	3016.28	0.00	B2
224	1413.85	61.06	B1	279	3016.31	0.00	B1
226	1415.32	6.95	B1	280	3016.37	12.69	A1
227	1419.60	0.37	A1	281	3030.50	20.46	B2
228	1420.13	109.05	B2	283	3030.59	0.01	A1
230	1462.33	8.13	B2	284	3030.68	5.94	B1
231	1463.60	0.00	A1	285	3254.45	8664.06	A1
232	1463.78	18.82	B1	287	3268.65	0.00	B2
233	1532.77	0.01	B2	288	3273.26	0.00	B1
234	1532.79	216.89	A1	289	3290.48	0.00	A1
236	1535.29	0.02	B1	290	3291.94	22.75	B2
237	1608.43	2489.34	A1	292	3299.77	62.53	B1
239	1624.02	0.25	B2	293	3404.84	0.25	B2
240	1627.98	0.71	B1	294	3404.88	0.17	B1
241	1637.10	1167.45	B1	295	3406.72	0.03	A1
242	1640.84	728.03	B2	297	3417.11	258.61	A1
243	1648.00	0.11	A1	299	3419.83	2232.43	B1
246	1657.34	1.87	A1	300	3426.82	3821.89	B2
247	1664.66	1436.47	B1				
248	1672.55	1725.48	B2				
249	1676.12	0.20	A1				
250	1677.12	0.08	B1				
252	1681.54	0.46	B2				
253	2801.74	24836.46	A1				
254	2806.93	0.02	B2				
256	2840.08	0.07	B1				
258	2907.75	0.17	A1				
259	2925.57	2126.84	B1				
260	2927.18	285.61	B2				
261	2964.46	111.97	B2				
262	2964.53	0.02	B1				
264	2964.91	0.01	A1				

Table A-16. Solid-state DFT Raman-active modes with frequencies (cm^{-1}), relative intensities (normalized to 1000), and mode symmetries for T:GA at 78 K.

Mode Label (v)	Frequency (cm^{-1})	Relative Intensity	Mode Symmetry	Mode Label (v)	Frequency (cm^{-1})	Relative Intensity	Mode Symmetry
4	27.07	0.02	A2	40	114.11	43.43	B1
5	42.29	722.30	A1	41	116.52	8.91	A2
6	44.84	59.64	B1	42	116.77	2.90	B2
7	44.95	34.08	B2	43	124.93	1.23	A2
8	47.12	0.01	A2	44	125.93	0.00	A2
9	48.86	0.00	B1	45	128.52	8.83	A1
10	51.25	0.01	B2	46	128.90	67.68	A1
11	53.98	1.71	A1	47	132.29	0.00	B2
12	54.55	30.88	A1	48	133.73	0.00	B1
13	56.13	3.83	B1	49	144.60	0.01	A1
14	56.71	18.92	A2	50	145.66	0.00	A2
15	59.37	0.27	B2	51	151.20	15.39	B1
16	60.56	25.19	B2	52	154.02	7.39	B2
17	64.42	52.57	A2	53	155.15	0.00	A1
18	68.21	0.00	A2	54	157.91	1.39	A2
19	83.52	0.00	B1	55	157.95	90.49	B2
20	85.54	89.56	A1	56	158.23	0.12	A2
21	90.42	0.04	A1	57	161.17	0.04	B1
22	91.80	177.02	A2	58	164.26	49.90	B1
23	92.34	211.27	B1	59	168.23	0.04	B2
24	92.68	35.26	A1	60	168.26	27.40	A1
25	95.74	0.09	B2	61	178.70	30.51	A1
26	98.51	0.04	B1	62	187.33	0.00	A2
27	99.37	158.33	B2	63	193.59	0.00	B2
28	100.11	0.00	A2	64	199.86	0.00	B1
29	101.13	4.51	A2	65	210.72	0.00	A1
30	101.56	112.92	B1	66	211.19	0.00	A2
31	103.71	0.25	A1	67	212.50	2.81	B2
32	104.68	52.45	A2	68	213.44	5.33	B1
33	105.63	78.20	A1	69	271.07	6.68	B2
34	108.82	0.03	B1	70	271.18	5.45	B1
35	109.30	0.04	B2	71	271.79	0.00	A1
36	109.36	568.79	A1	72	272.01	0.00	A2
37	110.63	1.28	B2	73	296.09	0.00	B1
38	110.88	3.56	B2	74	297.52	0.00	B2
39	110.96	0.01	B1	75	297.99	0.71	A2

76	299.32	77.93	A1	117	664.90	0.00	B2
77	439.19	0.02	A1	118	665.99	5.19	A1
78	439.26	0.00	A2	119	670.71	0.00	B1
79	439.79	13.70	B2	120	672.22	0.09	A2
80	439.97	16.39	B1	121	675.12	0.13	B1
81	453.83	0.00	B1	122	675.17	5.53	B2
82	455.42	2.64	A2	123	687.77	0.35	A1
83	456.69	0.00	B2	124	696.30	0.00	A2
84	457.17	76.18	A1	125	714.61	1.58	A2
85	485.73	2.58	A2	126	714.88	206.91	A1
86	485.83	69.07	A1	127	716.74	0.00	B2
87	487.65	0.00	B2	128	717.59	0.00	B1
88	487.78	0.00	B1	129	753.60	3.26	A1
89	532.14	0.00	A2	130	753.70	0.00	B2
90	533.27	0.02	B1	131	756.22	0.00	B1
91	534.04	0.00	A1	132	757.42	9.17	A2
92	535.50	6.43	B2	133	800.29	6.70	A2
93	538.99	0.00	A1	134	800.53	6.04	A1
94	539.25	0.12	B2	135	807.13	0.00	B1
95	544.99	0.00	A2	136	812.87	0.00	B2
96	545.64	6.22	B1	137	835.61	0.00	B1
97	552.48	0.00	B2	138	836.90	0.00	B2
98	552.64	0.00	B1	139	838.46	0.78	B1
99	552.79	3.78	A1	140	840.25	11.35	A1
100	553.43	0.18	A2	141	840.86	0.00	A2
101	573.50	55.09	B2	142	843.19	0.39	B2
102	573.71	0.06	B1	143	844.00	0.10	A2
103	578.03	0.03	A1	144	844.46	0.00	A1
104	579.25	0.00	A2	145	851.39	0.00	A1
105	594.99	9.29	A1	146	855.08	0.00	A2
106	598.64	32.35	A2	147	855.93	11.40	B2
107	612.56	0.00	B1	148	858.04	11.96	B1
108	617.01	0.00	B2	149	876.82	0.05	B1
109	619.65	0.29	A2	150	877.08	0.00	A2
110	619.93	0.55	A1	151	878.07	0.01	A1
111	622.73	0.00	B1	152	878.27	0.68	B2
112	640.58	2.80	B1	153	927.71	91.46	A1
113	640.67	5.62	B2	154	927.85	9.69	A2
114	640.73	0.00	A2	155	928.04	0.00	B1
115	641.06	0.01	A1	156	928.39	0.00	B2
116	652.50	0.00	B2	157	1041.98	13.97	B1

158	1042.01	25.07	B2	199	1281.05	10.94	B2
159	1049.37	0.01	A1	200	1281.17	0.00	A1
160	1049.70	0.30	A2	201	1308.35	0.00	B2
161	1049.98	0.00	B2	202	1310.72	6.04	A1
162	1049.99	2.79	A1	203	1310.87	0.00	B1
163	1050.09	0.00	B1	204	1313.58	6.20	A2
164	1050.61	0.01	A2	205	1341.55	0.00	A1
165	1061.53	5.74	B2	206	1341.64	0.26	B2
166	1061.60	2.56	B1	207	1342.35	0.00	A2
167	1061.62	0.00	A1	208	1342.49	0.38	B1
168	1061.67	0.00	A2	209	1349.41	9.22	A1
169	1069.01	2.41	A1	210	1352.42	0.00	B2
170	1069.12	0.00	B2	211	1352.42	0.00	B1
171	1070.41	0.00	B1	212	1354.64	17.57	A2
172	1070.68	2.23	A2	213	1385.81	5.14	B1
173	1100.65	53.54	A1	214	1385.86	0.00	A2
174	1100.98	5.29	A2	215	1389.94	0.70	B2
175	1102.58	0.00	B1	216	1391.19	0.32	A1
176	1104.01	0.00	B2	217	1391.27	0.00	B2
177	1139.02	0.00	A2	218	1391.34	20.39	A1
178	1139.11	2.54	B1	219	1394.56	0.00	B1
179	1139.28	0.72	B2	220	1395.74	74.73	A2
180	1139.36	0.00	A1	221	1402.65	0.00	A1
181	1163.98	0.00	A2	222	1403.02	0.49	B2
182	1164.08	17.70	B1	223	1411.75	0.39	A2
183	1175.53	0.00	A1	224	1413.85	0.47	B1
184	1175.86	3.07	B2	225	1414.74	0.03	A2
185	1193.46	8.21	A1	226	1415.32	4.07	B1
186	1199.77	0.00	B2	227	1419.60	20.56	A1
187	1216.83	0.16	A2	228	1420.13	0.00	B2
188	1231.79	0.00	B1	229	1462.23	4.13	A2
189	1253.72	0.00	A2	230	1462.33	0.00	B2
190	1253.96	4.37	B1	231	1463.60	5.80	A1
191	1257.28	2.40	A1	232	1463.78	0.00	B1
192	1257.42	0.00	B2	233	1532.77	6.72	B2
193	1258.05	0.00	A1	234	1532.79	0.00	A1
194	1258.33	7.39	B2	235	1533.25	0.00	A2
195	1258.42	1.49	A2	236	1535.29	7.51	B1
196	1258.57	0.00	B1	237	1608.43	0.00	A1
197	1280.42	0.00	A2	238	1609.07	0.00	A2
198	1280.64	8.22	B1	239	1624.02	7.77	B2

240	1627.98	1.50	B1	281	3030.50	0.00	B2
241	1637.10	0.00	B1	282	3030.59	1.02	A2
242	1640.84	0.00	B2	283	3030.59	4.01	A1
243	1648.00	40.63	A1	284	3030.68	0.00	B1
244	1648.30	8.32	A2	285	3254.45	0.00	A1
245	1656.66	0.00	A2	286	3255.39	0.00	A2
246	1657.34	0.03	A1	287	3268.65	0.94	B2
247	1664.66	0.00	B1	288	3273.26	2.02	B1
248	1672.55	0.00	B2	289	3290.48	222.73	A1
249	1676.12	83.94	A1	290	3291.94	0.00	B2
250	1677.12	1.96	B1	291	3292.05	7.63	A2
251	1680.08	4.17	A2	292	3299.77	0.00	B1
252	1681.54	0.36	B2	293	3404.84	46.28	B2
253	2801.74	0.01	A1	294	3404.88	45.05	B1
254	2806.93	13.23	B2	295	3406.72	127.60	A1
255	2827.56	0.00	A2	296	3407.05	38.08	A2
256	2840.08	117.87	B1	297	3417.11	0.01	A1
257	2904.53	6.57	A2	298	3419.47	0.00	A2
258	2907.75	1000.00	A1	299	3419.83	0.00	B1
259	2925.57	0.00	B1	300	3426.82	0.00	B2
260	2927.18	0.00	B2				
261	2964.46	0.00	B2				
262	2964.53	0.00	B1				
263	2964.63	17.06	A2				
264	2964.91	452.91	A1				
265	2980.47	0.00	A1				
266	2980.50	4.34	B2				
267	2980.79	0.00	A2				
268	2980.81	1.45	B1				
269	2986.60	10.85	A2				
270	2986.67	0.00	B2				
271	2986.75	0.00	B1				
272	2986.96	72.85	A1				
273	2999.66	0.00	B2				
274	2999.69	0.01	A2				
275	2999.83	0.00	B1				
276	2999.87	201.67	A1				
277	3016.24	0.00	A2				
278	3016.28	0.19	B2				
279	3016.31	0.92	B1				
280	3016.37	0.00	A1				

Table A-17. Solid-state DFT IR-active modes with frequencies (cm^{-1}), intensities (km/mol), and mode symmetries for U:TA.

Mode Label (ν)	Frequency (cm^{-1})	Intensity (km/mol)	Mode Symmetry	Mode Label (ν)	Frequency (cm^{-1})	Intensity (km/mol)	Mode Symmetry
4	23.17	0.31	A	40	135.55	0.04	A
5	30.90	0.42	A	41	141.07	22.34	B
6	33.35	0.14	A	42	141.59	2.24	A
7	37.22	1.74	B	43	144.57	15.89	B
8	39.63	0.00	B	44	145.06	7.38	A
9	48.14	0.62	A	45	148.89	5.63	B
10	49.27	2.59	B	46	150.10	0.36	A
11	55.49	6.20	B	47	163.20	24.02	B
12	55.93	6.72	A	48	165.59	0.03	A
13	64.86	3.74	A	49	167.92	14.14	B
14	70.48	9.04	B	50	168.72	16.29	A
15	74.22	11.01	B	51	179.04	0.28	A
16	78.89	0.24	A	52	181.12	6.13	B
17	83.37	0.00	A	53	193.11	8.42	A
18	86.05	0.01	A	54	194.71	8.32	B
19	87.92	1.47	B	55	197.77	7.57	A
20	90.57	9.52	B	56	199.81	18.06	B
21	92.18	28.72	B	57	204.53	0.29	A
22	95.10	0.16	A	58	205.49	91.83	B
23	99.59	1.89	B	59	220.14	0.93	A
24	101.25	1.52	A	60	220.16	6.76	B
25	108.28	0.17	A	61	233.46	8.28	A
26	108.66	0.54	A	62	233.92	72.26	B
27	108.70	21.63	B	63	239.82	0.50	B
28	111.12	2.53	B	64	240.14	3.07	A
29	113.40	0.79	A	65	245.95	41.31	A
30	114.46	15.73	B	66	247.07	76.11	B
31	116.44	18.55	B	67	257.44	38.25	A
32	118.44	1.16	A	68	261.01	94.59	B
33	119.79	10.32	A	69	286.51	332.84	B
34	121.13	42.12	B	70	288.43	7.58	A
35	126.33	1.93	A	71	300.07	2.20	A
36	126.55	17.75	B	72	300.73	4.08	B
37	129.30	31.48	B	73	343.57	31.09	B
38	131.35	2.41	A	74	344.98	0.47	A
39	132.77	6.97	B	75	352.61	5.49	A

76	353.84	135.31	B	117	666.62	0.53	A
77	387.28	7.82	A	118	667.06	1.19	B
78	387.70	9.56	B	119	678.11	104.82	A
79	403.25	37.96	A	120	679.94	265.91	B
80	404.00	28.45	B	121	688.24	85.44	A
81	454.60	49.81	A	122	688.87	128.52	B
82	455.47	931.45	B	123	735.04	33.64	B
83	470.03	14.82	B	124	735.38	46.95	A
84	471.12	13.74	A	125	744.06	0.10	A
85	477.48	157.17	A	126	746.52	3.63	B
86	484.80	192.40	B	127	751.93	115.22	B
87	491.94	90.87	A	128	753.75	0.56	A
88	492.81	853.24	B	129	757.94	0.22	A
89	503.17	139.50	B	130	759.74	35.97	B
90	504.23	5.33	A	131	762.76	12.95	B
91	512.77	398.91	B	132	762.84	101.97	A
92	517.15	31.44	A	133	771.01	88.33	A
93	526.03	27.84	A	134	772.29	132.55	B
94	531.31	17.98	B	135	797.20	8.25	A
95	538.64	200.25	B	136	797.73	147.65	B
96	538.93	9.20	A	137	811.30	189.93	A
97	547.31	102.72	A	138	813.69	78.39	B
98	549.13	139.66	B	139	819.50	6.62	B
99	558.23	1.96	A	140	819.58	7.53	A
100	558.42	105.30	B	141	825.82	43.07	A
101	563.78	29.43	A	142	826.29	25.89	B
102	563.79	28.19	B	143	857.73	17.51	B
103	569.12	0.99	A	144	857.82	0.00	A
104	569.27	272.59	B	145	860.61	2.75	A
105	581.28	36.93	A	146	860.84	19.12	B
106	582.17	245.84	B	147	867.06	85.18	A
107	594.97	41.01	A	148	868.30	7.47	B
108	595.47	92.33	B	149	900.14	5.26	A
109	599.95	36.11	A	150	900.46	0.95	B
110	600.66	43.97	B	151	903.18	47.76	A
111	601.85	9.99	A	152	903.45	112.57	B
112	602.05	7.35	B	153	967.62	4.28	A
113	615.44	1.23	A	154	967.68	49.48	B
114	615.80	62.14	B	155	972.96	2.72	A
115	655.78	94.74	A	156	972.96	15.52	B
116	656.89	27.49	B	157	994.69	85.63	A

158	995.54	85.37	B	199	1283.31	183.92	A
159	1011.19	39.76	B	200	1283.99	885.29	B
160	1011.32	15.67	A	201	1293.88	380.19	A
161	1015.89	202.34	B	202	1295.79	1027.41	B
162	1015.95	1.68	A	203	1301.14	471.71	A
163	1020.39	110.45	B	204	1304.88	207.94	B
164	1020.53	13.88	A	205	1309.90	44.01	A
165	1030.58	253.51	A	206	1310.51	175.43	B
166	1032.89	720.06	B	207	1315.14	520.53	A
167	1043.60	8.20	A	208	1320.52	575.62	B
168	1043.82	7.56	B	209	1356.36	31.80	B
169	1068.24	19.47	A	210	1357.41	1.01	A
170	1068.30	30.11	B	211	1366.39	39.25	A
171	1070.46	14.85	A	212	1368.56	29.91	B
172	1070.49	123.79	B	213	1438.47	360.38	A
173	1074.98	4.85	A	214	1441.23	298.80	B
174	1075.02	412.55	B	215	1444.67	35.52	A
175	1105.08	716.47	A	216	1445.30	238.42	B
176	1109.26	68.46	B	217	1449.47	181.89	B
177	1112.39	253.75	A	218	1450.06	2.03	A
178	1116.18	60.23	B	219	1462.76	196.94	A
179	1118.56	5.71	A	220	1463.57	278.92	B
180	1119.32	451.05	B	221	1468.50	24.27	B
181	1137.56	13.57	A	222	1468.77	1.59	A
182	1137.80	44.54	B	223	1470.27	8.84	A
183	1148.64	100.36	A	224	1470.53	94.64	B
184	1149.52	28.89	B	225	1482.03	47.21	A
185	1189.65	11.09	A	226	1482.66	274.62	B
186	1189.74	28.66	B	227	1492.04	168.39	A
187	1201.39	13.61	B	228	1493.17	283.07	B
188	1201.40	10.75	A	229	1522.24	105.28	A
189	1225.73	7.44	A	230	1522.81	437.12	B
190	1225.81	200.05	B	231	1550.63	1030.62	A
191	1237.25	39.09	A	232	1557.36	84.57	B
192	1237.43	206.20	B	233	1581.16	91.47	A
193	1246.31	302.22	A	234	1581.88	1026.00	B
194	1248.35	220.30	B	235	1601.01	301.16	A
195	1254.52	19.53	A	236	1602.93	20.88	B
196	1254.73	62.95	B	237	1622.06	58.45	A
197	1271.55	0.78	A	238	1622.40	1273.95	B
198	1271.80	87.83	B	239	1633.82	19.59	B

240	1633.94	27.33	A		281	3448.79	462.05	A
241	1644.85	96.20	A		282	3449.90	1177.30	B
242	1645.22	237.76	B		283	3481.79	1569.18	A
243	1669.94	3358.70	A		284	3487.56	303.86	B
244	1689.15	2163.05	B		285	3545.47	232.54	A
245	1699.09	419.04	A		286	3546.16	276.27	B
246	1705.48	229.86	B		287	3561.02	1545.82	A
247	1705.90	151.45	A		288	3567.42	265.20	B
248	1712.76	295.50	B					
249	2153.38	937.87	A					
250	2158.72	7614.21	B					
251	2437.22	883.66	A					
252	2441.59	6664.03	B					
253	2564.13	280.40	A					
254	2565.37	1299.93	B					
255	2709.23	2863.16	A					
256	2722.27	10207.23	B					
257	2956.30	42.82	B					
258	2956.36	0.07	A					
259	2974.05	28.09	B					
260	2974.38	1.34	A					
261	2982.95	1022.17	A					
262	2987.56	1794.95	B					
263	3005.39	48.00	B					
264	3005.57	28.17	A					
265	3014.22	70.32	A					
266	3014.69	380.70	B					
267	3186.29	626.49	A					
268	3188.62	3156.71	B					
269	3212.88	125.78	A					
270	3213.46	2614.82	B					
271	3270.16	489.26	A					
272	3272.02	1657.75	B					
273	3293.01	43.43	A					
274	3293.26	1782.93	B					
275	3347.68	14.37	A					
276	3347.81	1168.82	B					
277	3427.26	193.61	B					
278	3427.33	178.22	A					
279	3432.25	203.20	A					
280	3432.94	58.66	B					

Table A-18. Solid-state DFT Raman-active modes with frequencies (cm^{-1}), relative intensities (normalized to 1000), and mode symmetries for U:TA at 78 K.

Mode Label (v)	Frequency (cm^{-1})	Relative Intensity	Mode Symmetry	Mode Label (v)	Frequency (cm^{-1})	Relative Intensity	Mode Symmetry
4	23.17	49.52	A	40	135.55	45.09	A
5	30.90	96.06	A	41	141.07	150.35	B
6	33.35	118.77	A	42	141.59	153.30	A
7	37.22	7.89	B	43	144.57	104.59	B
8	39.63	181.23	B	44	145.06	167.52	A
9	48.14	161.12	A	45	148.89	40.03	B
10	49.27	407.69	B	46	150.10	43.11	A
11	55.49	133.36	B	47	163.20	18.39	B
12	55.93	63.29	A	48	165.59	26.49	A
13	64.86	140.14	A	49	167.92	29.81	B
14	70.48	174.16	B	50	168.72	11.62	A
15	74.22	204.99	B	51	179.04	17.05	A
16	78.89	231.45	A	52	181.12	3.52	B
17	83.37	485.69	A	53	193.11	55.56	A
18	86.05	59.20	A	54	194.71	14.07	B
19	87.92	274.16	B	55	197.77	44.21	A
20	90.57	50.69	B	56	199.81	38.38	B
21	92.18	282.98	B	57	204.53	3.81	A
22	95.10	260.02	A	58	205.49	57.99	B
23	99.59	243.53	B	59	220.14	59.61	A
24	101.25	101.74	A	60	220.16	99.61	B
25	108.28	110.96	A	61	233.46	10.66	A
26	108.66	174.59	A	62	233.92	21.42	B
27	108.70	121.59	B	63	239.82	17.54	B
28	111.12	71.62	B	64	240.14	60.77	A
29	113.40	340.85	A	65	245.95	3.06	A
30	114.46	42.58	B	66	247.07	12.56	B
31	116.44	69.39	B	67	257.44	16.33	A
32	118.44	60.61	A	68	261.01	176.26	B
33	119.79	195.77	A	69	286.51	14.58	B
34	121.13	3.75	B	70	288.43	14.23	A
35	126.33	163.62	A	71	300.07	45.56	A
36	126.55	18.99	B	72	300.73	19.48	B
37	129.30	38.36	B	73	343.57	2.89	B
38	131.35	105.79	A	74	344.98	12.60	A
39	132.77	99.62	B	75	352.61	4.10	A

76	353.84	11.28	B	117	666.62	31.18	A
77	387.28	39.07	A	118	667.06	40.21	B
78	387.70	0.44	B	119	678.11	4.01	A
79	403.25	10.39	A	120	679.94	0.42	B
80	404.00	1.29	B	121	688.24	15.03	A
81	454.60	23.15	A	122	688.87	8.39	B
82	455.47	28.20	B	123	735.04	6.45	B
83	470.03	53.35	B	124	735.38	4.16	A
84	471.12	93.80	A	125	744.06	344.29	A
85	477.48	34.03	A	126	746.52	6.06	B
86	484.80	2.51	B	127	751.93	2.47	B
87	491.94	38.35	A	128	753.75	305.75	A
88	492.81	44.98	B	129	757.94	124.30	A
89	503.17	0.41	B	130	759.74	8.21	B
90	504.23	205.86	A	131	762.76	18.65	B
91	512.77	12.37	B	132	762.84	11.96	A
92	517.15	122.53	A	133	771.01	5.03	A
93	526.03	300.49	A	134	772.29	10.23	B
94	531.31	1.05	B	135	797.20	4.08	A
95	538.64	12.83	B	136	797.73	5.95	B
96	538.93	58.03	A	137	811.30	38.79	A
97	547.31	56.37	A	138	813.69	4.10	B
98	549.13	12.94	B	139	819.50	1.70	B
99	558.23	88.29	A	140	819.58	15.86	A
100	558.42	57.43	B	141	825.82	20.43	A
101	563.78	64.02	A	142	826.29	3.94	B
102	563.79	63.00	B	143	857.73	27.88	B
103	569.12	4.27	A	144	857.82	255.81	A
104	569.27	69.53	B	145	860.61	208.00	A
105	581.28	20.21	A	146	860.84	24.16	B
106	582.17	11.94	B	147	867.06	16.14	A
107	594.97	54.27	A	148	868.30	42.95	B
108	595.47	26.56	B	149	900.14	38.47	A
109	599.95	17.08	A	150	900.46	15.66	B
110	600.66	26.76	B	151	903.18	11.76	A
111	601.85	118.50	A	152	903.45	0.53	B
112	602.05	95.86	B	153	967.62	109.32	A
113	615.44	38.82	A	154	967.68	19.16	B
114	615.80	13.92	B	155	972.96	15.22	A
115	655.78	4.51	A	156	972.96	3.80	B
116	656.89	60.94	B	157	994.69	11.33	A

158	995.54	4.90	B	199	1283.31	156.41	A
159	1011.19	30.91	B	200	1283.99	66.23	B
160	1011.32	114.38	A	201	1293.88	116.12	A
161	1015.89	10.67	B	202	1295.79	29.23	B
162	1015.95	581.22	A	203	1301.14	106.86	A
163	1020.39	0.46	B	204	1304.88	3.01	B
164	1020.53	363.12	A	205	1309.90	16.51	A
165	1030.58	2.15	A	206	1310.51	31.43	B
166	1032.89	0.10	B	207	1315.14	45.14	A
167	1043.60	103.19	A	208	1320.52	3.80	B
168	1043.82	40.76	B	209	1356.36	1.21	B
169	1068.24	51.04	A	210	1357.41	10.58	A
170	1068.30	32.81	B	211	1366.39	68.29	A
171	1070.46	9.19	A	212	1368.56	137.35	B
172	1070.49	27.78	B	213	1438.47	69.13	A
173	1074.98	10.97	A	214	1441.23	14.10	B
174	1075.02	17.71	B	215	1444.67	10.29	A
175	1105.08	26.54	A	216	1445.30	18.05	B
176	1109.26	106.45	B	217	1449.47	9.14	B
177	1112.39	57.90	A	218	1450.06	61.06	A
178	1116.18	152.67	B	219	1462.76	45.94	A
179	1118.56	26.63	A	220	1463.57	19.81	B
180	1119.32	6.37	B	221	1468.50	54.62	B
181	1137.56	79.23	A	222	1468.77	137.73	A
182	1137.80	11.80	B	223	1470.27	164.41	A
183	1148.64	59.03	A	224	1470.53	68.32	B
184	1149.52	3.64	B	225	1482.03	205.27	A
185	1189.65	102.55	A	226	1482.66	67.16	B
186	1189.74	29.93	B	227	1492.04	213.95	A
187	1201.39	2.62	B	228	1493.17	99.62	B
188	1201.40	101.93	A	229	1522.24	61.81	A
189	1225.73	4.31	A	230	1522.81	26.20	B
190	1225.81	0.31	B	231	1550.63	56.46	A
191	1237.25	6.63	A	232	1557.36	27.97	B
192	1237.43	64.09	B	233	1581.16	27.08	A
193	1246.31	81.42	A	234	1581.88	28.91	B
194	1248.35	81.88	B	235	1601.01	26.17	A
195	1254.52	341.30	A	236	1602.93	17.84	B
196	1254.73	18.67	B	237	1622.06	33.94	A
197	1271.55	240.80	A	238	1622.40	6.39	B
198	1271.80	22.72	B	239	1633.82	41.95	B

240	1633.94	664.40	A	281	3487.56	83.89	B
241	1644.85	181.41	A	282	3545.47	127.34	A
242	1645.22	19.78	B	283	3546.16	9.49	B
243	1669.94	9.39	A	284	3561.02	41.66	A
244	1689.15	0.02	B	285	3567.42	149.43	B
245	1699.09	9.46	A	286	3487.56	83.89	B
246	1705.48	10.92	B	287	3545.47	127.34	A
247	1705.90	262.99	A	288	3546.16	9.49	B
248	1712.76	26.57	B				
249	2153.38	640.29	A				
250	2158.72	94.73	B				
251	2437.22	548.87	A				
252	2441.59	292.82	B				
253	2564.13	875.29	A				
254	2565.37	391.12	B				
255	2709.23	83.86	A				
256	2722.27	36.30	B				
257	2956.30	82.71	B				
258	2956.36	336.93	A				
259	2974.05	81.04	B				
260	2974.38	253.25	A				
261	2982.95	1000.00	A				
262	2987.56	270.48	B				
263	3005.39	188.96	B				
264	3005.57	547.00	A				
265	3014.22	62.96	A				
266	3014.69	61.14	B				
267	3186.29	446.45	A				
268	3188.62	55.85	B				
269	3212.88	764.88	A				
270	3213.46	110.61	B				
271	3270.16	147.88	A				
272	3272.02	35.18	B				
273	3293.01	290.74	A				
274	3293.26	86.42	B				
275	3347.68	279.71	A				
276	3347.81	38.09	B				
277	3427.26	3.42	B				
278	3427.33	318.73	A				
279	3432.25	167.70	A				
280	3432.94	3.61	B				

Table A-19. Solid-state DFT IR-active modes with frequencies (cm-1), intensities (km/mol), and mode symmetries for thiourea-DL-tartaric acid (T:TA).

Mode Label (v)	Frequency (cm^{-1})	Intensity (km/mol)	Mode Symmetry	Mode Label (v)	Frequency (cm^{-1})	Intensity (km/mol)	Mode Symmetry
4	17.72	0.46	A	40	130.07	43.99	B
5	22.95	0.00	A	41	130.93	0.40	A
6	27.54	0.01	A	42	134.27	11.40	B
7	30.69	1.20	B	43	137.14	1.66	A
8	35.99	4.22	B	44	137.52	16.17	B
9	41.99	1.75	A	45	143.24	6.60	B
10	50.08	20.67	B	46	147.06	66.51	B
11	50.59	0.15	A	47	147.18	24.55	A
12	52.86	2.11	B	48	149.85	1.90	A
13	58.73	9.60	A	49	153.82	36.81	B
14	64.08	0.88	B	50	154.83	0.08	A
15	66.59	2.35	B	51	165.75	9.03	B
16	69.56	0.48	A	52	167.85	8.58	A
17	72.47	0.16	B	53	175.13	12.39	A
18	75.67	1.46	B	54	176.92	6.90	B
19	79.27	0.18	A	55	178.21	8.56	B
20	79.96	2.43	A	56	180.37	1.05	A
21	82.22	5.75	A	57	189.45	2.87	A
22	84.42	1.84	B	58	190.29	31.63	B
23	88.90	1.51	A	59	197.61	11.61	A
24	91.57	0.99	A	60	206.92	6.50	B
25	91.75	12.29	B	61	209.12	0.07	A
26	92.76	1.46	B	62	211.47	3.98	B
27	100.51	23.45	B	63	218.30	26.29	A
28	101.70	0.52	A	64	218.39	46.75	B
29	102.91	14.04	B	65	232.86	106.86	B
30	107.82	0.80	A	66	234.20	19.39	A
31	112.35	21.19	A	67	239.25	1.83	B
32	115.61	1.27	B	68	242.19	0.01	A
33	117.77	1.01	A	69	270.31	52.37	B
34	118.39	37.75	B	70	271.35	20.32	A
35	122.03	15.47	B	71	277.56	11.64	A
36	123.54	0.76	A	72	280.73	2.45	B
37	126.31	0.20	A	73	332.03	21.33	B
38	126.60	2.17	B	74	333.28	3.50	A
39	128.06	3.19	A	75	341.42	35.70	A

76	342.13	138.26	B	117	626.40	36.71	A
77	368.62	58.55	A	118	626.63	17.04	B
78	369.87	23.50	B	119	655.18	2.97	A
79	373.54	49.15	A	120	655.91	51.80	B
80	376.07	5.47	B	121	658.91	27.45	B
81	393.00	6.16	B	122	659.45	0.43	A
82	393.03	2.08	A	123	667.53	209.95	B
83	414.18	4.32	B	124	667.85	1.63	A
84	414.26	1.35	A	125	685.57	126.00	A
85	449.71	9.07	B	126	686.24	55.70	B
86	449.99	55.25	A	127	688.83	37.63	A
87	463.90	78.71	A	128	689.17	508.91	B
88	470.16	332.88	B	129	693.94	116.27	A
89	477.43	110.69	A	130	696.23	91.89	B
90	478.73	140.41	B	131	727.27	156.80	A
91	479.10	25.71	B	132	727.76	26.04	B
92	483.03	159.95	A	133	730.93	84.21	A
93	487.46	14.70	B	134	733.78	5.61	B
94	487.73	0.48	A	135	740.44	30.55	B
95	510.38	13.31	A	136	740.84	6.83	A
96	514.61	182.42	B	137	741.36	14.89	A
97	518.31	239.74	A	138	744.95	56.12	B
98	522.40	833.49	B	139	753.21	23.22	B
99	525.30	66.87	B	140	755.28	61.08	A
100	525.88	4.52	A	141	782.31	377.48	B
101	559.57	34.18	A	142	782.31	2.87	A
102	559.64	107.77	B	143	800.98	36.40	A
103	572.74	86.42	A	144	801.52	1.03	B
104	573.88	93.13	B	145	812.53	61.19	A
105	575.10	59.54	A	146	813.20	17.83	B
106	576.81	1.68	B	147	818.58	38.82	A
107	584.82	23.28	B	148	819.11	50.74	B
108	585.03	5.85	A	149	848.76	54.09	B
109	594.45	349.21	B	150	848.88	3.50	A
110	595.31	4.61	A	151	851.75	6.40	A
111	599.20	22.53	A	152	851.91	47.54	B
112	601.09	77.67	B	153	868.16	59.34	B
113	601.76	6.53	A	154	868.25	0.28	A
114	601.83	372.12	B	155	886.13	18.60	A
115	612.37	19.93	A	156	886.36	5.60	B
116	612.59	411.33	B	157	891.40	55.72	A

158	891.86	159.34	B	199	1253.75	6.62	A
159	907.86	0.00	A	200	1253.76	1029.13	B
160	907.88	165.88	B	201	1273.53	7.21	B
161	957.70	29.79	B	202	1273.57	0.16	A
162	957.79	0.01	A	203	1285.28	1664.08	A
163	960.32	33.41	A	204	1294.97	240.65	B
164	960.36	137.45	B	205	1295.87	40.34	A
165	990.58	22.91	A	206	1297.46	4.16	A
166	990.83	3.16	B	207	1297.55	36.78	B
167	1014.90	540.04	A	208	1298.45	319.88	B
168	1019.14	862.75	B	209	1342.40	30.62	A
169	1061.97	61.12	A	210	1342.72	61.92	B
170	1062.23	104.69	B	211	1348.49	21.92	B
171	1065.57	14.86	A	212	1348.57	1.34	A
172	1065.92	427.83	B	213	1374.86	411.15	A
173	1072.06	94.17	A	214	1378.13	226.00	B
174	1072.62	20.34	B	215	1390.84	701.03	A
175	1074.59	106.52	A	216	1396.24	216.30	B
176	1075.44	94.27	B	217	1406.90	179.49	A
177	1084.88	7.48	B	218	1408.33	155.96	B
178	1085.12	11.88	A	219	1413.19	7.30	B
179	1090.71	642.85	A	220	1413.36	0.45	A
180	1095.33	45.89	B	221	1439.70	1.87	A
181	1099.47	46.62	A	222	1440.24	576.37	B
182	1100.90	353.72	B	223	1445.97	2.90	B
183	1103.42	44.11	B	224	1446.78	10.13	A
184	1103.45	14.82	A	225	1448.76	320.07	A
185	1177.98	75.05	A	226	1452.11	76.52	B
186	1178.66	103.64	B	227	1464.08	1.40	B
187	1183.20	268.85	B	228	1464.11	0.23	A
188	1183.41	18.44	A	229	1471.66	32.28	B
189	1197.95	327.56	B	230	1471.67	3.85	A
190	1197.99	0.22	A	231	1483.37	5.12	A
191	1201.01	3.43	A	232	1483.39	135.71	B
192	1201.11	137.07	B	233	1576.11	9.30	A
193	1227.09	260.76	A	234	1576.17	869.69	B
194	1227.66	43.92	B	235	1598.28	319.21	B
195	1228.92	262.73	A	236	1598.30	20.14	A
196	1231.58	515.32	B	237	1608.81	106.56	A
197	1239.72	42.44	A	238	1609.40	367.42	B
198	1240.13	108.22	B	239	1632.33	102.81	A

240	1632.80	210.21	B	281	3437.43	1086.32	A
241	1636.81	5.96	A	282	3440.54	628.88	B
242	1637.17	25.13	B	283	3479.67	40.59	A
243	1676.34	1558.13	A	284	3479.81	1129.37	B
244	1684.93	362.52	B	285	3486.39	1135.13	A
245	1695.12	76.01	A	286	3490.44	36.21	B
246	1695.65	2077.61	B	287	3526.59	235.04	A
247	1718.72	746.72	A	288	3527.44	278.33	B
248	1724.49	94.38	B				
249	2491.79	914.25	A				
250	2494.97	8356.99	B				
251	2628.73	14.06	A				
252	2628.76	19.16	B				
253	2740.92	3648.49	A				
254	2753.72	8943.92	B				
255	2825.45	830.08	A				
256	2829.17	7431.41	B				
257	2970.53	25.89	B				
258	2970.55	3.21	A				
259	2975.85	3.39	A				
260	2975.90	8.14	B				
261	3000.57	63.06	A				
262	3000.66	51.30	B				
263	3021.12	18.28	B				
264	3021.16	14.87	A				
265	3084.34	1227.33	A				
266	3088.16	1954.46	B				
267	3251.53	577.29	A				
268	3252.95	3279.63	B				
269	3274.36	1199.30	A				
270	3278.00	214.93	B				
271	3287.99	227.10	A				
272	3288.86	2951.68	B				
273	3318.10	126.34	A				
274	3318.25	301.15	B				
275	3345.14	609.39	A				
276	3346.32	2161.04	B				
277	3350.25	402.24	A				
278	3352.19	972.58	B				
279	3376.20	324.72	A				
280	3376.71	201.96	B				

Table A-20. Solid-state DFT Raman-active modes with frequencies (cm⁻¹), relative intensities (normalized to 1000), and mode symmetries for T:TA at 78 K.

Mode Label (ν)	Frequency (cm⁻¹)	Relative Intensity	Mode Symmetry	Mode Label (ν)	Frequency (cm⁻¹)	Relative Intensity	Mode Symmetry
4	17.72	142.02	A	40	130.07	31.34	B
5	22.95	394.09	A	41	130.93	235.11	A
6	27.54	207.78	A	42	134.27	6.96	B
7	30.69	362.44	B	43	137.14	36.05	A
8	35.99	195.22	B	44	137.52	115.40	B
9	41.99	221.20	A	45	143.24	94.78	B
10	50.08	754.10	B	46	147.06	25.50	B
11	50.59	579.24	A	47	147.18	126.45	A
12	52.86	269.25	B	48	149.85	97.30	A
13	58.73	102.17	A	49	153.82	73.03	B
14	64.08	5.98	B	50	154.83	75.98	A
15	66.59	40.69	B	51	165.75	60.60	B
16	69.56	35.69	A	52	167.85	37.85	A
17	72.47	214.72	B	53	175.13	39.74	A
18	75.67	148.51	B	54	176.92	38.30	B
19	79.27	429.32	A	55	178.21	11.32	B
20	79.96	140.31	A	56	180.37	4.81	A
21	82.22	266.77	A	57	189.45	120.09	A
22	84.42	86.32	B	58	190.29	23.30	B
23	88.90	384.99	A	59	197.61	29.30	A
24	91.57	91.11	A	60	206.92	78.85	B
25	91.75	124.24	B	61	209.12	37.36	A
26	92.76	132.46	B	62	211.47	73.07	B
27	100.51	4.52	B	63	218.30	18.13	A
28	101.70	93.71	A	64	218.39	40.45	B
29	102.91	334.80	B	65	232.86	11.86	B
30	107.82	243.91	A	66	234.20	10.55	A
31	112.35	28.44	A	67	239.25	16.26	B
32	115.61	8.33	B	68	242.19	16.08	A
33	117.77	289.65	A	69	270.31	15.54	B
34	118.39	7.27	B	70	271.35	15.59	A
35	122.03	53.58	B	71	277.56	23.56	A
36	123.54	146.51	A	72	280.73	28.65	B
37	126.31	54.86	A	73	332.03	12.34	B
38	126.60	87.77	B	74	333.28	9.09	A
39	128.06	143.59	A	75	341.42	8.22	A

76	342.13	2.71	B	117	626.40	16.11	A
77	368.62	16.29	A	118	626.63	3.60	B
78	369.87	2.91	B	119	655.18	40.47	A
79	373.54	21.72	A	120	655.91	34.37	B
80	376.07	1.46	B	121	658.91	25.72	B
81	393.00	3.23	B	122	659.45	26.41	A
82	393.03	14.44	A	123	667.53	0.64	B
83	414.18	67.63	B	124	667.85	18.43	A
84	414.26	15.00	A	125	685.57	54.97	A
85	449.71	2.93	B	126	686.24	5.93	B
86	449.99	42.15	A	127	688.83	25.74	A
87	463.90	65.21	A	128	689.17	22.98	B
88	470.16	3.41	B	129	693.94	83.45	A
89	477.43	143.48	A	130	696.23	7.78	B
90	478.73	15.26	B	131	727.27	367.01	A
91	479.10	56.39	B	132	727.76	0.20	B
92	483.03	27.16	A	133	730.93	752.32	A
93	487.46	33.94	B	134	733.78	29.74	B
94	487.73	65.04	A	135	740.44	4.05	B
95	510.38	317.02	A	136	740.84	309.45	A
96	514.61	53.61	B	137	741.36	244.78	A
97	518.31	103.00	A	138	744.95	0.39	B
98	522.40	27.76	B	139	753.21	24.83	B
99	525.30	4.86	B	140	755.28	5.88	A
100	525.88	17.57	A	141	782.31	7.07	B
101	559.57	167.74	A	142	782.31	16.99	A
102	559.64	29.22	B	143	800.98	12.74	A
103	572.74	3.29	A	144	801.52	1.41	B
104	573.88	7.64	B	145	812.53	7.86	A
105	575.10	14.51	A	146	813.20	4.18	B
106	576.81	1.01	B	147	818.58	5.75	A
107	584.82	36.03	B	148	819.11	0.69	B
108	585.03	136.87	A	149	848.76	3.45	B
109	594.45	13.12	B	150	848.88	164.42	A
110	595.31	36.20	A	151	851.75	100.09	A
111	599.20	41.13	A	152	851.91	8.97	B
112	601.09	46.16	B	153	868.16	14.59	B
113	601.76	66.56	A	154	868.25	43.19	A
114	601.83	46.94	B	155	886.13	20.44	A
115	612.37	65.02	A	156	886.36	3.17	B
116	612.59	3.73	B	157	891.40	16.24	A

158	891.86	4.23	B	199	1253.75	10.42	A
159	907.86	59.08	A	200	1253.76	25.39	B
160	907.88	6.99	B	201	1273.53	39.59	B
161	957.70	32.07	B	202	1273.57	608.03	A
162	957.79	112.28	A	203	1285.28	5.71	A
163	960.32	6.08	A	204	1294.97	1.61	B
164	960.36	0.90	B	205	1295.87	3.05	A
165	990.58	17.04	A	206	1297.46	36.73	A
166	990.83	14.80	B	207	1297.55	5.01	B
167	1014.90	0.16	A	208	1298.45	5.76	B
168	1019.14	0.02	B	209	1342.40	37.07	A
169	1061.97	15.94	A	210	1342.72	38.05	B
170	1062.23	15.24	B	211	1348.49	59.93	B
171	1065.57	10.26	A	212	1348.57	48.53	A
172	1065.92	7.38	B	213	1374.86	44.98	A
173	1072.06	11.10	A	214	1378.13	18.96	B
174	1072.62	20.61	B	215	1390.84	75.97	A
175	1074.59	12.82	A	216	1396.24	3.75	B
176	1075.44	18.64	B	217	1406.90	59.50	A
177	1084.88	10.35	B	218	1408.33	8.17	B
178	1085.12	247.29	A	219	1413.19	1.39	B
179	1090.71	34.60	A	220	1413.36	16.65	A
180	1095.33	82.48	B	221	1439.70	3.82	A
181	1099.47	99.84	A	222	1440.24	1.59	B
182	1100.90	11.32	B	223	1445.97	59.94	B
183	1103.42	82.28	B	224	1446.78	1.14	A
184	1103.45	61.95	A	225	1448.76	1.17	A
185	1177.98	59.32	A	226	1452.11	0.23	B
186	1178.66	26.02	B	227	1464.08	61.91	B
187	1183.20	79.00	B	228	1464.11	119.78	A
188	1183.41	123.12	A	229	1471.66	53.35	B
189	1197.95	3.04	B	230	1471.67	23.54	A
190	1197.99	37.79	A	231	1483.37	16.17	A
191	1201.01	3.89	A	232	1483.39	21.24	B
192	1201.11	12.43	B	233	1576.11	8.07	A
193	1227.09	31.13	A	234	1576.17	16.31	B
194	1227.66	199.38	B	235	1598.28	5.47	B
195	1228.92	33.38	A	236	1598.30	14.19	A
196	1231.58	15.07	B	237	1608.81	4.11	A
197	1239.72	19.03	A	238	1609.40	1.65	B
198	1240.13	2.26	B	239	1632.33	49.88	A

240	1632.80	2.08	B	281	3437.43	157.63	A
241	1636.81	415.07	A	282	3440.54	65.09	B
242	1637.17	32.28	B	283	3479.67	65.85	A
243	1676.34	157.45	A	284	3479.81	24.60	B
244	1684.93	3.15	B	285	3486.39	53.74	A
245	1695.12	40.89	A	286	3490.44	160.41	B
246	1695.65	0.51	B	287	3526.59	90.93	A
247	1718.72	286.02	A	288	3527.44	5.97	B
248	1724.49	13.80	B				
249	2491.79	985.44	A				
250	2494.97	211.01	B				
251	2628.73	579.61	A				
252	2628.76	269.44	B				
253	2740.92	3.25	A				
254	2753.72	9.58	B				
255	2825.45	1000.00	A				
256	2829.17	573.52	B				
257	2970.53	34.78	B				
258	2970.55	155.39	A				
259	2975.85	137.34	A				
260	2975.90	46.69	B				
261	3000.57	433.72	A				
262	3000.66	133.54	B				
263	3021.12	91.73	B				
264	3021.16	278.88	A				
265	3084.34	578.51	A				
266	3088.16	292.11	B				
267	3251.53	285.34	A				
268	3252.95	34.43	B				
269	3274.36	323.11	A				
270	3278.00	20.02	B				
271	3287.99	655.83	A				
272	3288.86	266.60	B				
273	3318.10	172.03	A				
274	3318.25	18.21	B				
275	3345.14	199.23	A				
276	3346.32	59.46	B				
277	3350.25	52.83	A				
278	3352.19	11.63	B				
279	3376.20	581.16	A				
280	3376.71	35.10	B				
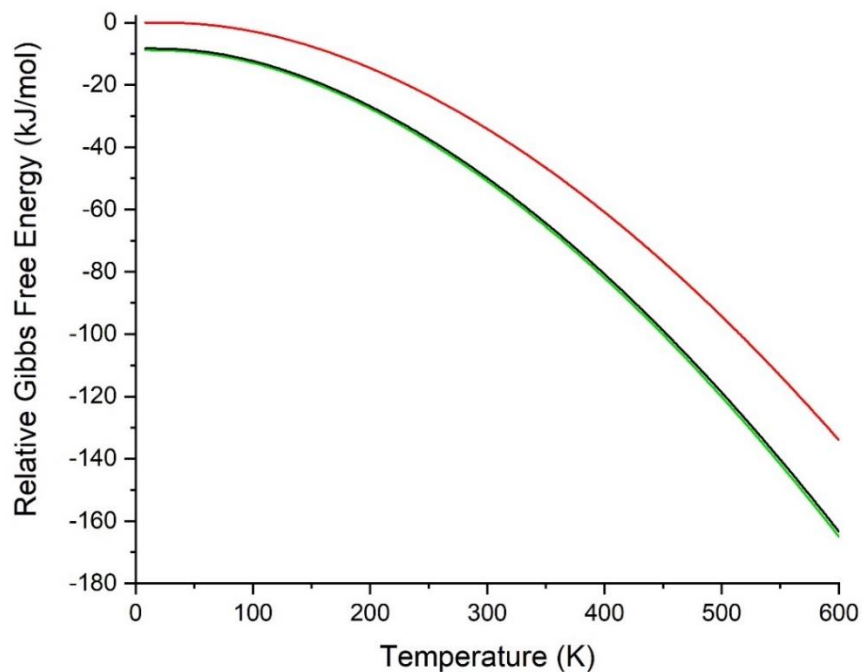
Figure A-8. Gibbs free energy curves for cocrystallized U:GA-I (green), U:GA-II (black) and the linear combination of Gibbs free energies of pure urea and pure glutaric acid (red). For clarity, the energy values have been set relative to a common zero and are per asymmetric unit.
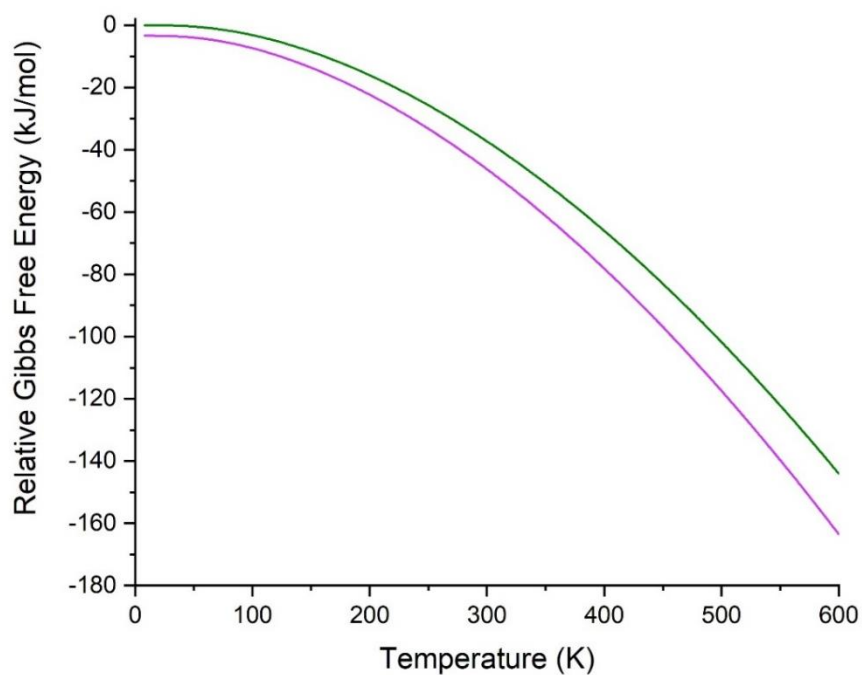
Figure A-9. Gibbs free energy curves for cocrystallized T:GA (purple) and the linear combination of Gibbs free energies of pure thiourea and pure glutaric acid (green). For clarity, the energy values have been set relative to a common zero and are per asymmetric unit.
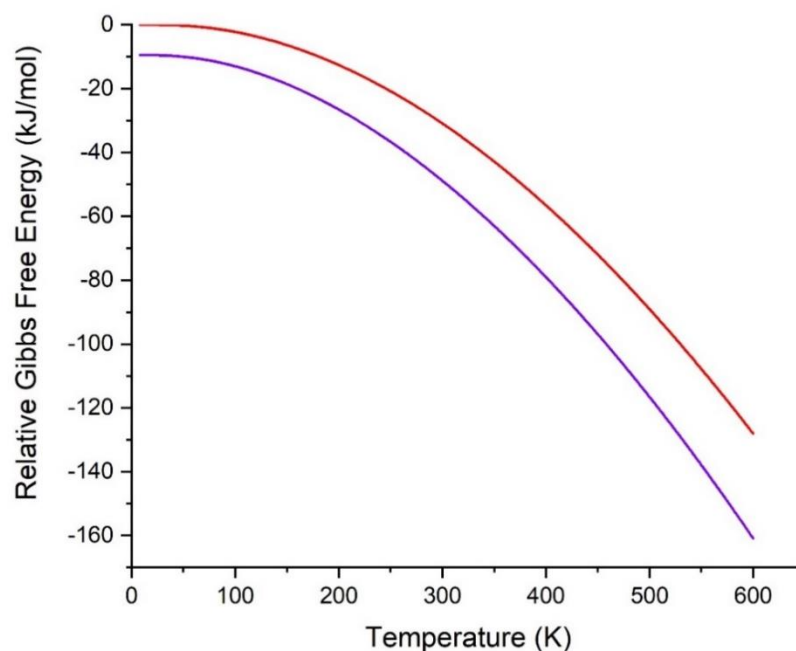
Figure A-10. Gibbs free energy curves for cocrystallized U:TA (purple) and the linear combination of Gibbs free energies of pure urea and pure DL-tartaric acid (red). For clarity, the energy values have been set relative to a common zero and are per asymmetric unit.
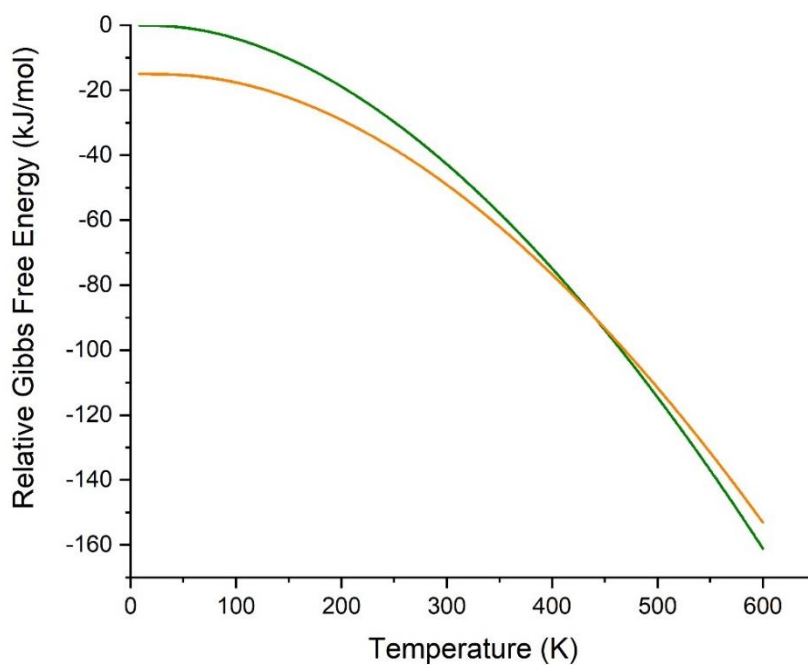
Figure A-11. Relative Gibbs free energy curve for cocrystallized T:TA (green) and the linear combination of relative Gibbs free energies of pure thiourea and pure DL-tartaric acid (orange). For clarity, the energy values have been set relative to a common zero and are per asymmetric unit.

Appendix B: Supporting Information for Chapter 5

Supporting Information Table of Contents

Table B-1. Solid-state DFT optimized lattice parameters for EM-I and EM-II.

	Lattice Parameters						
	Space Group	a (Å)	b (Å)	c (Å)	α (°)	β (°)	γ (°)
EM-I	P2$_1$	11.15766	6.59589	17.55754	90	103.839°	90
EM-II	P2$_1$2$_1$2$_1$	33.72019	11.14380	6.55968	90	90	90

Table B-2. Solid-state DFT optimized atomic positions in fractional coordinates for the asymmetric unit cell of EM-I.

Atom (Atomic Number)	X/A	Y/B	Z/C
6	-1.47913E-01	-1.77062E-01	-2.41888E-01
6	-2.73954E-01	-1.02456E-01	-2.41515E-01
8	-2.97756E-01	9.27189E-02	-2.44406E-01
8	-3.55287E-01	-2.29713E-01	-2.38619E-01
6	-4.18382E-02	-7.25390E-02	-2.35147E-01
6	-1.70186E-02	1.50508E-01	-2.24217E-01
8	-1.06618E-01	2.77921E-01	-2.35806E-01
8	9.52602E-02	2.01914E-01	-2.02999E-01
1	-1.43798E-01	-3.42404E-01	-2.45681E-01
1	4.11217E-02	-1.60541E-01	-2.35175E-01
1	-2.12711E-01	1.83149E-01	-2.43326E-01
6	2.98634E-01	-3.05031E-01	-2.67961E-01
8	3.70899E-01	-4.46102E-01	-2.53354E-01
8	1.83685E-01	-3.12968E-01	-3.13997E-01
6	1.44904E-01	4.90985E-01	-3.50917E-01
6	1.63613E-02	-4.84755E-01	-4.02281E-01
6	3.26229E-01	-8.97081E-02	-2.37774E-01
6	3.16178E-01	6.39626E-02	-3.04102E-01
6	3.99775E-01	2.76043E-02	-3.60663E-01
6	3.80846E-01	1.94433E-01	-4.21079E-01
6	4.53914E-01	3.69994E-01	-4.08075E-01
6	2.85781E-01	1.82040E-01	-4.89513E-01
6	4.33194E-01	-4.71636E-01	-4.62451E-01
6	2.63834E-01	3.41097E-01	4.56327E-01
6	3.37764E-01	-4.85283E-01	4.69616E-01
7	4.50249E-01	-9.11701E-02	-1.81260E-01
6	4.91068E-01	1.10984E-01	-1.44026E-01
6	-3.86132E-01	7.28693E-02	-8.48327E-02
8	-3.62782E-01	-9.83567E-02	-5.51728E-02
6	3.97107E-01	1.96831E-01	-1.02605E-01
7	-3.09512E-01	2.31911E-01	-6.45246E-02
6	-1.89170E-01	2.01089E-01	-9.57193E-03
6	-1.99243E-01	1.03899E-01	6.75236E-02
8	-1.12067E-01	-3.56266E-02	9.00720E-02
8	-2.73600E-01	1.58133E-01	1.04834E-01
6	-1.34350E-01	4.15911E-01	2.51626E-03

6	-1.90325E-01	-4.79150E-01	-7.57118E-02
6	-3.21999E-01	4.37409E-01	-9.90472E-02
1	-4.72440E-01	3.83029E-01	-3.54668E-01
1	4.92564E-01	-3.38135E-01	-4.52359E-01
1	3.22479E-01	-3.62049E-01	4.26879E-01
1	1.89764E-01	3.28941E-01	4.03219E-01
1	2.29141E-01	4.51037E-02	4.99393E-01
1	-4.80048E-01	-1.47500E-01	-2.08366E-01
1	4.47126E-01	-1.92683E-01	-1.36791E-01
1	-4.95743E-01	2.11739E-01	-1.90984E-01
1	-3.32296E-02	4.11095E-01	1.64882E-02
1	-1.63886E-01	4.91047E-01	5.09142E-02
1	-1.39062E-01	4.78417E-01	-1.19461E-01
1	-1.91054E-01	-3.13750E-01	-7.02030E-02
1	-3.58082E-01	4.32134E-01	-1.62848E-01
1	-3.84682E-01	-4.70188E-01	-7.35845E-02
1	2.57941E-01	-4.89032E-02	-2.04463E-01
1	3.32172E-01	2.16920E-01	-2.79024E-01
1	2.19185E-01	5.98908E-02	-3.37047E-01
1	3.78730E-01	-1.20622E-01	-3.89618E-01
1	4.97238E-01	2.43672E-02	-3.28586E-01
1	1.47054E-01	3.80454E-01	-3.03899E-01
1	2.11813E-01	4.46687E-01	-3.84686E-01
1	-1.32365E-01	1.01603E-01	-3.70677E-02
1	3.10570E-01	2.36871E-01	-1.44177E-01
1	4.33013E-01	3.34653E-01	-7.04130E-02
1	3.77875E-01	8.69431E-02	-6.00289E-02
1	1.28239E-02	-3.66008E-01	-4.46671E-01
1	-5.03138E-02	-4.48912E-01	-3.67285E-01
1	-1.20479E-02	3.71319E-01	-4.32985E-01
1	-1.14442E-01	-1.09456E-01	1.40866E-01

Table B-3. Solid-state DFT optimized atomic positions in fractional coordinates for the asymmetric unit cell of EM-II.

Atom (Atomic Number)	X/A	Y/B	Z/C
6	-2.88702E-01	-3.34820E-01	-4.31713E-02
6	-3.00400E-01	-2.11632E-01	4.05224E-02
7	-2.83253E-01	-2.11256E-01	2.47757E-01
6	-2.55597E-01	-3.11304E-01	2.79305E-01
6	-2.49381E-01	-3.62173E-01	6.37433E-02
6	-2.16518E-01	-2.73145E-01	3.76686E-01
8	-1.97222E-01	-1.85645E-01	3.20959E-01
8	-2.05608E-01	-3.51949E-01	-4.82371E-01
6	-2.93854E-01	-1.42383E-01	4.07498E-01
8	-2.78804E-01	-1.53570E-01	-4.20310E-01
6	-3.24388E-01	-4.34619E-02	3.68326E-01
6	-3.04278E-01	6.59264E-02	2.76135E-01
7	-3.42903E-01	-1.45131E-02	-4.28012E-01
6	-3.72267E-01	8.65745E-02	-4.32282E-01
6	-3.85476E-01	1.11335E-01	-2.14379E-01
8	-3.80803E-01	4.35808E-02	-7.07613E-02
8	-4.04326E-01	2.17528E-01	-2.10681E-01
6	-4.24041E-01	2.52991E-01	-2.08698E-02
6	-4.64562E-01	1.95760E-01	-5.78166E-03
6	-4.08114E-01	6.22307E-02	4.29905E-01
6	-4.36202E-01	-3.80765E-02	-4.98583E-01
6	-4.67347E-01	-6.23397E-02	3.41780E-01
6	4.95275E-01	-7.68391E-03	3.51058E-01
6	4.67357E-01	-2.52836E-02	1.96481E-01
6	4.76411E-01	-9.87988E-02	3.02157E-02
6	-4.86344E-01	-1.53847E-01	1.94637E-02
6	-4.58462E-01	-1.35669E-01	1.73761E-01
1	-1.80027E-01	-3.31756E-01	-4.05584E-01
1	-2.24661E-01	-3.15212E-01	-1.11181E-02
1	-2.42630E-01	-4.58366E-01	6.92507E-02
1	-2.85633E-01	-3.31912E-01	-2.09327E-01
1	-3.10974E-01	-4.02287E-01	-1.27857E-03
1	-2.69640E-01	-3.78144E-01	3.79603E-01
1	-3.32649E-01	-1.99126E-01	4.44674E-02
1	-2.87272E-01	-1.39490E-01	-5.18931E-02
1	-3.48227E-01	-7.69541E-02	2.70104E-01
1	-2.87096E-01	4.00753E-02	1.41551E-01

1	-2.83628E-01	1.06281E-01	3.86063E-01
1	-3.25886E-01	1.33300E-01	2.27779E-01
1	-3.20266E-01	9.12631E-03	-3.28975E-01
1	-3.55868E-01	-9.41464E-02	-3.66938E-01
1	-3.56754E-01	1.66444E-01	-4.89803E-01
1	-3.97744E-01	4.40375E-02	2.74012E-01
1	-4.24625E-01	1.47195E-01	4.21928E-01
1	-4.50358E-01	-1.24864E-02	-3.53673E-01
1	-4.19364E-01	-1.20641E-01	-4.68943E-01
1	-4.29357E-01	-1.78327E-01	1.63956E-01
1	-4.78730E-01	-2.10795E-01	-1.10223E-01
1	4.54505E-01	-1.13269E-01	-8.97398E-02
1	4.38492E-01	1.84336E-02	2.06528E-01
1	4.88077E-01	5.03012E-02	4.80294E-01
1	-4.25801E-01	3.51026E-01	-3.17041E-02
1	-4.04576E-01	2.29984E-01	1.07007E-01
1	-4.62472E-01	9.76810E-02	4.14061E-03
1	-4.82931E-01	2.19763E-01	-1.37929E-01
1	-4.79756E-01	2.28294E-01	1.31522E-01
6	3.71350E-01	5.89881E-02	-1.64868E-01
6	3.71762E-01	1.85140E-01	-8.97181E-02
8	3.71640E-01	2.67844E-01	-2.17715E-01
8	3.72294E-01	2.07915E-01	1.06675E-01
6	3.66461E-01	-4.44672E-02	-6.08089E-02
6	3.60142E-01	-6.55080E-02	1.62562E-01
8	3.49977E-01	-1.70461E-01	2.13260E-01
8	3.64916E-01	2.01722E-02	2.91557E-01
1	3.69936E-01	1.23293E-01	1.97077E-01
1	3.66082E-01	-1.27329E-01	-1.49559E-01
1	3.73863E-01	5.33072E-02	-3.30845E-01

Table B-4. Solid-state DFT IR-active modes with frequencies (THz), mode symmetries, and IR intensities (km/mol) for EM-I.

Frequency (THz)	Mode Symmetry	IR Intensity (km/mol)
0.67	B	0.55
0.90	A	0.64
1.00	B	0.31
1.03	A	1.97
1.27	A	5.82
1.37	A	0.58
1.39	B	3.49
1.48	B	6.51
1.60	B	0.60
1.64	B	0.56
1.66	A	0.07
1.83	A	1.03
1.90	B	8.10
1.92	A	0.95
1.99	A	3.15
2.05	A	0.23
2.09	B	2.91
2.15	B	1.58
2.23	A	0.52
2.30	B	19.44
2.33	A	1.08
2.39	B	7.81
2.49	A	0.04
2.66	A	5.57
2.67	B	2.24
2.70	A	0.00
2.73	B	2.84
2.81	B	9.67
3.01	A	0.39
3.07	B	6.46
3.07	A	0.32
3.13	A	4.52
3.20	B	0.41
3.22	A	1.64
3.29	B	34.47
3.29	A	5.49
3.40	B	4.58
3.41	A	5.55
3.43	B	4.51
3.55	A	0.00
3.62	A	0.20

3.64	B	8.70
3.73	B	3.25
3.86	B	1.29
3.91	A	2.74
3.96	A	0.01
3.99	B	37.91
4.01	A	8.60
4.16	B	21.14
4.29	A	0.18
4.30	B	5.18
4.64	A	13.37
4.65	B	16.40
4.75	A	2.53
4.76	B	1.17
4.98	B	3.26
5.03	A	2.63
5.21	A	29.18
5.32	B	120.77
5.54	B	86.45
5.61	A	11.07
5.67	A	3.40
5.81	B	15.74
6.87	A	9.24
6.91	B	216.10
7.25	B	0.40
7.25	A	0.18
7.72	B	39.39
7.75	A	2.46
7.90	B	32.34
7.95	A	0.30
8.21	B	29.09
8.26	A	3.15
8.50	A	0.98
8.50	B	1.37
8.88	B	140.40
8.88	A	14.31
8.94	B	68.98
9.02	A	8.87
9.48	B	10.26
9.51	A	2.12
9.63	A	0.51
9.63	B	15.97
9.74	A	2.39
9.76	B	74.72
10.26	B	12.36

10.31	A	0.09
10.78	A	30.10
10.94	B	36.94
11.27	B	201.30
11.37	A	20.35
11.50	B	4.00
11.52	A	6.30
12.00	B	32.87
12.10	A	14.29
12.13	B	1.01
12.18	A	0.05
12.88	A	65.16
12.93	B	57.70
13.42	A	4.65
13.44	B	33.08
14.22	B	45.05
14.32	A	5.06
14.89	A	4.47
14.99	B	28.91
15.82	A	0.34
15.84	B	39.09
16.22	A	60.85
16.25	B	5.69
17.49	A	34.18
17.51	B	43.45
17.64	A	40.25
17.65	B	11.61
17.85	B	14.21
17.88	A	31.68
18.06	A	9.61
18.08	B	10.45
18.55	B	1.13
18.55	A	0.18
19.54	A	287.10
19.55	B	327.56
19.84	B	3.90
19.87	A	1.09
20.02	B	44.32
20.05	A	0.13
20.64	A	41.95
20.70	B	88.65
20.73	B	117.58
20.85	A	28.70
21.35	A	6.00
21.35	B	14.86

21.63	B	61.01
21.65	A	0.09
22.32	B	30.57
22.32	A	0.24
22.38	A	4.61
22.44	B	132.92
22.83	A	4.63
22.83	B	57.56
23.20	B	10.50
23.21	A	35.43
23.60	B	81.27
23.63	A	7.22
23.74	A	1.80
23.76	B	4.71
24.44	A	3.17
24.47	B	23.16
24.73	B	9.12
24.74	A	1.17
25.15	A	12.74
25.17	B	12.40
25.18	A	70.80
25.22	B	4.38
25.66	B	192.00
25.68	A	5.33
25.70	B	39.05
25.73	A	10.48
25.91	A	23.93
25.96	B	18.98
26.13	A	21.47
26.14	B	71.33
26.43	B	196.31
26.43	A	46.15
26.78	B	68.07
26.80	A	27.99
26.95	A	3.86
26.98	B	0.13
27.03	A	27.83
27.10	B	2.61
27.95	A	1.42
27.95	B	10.84
27.99	A	3.75
28.00	B	0.31
28.11	B	13.76
28.12	A	0.79
28.50	A	70.45

28.51	B	79.14
28.57	A	8.84
28.63	B	5.16
28.67	B	45.37
28.74	A	481.92
29.13	B	2.30
29.25	A	3.06
29.46	A	33.39
29.54	B	15.70
29.78	A	3.46
29.78	B	7.27
29.85	B	0.38
29.88	A	0.06
29.96	B	35.99
29.96	A	0.57
30.25	A	16.36
30.27	B	7.16
30.33	A	131.15
30.33	B	7.88
30.69	B	110.93
30.71	A	4.15
30.85	A	8.38
30.89	B	15.66
31.02	A	15.88
31.15	B	11.51
31.44	A	102.84
31.45	B	69.55
32.34	B	2.87
32.35	A	0.63
32.56	B	5.17
32.57	A	2.64
32.72	A	8.99
32.79	B	9.43
33.05	B	132.37
33.07	A	8.21
33.34	A	12.16
33.36	B	54.88
33.59	B	8.15
33.64	A	1.13
33.94	A	0.65
33.99	B	14.42
34.32	A	56.00
34.38	B	216.71
34.52	A	10.39
34.53	B	91.88

34.70	B	2738.39
34.74	A	828.03
35.06	B	234.90
35.07	A	3.10
35.16	A	6.11
35.24	B	202.51
35.29	A	124.26
35.31	B	12.51
35.47	A	109.41
35.54	B	445.41
35.87	A	186.99
36.03	B	131.83
36.05	B	259.47
36.09	A	0.01
36.11	A	35.50
36.13	B	241.10
36.16	B	257.61
36.17	A	11.60
36.48	B	71.64
36.52	A	26.73
36.57	B	137.58
36.61	A	121.85
36.88	A	3.97
36.93	B	19.77
37.64	B	269.52
37.73	A	87.99
37.83	B	8.53
37.88	A	148.40
38.29	A	0.66
38.30	B	4.33
38.39	B	4.99
38.41	A	3.81
38.59	A	218.29
38.65	B	179.97
38.71	A	20.35
38.73	B	30.87
39.02	A	169.18
39.03	B	76.41
39.22	A	3.81
39.27	B	5.26
39.37	B	3.76
39.38	A	0.69
39.43	A	0.59
39.48	B	6.75
39.68	A	1.35

39.68	B	17.93
40.30	A	19.22
40.31	B	7.26
40.43	B	37.20
40.46	A	10.26
40.53	B	54.32
40.53	A	157.69
40.63	A	0.03
40.65	B	6.25
40.95	B	728.93
40.96	A	131.73
41.01	A	75.66
41.03	B	390.90
41.09	A	14.75
41.16	B	8.08
41.36	B	406.64
41.40	A	20.22
41.63	A	52.66
41.65	B	116.95
41.73	B	20.97
41.74	A	5.49
42.58	A	3.88
42.61	B	98.94
42.94	A	0.01
43.05	B	92.56
43.06	A	30.96
43.13	A	3.42
43.13	B	142.38
43.18	B	8.08
43.25	B	8.75
43.27	A	72.28
43.32	A	81.70
43.34	A	3.80
43.38	B	407.44
43.40	B	27.78
43.48	A	1.10
43.51	B	42.92
43.64	A	8.82
43.67	B	362.77
43.74	A	59.21
43.78	B	46.96
43.93	B	1622.86
43.95	A	115.18
44.00	A	294.25
44.01	B	1412.86

44.29	A	120.30
44.30	B	681.60
44.49	B	52.50
44.52	A	18.56
44.88	A	88.52
44.97	B	1280.14
46.51	A	767.32
46.51	B	29.03
47.36	B	3.30
47.38	A	0.48
47.97	B	22.93
47.97	A	15.83
48.22	A	26.09
48.24	A	22.19
48.24	B	12.43
48.28	B	103.53
49.11	A	1474.78
49.14	B	26.97
50.09	A	60.06
50.09	B	270.09
50.98	B	829.83
51.03	A	416.14
51.97	B	598.77
51.99	A	429.72
52.78	B	576.45
52.79	A	619.92
81.15	B	3908.32
81.19	A	118.23
85.08	B	3073.06
85.15	A	2715.28
89.30	A	0.48
89.31	B	47.23
89.47	B	2.78
89.47	A	27.58
89.57	A	11.10
89.57	B	49.50
89.68	A	9.68
89.69	B	34.48
90.00	B	26.72
90.01	A	15.11
90.09	A	1.23
90.09	B	22.17
90.12	A	0.46
90.13	B	10.28
90.21	B	5.85

90.21	A	0.06
90.52	A	3.29
90.53	B	22.71
90.65	B	42.54
90.65	A	22.74
91.10	A	19.54
91.10	B	7.24
91.41	B	3.03
91.42	A	48.47
91.62	A	1.20
91.62	B	38.02
91.69	A	5.39
91.69	B	5.93
91.74	A	0.24
91.74	B	10.89
91.83	A	8.39
91.83	B	6.16
92.00	B	51.02
92.01	A	0.01
92.31	B	3.27
92.31	A	0.05
92.44	A	11.84
92.45	B	0.76
92.59	B	1.60
92.59	A	41.87
92.67	B	16.54
92.68	A	7.96
92.85	A	18.61
92.85	B	1.82
93.07	A	0.01
93.07	B	3.67
93.24	A	14.13
93.24	B	6.04
93.24	A	0.02
93.25	B	0.37
93.26	B	5.59
93.27	A	4.16
93.66	A	0.82
93.67	B	19.12
93.89	B	1.55
93.92	A	9.42
99.01	B	255.53
99.03	A	130.06

Table B-5. Solid-state DFT IR-active modes with frequencies (THz), mode symmetries, and IR intensities (km/mol) for EM-II.

Frequency (THz)	Mode Symmetry	IR Intensity (km/mol)
0.46	B2	0.32
0.65	B2	0.49
0.75	B3	0.01
0.91	B1	3.04
0.95	B1	1.88
0.95	B3	0.25
1.14	B2	0.00
1.15	B1	0.01
1.15	B3	1.43
1.36	B3	1.44
1.36	B2	0.13
1.37	B1	4.86
1.39	B3	14.56
1.55	B1	0.25
1.57	B2	0.22
1.63	B1	5.94
1.66	B2	8.14
1.68	B3	2.25
1.70	B2	0.29
1.80	B3	3.50
2.02	B1	0.94
2.11	B3	0.01
2.13	B1	13.31
2.13	B3	0.13
2.14	B2	5.20
2.15	B1	0.40
2.26	B1	9.57
2.28	B2	0.03
2.30	B3	11.31
2.30	B2	1.14
2.42	B2	0.06
2.43	B1	4.16
2.43	B3	49.69
2.48	B3	5.68
2.60	B1	1.49
2.62	B2	3.11
2.73	B3	0.08
2.77	B2	0.24
2.78	B1	4.82
2.83	B3	0.01
2.84	B2	10.22

2.86	B1	0.10
3.02	B1	2.46
3.05	B2	1.31
3.09	B1	2.48
3.10	B3	4.99
3.10	B2	0.24
3.11	B3	0.94
3.13	B1	0.04
3.16	B3	22.60
3.17	B2	10.79
3.23	B2	13.54
3.25	B1	0.59
3.29	B2	41.92
3.30	B3	23.01
3.39	B1	1.18
3.39	B3	0.04
3.44	B2	0.37
3.48	B1	8.62
3.55	B1	11.05
3.56	B3	2.06
3.63	B2	19.19
3.64	B3	1.80
3.67	B1	1.15
3.70	B3	0.94
3.73	B2	0.94
3.85	B3	10.87
3.88	B1	0.99
3.88	B2	9.95
3.92	B2	2.17
3.96	B3	7.23
4.00	B2	0.29
4.00	B1	24.75
4.10	B3	48.95
4.10	B1	0.16
4.34	B2	90.74
4.39	B1	4.68
4.42	B3	6.84
4.61	B1	0.26
4.67	B3	4.17
4.68	B2	1.06
4.79	B1	0.43
4.82	B3	45.11
4.82	B2	8.10
5.08	B1	59.73
5.16	B3	119.62

5.16	B2	12.23
5.18	B2	50.07
5.21	B3	2.75
5.31	B1	0.05
5.44	B2	91.80
5.45	B1	69.43
5.51	B3	109.02
6.19	B1	8.56
6.19	B3	76.20
6.20	B2	9.07
6.81	B1	7.60
6.88	B2	25.56
6.90	B3	298.89
7.12	B2	7.93
7.13	B1	0.00
7.15	B3	9.48
7.79	B1	5.14
7.80	B2	91.82
7.91	B3	19.58
7.99	B2	0.79
8.03	B3	71.63
8.05	B1	6.65
8.30	B3	9.93
8.43	B1	9.14
8.43	B2	31.52
8.62	B1	1.88
8.62	B3	5.66
8.63	B2	1.40
8.88	B2	4.54
8.89	B3	0.00
8.91	B1	7.68
9.23	B2	90.02
9.27	B3	153.86
9.27	B1	26.15
9.54	B2	27.15
9.55	B3	198.37
9.56	B1	10.03
9.70	B2	52.66
9.72	B1	6.71
9.73	B3	49.51
9.78	B3	57.45
9.78	B2	8.38
9.78	B1	0.73
10.30	B1	0.00
10.30	B2	1.01

10.32	B3	128.64
10.87	B1	82.57
11.02	B2	70.20
11.05	B3	66.16
11.32	B2	6.37
11.32	B3	362.32
11.34	B1	0.54
11.48	B2	0.07
11.48	B3	1.94
11.58	B1	4.76
11.91	B3	0.20
12.00	B2	1.17
12.00	B1	0.51
12.05	B3	56.77
12.05	B2	1.75
12.19	B1	28.95
12.95	B1	153.91
13.05	B2	106.07
13.08	B3	31.84
13.82	B2	0.00
13.83	B3	39.84
13.85	B1	37.92
14.25	B3	75.44
14.25	B2	8.15
14.31	B1	5.80
14.79	B3	35.30
14.82	B2	11.01
14.82	B1	27.09
15.74	B3	8.62
15.76	B2	32.26
15.76	B1	0.37
16.24	B1	110.69
16.28	B2	13.73
16.28	B3	3.53
17.54	B1	77.59
17.56	B2	21.85
17.57	B3	52.25
17.74	B3	29.03
17.75	B1	61.21
17.76	B2	10.95
17.89	B2	0.02
17.89	B3	16.33
17.91	B1	29.08
18.05	B1	49.48
18.07	B2	22.32

18.07	B3	1.91
18.54	B2	0.38
18.54	B1	0.80
18.57	B3	1.72
19.61	B1	566.23
19.63	B2	75.78
19.64	B3	535.56
19.92	B2	13.27
19.92	B3	7.60
19.95	B1	8.86
20.01	B2	54.31
20.02	B3	11.12
20.03	B1	8.72
20.56	B3	248.60
20.61	B1	103.30
20.66	B2	215.30
20.68	B2	28.53
20.69	B1	72.31
20.70	B3	12.83
21.38	B1	10.72
21.38	B2	5.20
21.38	B3	28.26
21.62	B2	120.59
21.63	B1	0.15
21.64	B3	14.99
22.07	B3	5.58
22.07	B2	35.21
22.07	B1	12.21
22.16	B3	166.87
22.20	B2	67.74
22.21	B1	47.44
22.94	B1	0.16
22.94	B3	35.87
22.94	B2	1.79
22.96	B3	90.42
22.98	B1	28.55
22.99	B2	6.12
23.22	B3	2.85
23.23	B2	5.15
23.23	B1	48.57
23.68	B2	0.00
23.68	B3	220.68
23.72	B1	9.75
23.78	B1	10.05
23.80	B2	0.00

23.81	B3	0.05
24.70	B1	17.47
24.71	B2	0.02
24.73	B3	43.92
24.89	B1	61.48
24.89	B2	0.02
24.96	B3	11.43
24.97	B2	50.25
24.97	B1	120.46
25.10	B3	0.90
25.49	B2	0.95
25.50	B1	3.83
25.52	B3	54.51
25.81	B2	427.23
25.87	B3	28.95
25.88	B1	60.89
25.94	B1	35.09
25.95	B3	131.34
25.95	B2	15.27
26.03	B1	4.55
26.07	B2	22.89
26.07	B3	12.97
26.47	B1	103.81
26.48	B3	347.20
26.48	B2	46.51
26.78	B1	90.36
26.79	B2	0.47
26.79	B3	107.41
26.87	B3	0.75
26.88	B2	1.83
26.88	B1	10.39
26.98	B2	0.13
26.98	B3	18.47
26.98	B1	1.25
27.88	B1	66.97
27.89	B2	13.70
27.90	B3	31.39
28.02	B1	0.09
28.02	B3	16.23
28.02	B2	0.47
28.03	B2	0.34
28.03	B3	3.01
28.04	B1	6.84
28.25	B1	67.70
28.27	B2	25.69

28.28	B3	138.12
28.47	B3	0.79
28.60	B2	1.06
28.60	B1	0.84
28.71	B2	30.86
28.71	B3	103.57
28.76	B1	1041.62
28.81	B2	1.15
28.81	B1	65.36
28.89	B3	4.61
29.54	B1	42.07
29.61	B2	47.62
29.62	B3	0.38
29.78	B2	49.24
29.78	B3	27.02
29.79	B1	183.89
29.83	B3	1.27
29.88	B2	13.21
29.88	B1	78.81
29.90	B2	1.26
29.91	B3	23.33
29.91	B1	0.00
30.14	B1	3.46
30.14	B3	12.25
30.14	B2	31.38
30.23	B1	33.27
30.27	B2	2.37
30.27	B3	0.05
30.63	B2	112.77
30.63	B3	24.40
30.64	B1	32.71
30.78	B3	0.00
30.80	B2	20.89
30.81	B1	17.44
31.05	B1	38.50
31.17	B3	26.39
31.17	B2	0.15
31.39	B1	187.17
31.40	B2	114.65
31.41	B3	36.19
32.30	B3	0.10
32.31	B2	7.59
32.32	B1	7.18
32.49	B3	93.54
32.51	B2	8.18

32.52	B1	45.17
32.59	B1	52.50
32.59	B2	0.63
32.60	B3	95.99
32.73	B1	24.36
32.78	B2	36.75
32.79	B3	6.06
32.86	B2	105.34
32.86	B1	2.95
32.88	B3	91.64
33.60	B2	0.11
33.60	B3	102.77
33.63	B1	30.22
33.98	B1	0.30
34.03	B2	39.23
34.03	B3	3.73
34.46	B2	43.11
34.46	B1	109.69
34.46	B3	206.31
34.54	B3	19.10
34.56	B2	11.28
34.57	B1	6.68
34.88	B1	1381.68
34.89	B2	1296.50
34.97	B3	2618.35
35.08	B1	5.38
35.09	B2	2.09
35.13	B3	1585.08
35.13	B2	205.01
35.15	B1	144.09
35.21	B1	450.63
35.23	B3	30.69
35.36	B2	9.78
35.37	B3	176.27
35.56	B2	149.87
35.58	B3	1068.14
35.59	B1	95.23
35.91	B1	421.26
36.03	B2	45.63
36.03	B3	483.38
36.04	B1	2.80
36.08	B2	124.98
36.08	B3	390.64
36.12	B2	196.88
36.14	B3	2.64

36.15	B1	21.44
36.17	B2	101.53
36.20	B1	54.87
36.21	B3	123.55
36.53	B3	163.09
36.54	B2	135.03
36.56	B1	243.35
36.66	B2	66.62
36.67	B3	20.89
36.68	B1	26.43
36.93	B1	7.25
36.97	B2	0.54
36.97	B3	36.03
37.59	B2	217.02
37.61	B3	287.09
37.65	B1	77.00
37.79	B2	37.27
37.79	B3	10.93
37.85	B1	373.86
38.39	B2	14.80
38.40	B3	0.22
38.40	B1	40.83
38.51	B3	244.14
38.53	B2	97.15
38.54	B1	203.74
38.61	B1	232.82
38.69	B3	117.15
38.69	B2	50.08
38.71	B1	30.05
38.73	B3	39.50
38.73	B2	35.05
39.02	B1	295.68
39.03	B2	3.84
39.03	B3	129.85
39.29	B1	5.94
39.35	B3	1.59
39.35	B2	0.01
39.47	B1	11.99
39.50	B2	2.17
39.50	B3	0.50
39.51	B1	6.22
39.53	B2	5.95
39.53	B3	4.54
39.74	B3	9.83
39.74	B2	0.16

39.74	B1	2.18
40.39	B3	124.26
40.40	B1	0.09
40.40	B2	21.03
40.45	B3	14.34
40.45	B1	37.92
40.45	B2	3.05
40.48	B1	9.13
40.48	B3	12.91
40.48	B2	4.30
40.61	B3	57.55
40.61	B2	3.22
40.62	B1	242.64
40.91	B2	234.03
40.93	B3	276.36
40.93	B1	384.10
41.03	B1	107.04
41.04	B3	774.45
41.05	B2	25.08
41.07	B3	837.00
41.07	B1	27.23
41.07	B2	77.86
41.32	B3	277.34
41.32	B2	5.90
41.34	B1	0.63
41.47	B3	671.00
41.48	B2	13.41
41.53	B1	133.56
41.72	B2	0.60
41.72	B3	113.57
41.77	B1	12.72
42.53	B1	12.87
42.55	B2	38.05
42.55	B3	175.93
42.88	B3	93.46
42.90	B1	23.16
42.91	B2	0.01
43.02	B3	207.46
43.05	B1	6.18
43.05	B2	13.39
43.15	B1	31.67
43.16	B2	132.56
43.17	B3	80.36
43.25	B3	596.90
43.26	B1	125.94

43.26	B2	0.23
43.29	B1	106.84
43.32	B3	10.40
43.35	B3	179.09
43.35	B2	18.25
43.36	B1	4.67
43.36	B2	27.54
43.47	B1	4.49
43.50	B3	241.62
43.50	B2	34.86
43.53	B3	2.27
43.53	B1	28.27
43.54	B2	1.20
43.64	B1	1.43
43.68	B2	51.61
43.69	B3	0.40
43.84	B1	710.02
43.84	B2	34.79
43.84	B3	1977.86
44.02	B2	6.20
44.02	B3	148.65
44.03	B1	28.67
44.17	B1	283.00
44.18	B3	3165.38
44.18	B2	83.21
44.56	B3	24.88
44.57	B2	81.66
44.57	B1	22.51
44.83	B1	462.31
44.94	B3	5209.80
44.95	B2	20.09
46.46	B1	1590.75
46.47	B2	49.62
46.47	B3	2.54
47.36	B2	1.89
47.36	B1	1.53
47.38	B3	3.17
47.99	B2	32.80
47.99	B1	13.90
48.02	B3	0.42
48.18	B1	45.39
48.24	B2	9.80
48.25	B3	183.48
48.31	B3	24.17
48.31	B2	7.81

48.32	B1	87.74
49.11	B1	2957.18
49.14	B3	26.42
49.14	B2	38.73
50.08	B3	429.84
50.09	B2	81.09
50.10	B1	82.32
50.87	B2	541.00
50.91	B3	1239.78
50.91	B1	824.59
52.03	B3	1033.75
52.03	B2	142.28
52.05	B1	803.22
52.85	B3	1276.19
52.89	B2	1.11
52.89	B1	1193.45
82.64	B2	240.02
82.65	B3	7208.23
82.67	B1	60.73
84.15	B2	6224.31
84.23	B1	6053.44
84.44	B3	96.10
89.47	B1	81.45
89.47	B2	5.13
89.47	B3	28.50
89.55	B2	3.59
89.55	B3	88.39
89.55	B1	24.41
89.71	B1	31.36
89.71	B2	6.73
89.72	B3	46.54
89.72	B1	9.31
89.73	B2	2.97
89.73	B3	35.06
89.91	B3	10.52
89.92	B2	1.60
89.92	B1	3.33

Appendix C: Supporting Information for Chapter 6

Supporting Information Table of Contents

Figure C-1. Observed powder X-ray diffraction (PXRD) pattern of EZT-MH form which was obtained by keeping EZT at room temperature at a relative humidity of 55-75% overnight.
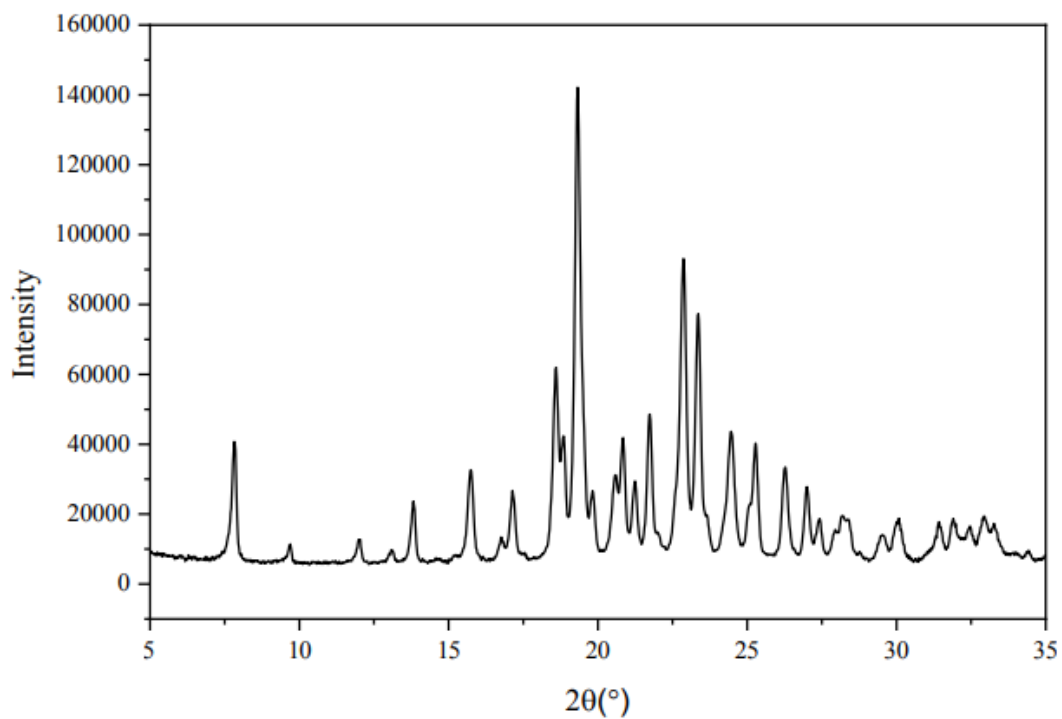
Appendix D: Supporting Information for Chapter 7

Supporting Information Table of Contents

Table D-1. Solid-state DFT IR-active modes with frequencies (THz), mode symmetries, and IR intensities (km/mol) for fully-optimized ofloxacin anhydrous.

Frequency (THz)	Mode Symmetry	Intensity (km/mol)	Frequency (THz)	Mode Symmetry	Intensity (km/mol)
0.93	Bu	1.37	7.32	Au	5.13
1.10	Bu	15.43	7.44	Au	23.78
1.16	Au	0.14	7.50	Bu	51.22
1.21	Au	3.45	7.88	Bu	48.34
1.42	Bu	1.37	8.11	Au	0.94
1.69	Au	1.17	8.47	Au	0.49
1.92	Au	5.48	8.51	Bu	66.33
2.02	Bu	4.23	8.84	Bu	12.25
2.24	Au	2.12	8.98	Au	6.90
2.27	Bu	0.12	9.54	Au	0.66
2.33	Au	7.63	9.58	Bu	19.22
2.51	Au	0.34	9.95	Bu	92.76
2.63	Bu	0.44	10.19	Au	18.09
2.82	Au	14.05	10.36	Au	7.17
2.97	Au	0.13	10.38	Bu	33.31
3.02	Bu	5.23	10.76	Au	18.40
3.32	Au	26.49	10.78	Bu	24.24
3.33	Bu	5.96	11.12	Au	1.31
3.61	Bu	26.40	11.13	Bu	68.62
3.70	Au	10.71	11.68	Bu	0.47
3.84	Bu	25.93	11.73	Au	0.57
4.20	Bu	21.54	12.18	Au	0.12
4.23	Au	3.76	12.37	Bu	205.40
4.75	Au	3.09	12.58	Au	8.33
4.76	Bu	7.74	12.65	Bu	79.00
5.07	Bu	15.36	12.81	Bu	45.96
5.14	Au	11.81	12.84	Au	5.20
5.27	Au	4.61	13.04	Bu	45.40
5.40	Bu	9.51	13.06	Au	0.32
5.94	Bu	6.72	13.43	Au	0.17
5.94	Au	0.42	13.46	Bu	33.75
6.16	Au	1.76	14.60	Au	11.50
6.21	Bu	23.28	14.62	Bu	36.37
6.49	Bu	0.60	14.83	Au	2.25
6.53	Au	0.31	14.86	Bu	12.59
6.74	Au	56.38	14.95	Bu	35.87
6.79	Bu	13.27	15.00	Au	2.15
7.20	Bu	16.84	16.29	Bu	12.72

16.33	Au	0.07	28.41	Au	19.57
16.37	Bu	15.17	28.55	Au	8.45
16.40	Au	13.22	29.04	Bu	494.82
16.73	Bu	90.47	29.07	Au	0.81
16.76	Au	21.70	29.64	Au	0.44
17.78	Bu	0.12	29.69	Bu	129.56
17.78	Au	1.27	30.02	Au	0.00
18.73	Bu	23.38	30.02	Bu	489.00
18.76	Au	2.77	30.83	Au	9.00
19.30	Bu	42.20	30.94	Bu	108.49
19.32	Au	5.87	31.01	Bu	148.42
19.75	Bu	53.55	31.04	Au	682.52
19.77	Au	0.03	31.07	Au	21.82
20.26	Bu	21.12	31.11	Bu	30.26
20.29	Au	2.89	31.25	Bu	930.47
21.03	Au	0.29	31.27	Au	69.85
21.05	Bu	175.35	31.78	Au	39.56
21.38	Bu	6.31	31.81	Bu	16.46
21.38	Au	5.65	31.95	Bu	2.75
21.86	Bu	0.50	32.01	Au	13.19
21.87	Au	13.13	32.42	Bu	180.42
22.15	Bu	40.66	32.55	Au	5.07
22.17	Au	1.89	33.17	Bu	532.50
23.08	Au	302.87	33.23	Au	2.33
23.09	Bu	2.83	33.58	Bu	229.63
23.19	Au	22.47	33.64	Au	30.95
23.20	Bu	133.27	33.76	Bu	152.99
24.76	Bu	99.86	33.77	Au	1.04
24.78	Au	20.92	33.86	Au	17.71
25.07	Bu	21.05	33.91	Bu	39.59
25.08	Au	1.44	34.14	Bu	132.89
25.25	Bu	8.81	34.14	Au	232.34
25.26	Au	9.40	34.30	Bu	452.82
25.28	Bu	61.94	34.33	Au	5.46
25.38	Au	161.50	34.76	Au	35.73
26.59	Bu	35.67	34.80	Bu	170.04
26.60	Au	4.07	35.56	Au	57.78
27.56	Bu	80.12	35.60	Bu	66.03
27.61	Au	14.06	35.66	Bu	332.09
27.91	Au	0.90	35.82	Au	0.27
27.91	Bu	8.19	36.47	Bu	175.89
28.25	Bu	9.01	36.51	Au	3.68
28.40	Bu	18.51	36.79	Au	25.68

36.82	Bu	556.01	43.05	Au	2.76
37.44	Au	3.66	43.09	Bu	99.74
37.49	Bu	228.77	43.10	Bu	760.84
38.15	Au	105.26	43.17	Au	34.45
38.18	Au	96.68	43.24	Bu	967.35
38.18	Bu	89.20	43.30	Au	16.23
38.28	Bu	24.52	43.31	Au	37.82
38.56	Bu	71.18	43.40	Bu	673.26
38.63	Au	1.22	43.47	Au	0.75
38.82	Au	48.38	43.50	Bu	257.46
38.90	Bu	578.47	43.62	Bu	32.33
39.10	Bu	58.89	43.67	Bu	1458.98
39.13	Au	5.26	43.68	Au	59.90
39.44	Au	0.79	43.72	Au	0.44
39.46	Bu	12.66	44.48	Bu	230.91
39.59	Au	0.00	44.49	Au	16.07
39.66	Bu	136.82	45.60	Bu	2951.50
39.85	Bu	95.00	45.64	Au	137.48
39.90	Au	1.12	46.00	Bu	200.82
40.06	Bu	319.92	46.02	Au	30.93
40.14	Au	0.00	46.66	Bu	384.43
40.49	Bu	313.22	46.70	Au	27.57
40.58	Au	5.45	47.70	Au	6.52
40.63	Bu	78.47	47.71	Bu	78.35
40.66	Au	26.42	48.22	Bu	2347.14
40.85	Au	13.56	48.26	Au	40.00
40.91	Bu	36.69	51.03	Bu	3700.60
41.02	Au	13.52	51.21	Au	0.95
41.12	Bu	239.95	73.86	Bu	4517.89
41.17	Bu	106.24	74.03	Au	44.15
41.25	Au	16.01	84.56	Bu	627.11
41.73	Au	50.89	84.59	Au	20.48
41.73	Bu	609.56	85.06	Bu	288.20
42.08	Bu	4.63	85.09	Au	457.18
42.11	Bu	521.47	85.72	Bu	1214.26
42.14	Au	2.04	85.79	Au	26.85
42.18	Au	0.00	87.58	Bu	198.33
42.80	Bu	2.92	87.59	Au	156.74
42.82	Au	0.71	88.05	Au	1.11
42.82	Au	10.10	88.06	Bu	828.64
42.87	Bu	374.41	89.35	Au	182.06
42.95	Bu	390.75	89.36	Bu	55.90
42.96	Au	42.61	89.50	Bu	33.86

89.50	Au	26.87
89.70	Bu	367.23
89.70	Au	30.01
89.83	Bu	139.12
89.84	Au	3.96
90.37	Au	1.24
90.38	Bu	43.22
91.16	Bu	96.94
91.18	Au	0.13
91.24	Bu	28.58
91.24	Au	79.98
91.61	Bu	30.98
91.62	Au	0.22
91.89	Bu	84.21
91.92	Au	10.33
91.97	Au	6.82
91.97	Bu	28.70
92.07	Bu	59.54
92.09	Au	2.40
92.76	Bu	21.17
92.79	Au	0.05
93.43	Bu	883.93
93.49	Au	5.39
94.83	Au	1.27
94.84	Bu	112.33

Table D-2. Solid-state DFT IR-active modes with frequencies (THz), mode symmetries, and IR intensities (km/mol) for fixed-lattice ofloxacin anhydrous optimization.

Frequency (THz)	Mode Symmetry	Intensity (km/mol)	Frequency (THz)	Mode Symmetry	Intensity (km/mol)
0.83	Bu	0.74	7.28	Au	13.98
1.01	Au	1.29	7.38	Au	11.82
1.06	Bu	10.68	7.40	Bu	31.89
1.08	Au	1.37	7.85	Bu	49.04
1.33	Bu	0.70	8.01	Au	0.53
1.56	Au	1.76	8.41	Au	0.98
1.76	Au	5.24	8.46	Bu	62.43
1.88	Bu	3.72	8.78	Bu	10.73
2.03	Au	0.83	8.86	Au	5.34
2.15	Bu	0.83	9.49	Au	0.33
2.24	Au	12.19	9.52	Bu	16.34
2.41	Au	0.08	9.95	Bu	95.14
2.54	Bu	1.14	10.11	Au	20.80
2.66	Au	13.73	10.34	Au	5.02
2.86	Au	1.00	10.34	Bu	33.55
2.91	Bu	5.05	10.73	Au	14.72
3.13	Au	20.18	10.75	Bu	22.59
3.14	Bu	4.34	11.09	Bu	72.85
3.40	Bu	44.39	11.09	Au	1.79
3.58	Au	12.06	11.64	Bu	1.45
3.63	Bu	11.99	11.70	Au	0.42
4.11	Bu	11.65	12.21	Au	0.42
4.14	Au	3.03	12.31	Bu	183.22
4.66	Bu	10.92	12.55	Au	8.75
4.68	Au	3.12	12.60	Bu	96.25
5.01	Bu	18.60	12.79	Bu	43.06
5.05	Au	10.82	12.82	Au	4.38
5.25	Au	6.09	13.01	Bu	30.70
5.34	Bu	14.50	13.03	Au	0.27
5.87	Au	0.12	13.40	Au	0.13
5.89	Bu	5.44	13.44	Bu	33.24
6.05	Au	0.73	14.58	Au	10.61
6.07	Bu	12.65	14.59	Bu	40.11
6.36	Bu	5.24	14.81	Au	2.39
6.41	Au	0.28	14.82	Bu	7.72
6.69	Au	54.94	14.94	Bu	29.71
6.73	Bu	14.10	14.97	Au	2.28
7.20	Bu	4.96	16.25	Bu	10.46

16.30	Au	0.18	28.36	Bu	23.76
16.36	Bu	16.42	28.44	Au	6.14
16.38	Au	13.03	29.01	Bu	442.23
16.71	Bu	88.17	29.06	Au	1.40
16.75	Au	22.02	29.62	Au	0.07
17.75	Bu	0.23	29.66	Bu	89.96
17.77	Au	0.91	30.01	Au	0.06
18.73	Bu	18.89	30.02	Bu	528.51
18.75	Au	2.87	30.80	Au	19.84
19.29	Bu	40.79	30.89	Bu	68.98
19.31	Au	4.49	30.97	Bu	176.66
19.75	Bu	54.18	30.97	Au	659.60
19.78	Au	0.04	31.07	Au	36.49
20.27	Bu	19.60	31.10	Bu	28.31
20.29	Au	2.56	31.23	Bu	913.26
21.02	Au	0.45	31.24	Au	63.39
21.03	Bu	141.86	31.76	Au	37.38
21.37	Bu	2.84	31.79	Bu	28.96
21.38	Au	4.64	31.94	Bu	10.37
21.86	Bu	0.65	31.99	Au	14.27
21.86	Au	12.75	32.39	Bu	195.30
22.14	Bu	43.46	32.52	Au	5.73
22.16	Au	1.46	33.12	Bu	515.15
23.07	Bu	3.15	33.21	Au	1.58
23.08	Au	305.03	33.55	Bu	235.03
23.19	Au	23.08	33.62	Au	27.16
23.19	Bu	134.16	33.74	Bu	129.48
24.74	Bu	89.13	33.75	Au	0.04
24.76	Au	21.18	33.83	Au	22.64
25.06	Bu	13.43	33.88	Bu	58.49
25.07	Au	0.26	34.11	Au	215.61
25.18	Bu	10.51	34.11	Bu	201.14
25.24	Au	30.52	34.30	Bu	398.73
25.27	Bu	67.59	34.33	Au	18.73
25.34	Au	134.38	34.74	Au	30.84
26.54	Au	2.94	34.78	Bu	161.97
26.57	Bu	40.16	35.56	Au	59.47
27.53	Bu	68.10	35.60	Bu	103.90
27.59	Au	13.48	35.62	Bu	278.86
27.88	Au	1.42	35.76	Au	0.47
27.90	Bu	4.79	36.45	Bu	168.76
28.13	Bu	7.52	36.50	Au	3.01
28.35	Au	20.40	36.75	Au	24.72

36.79	Bu	605.62	43.04	Au	0.58
37.43	Au	4.85	43.08	Bu	908.05
37.46	Bu	229.02	43.08	Bu	139.88
38.14	Au	95.09	43.14	Au	27.85
38.16	Au	106.29	43.21	Bu	782.93
38.17	Bu	64.68	43.26	Au	0.10
38.25	Bu	14.63	43.31	Au	52.83
38.53	Bu	73.26	43.37	Bu	665.82
38.60	Au	0.16	43.46	Au	3.48
38.79	Au	54.26	43.48	Bu	215.87
38.88	Bu	596.29	43.57	Bu	162.76
39.06	Bu	39.44	43.63	Au	57.61
39.09	Au	5.17	43.65	Bu	1154.27
39.47	Au	0.12	43.66	Au	0.03
39.49	Bu	1.61	44.45	Bu	254.30
39.59	Au	0.00	44.45	Au	14.74
39.65	Bu	109.02	45.59	Bu	3033.98
39.82	Bu	91.92	45.63	Au	136.66
39.86	Au	1.05	45.97	Bu	164.59
40.05	Bu	283.25	45.98	Au	24.88
40.12	Au	0.00	46.59	Bu	355.41
40.48	Bu	323.37	46.64	Au	24.58
40.55	Au	8.24	47.65	Au	6.18
40.63	Bu	115.07	47.67	Bu	60.57
40.65	Au	23.33	48.21	Bu	2296.29
40.81	Au	9.42	48.24	Au	41.66
40.86	Bu	33.57	51.03	Bu	3682.32
41.01	Au	11.11	51.21	Au	1.64
41.09	Bu	177.24	74.25	Bu	4401.08
41.15	Bu	100.34	74.40	Au	48.73
41.21	Au	18.37	84.51	Bu	503.21
41.68	Bu	601.30	84.52	Au	5.23
41.68	Au	52.90	84.77	Bu	433.92
42.06	Bu	16.92	84.81	Au	455.63
42.07	Bu	503.82	85.45	Bu	1288.52
42.13	Au	1.27	85.53	Au	31.32
42.15	Au	0.00	87.33	Bu	240.21
42.80	Bu	4.41	87.33	Au	182.24
42.80	Au	2.98	88.05	Au	0.02
42.83	Au	11.76	88.06	Bu	694.51
42.86	Bu	401.89	89.37	Au	181.65
42.94	Au	48.52	89.37	Bu	42.99
42.94	Bu	297.36	89.39	Bu	10.35

89.41	Au	20.75
89.63	Bu	349.84
89.64	Au	34.24
89.77	Bu	98.76
89.77	Au	5.17
90.16	Bu	69.64
90.17	Au	0.35
91.16	Bu	28.18
91.16	Au	81.89
91.21	Au	0.53
91.22	Bu	91.31
91.49	Bu	23.74
91.49	Au	0.21
91.80	Au	10.46
91.80	Bu	6.83
91.86	Au	6.50
91.86	Bu	11.37
92.01	Bu	20.92
92.01	Au	1.42
92.69	Bu	12.56
92.69	Au	0.13
93.49	Bu	785.01
93.55	Au	4.82
94.68	Au	2.07
94.68	Bu	63.32

Table D-3. Solid-state DFT IR-active modes with frequencies (THz), mode symmetries, and IR intensities (km/mol) for fully-optimized gamma polymorph of levofloxacin.

Frequency (THz)	Mode Symmetry	Intensity (km/mol)	Frequency (THz)	Mode Symmetry	Intensity (km/mol)
0.93	B	4.11	7.53	B	6.53
1.01	A	0.81	7.69	B	19.73
1.18	B	2.07	7.90	A	2.16
1.38	B	0.26	7.94	B	14.50
1.39	A	0.66	7.98	A	0.01
1.47	A	0.01	8.65	B	7.04
1.71	A	0.01	8.66	A	11.12
1.75	B	5.00	8.81	B	6.67
1.93	A	0.20	8.83	A	3.88
2.01	A	0.00	9.33	A	1.04
2.16	B	2.56	9.39	B	40.82
2.22	A	8.29	9.56	A	27.42
2.38	B	1.68	9.57	B	10.34
2.67	A	8.81	10.37	A	0.04
2.73	B	0.94	10.38	B	16.93
2.87	A	0.13	10.76	A	1.60
2.87	B	0.52	10.86	B	6.51
3.18	A	0.56	11.11	A	1.57
3.26	A	13.82	11.15	B	58.16
3.27	B	15.10	11.58	B	12.08
3.63	B	1.45	11.72	A	0.01
4.16	A	2.46	12.25	A	7.12
4.22	B	5.27	12.28	B	90.48
4.52	B	3.80	12.37	A	0.09
4.73	A	0.22	12.44	B	9.76
4.89	B	1.05	12.71	A	0.17
4.94	A	6.82	12.73	B	12.78
5.45	B	6.04	13.02	B	3.18
5.49	A	5.41	13.03	A	0.41
5.63	B	6.50	13.39	A	0.10
5.76	A	0.90	13.42	B	9.20
5.98	B	1.98	14.64	A	2.42
6.01	A	4.49	14.67	B	9.07
6.54	B	7.87	14.71	B	16.11
6.58	A	30.33	14.79	A	2.59
6.65	A	2.18	14.80	B	26.33
6.70	B	13.52	14.84	A	0.46
7.52	A	2.40	16.00	B	27.39

16.05	A	7.01	28.36	B	19.56
16.26	B	19.94	28.37	A	1.31
16.28	A	9.34	29.04	B	259.41
16.65	B	10.54	29.06	A	5.58
16.69	A	8.60	29.75	A	9.23
17.54	B	0.27	29.81	B	18.59
17.58	A	2.52	29.86	A	2.33
18.82	A	0.24	29.92	B	245.57
18.85	B	21.03	30.72	A	18.21
19.01	A	0.04	30.78	B	84.46
19.01	B	13.13	30.85	A	318.13
19.55	A	2.84	30.90	B	39.80
19.56	B	25.21	30.97	B	10.17
20.15	B	4.18	30.99	A	33.20
20.19	A	0.01	31.16	B	439.57
21.04	A	0.09	31.22	A	10.54
21.05	B	27.34	31.59	B	2.56
21.07	B	37.20	31.75	A	2.87
21.09	A	0.48	31.80	B	7.43
21.65	B	4.38	31.84	A	4.47
21.68	A	0.94	32.53	B	65.64
22.11	B	21.05	32.54	A	52.60
22.12	A	1.06	33.15	A	6.79
22.98	B	0.61	33.17	B	226.73
22.99	A	117.77	33.64	B	66.52
23.25	A	39.59	33.67	A	10.81
23.27	B	16.23	33.71	A	0.68
24.76	A	12.35	33.74	B	50.80
24.81	B	4.41	33.91	A	42.08
24.88	B	3.89	33.92	B	131.53
24.88	A	62.28	34.38	B	185.60
24.90	B	30.77	34.40	A	4.87
24.90	A	3.80	34.53	B	135.57
25.25	A	2.80	34.53	A	58.92
25.27	B	12.68	34.91	A	4.74
26.65	B	21.53	34.92	B	84.83
26.68	A	12.94	35.58	B	148.67
27.65	B	11.55	35.68	A	8.78
27.70	A	0.11	35.78	A	0.06
27.83	B	0.70	35.81	B	131.86
28.01	A	2.69	36.68	B	29.76
28.05	B	46.16	36.73	A	3.66
28.20	A	12.05	36.73	A	28.96

36.89	B	346.20	42.98	B	978.35
37.50	B	127.60	43.12	A	1.10
37.50	A	4.18	43.16	A	32.73
38.27	A	28.08	43.17	B	22.15
38.28	B	136.12	43.33	B	45.12
38.30	A	29.55	43.34	A	14.86
38.32	B	39.83	43.41	B	158.65
38.62	B	42.73	43.44	A	4.06
38.66	A	4.50	43.53	B	7.94
38.78	A	16.65	43.54	A	27.13
38.86	B	396.57	43.60	B	171.83
39.09	A	0.03	43.61	A	1.79
39.15	B	24.09	43.85	A	0.59
39.52	B	2.09	43.90	B	1856.72
39.56	A	1.56	44.72	B	155.00
39.63	B	181.09	44.85	A	5.16
39.71	A	0.07	45.42	A	23.24
40.02	A	0.21	45.56	B	1503.67
40.04	B	5.58	45.83	B	21.21
40.18	A	4.29	45.91	A	2.32
40.18	B	139.32	46.32	B	146.29
40.64	A	8.30	46.41	A	0.22
40.66	B	124.70	47.64	B	2.12
40.79	B	66.62	47.70	A	2.22
40.86	A	3.63	48.08	A	0.01
40.97	B	45.36	48.14	B	1425.55
40.98	A	5.69	51.01	B	2023.96
41.17	A	16.13	51.07	A	0.51
41.19	B	6.91	76.21	A	1.46
41.34	A	5.48	76.21	B	2398.70
41.34	B	68.94	83.98	B	190.83
41.77	B	294.99	84.07	A	139.88
41.81	A	6.38	84.64	B	462.62
42.12	B	30.68	84.68	A	148.39
42.14	A	0.33	86.09	A	154.96
42.33	B	167.40	86.10	B	27.53
42.35	A	7.38	88.06	A	81.33
42.65	B	17.63	88.06	B	78.36
42.67	A	4.21	89.05	A	10.25
42.76	A	3.77	89.07	B	173.31
42.85	A	27.48	89.46	A	0.98
42.85	B	45.42	89.46	B	75.63
42.90	B	65.64	89.58	B	103.47

89.60	A	28.18
89.62	B	65.83
89.63	A	0.34
90.48	B	74.76
90.49	A	33.99
90.51	B	49.28
90.53	A	16.03
90.67	B	50.97
90.68	A	4.03
91.45	B	38.93
91.47	A	9.08
91.94	B	3.74
91.95	A	0.57
92.00	B	15.20
92.00	A	16.42
92.11	A	1.39
92.12	B	36.15
92.38	B	20.46
92.39	A	10.58
92.94	B	12.55
92.94	A	0.20
93.31	B	308.04
93.40	A	0.26
94.48	B	5.08
94.48	A	0.16

Table D-4. Solid-state DFT IR-active modes with frequencies (THz), mode symmetries, and IR intensities (km/mol) for fully-optimized alpha polymorph of levofloxacin.

Frequency (THz)	Mode Symmetry	Intensity (km/mol)	Frequency (THz)	Mode Symmetry	Intensity (km/mol)
0.76	B1	2.81	4.70	B3	1.22
0.92	B1	2.55	4.94	B1	0.59
0.96	B3	0.01	4.99	B2	7.18
0.97	B1	0.84	5.08	B3	21.11
1.08	B2	0.53	5.23	B2	0.04
1.09	B3	2.82	5.34	B3	2.61
1.15	B2	0.76	5.39	B1	8.52
1.29	B2	1.53	5.80	B1	0.31
1.50	B3	0.05	5.81	B3	4.51
1.54	B3	3.53	5.84	B2	0.18
1.56	B1	0.28	5.98	B3	12.27
1.74	B2	0.14	6.03	B1	0.00
1.75	B1	5.90	6.36	B2	4.14
1.81	B3	13.13	6.69	B2	57.46
1.82	B1	0.04	6.77	B3	0.97
1.98	B2	2.40	6.90	B1	11.48
2.05	B3	0.46	7.30	B2	29.72
2.31	B2	12.07	7.39	B1	1.17
2.49	B2	14.28	7.43	B3	12.03
2.54	B3	0.15	7.48	B3	15.30
2.67	B2	14.15	7.54	B2	0.00
2.81	B1	0.70	7.61	B1	2.62
2.90	B2	11.11	7.82	B1	27.74
3.10	B3	0.61	8.02	B3	33.17
3.17	B1	0.35	8.04	B2	0.71
3.24	B3	0.10	8.11	B3	0.96
3.26	B1	0.23	8.14	B2	1.47
3.28	B2	7.45	8.16	B1	8.86
3.41	B1	19.84	8.35	B1	9.36
3.58	B3	32.99	8.41	B2	1.90
3.69	B2	0.82	8.44	B3	58.73
3.92	B3	0.01	8.72	B3	0.29
3.98	B1	1.29	8.75	B1	0.05
4.07	B3	12.17	8.83	B2	2.45
4.07	B2	1.34	9.45	B3	34.83
4.21	B1	3.65	9.50	B1	0.00
4.50	B2	11.75	9.57	B2	0.00
4.58	B1	0.18	9.86	B1	107.21

9.90	B3	2.72	16.43	B2	17.93
10.01	B2	13.73	16.66	B2	9.99
10.36	B2	1.58	16.69	B1	33.19
10.37	B1	86.96	16.70	B3	48.22
10.43	B3	4.05	17.74	B1	0.05
10.72	B2	10.51	17.75	B2	6.97
10.76	B3	1.27	17.76	B3	0.49
10.78	B1	4.08	18.76	B2	0.61
10.98	B3	96.30	18.76	B3	13.39
11.01	B2	1.93	18.76	B1	0.75
11.06	B1	1.42	19.25	B1	53.77
11.66	B2	0.02	19.26	B2	7.59
11.68	B1	1.63	19.27	B3	8.39
11.76	B3	0.57	19.69	B2	0.14
12.25	B2	0.00	19.74	B1	35.20
12.34	B3	246.47	19.74	B3	7.76
12.38	B1	1.89	20.26	B1	7.35
12.47	B2	1.43	20.29	B3	10.97
12.59	B3	0.14	20.29	B2	2.53
12.63	B1	9.33	21.04	B2	3.83
12.78	B2	1.20	21.05	B3	6.20
12.80	B1	23.94	21.06	B1	50.06
12.82	B3	0.00	21.26	B2	2.46
13.03	B1	4.49	21.26	B1	15.61
13.07	B3	8.15	21.27	B3	1.47
13.08	B2	5.57	21.78	B2	15.03
13.29	B2	0.37	21.81	B3	7.73
13.33	B1	12.07	21.82	B1	0.68
13.35	B3	16.91	22.12	B3	1.99
14.63	B3	40.06	22.15	B2	0.17
14.71	B2	1.96	22.15	B1	16.00
14.71	B1	12.57	22.94	B2	299.48
14.77	B2	1.22	23.15	B3	0.36
14.78	B3	26.51	23.15	B1	0.06
14.80	B1	3.73	23.21	B2	20.21
14.90	B3	13.05	23.22	B1	112.89
14.90	B1	3.29	23.22	B3	5.97
14.93	B2	7.29	24.70	B2	17.03
16.11	B1	7.30	24.72	B1	23.11
16.11	B3	14.27	24.75	B3	37.96
16.19	B2	0.01	24.94	B2	138.50
16.42	B3	22.65	24.97	B3	3.73
16.42	B1	0.58	24.98	B1	0.74

25.12	B1	1.96	31.72	B1	3.93
25.13	B3	13.47	31.73	B3	0.38
25.14	B2	0.42	31.82	B1	5.87
25.30	B3	9.00	31.83	B3	18.60
25.30	B1	81.59	31.90	B2	51.07
25.30	B2	22.79	32.52	B1	136.44
26.56	B2	2.13	32.56	B3	98.08
26.57	B1	0.27	32.57	B2	4.69
26.58	B3	71.07	33.06	B1	478.86
27.16	B1	9.94	33.14	B3	187.95
27.16	B3	1.63	33.18	B2	2.65
27.17	B2	27.98	33.49	B3	153.49
27.60	B3	0.08	33.49	B2	10.20
27.61	B1	32.99	33.52	B1	120.83
27.62	B2	11.19	33.62	B2	4.46
27.87	B1	8.97	33.63	B1	507.54
27.90	B3	2.52	33.65	B3	32.29
27.91	B2	0.47	33.72	B2	23.57
28.41	B2	17.28	33.73	B1	5.45
28.45	B3	47.13	33.75	B3	0.71
28.49	B1	0.34	34.14	B1	2.76
29.07	B1	74.68	34.15	B3	95.88
29.09	B3	292.09	34.24	B2	151.41
29.10	B2	0.16	34.30	B2	37.71
29.69	B3	189.68	34.33	B1	258.74
29.72	B2	0.02	34.35	B3	82.26
29.75	B1	7.35	34.74	B1	29.05
29.94	B1	28.58	34.76	B3	82.27
29.94	B2	0.01	34.82	B2	0.07
29.94	B3	359.63	35.42	B2	16.10
30.63	B3	0.17	35.42	B1	321.90
30.63	B1	3.06	35.44	B2	28.00
30.63	B2	765.18	35.45	B3	231.77
30.81	B2	12.20	35.51	B3	73.36
30.85	B1	46.33	35.51	B1	6.12
30.87	B3	3.40	36.49	B1	328.67
31.07	B1	125.75	36.53	B3	673.05
31.10	B3	17.14	36.56	B2	0.04
31.10	B2	17.17	36.62	B1	11.79
31.35	B1	711.32	36.64	B3	110.17
31.36	B2	2.59	36.67	B2	39.08
31.38	B3	7.12	37.40	B3	20.52
31.72	B2	14.85	37.41	B2	0.88

37.42	B1	148.95	41.80	B1	24.60
38.06	B1	142.24	41.80	B3	909.91
38.06	B2	223.61	41.83	B2	2.92
38.07	B3	48.39	42.14	B1	537.42
38.12	B2	5.65	42.15	B2	6.57
38.13	B3	3.06	42.16	B3	45.91
38.22	B1	0.77	42.25	B1	0.08
38.33	B2	25.42	42.28	B3	0.28
38.35	B3	16.51	42.29	B2	0.55
38.37	B1	49.88	42.76	B2	0.56
38.68	B2	0.20	42.76	B3	100.74
38.71	B3	867.23	42.77	B1	5.14
38.81	B1	60.20	42.91	B2	8.44
39.08	B1	47.01	42.96	B1	0.19
39.10	B2	2.79	42.97	B2	0.02
39.11	B3	98.72	42.97	B3	293.99
39.32	B2	0.00	43.04	B3	53.95
39.33	B3	13.99	43.08	B1	251.10
39.33	B1	3.08	43.09	B3	250.89
39.48	B3	240.34	43.11	B1	4.83
39.50	B1	43.23	43.17	B2	34.13
39.51	B2	4.22	43.18	B3	1128.75
39.84	B1	249.25	43.22	B1	116.75
39.89	B3	12.36	43.26	B2	43.28
39.90	B2	0.09	43.33	B2	2.57
39.95	B1	15.99	43.37	B1	71.35
39.96	B3	187.66	43.40	B3	149.29
40.00	B2	0.19	43.46	B3	289.94
40.52	B3	403.51	43.48	B1	26.02
40.54	B1	80.18	43.50	B2	0.39
40.57	B2	10.18	43.60	B3	1827.83
40.67	B3	7.14	43.66	B1	73.19
40.67	B2	18.42	43.66	B2	0.20
40.68	B1	80.73	43.77	B1	115.68
40.74	B2	23.31	43.79	B3	25.49
40.74	B3	10.26	43.81	B2	17.34
40.77	B1	7.17	43.83	B2	9.41
40.95	B3	158.11	43.87	B1	40.08
40.99	B2	0.49	43.89	B3	551.03
40.99	B1	0.61	44.34	B2	1.96
41.13	B1	17.71	44.54	B1	0.00
41.20	B3	42.12	44.54	B3	36.89
41.24	B2	28.60	45.42	B2	16.29

45.74	B1	1582.27	89.75	B1	26.08
45.80	B3	2063.64	89.98	B3	17.28
46.11	B1	68.10	89.99	B2	22.05
46.12	B3	284.58	89.99	B1	1.94
46.19	B2	0.59	90.07	B2	36.20
46.50	B1	183.43	90.08	B3	149.04
46.53	B3	0.16	90.08	B1	20.96
46.60	B2	1.59	90.61	B3	33.40
47.59	B2	3.52	90.61	B1	6.51
47.77	B3	241.12	90.62	B2	2.61
47.90	B1	0.33	91.27	B2	13.29
48.16	B2	1.32	91.27	B3	3.43
48.26	B3	2206.97	91.28	B1	3.68
48.38	B1	23.08	91.51	B1	16.87
51.21	B1	2406.82	91.53	B3	23.90
51.28	B3	581.68	91.55	B2	7.78
51.43	B2	0.97	91.60	B2	40.96
76.04	B2	0.10	91.60	B3	6.00
76.14	B1	1665.78	91.60	B1	15.36
76.19	B3	2454.77	92.15	B2	1.89
83.89	B2	318.00	92.16	B3	22.46
83.89	B1	0.51	92.16	B1	21.12
83.89	B3	4.73	92.53	B1	12.31
84.20	B1	1499.26	92.54	B3	14.62
84.21	B3	121.53	92.55	B2	4.81
84.33	B2	150.71	92.79	B3	13.66
85.80	B1	713.10	92.80	B1	41.35
85.81	B3	30.72	92.81	B2	0.02
85.87	B2	92.01	93.75	B1	19.05
87.17	B2	214.94	93.75	B3	14.91
87.17	B1	95.67	93.75	B2	2.23
87.17	B3	93.74	94.56	B1	9.15
88.19	B2	0.06	94.56	B3	27.57
88.19	B1	264.53	94.57	B2	0.23
88.20	B3	441.13			
89.56	B2	311.38			
89.56	B1	5.43			
89.56	B3	48.36			
89.57	B1	14.18			
89.57	B3	26.12			
89.58	B2	1.40			
89.74	B2	9.68			
89.74	B3	29.69			

Table D-5. Solid-state DFT IR-active modes with frequencies (THz), mode symmetries, and IR intensities (km/mol) for fixed-lattice alpha polymorph of levofloxacin simulation.

Frequency (THz)	Mode Symmetry	Intensity (km/mol)	Frequency (THz)	Mode Symmetry	Intensity (km/mol)
0.77	B1	2.87	4.60	B3	1.19
0.88	B1	0.12	4.90	B1	0.74
0.92	B1	4.75	4.97	B2	7.70
0.94	B3	0.06	5.04	B3	22.66
1.00	B2	0.95	5.18	B2	0.04
1.05	B3	3.06	5.30	B3	1.68
1.17	B2	0.19	5.35	B1	16.08
1.22	B2	1.82	5.75	B1	0.42
1.38	B3	0.03	5.77	B3	4.45
1.47	B3	2.86	5.80	B2	0.17
1.47	B1	0.23	5.97	B3	13.68
1.65	B2	0.00	6.01	B1	0.15
1.68	B1	2.74	6.30	B2	3.01
1.70	B3	13.92	6.66	B2	57.81
1.74	B1	0.60	6.73	B3	0.82
1.87	B2	3.32	6.84	B1	7.15
1.95	B3	0.00	7.26	B2	27.09
2.17	B2	19.34	7.33	B1	2.63
2.40	B2	12.14	7.36	B3	19.79
2.47	B3	0.17	7.42	B3	11.54
2.53	B2	7.25	7.46	B2	0.01
2.73	B1	0.79	7.53	B1	2.26
2.82	B2	10.43	7.80	B1	31.81
2.98	B3	0.44	7.93	B3	25.71
3.04	B1	0.08	7.96	B2	2.02
3.12	B3	0.04	8.00	B3	6.82
3.16	B1	0.52	8.02	B1	6.94
3.19	B2	7.21	8.04	B2	0.16
3.26	B1	17.91	8.32	B1	8.12
3.43	B3	29.24	8.39	B2	2.39
3.59	B2	1.32	8.40	B3	65.62
3.78	B3	0.24	8.70	B3	0.17
3.80	B1	1.24	8.73	B1	0.27
4.01	B2	1.05	8.79	B2	2.50
4.03	B3	14.27	9.42	B3	33.01
4.15	B1	1.93	9.45	B1	0.64
4.46	B2	11.30	9.53	B2	0.09
4.53	B1	0.09	9.84	B1	112.50

9.86	B3	4.78	16.41	B2	17.43
9.97	B2	14.30	16.63	B2	10.99
10.34	B1	79.26	16.66	B1	30.69
10.34	B2	1.42	16.67	B3	49.63
10.39	B3	2.89	17.71	B1	0.40
10.69	B2	10.43	17.72	B2	6.55
10.73	B3	0.71	17.74	B3	0.58
10.74	B1	2.48	18.75	B3	13.90
10.97	B3	97.55	18.75	B2	0.52
10.98	B2	1.54	18.76	B1	1.60
11.03	B1	3.64	19.24	B1	54.08
11.64	B2	0.02	19.24	B2	7.10
11.67	B1	1.39	19.26	B3	8.00
11.72	B3	0.16	19.69	B2	0.09
12.24	B2	0.01	19.72	B1	42.14
12.31	B3	227.97	19.73	B3	6.61
12.36	B1	1.80	20.27	B1	10.55
12.46	B2	1.61	20.28	B3	11.56
12.56	B3	1.98	20.28	B2	2.42
12.60	B1	13.13	21.04	B3	5.78
12.77	B2	1.02	21.04	B2	3.32
12.79	B1	23.30	21.05	B1	51.35
12.80	B3	0.00	21.25	B1	15.56
13.00	B1	2.07	21.25	B3	0.99
13.04	B3	7.39	21.25	B2	3.34
13.05	B2	5.93	21.77	B2	14.20
13.28	B2	0.44	21.80	B3	7.64
13.31	B1	10.52	21.80	B1	1.74
13.32	B3	15.56	22.11	B2	0.17
14.62	B3	40.55	22.12	B3	1.64
14.68	B2	1.80	22.14	B1	11.39
14.69	B1	11.63	22.94	B2	299.74
14.76	B2	1.03	23.13	B3	0.36
14.77	B3	23.78	23.13	B1	0.00
14.78	B1	4.40	23.19	B2	20.30
14.87	B3	13.45	23.20	B1	122.85
14.88	B1	4.67	23.20	B3	5.81
14.91	B2	6.81	24.69	B2	17.55
16.07	B1	6.81	24.69	B1	24.37
16.08	B3	12.68	24.71	B3	36.10
16.16	B2	0.03	24.88	B2	132.35
16.39	B3	26.05	24.93	B3	2.81
16.40	B1	0.19	24.94	B1	1.07

25.10	B1	2.73	31.70	B1	6.27
25.12	B3	11.08	31.71	B3	0.06
25.13	B2	0.00	31.78	B1	5.47
25.28	B2	27.67	31.79	B3	13.99
25.29	B1	72.45	31.86	B2	51.28
25.30	B3	8.97	32.50	B1	156.82
26.53	B1	0.18	32.53	B3	78.17
26.54	B2	2.21	32.55	B2	3.72
26.55	B3	70.80	33.03	B1	474.80
27.14	B1	10.88	33.11	B3	171.46
27.15	B3	1.83	33.15	B2	3.61
27.16	B2	28.66	33.46	B3	159.02
27.57	B3	0.01	33.47	B2	10.28
27.58	B1	31.29	33.49	B1	145.39
27.59	B2	9.37	33.59	B2	5.14
27.85	B1	6.42	33.60	B1	494.46
27.87	B3	2.02	33.62	B3	31.48
27.89	B2	0.42	33.69	B1	2.35
28.39	B2	16.29	33.70	B2	21.77
28.43	B3	39.72	33.72	B3	0.09
28.47	B1	0.19	34.13	B3	89.87
29.05	B1	81.46	34.13	B1	0.42
29.08	B2	0.19	34.22	B2	111.21
29.08	B3	301.41	34.28	B2	75.88
29.66	B3	157.98	34.32	B1	268.08
29.70	B2	0.07	34.34	B3	81.19
29.71	B1	8.73	34.73	B1	38.68
29.92	B2	0.01	34.74	B3	74.84
29.93	B1	29.92	34.80	B2	0.21
29.93	B3	397.93	35.39	B2	0.36
30.59	B3	0.12	35.40	B1	321.80
30.59	B1	2.92	35.43	B3	210.12
30.59	B2	766.83	35.44	B2	40.18
30.80	B2	10.61	35.51	B3	104.38
30.83	B1	44.83	35.51	B1	0.49
30.86	B3	0.80	36.48	B1	348.90
31.05	B1	121.28	36.52	B3	679.76
31.08	B3	21.03	36.54	B2	0.59
31.08	B2	17.88	36.61	B1	15.22
31.32	B1	689.33	36.63	B3	80.04
31.35	B2	3.54	36.66	B2	40.07
31.35	B3	5.40	37.38	B3	29.93
31.70	B2	14.77	37.40	B2	1.12

37.40	B1	175.80	41.76	B1	16.70
38.05	B2	215.52	41.77	B3	964.88
38.05	B1	123.47	41.79	B2	3.44
38.06	B3	35.40	42.10	B1	510.64
38.12	B2	12.20	42.11	B2	5.69
38.13	B3	4.41	42.13	B3	23.43
38.20	B1	0.09	42.23	B1	1.95
38.33	B2	21.86	42.25	B3	1.62
38.34	B3	27.74	42.26	B2	0.57
38.35	B1	30.95	42.77	B2	0.63
38.64	B2	0.57	42.77	B3	77.22
38.66	B3	920.05	42.78	B1	6.82
38.75	B1	59.77	42.90	B2	8.46
39.05	B1	51.15	42.96	B2	0.12
39.07	B2	2.60	42.97	B1	0.07
39.08	B3	93.02	42.98	B3	266.92
39.33	B2	0.01	43.02	B3	94.57
39.33	B3	12.50	43.04	B1	196.82
39.34	B1	6.39	43.05	B3	218.17
39.46	B3	217.74	43.10	B1	13.04
39.49	B2	4.11	43.15	B2	18.35
39.49	B1	24.54	43.18	B3	1177.17
39.83	B1	259.70	43.21	B1	136.45
39.88	B3	11.45	43.24	B2	55.77
39.88	B2	0.01	43.34	B2	5.08
39.95	B1	0.49	43.38	B1	73.33
39.95	B3	157.59	43.39	B3	58.77
39.99	B2	0.12	43.45	B3	269.63
40.50	B3	396.45	43.47	B1	40.11
40.52	B1	80.44	43.49	B2	0.02
40.56	B2	10.13	43.59	B3	1808.24
40.65	B3	15.87	43.64	B1	115.06
40.66	B2	11.91	43.64	B2	0.31
40.67	B1	51.10	43.75	B1	86.21
40.71	B3	21.22	43.77	B3	7.06
40.71	B2	26.32	43.78	B2	9.42
40.76	B1	4.33	43.80	B2	16.84
40.93	B3	165.94	43.85	B1	37.36
40.96	B2	0.71	43.86	B3	536.86
40.97	B1	0.06	44.31	B2	1.42
41.12	B1	22.72	44.52	B1	1.16
41.19	B3	50.56	44.53	B3	39.48
41.22	B2	29.61	45.40	B2	14.36

45.73	B1	1561.32	89.67	B2	8.15
45.79	B3	2091.09	89.94	B3	13.06
46.07	B3	249.64	89.94	B2	19.53
46.07	B1	81.96	89.94	B1	13.18
46.14	B2	0.63	89.98	B2	34.09
46.48	B1	152.78	89.99	B3	164.71
46.50	B3	1.04	89.99	B1	15.94
46.57	B2	0.90	90.50	B2	2.15
47.55	B2	3.82	90.51	B3	43.47
47.74	B3	264.97	90.52	B1	1.14
47.87	B1	1.07	91.19	B2	18.48
48.13	B2	1.00	91.19	B3	6.16
48.22	B3	2182.03	91.20	B1	1.46
48.34	B1	15.28	91.45	B1	13.62
51.20	B1	2449.21	91.46	B3	18.37
51.27	B3	563.40	91.47	B2	5.08
51.41	B2	0.60	91.50	B3	3.88
76.30	B2	0.37	91.50	B2	48.25
76.39	B1	1520.45	91.50	B1	22.27
76.44	B3	2408.05	92.07	B2	2.30
83.85	B2	365.20	92.08	B1	25.05
83.85	B1	2.28	92.08	B3	26.10
83.85	B3	26.13	92.38	B2	5.50
84.20	B3	141.47	92.39	B3	2.13
84.21	B1	1304.14	92.40	B1	17.41
84.31	B2	106.24	92.70	B1	25.16
85.81	B1	753.01	92.70	B3	12.90
85.82	B3	26.19	92.71	B2	0.17
85.86	B2	93.41	93.73	B2	2.08
87.07	B3	107.09	93.73	B3	11.97
87.07	B2	230.71	93.74	B1	11.93
87.08	B1	90.64	94.53	B1	14.93
88.13	B2	0.14	94.55	B3	25.48
88.14	B1	266.64	94.56	B2	0.17
88.15	B3	432.71			
89.47	B1	11.04			
89.47	B3	0.18			
89.47	B2	163.55			
89.57	B2	155.36			
89.57	B1	1.09			
89.58	B3	65.55			
89.64	B1	22.34			
89.66	B3	30.20			

Table D-6. Solid-state DFT IR-active modes with frequencies (THz), mode symmetries, and IR intensities (km/mol) for fully-optimized levofloxacin hemihydrate.

Frequency (THz)	Mode Symmetry	Intensity (km/mol)	Frequency (THz)	Mode Symmetry	Intensity (km/mol)
0.47	B	0.83	3.65	B	3.22
0.69	B	0.64	3.65	A	0.00
0.93	A	0.13	3.72	A	8.26
0.98	B	0.55	3.78	B	0.50
1.01	A	1.95	3.89	B	3.38
1.10	B	5.36	4.03	B	4.35
1.26	A	0.04	4.03	A	0.03
1.28	B	0.16	4.12	B	2.27
1.30	A	0.06	4.14	A	0.28
1.39	A	0.00	4.28	B	1.29
1.49	B	7.50	4.30	A	0.09
1.50	A	0.15	4.41	B	2.71
1.58	A	0.25	4.52	A	0.01
1.61	B	4.95	4.75	B	0.32
1.69	A	2.80	4.82	B	0.32
1.70	B	11.45	4.85	A	17.53
1.72	B	6.51	4.91	B	15.45
1.81	A	0.10	4.94	B	0.45
2.06	B	0.18	4.96	A	6.79
2.11	A	1.50	5.11	A	20.40
2.16	B	1.20	5.15	B	3.72
2.24	A	1.28	5.22	A	0.00
2.31	B	27.90	5.30	B	10.38
2.36	A	0.11	5.33	A	2.90
2.37	B	8.76	5.46	A	2.93
2.44	A	1.47	5.51	B	21.91
2.54	B	112.09	5.52	A	2.76
2.77	A	0.97	5.67	A	4.92
2.79	A	0.14	5.67	B	7.12
2.84	B	22.34	5.83	B	3.15
2.86	B	4.39	5.86	A	4.07
2.98	A	31.67	5.97	B	0.38
3.07	B	7.71	6.17	A	10.00
3.19	A	7.73	6.37	B	12.91
3.19	B	8.51	6.41	A	0.01
3.33	A	14.95	6.46	A	6.28
3.47	A	1.56	6.53	B	32.56
3.56	B	9.12	6.99	B	14.09

7.02	A	32.94	10.84	B	2.89
7.05	B	0.06	10.86	A	26.54
7.12	B	7.02	10.88	B	36.38
7.17	A	1.74	10.93	A	5.57
7.19	A	6.62	11.29	B	71.41
7.24	A	76.74	11.35	A	0.17
7.30	B	1.54	11.41	B	0.47
7.42	A	0.00	11.45	A	0.55
7.43	B	4.95	12.20	A	2.31
7.73	A	2.43	12.20	B	35.96
7.76	B	0.19	12.26	A	2.09
7.86	A	0.08	12.27	B	57.38
7.96	B	3.21	12.33	A	0.02
8.20	B	11.13	12.36	B	53.41
8.23	A	0.59	12.52	A	0.01
8.35	A	11.30	12.59	B	58.04
8.47	A	0.39	12.87	B	2.16
8.49	B	3.22	12.87	A	0.60
8.59	B	0.44	12.89	B	88.57
8.64	A	6.34	12.92	A	0.24
8.70	B	16.67	13.08	B	0.67
8.81	B	2.33	13.14	A	0.12
8.84	A	2.22	13.22	B	1.50
9.02	B	62.36	13.30	A	0.58
9.03	A	0.78	13.66	A	0.05
9.10	A	1.44	13.69	B	49.26
9.10	B	17.84	13.72	A	0.44
9.41	B	26.76	13.73	B	69.16
9.43	A	0.79	14.38	A	0.17
10.00	B	11.54	14.38	B	4.81
10.06	A	0.01	14.39	A	4.15
10.19	B	5.32	14.40	B	28.78
10.20	A	3.05	14.64	B	0.43
10.21	A	0.03	14.66	A	3.43
10.28	B	10.73	14.67	A	1.15
10.38	B	50.01	14.69	B	13.38
10.43	A	0.17	14.77	B	1.35
10.50	A	7.46	14.86	B	12.60
10.53	B	56.47	14.86	A	2.00
10.69	B	8.17	14.92	A	0.63
10.71	A	21.05	15.93	A	6.83
10.73	B	2.00	15.94	B	32.24
10.75	A	33.61	16.09	B	20.74

16.11	A	8.89	21.93	A	0.52
16.35	B	2.22	21.95	B	95.11
16.39	A	0.01	21.98	A	0.06
16.40	B	8.78	21.99	B	47.53
16.48	A	0.22	22.76	A	141.06
16.60	A	8.86	22.88	A	149.60
16.64	B	16.00	22.96	B	0.20
16.66	A	6.20	23.01	B	0.43
16.68	B	38.99	23.15	A	11.64
16.93	A	1.43	23.15	B	95.03
16.94	B	4.51	23.22	B	37.11
17.13	A	1.10	23.23	A	14.68
17.14	B	16.00	23.45	A	2.14
17.37	A	0.33	23.61	A	0.03
17.38	B	1.40	24.81	B	200.95
17.40	A	0.69	24.84	A	46.91
17.43	B	1.59	24.89	B	7.95
18.81	B	7.42	24.89	A	4.12
18.81	A	0.90	24.90	B	1.95
18.89	B	23.80	24.93	A	44.67
18.92	A	0.91	24.95	A	44.44
19.19	B	66.81	24.95	B	8.87
19.20	A	1.95	25.01	A	0.58
19.25	A	2.77	25.01	B	24.70
19.26	B	16.11	25.04	A	25.62
19.69	B	13.72	25.04	B	60.32
19.72	A	0.01	25.09	B	8.75
19.84	B	22.92	25.11	A	0.26
19.85	A	0.16	25.12	B	7.15
20.59	B	2.36	25.13	A	4.47
20.62	A	0.67	25.19	B	214.13
20.63	B	0.02	25.57	B	155.78
20.64	A	0.03	26.65	B	46.47
20.97	A	0.56	26.66	A	4.24
20.98	B	7.58	26.71	A	3.51
21.03	B	3.31	26.72	B	17.06
21.04	A	0.32	27.29	B	6.96
21.29	A	1.70	27.29	A	10.94
21.40	A	1.85	27.45	B	4.71
21.41	B	10.59	27.45	A	9.40
21.43	B	5.14	27.51	A	4.49
21.62	B	106.19	27.52	B	1.23
21.86	B	139.83	27.62	A	10.21

27.63	B	11.85	32.18	A	22.97
28.32	B	30.90	32.18	B	191.02
28.32	A	4.54	32.88	A	9.98
28.41	B	66.63	32.89	B	16.40
28.45	A	0.09	32.95	A	3.79
28.52	A	14.34	33.02	B	159.87
28.53	B	22.90	33.11	A	0.04
28.66	B	104.18	33.16	B	183.71
28.67	A	0.87	33.19	A	0.47
29.16	B	269.02	33.19	B	45.53
29.19	A	2.08	33.34	A	1.13
29.20	B	53.04	33.40	B	38.09
29.22	A	8.24	33.50	A	0.68
29.68	B	68.69	33.54	B	22.39
29.69	A	1.84	33.86	A	16.87
29.73	B	19.35	33.88	B	41.60
29.78	A	5.87	33.93	A	14.68
29.82	B	36.53	33.96	B	186.61
29.83	B	715.98	33.99	B	73.79
29.86	A	2.61	34.03	A	21.50
29.91	A	6.76	34.10	B	14.74
30.38	A	292.16	34.16	A	13.31
30.38	B	10.90	34.22	B	43.86
30.51	A	330.10	34.23	A	5.81
30.52	B	2.83	34.35	B	227.75
30.80	A	3.91	34.35	A	32.55
30.80	B	0.96	34.41	B	173.46
30.88	A	1.09	34.42	A	23.97
30.92	B	2.34	34.52	B	94.83
30.96	A	6.19	34.53	A	35.01
30.99	A	25.40	34.97	A	0.40
30.99	B	46.46	35.01	A	0.16
31.01	B	44.00	35.03	B	129.90
31.55	A	19.25	35.09	B	33.30
31.59	B	185.98	35.26	A	0.60
31.71	A	0.91	35.30	B	177.21
31.73	B	51.60	35.35	A	5.05
31.90	A	2.89	35.40	B	62.71
31.92	B	51.12	35.82	B	10.75
31.96	A	4.54	35.86	A	0.01
31.98	B	872.74	35.89	B	395.11
32.00	B	105.34	35.94	A	10.73
32.03	A	0.52	36.54	B	16.87

36.55	A	0.37	40.33	A	3.73
36.55	B	48.69	40.33	B	477.10
36.58	A	6.43	40.36	A	0.00
36.85	A	30.58	40.44	B	13.57
36.92	B	393.64	40.50	B	67.15
37.01	A	0.16	40.54	A	2.37
37.02	B	77.25	40.68	B	44.83
37.64	A	0.03	40.72	B	11.46
37.65	B	14.76	40.72	A	0.52
37.82	A	8.16	40.74	A	13.37
37.90	B	34.40	40.75	B	12.59
38.25	B	123.17	40.81	A	6.95
38.28	A	69.76	40.82	B	148.30
38.29	B	3.74	40.84	A	1.03
38.35	A	4.50	40.95	B	15.30
38.39	A	0.16	40.96	A	12.48
38.39	B	179.79	41.13	B	64.98
38.41	A	22.27	41.13	A	17.93
38.44	B	14.99	41.42	B	121.79
38.54	A	4.19	41.42	A	0.27
38.64	A	0.13	41.48	B	34.23
38.64	B	95.02	41.49	A	0.38
38.76	B	21.25	41.59	A	10.09
38.81	B	219.40	41.60	B	75.60
38.83	B	442.88	41.77	B	58.26
38.84	A	0.01	41.78	A	3.95
38.84	A	2.62	41.85	B	161.48
39.08	B	779.91	41.86	A	1.31
39.18	A	3.12	42.13	B	3.33
39.35	A	1.27	42.15	B	29.33
39.36	B	300.99	42.17	A	0.16
39.56	B	41.90	42.19	A	0.00
39.57	A	0.36	42.23	B	157.98
39.65	A	0.56	42.26	A	0.18
39.65	B	7.73	42.31	B	156.94
39.77	A	0.21	42.31	A	2.91
39.78	B	107.60	42.65	B	600.81
39.81	B	246.44	42.65	A	29.51
39.85	A	0.00	42.79	B	179.34
40.11	A	3.54	42.79	A	19.54
40.12	B	11.24	42.80	A	0.23
40.15	A	0.12	42.86	A	0.09
40.18	B	20.20	42.87	B	625.97

42.88	A	10.61	45.96	B	286.95
42.92	B	162.04	45.99	A	0.63
42.95	A	9.06	46.14	B	153.68
42.98	B	93.59	46.16	B	53.72
43.00	B	12.22	46.19	A	0.95
43.07	A	10.38	46.25	A	1.90
43.09	A	0.15	47.56	A	0.07
43.11	B	57.80	47.59	B	16.27
43.13	B	107.67	47.67	A	3.48
43.19	B	143.92	47.74	B	4.02
43.20	A	1.34	48.06	A	1.30
43.30	B	15.66	48.11	A	0.05
43.30	A	0.86	48.20	B	1639.27
43.40	B	2723.06	48.23	B	798.96
43.42	A	48.97	50.17	A	19.71
43.45	B	222.22	50.24	A	29.19
43.49	A	12.47	51.31	B	2940.57
43.50	B	58.38	51.42	A	0.31
43.56	B	83.00	51.51	B	3.53
43.58	A	75.72	51.52	A	1.21
43.59	A	46.37	77.76	A	0.29
43.69	B	103.13	77.84	B	2526.94
43.75	A	4.02	78.51	A	0.01
43.79	B	99.00	78.58	B	1754.44
43.80	A	14.71	86.30	B	247.06
43.84	A	0.88	86.32	A	1.70
43.85	B	566.33	86.42	B	91.12
43.86	A	31.21	86.42	A	0.57
43.97	B	593.96	86.63	B	400.42
43.98	A	5.30	86.66	A	167.81
44.03	B	261.35	86.73	B	113.54
44.17	B	31.50	86.75	A	127.21
44.19	A	40.27	87.09	B	17.42
44.90	B	849.67	87.11	A	134.83
44.93	B	197.03	87.37	B	19.86
45.15	A	0.13	87.39	A	109.02
45.21	A	0.01	88.00	B	158.76
45.22	A	1.96	88.02	A	53.43
45.26	A	0.32	88.19	B	61.66
45.48	B	3360.04	88.20	A	55.54
45.57	B	210.54	88.47	B	408.62
45.92	B	71.34	88.48	A	31.44
45.94	A	0.48	88.73	B	256.04

88.76	A	21.54	93.00	B	11.01
89.02	B	54.03	93.00	A	3.68
89.04	A	15.16	93.22	B	5.56
89.17	B	37.28	93.22	A	0.02
89.17	A	2.41	93.58	B	7.14
89.44	A	8.42	93.58	A	0.24
89.45	B	3.74	94.63	B	54.05
89.55	B	10.03	94.64	A	0.87
89.55	A	0.01	94.67	B	66.02
89.76	B	6.00	94.68	A	0.87
89.78	A	35.92	94.69	A	0.26
89.96	B	5.66	94.69	B	8.12
89.96	A	3.35	94.81	B	78.70
90.08	A	1.23	94.81	A	0.30
90.10	B	141.08	95.75	B	4957.59
90.11	B	146.76	95.86	A	935.78
90.18	A	17.34	95.95	A	667.89
90.18	B	111.27	96.10	B	1253.47
90.19	A	25.33			
90.28	B	89.78			
90.31	A	6.61			
90.37	B	138.76			
90.38	A	32.22			
90.46	B	43.74			
90.46	A	9.22			
91.68	B	19.68			
91.69	A	29.26			
91.71	B	8.81			
91.72	A	9.53			
91.81	B	18.45			
91.81	A	17.11			
91.91	B	4.66			
91.91	A	0.08			
92.11	A	1.27			
92.11	B	22.59			
92.12	A	1.85			
92.12	B	4.07			
92.24	B	19.35			
92.24	A	8.41			
92.56	B	0.03			
92.57	A	1.22			
92.85	B	8.64			
92.85	A	2.39			

Table D-7. Solid-state DFT IR-active modes with frequencies (THz), mode symmetries, and IR intensities (km/mol) for the fixed-lattice simulation of levofloxacin hemihydrate.

Frequency (THz)	Mode Symmetry	Intensity (km/mol)	Frequency (THz)	Mode Symmetry	Intensity (km/mol)
0.48	B	0.45	3.64	A	0.00
0.70	B	0.69	3.68	B	2.72
0.92	A	0.26	3.73	A	7.45
0.95	B	0.66	3.80	B	0.23
1.01	A	1.71	3.93	B	4.18
1.11	B	4.84	4.04	A	0.08
1.21	A	0.07	4.05	B	3.95
1.26	B	0.15	4.13	B	2.87
1.30	A	0.10	4.14	A	0.39
1.40	A	0.00	4.28	B	1.33
1.48	B	5.62	4.29	A	0.07
1.50	A	0.10	4.41	B	1.50
1.55	A	0.30	4.51	A	0.02
1.58	B	4.81	4.70	B	0.91
1.65	B	8.26	4.80	B	0.04
1.67	A	3.24	4.87	A	17.37
1.70	B	3.81	4.92	B	6.84
1.80	A	0.05	4.93	B	8.20
2.06	B	0.20	4.96	A	4.06
2.07	A	1.39	5.10	A	20.39
2.14	B	1.27	5.14	B	0.59
2.25	A	1.16	5.21	A	0.06
2.31	B	29.99	5.29	A	7.59
2.37	A	0.00	5.30	B	11.65
2.37	B	8.95	5.41	A	3.27
2.39	A	0.87	5.48	B	22.19
2.50	B	32.68	5.49	A	0.12
2.79	A	0.31	5.62	A	3.42
2.81	B	0.50	5.64	B	7.84
2.82	A	0.06	5.83	B	2.88
2.90	B	3.96	5.88	A	4.86
2.98	A	33.73	5.99	B	0.23
3.09	B	9.36	6.20	A	10.78
3.22	A	9.04	6.37	B	13.27
3.22	B	6.50	6.40	A	0.04
3.34	A	12.35	6.45	A	6.64
3.49	A	1.93	6.53	B	29.53
3.57	B	14.41	7.00	B	20.61

7.02	A	25.58	10.83	B	12.32
7.05	B	1.90	10.85	A	20.11
7.09	B	7.24	10.87	B	26.26
7.16	A	0.05	10.89	A	3.27
7.18	A	1.07	11.29	B	70.55
7.25	A	93.23	11.34	A	0.16
7.26	B	2.08	11.41	B	0.11
7.40	B	4.36	11.45	A	0.41
7.40	A	0.74	12.20	B	25.34
7.72	A	2.70	12.20	A	2.69
7.74	B	0.50	12.25	A	1.52
7.85	A	0.03	12.26	B	59.23
7.96	B	5.37	12.34	A	0.03
8.20	B	11.10	12.36	B	46.85
8.23	A	0.76	12.53	A	0.03
8.35	A	11.34	12.58	B	66.42
8.48	A	0.57	12.85	B	3.85
8.49	B	1.91	12.86	A	0.88
8.61	B	0.44	12.88	B	90.89
8.65	A	5.92	12.92	A	0.37
8.71	B	19.64	13.06	B	0.44
8.84	B	2.43	13.13	A	0.16
8.86	A	2.61	13.19	B	1.74
9.02	B	74.86	13.27	A	0.69
9.03	A	0.41	13.65	A	0.06
9.08	A	1.88	13.69	B	49.00
9.09	B	13.07	13.71	A	0.42
9.40	B	24.59	13.73	B	63.97
9.43	A	0.98	14.39	A	0.34
10.00	B	9.68	14.39	B	0.30
10.06	A	0.01	14.40	A	4.15
10.17	B	5.05	14.40	B	28.08
10.20	A	2.70	14.65	B	0.57
10.21	A	0.03	14.67	A	2.59
10.28	B	8.49	14.67	A	1.71
10.36	B	57.88	14.69	B	12.86
10.40	A	1.15	14.78	B	1.03
10.46	A	15.62	14.86	B	12.59
10.51	B	54.56	14.87	A	2.21
10.69	A	12.87	14.93	A	0.83
10.69	B	2.37	15.94	A	6.81
10.70	A	41.54	15.95	B	30.55
10.71	B	4.66	16.11	B	18.18

16.13	A	8.44	21.93	A	0.65
16.35	B	2.20	21.95	B	86.42
16.40	A	0.00	21.97	A	0.07
16.40	B	10.27	21.99	B	44.40
16.48	A	0.17	22.75	A	142.65
16.60	A	8.67	22.88	A	149.96
16.64	B	21.08	22.96	B	0.02
16.66	A	6.31	23.01	B	0.20
16.68	B	37.23	23.15	B	98.53
16.93	A	1.35	23.15	A	11.85
16.93	B	2.89	23.21	B	30.99
17.13	A	1.25	23.23	A	15.88
17.14	B	17.79	23.41	A	1.44
17.36	A	0.21	23.63	A	0.32
17.37	B	3.28	24.70	B	288.78
17.40	A	0.76	24.84	A	52.56
17.42	B	2.47	24.86	B	25.52
18.82	B	5.46	24.89	A	0.87
18.82	A	0.92	24.90	B	17.29
18.90	B	22.31	24.95	A	0.01
18.93	A	0.90	24.96	B	5.76
19.21	B	69.13	24.97	A	40.10
19.21	A	1.87	25.01	A	8.43
19.27	A	3.04	25.02	B	64.64
19.28	B	19.39	25.05	A	67.33
19.70	B	13.80	25.06	B	55.42
19.72	A	0.01	25.07	B	8.74
19.84	B	23.40	25.11	A	0.95
19.85	A	0.22	25.13	B	27.04
20.60	B	2.97	25.13	B	23.14
20.62	A	0.92	25.13	A	1.76
20.64	B	0.13	25.41	B	190.75
20.66	A	0.03	26.65	A	4.56
20.98	A	0.58	26.65	B	57.97
20.98	B	6.71	26.69	A	2.86
21.03	B	5.48	26.71	B	19.34
21.05	A	0.33	27.27	B	7.28
21.30	A	1.85	27.28	A	10.31
21.40	A	2.12	27.45	B	4.50
21.42	B	13.15	27.45	A	10.05
21.44	B	9.69	27.51	A	3.46
21.58	B	106.25	27.52	B	0.67
21.79	B	142.97	27.63	A	10.97

27.64	B	18.61	32.18	A	23.12
28.32	B	31.09	32.18	B	193.47
28.33	A	4.64	32.89	A	7.94
28.41	B	63.19	32.90	B	13.13
28.44	A	0.13	32.94	A	5.21
28.51	A	15.29	33.02	B	151.47
28.54	B	27.28	33.11	A	0.06
28.66	B	101.63	33.15	B	169.02
28.68	A	0.74	33.20	A	0.64
29.16	B	267.51	33.20	B	45.11
29.20	A	1.27	33.35	A	1.00
29.21	B	47.27	33.40	B	31.70
29.21	A	8.91	33.50	A	0.53
29.68	B	72.00	33.54	B	29.02
29.69	A	1.39	33.84	A	18.46
29.73	B	19.58	33.86	B	43.56
29.78	A	5.97	33.90	A	12.83
29.82	B	56.62	33.92	B	187.04
29.84	B	669.25	33.98	B	82.24
29.86	A	3.42	34.01	A	22.82
29.92	A	7.08	34.10	B	9.68
30.37	A	287.75	34.16	A	13.14
30.37	B	10.83	34.21	B	32.96
30.47	A	336.86	34.21	A	4.27
30.47	B	4.44	34.32	B	229.48
30.81	A	4.27	34.32	A	29.01
30.82	B	0.03	34.42	B	173.43
30.88	A	0.84	34.44	A	25.08
30.92	B	0.94	34.53	B	106.20
30.97	A	7.16	34.54	A	34.65
30.99	A	25.53	34.97	A	0.42
30.99	B	52.26	35.01	A	0.30
31.01	B	45.32	35.04	B	108.39
31.56	A	17.25	35.09	B	41.25
31.59	B	199.35	35.27	A	0.71
31.73	A	1.07	35.30	B	172.03
31.74	B	68.51	35.36	A	4.84
31.90	A	3.77	35.40	B	65.19
31.91	B	111.58	35.83	B	0.88
31.94	A	5.46	35.86	A	0.01
31.97	B	264.17	35.89	B	379.04
31.99	B	642.59	35.95	A	10.47
32.04	A	0.77	36.54	B	30.76

36.56	A	0.55	40.31	A	3.68
36.56	B	46.85	40.31	B	455.76
36.59	A	6.79	40.35	A	0.16
36.84	A	29.02	40.43	B	24.97
36.91	B	473.12	40.49	B	61.65
37.00	A	0.06	40.53	A	2.48
37.01	B	82.90	40.67	B	47.85
37.65	A	0.06	40.71	B	12.72
37.68	B	5.51	40.71	A	2.70
37.82	A	8.10	40.73	A	11.59
37.92	B	35.79	40.75	B	9.96
38.26	B	118.45	40.81	A	5.86
38.28	A	73.44	40.83	B	138.07
38.29	B	4.32	40.85	A	0.80
38.34	A	3.22	40.97	B	10.20
38.37	A	2.34	40.98	A	12.79
38.38	B	171.08	41.13	A	17.67
38.40	A	23.30	41.13	B	71.21
38.44	B	30.88	41.41	B	95.43
38.54	A	2.99	41.42	A	0.21
38.64	A	0.08	41.48	A	0.25
38.64	B	94.74	41.49	B	50.32
38.74	B	19.89	41.60	A	9.44
38.80	B	121.79	41.61	B	68.54
38.84	B	530.95	41.76	B	68.51
38.85	A	0.61	41.78	A	4.44
38.85	A	2.04	41.85	B	174.13
39.08	B	770.78	41.86	A	1.64
39.17	A	3.18	42.12	B	3.46
39.35	A	1.39	42.15	B	35.03
39.36	B	292.14	42.15	A	0.21
39.57	B	48.94	42.18	A	0.01
39.57	A	0.41	42.21	B	171.43
39.65	A	0.66	42.27	A	0.34
39.67	B	2.60	42.29	B	162.26
39.77	A	0.22	42.29	A	3.29
39.77	B	107.11	42.62	B	626.11
39.82	B	254.35	42.63	A	30.35
39.85	A	0.00	42.78	B	225.77
40.09	A	3.45	42.79	A	17.67
40.10	B	9.27	42.80	A	0.37
40.14	A	0.26	42.86	A	0.07
40.18	B	24.33	42.86	B	504.53

42.88	A	8.98	45.97	B	293.19
42.91	B	204.29	45.98	A	0.64
42.94	A	8.40	46.13	B	201.67
42.97	B	97.75	46.15	B	29.14
42.99	B	12.07	46.19	A	0.57
43.05	A	9.79	46.25	A	1.69
43.08	A	1.25	47.55	A	0.06
43.10	B	63.37	47.59	B	15.81
43.12	B	57.60	47.65	A	3.33
43.18	B	144.77	47.72	B	4.07
43.19	A	1.52	48.05	A	1.19
43.29	A	1.57	48.10	A	0.08
43.30	B	16.59	48.18	B	1343.95
43.39	B	2683.69	48.23	B	1089.87
43.42	A	47.56	50.08	A	17.01
43.45	B	86.39	50.16	A	28.70
43.49	A	11.53	51.30	B	2900.87
43.49	B	77.00	51.39	A	0.27
43.56	B	44.38	51.49	A	1.06
43.58	A	90.34	51.50	B	2.19
43.60	A	25.04	77.92	A	0.42
43.69	B	119.83	78.01	B	2539.01
43.74	A	1.41	78.63	A	0.00
43.78	B	64.90	78.72	B	1727.62
43.79	A	24.03	86.22	B	238.73
43.82	A	2.39	86.24	A	0.56
43.85	B	529.19	86.36	B	110.28
43.85	A	28.31	86.37	A	0.14
43.97	A	5.25	86.64	B	414.11
43.97	B	687.54	86.67	A	135.71
44.01	B	255.19	86.76	B	118.21
44.17	B	31.67	86.77	A	131.31
44.19	A	40.60	86.97	B	27.08
44.87	B	801.09	86.99	A	159.61
44.90	B	208.16	87.29	B	33.14
45.13	A	0.18	87.29	A	121.49
45.19	A	0.21	87.96	B	123.76
45.21	A	1.37	87.98	A	53.80
45.25	A	0.39	88.15	B	70.43
45.48	B	3444.78	88.15	A	56.79
45.56	B	123.04	88.40	B	408.58
45.92	B	78.69	88.42	A	36.79
45.93	A	0.59	88.70	B	310.59

88.71	A	20.87	92.98	B	10.81
89.04	A	15.72	92.98	A	3.70
89.05	B	67.86	93.18	A	0.00
89.17	B	28.01	93.18	B	3.81
89.17	A	3.36	93.53	A	0.06
89.46	A	8.50	93.54	B	4.66
89.46	B	5.70	94.63	B	86.69
89.54	A	0.29	94.64	A	0.61
89.55	B	0.62	94.69	B	44.29
89.77	B	4.26	94.70	A	1.28
89.78	A	34.41	94.70	A	1.11
89.97	A	2.79	94.72	B	37.10
89.97	B	5.47	94.81	A	0.30
90.08	A	2.02	94.82	B	54.32
90.11	B	105.91	96.01	A	579.77
90.12	B	192.33	96.02	B	5048.14
90.17	A	11.88	96.12	A	996.53
90.18	B	102.14	96.34	B	1096.17
90.18	A	30.27			
90.26	B	96.78			
90.29	A	9.89			
90.36	B	119.61			
90.37	A	32.36			
90.43	B	36.95			
90.43	A	7.56			
91.65	B	36.60			
91.66	A	28.20			
91.70	A	10.87			
91.70	B	14.85			
91.78	B	27.67			
91.78	A	16.69			
91.88	B	0.32			
91.89	A	0.02			
92.06	B	0.22			
92.06	A	3.86			
92.09	A	0.01			
92.09	B	16.07			
92.23	B	25.58			
92.24	A	7.03			
92.52	A	1.78			
92.52	B	1.63			
92.84	B	9.64			
92.84	A	2.65			

Table D-8. Solid-state DFT IR-active modes with frequencies (THz), mode symmetries, and IR intensities (km/mol) for the fully-optimized levofloxacin monohydrate.

Frequency (THz)	Mode Symmetry	Intensity (km/mol)	Frequency (THz)	Mode Symmetry	Intensity (km/mol)
0.67	A	0.24	3.47	B	13.33
0.72	B	0.07	3.50	A	0.26
0.77	B	0.79	3.56	B	13.78
0.94	A	0.16	3.62	A	44.53
1.13	A	0.12	3.66	B	25.57
1.25	B	2.14	3.70	B	19.90
1.28	A	1.20	3.71	A	8.44
1.29	B	0.63	3.80	B	9.60
1.40	A	0.07	3.83	A	9.25
1.45	A	0.18	4.04	A	6.63
1.52	B	10.44	4.14	B	3.71
1.55	A	0.66	4.23	B	5.71
1.55	B	3.23	4.33	A	15.22
1.62	B	15.53	4.39	B	1.39
1.66	A	0.17	4.40	A	7.91
1.68	B	0.80	4.72	A	25.64
1.72	A	1.42	4.73	B	2.76
1.81	A	0.25	4.81	A	0.19
1.85	A	0.00	4.87	B	2.68
1.99	B	1.40	4.92	B	11.62
2.22	B	4.19	5.00	B	6.70
2.25	A	0.40	5.01	A	0.58
2.26	B	8.02	5.11	A	0.01
2.39	A	1.86	5.18	B	19.95
2.45	B	0.65	5.21	A	0.83
2.51	B	13.41	5.22	B	8.50
2.62	A	6.98	5.27	A	0.70
2.70	A	0.54	5.39	B	7.71
2.84	B	0.67	5.43	A	12.35
2.91	A	0.42	5.62	A	0.96
2.99	B	19.09	5.62	B	4.58
3.06	A	0.76	5.77	A	0.13
3.13	A	0.56	5.80	B	13.46
3.13	B	26.48	5.91	B	25.63
3.14	B	17.93	6.00	A	0.05
3.26	A	11.25	6.10	B	34.36
3.37	B	23.49	6.13	A	3.59
3.39	A	20.40	6.34	B	2.13

6.38	A	0.00	10.53	A	0.00
6.58	A	11.58	10.56	B	2.22
6.60	B	30.57	10.77	B	61.97
6.64	A	11.37	10.79	A	3.02
6.77	B	18.18	10.81	A	18.18
6.96	B	22.33	10.83	B	4.99
6.99	A	2.94	10.93	A	38.34
7.01	A	27.59	10.99	B	18.08
7.11	B	4.00	11.08	A	4.01
7.12	A	0.42	11.08	B	41.03
7.14	B	4.83	11.41	B	44.23
7.30	A	0.56	11.47	A	10.30
7.34	B	55.59	11.50	B	9.26
7.50	B	6.11	11.59	A	7.98
7.52	A	6.93	12.17	A	42.97
7.71	A	4.71	12.17	B	17.90
7.73	B	5.89	12.32	B	27.58
7.76	B	2.26	12.33	A	4.70
7.76	A	9.53	12.44	A	61.38
8.16	A	0.01	12.47	B	2.89
8.21	B	10.56	12.62	B	12.07
8.26	B	0.08	12.62	A	86.95
8.27	A	0.00	12.91	A	4.90
8.30	B	1.39	12.93	B	91.13
8.39	A	4.52	12.94	A	40.76
8.59	A	1.68	12.96	B	25.65
8.61	B	16.69	13.18	A	9.96
8.85	B	6.69	13.20	B	1.73
8.85	A	0.16	13.21	A	0.98
8.98	A	2.38	13.22	B	0.59
9.02	B	26.51	13.74	B	2.61
9.12	A	32.76	13.76	A	74.69
9.14	B	38.56	13.78	A	38.37
10.04	A	4.43	13.78	B	14.80
10.08	A	0.31	14.28	A	16.83
10.11	B	0.86	14.29	B	11.37
10.21	B	4.00	14.39	A	11.01
10.24	A	6.88	14.40	B	4.67
10.26	B	14.28	14.66	A	0.04
10.38	A	6.44	14.67	B	13.73
10.39	B	54.99	14.77	A	0.64
10.39	A	0.01	14.80	A	5.12
10.42	B	26.11	14.80	B	11.73

14.81	B	7.91	20.87	B	19.68
14.93	A	28.54	20.87	A	0.12
14.94	B	3.65	20.92	A	32.92
15.98	A	15.71	20.97	B	87.27
15.99	B	11.70	21.10	A	160.35
16.06	B	25.70	21.23	B	165.86
16.06	A	24.91	21.27	A	0.01
16.40	B	2.94	21.34	B	39.32
16.41	A	2.19	21.38	A	177.25
16.49	A	0.44	21.38	B	741.58
16.51	B	8.15	21.41	A	12.27
16.60	B	29.91	21.53	B	53.23
16.66	A	1.12	22.00	A	0.01
16.76	A	21.31	22.01	B	3.29
16.76	B	3.77	22.02	B	128.35
17.03	B	39.20	22.02	A	7.44
17.05	A	7.09	22.88	A	4.53
17.14	B	1.66	22.88	B	307.65
17.15	A	9.80	23.02	A	0.06
17.38	A	1.04	23.02	B	2.13
17.39	B	7.48	23.20	A	2.07
17.41	B	0.88	23.20	B	88.29
17.42	A	2.03	23.28	A	0.43
18.65	A	66.76	23.29	B	26.54
18.75	B	452.55	24.75	B	21.56
18.77	A	16.20	24.78	A	3.63
18.77	B	291.42	24.80	A	2.17
18.88	B	84.88	24.80	B	2.34
18.90	A	22.85	24.85	A	0.85
19.23	B	7.37	24.86	B	106.61
19.23	A	11.43	24.86	A	0.34
19.32	A	70.22	24.88	B	27.29
19.39	B	84.78	25.01	A	28.75
19.45	A	82.23	25.07	B	40.35
19.49	B	301.18	25.08	A	8.52
19.65	A	19.17	25.09	B	4.72
19.74	B	14.41	25.12	A	0.05
19.81	A	10.99	25.15	B	1.15
19.83	B	7.46	25.16	B	7.41
20.55	B	260.62	25.16	A	16.79
20.65	A	160.60	25.21	B	77.50
20.66	A	1.36	25.25	A	16.85
20.71	B	60.42	26.44	B	11.02

26.45	A	46.80	31.60	A	3.25
26.77	B	19.01	31.62	B	220.86
26.78	A	25.16	31.70	A	183.88
27.02	B	38.15	31.71	B	105.89
27.04	A	26.64	31.87	A	21.88
27.55	A	2.50	31.89	B	37.98
27.55	B	0.84	31.91	A	10.74
27.66	A	6.33	31.91	B	50.91
27.67	B	15.35	31.97	A	0.83
28.01	A	5.19	31.97	B	147.97
28.01	B	15.90	32.01	B	501.64
28.06	A	3.37	32.04	A	5.37
28.08	B	6.36	32.25	B	434.51
28.22	A	7.29	32.30	A	20.27
28.23	B	22.10	32.99	B	18.69
28.27	A	11.69	33.00	A	9.93
28.27	B	8.69	33.08	B	17.49
28.54	B	23.64	33.09	A	50.96
28.55	A	10.12	33.19	B	0.13
28.66	B	55.18	33.21	A	12.22
28.68	A	34.34	33.26	B	31.06
29.24	A	217.05	33.30	A	179.10
29.24	B	60.64	33.48	B	11.37
29.25	A	23.42	33.49	A	21.48
29.26	B	10.86	33.53	B	4.60
29.64	A	17.33	33.54	A	1.96
29.65	B	9.11	33.82	A	27.73
29.69	B	158.15	33.83	B	11.44
29.70	A	582.77	33.88	A	137.43
29.81	B	38.50	33.90	B	28.01
29.83	A	13.87	34.04	A	2.54
29.88	B	31.90	34.05	B	131.43
29.90	A	13.09	34.17	B	2.03
30.88	A	0.95	34.19	A	0.39
30.89	B	8.60	34.28	B	77.93
30.90	A	3.94	34.29	A	6.61
30.92	B	3.18	34.37	B	117.48
31.00	A	0.39	34.38	A	3.33
31.01	B	83.49	34.45	B	142.43
31.04	A	1.56	34.46	A	47.64
31.07	B	65.13	34.61	B	104.24
31.49	A	6.07	34.64	A	35.09
31.49	B	305.48	35.33	A	6.61

35.34	B	0.73	39.66	A	3.15
35.40	A	179.72	39.66	B	45.20
35.41	B	0.09	39.81	B	20.31
35.55	A	2.55	39.81	A	8.40
35.63	B	162.41	39.96	A	171.55
35.67	B	60.52	39.97	B	146.75
35.69	A	100.90	40.02	A	0.99
35.90	B	67.59	40.04	B	12.58
35.91	A	82.02	40.12	B	51.67
35.93	A	59.62	40.12	A	1.87
35.93	B	29.78	40.13	A	2.27
36.54	A	2.32	40.14	B	2.28
36.57	B	22.94	40.35	A	1.38
36.57	A	9.15	40.38	B	189.87
36.60	B	60.62	40.40	B	11.38
37.06	A	685.88	40.44	A	181.10
37.11	A	3.77	40.66	A	72.85
37.12	B	9.67	40.67	B	67.96
37.14	B	11.68	40.71	A	2.14
37.91	A	15.26	40.73	B	5.39
37.92	B	14.05	40.73	B	8.88
37.99	B	5.08	40.75	A	0.03
38.00	A	102.46	40.83	A	2.22
38.30	B	17.32	40.84	B	37.46
38.31	B	143.94	40.95	A	0.26
38.32	A	1.31	40.97	B	28.92
38.35	A	34.23	41.08	A	2.48
38.39	A	27.13	41.09	B	3.26
38.41	B	127.28	41.49	A	24.54
38.47	B	108.09	41.50	B	26.14
38.51	A	180.62	41.57	B	8.89
38.55	B	2.06	41.59	A	0.97
38.60	A	263.59	41.61	A	1.64
38.64	A	445.42	41.64	B	62.11
38.76	B	1.26	41.73	A	12.73
39.00	A	312.91	41.74	B	35.07
39.00	B	73.57	41.94	A	12.16
39.17	A	16.88	41.94	B	111.87
39.23	B	9.88	41.96	B	45.09
39.36	A	285.37	41.96	A	127.85
39.37	B	320.27	42.19	B	13.15
39.39	A	189.12	42.20	A	12.64
39.40	B	22.54	42.23	B	24.92

42.23	A	0.63	44.47	B	133.71
42.29	A	114.97	44.49	A	11.82
42.30	A	228.13	44.96	B	404.09
42.30	B	7.38	45.01	A	465.75
42.31	B	40.82	45.21	A	30.37
42.68	A	822.71	45.22	B	6.32
42.69	B	128.96	45.23	A	0.27
42.82	A	262.54	45.25	B	94.09
42.84	B	108.09	45.44	A	2876.53
42.88	A	123.99	45.46	B	629.94
42.89	B	14.31	45.97	A	41.28
42.90	B	15.08	45.97	B	97.65
42.91	A	406.68	46.03	A	50.56
42.98	A	126.47	46.03	B	115.09
42.98	B	9.76	46.44	B	452.23
43.05	A	494.60	46.45	A	274.03
43.05	B	0.95	46.51	A	87.97
43.07	A	0.35	46.56	B	5.23
43.08	B	25.52	47.54	A	16.74
43.13	B	18.50	47.63	A	0.06
43.14	A	97.74	47.63	B	5.09
43.24	A	0.23	47.68	B	10.43
43.24	B	8.47	47.76	A	170.16
43.41	A	775.01	47.80	B	16.75
43.44	B	23.93	47.95	A	319.53
43.45	A	88.66	47.95	B	36.59
43.46	B	71.52	48.06	A	14.33
43.53	B	473.53	48.07	B	64.28
43.53	A	211.18	48.18	B	542.01
43.57	B	4.40	48.20	A	1843.99
43.60	A	242.58	50.64	B	2759.00
43.61	B	21.86	50.69	A	8.71
43.66	A	986.24	50.78	A	253.92
43.75	A	238.71	50.83	B	19.15
43.75	A	222.03	73.77	B	1082.27
43.78	B	52.59	73.77	A	235.87
43.79	B	64.07	74.07	B	1410.31
43.90	A	203.78	74.15	A	983.36
43.91	B	84.87	86.23	B	123.74
43.98	B	466.80	86.24	A	3.77
44.04	A	368.47	86.35	B	337.09
44.14	A	157.66	86.37	A	3.59
44.15	B	66.98	86.45	B	167.57

86.46	A	3.33	91.63	A	4.00
86.74	B	431.51	91.64	B	16.13
86.74	A	106.27	91.78	A	6.54
86.90	B	88.37	91.79	B	4.77
86.92	A	17.97	91.94	B	19.73
87.27	A	49.19	91.94	A	10.97
87.27	B	350.50	92.06	B	55.20
87.83	A	101.33	92.06	A	25.39
87.85	B	470.13	92.16	B	23.13
88.20	A	132.70	92.16	A	2.42
88.20	B	339.96	92.36	A	11.11
88.59	B	120.71	92.36	B	38.02
88.61	A	19.92	92.55	A	5.03
88.92	B	63.58	92.55	B	20.84
88.93	A	16.51	92.57	B	0.83
89.10	A	6.23	92.57	A	9.77
89.10	B	10.03	92.82	A	139.96
89.11	A	3.06	92.90	B	3309.66
89.11	B	68.48	93.16	A	14.08
89.27	B	31.12	93.18	B	2.15
89.28	A	0.19	93.25	A	3.96
89.36	A	27.81	93.27	B	2.45
89.36	B	8.86	93.72	A	22.22
89.64	B	13.03	93.72	B	953.00
89.64	A	6.94	93.74	A	140.62
89.71	A	53.53	93.76	B	233.39
89.71	B	32.82	94.28	B	3.30
90.26	A	11.24	94.28	A	13.28
90.26	B	110.58	94.46	B	5.78
90.40	A	2.83	94.46	A	12.17
90.41	B	100.21	95.91	A	332.82
90.43	B	38.92	95.93	B	2424.94
90.44	A	108.47	105.02	A	250.64
90.52	A	0.42	105.09	B	3473.34
90.52	B	4.46	105.17	A	151.65
90.71	B	15.72	105.31	B	469.99
90.71	A	90.66			
90.74	B	2.90			
90.75	A	45.39			
91.25	A	82.58			
91.26	B	51.32			
91.31	A	133.53			
91.32	B	39.39			

Appendix E: Supporting Information for Chapter 8

Supporting Information Table of Contents

References

S-R1. Prusiner, P.; Sundaralingam, M., The Crystal and Molecular Structures of Two Polymorphic Crystalline Forms of Virazole (1-B-D-Ribofuranosyl-1, 2, 4-Triazole-3-Carboxamide). A New Synthetic Broad Sprectrum Antiviral Agent. *Acta Crystallographica Section B: Structural Crystallography and Crystal Chemistry* **1976,** *32* (2), 419-426.

S-R2. Macrae, C. F.; Sovago, I.; Cottrell, S. J.; Galek, P. T.; McCabe, P.; Pidcock, E.; Platings, M.; Shields, G. P.; Stevens, J. S.; Towler, M., Mercury 4.0: From Visualization to Analysis, Design and Prediction. *Journal of applied crystallography* **2020,** *53* (1), 226-235.
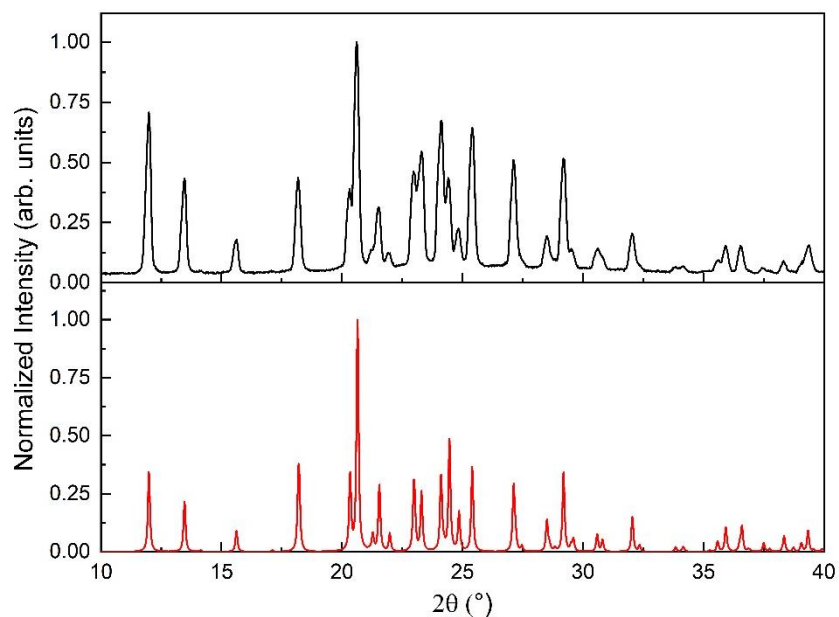
Figure E-1. Room temperature PXRD patterns of R-II (black) and CSD published pattern[S-R1] (red).

Figure E-2. shows the PXRD pattern of the mixture along with the PXRD patterns of pure R-I and R-II predicted from CSD data[S-R1] and generated using Mercury[S-R2]. Peaks marked with red asterisks in the mixture PXRD pattern represent peaks attributed to R-I and account for about 10% of the sample.
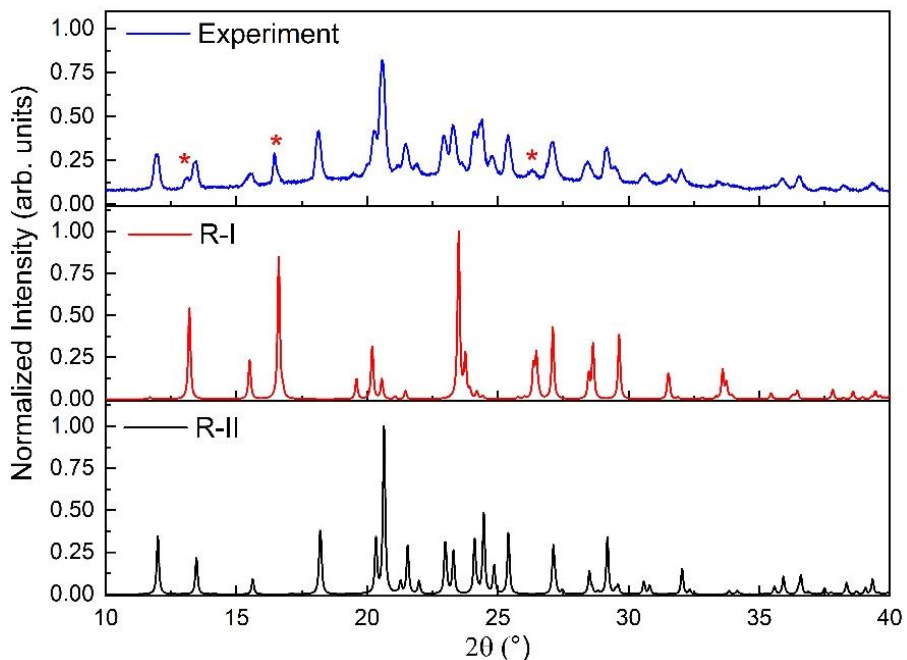
Figure E-2. PXRD of a mixture of R-I and R-II (blue, top) with peaks attributed to R-I marked with red asterisks, pure R-I (red, middle), and pure R-II (black, bottom). [S-R1]

A Bruker Invenio FTIR with a wide-range beamsplitter (T240-T) was used to confirm peaks at the end of the usable range for the Toptica Photonics TeraFlash. This data was taken by Kateryna Kushnir in Prof. Ruggiero's group at the University of Vermont. The Bruker Invenio FTIR has a usable spectral range from 80 to 6,000 cm^{-1} with a spectral resolution of 0.5 cm^{-1}. The experiment was done at room temperature (290 K) and the sample was ground first then placed on a diamond ATR crystal and the entire system was purged with nitrogen gas during the experiment.
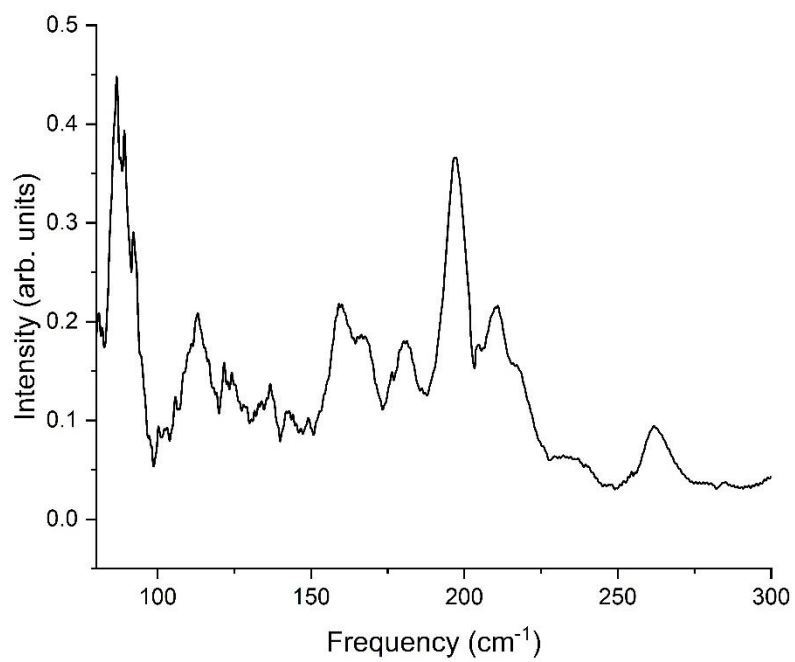
Figure E-3. FTIR spectrum of R-II from 80 to 300 cm^{-1}.
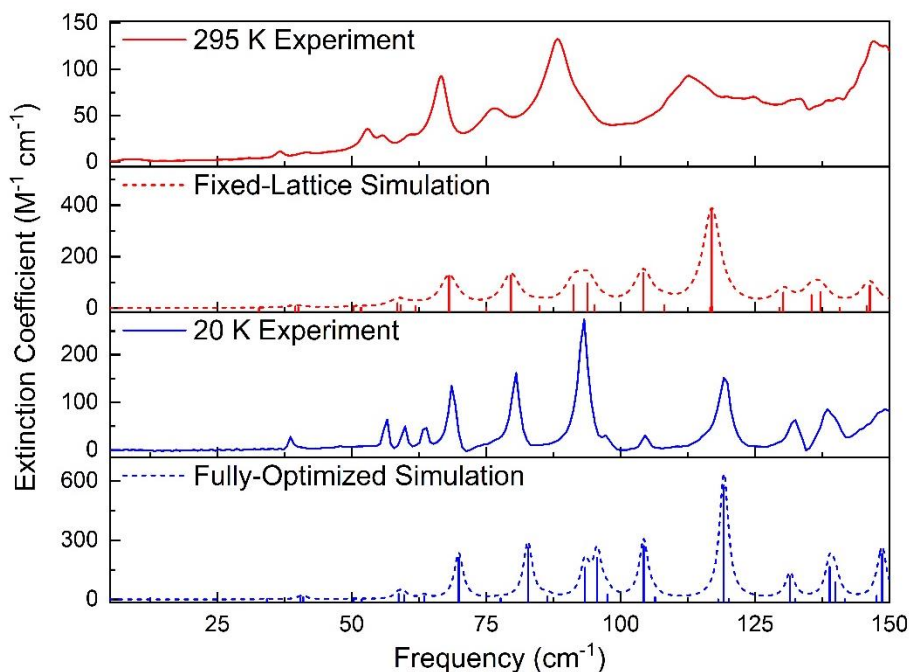
Figure E-4. Experimental 295 K (solid red line) and 20 K (solid blue line) THz spectra for R-II from 5 to 120 cm⁻¹. Simulated THz spectra are shown based on fixed-lattice (dashed red line, 2.0 cm⁻¹ FWHM) and full-optimization (dashed blue line, 1.0 cm⁻¹ FWHM) calculations.
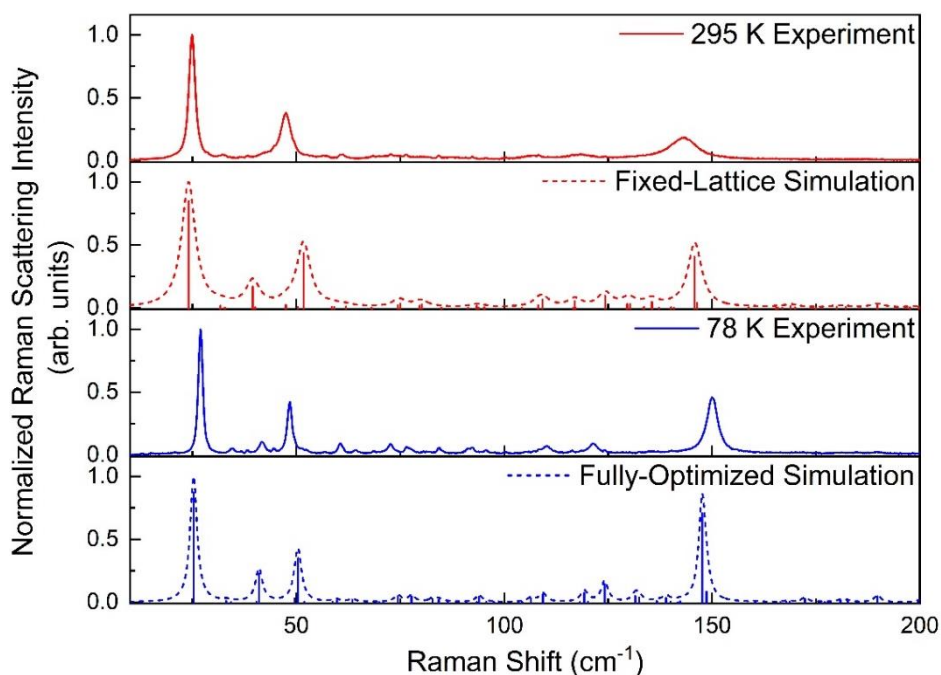
Figure E-5. Experimental 295 K (solid red line) and 78 K (solid blue line) Raman spectra for R-II from 10 to 200 cm⁻¹. Simulated Raman spectra are shown based on the fixed-lattice (dashed red line, 2.0 cm⁻¹ FWHM) and full-optimization (dashed blue line, 1.0 cm⁻¹ FWHM) calculations.

Table E-1. Solid-state DFT IR-active modes with frequencies (cm^{-1}), intensities (km/mol), and mode symmetries for R-I full optimization.

Mode Label (ν)	Frequency (cm^{-1})	Intensity (km/mol)	Mode Symmetry	Mode Label (ν)	Frequency (cm^{-1})	Intensity (km/mol)	Mode Symmetry
5	39.19	0.13	B1	54	214.08	25.56	B2
6	43.67	0.16	B2	55	240.53	8.54	B3
8	57.28	0.00	B3	56	242.93	2.98	B1
9	64.66	0.04	B2	58	245.14	24.30	B1
10	72.23	0.03	B3	59	245.36	1.16	B2
11	72.71	4.88	B1	60	246.49	1.30	B3
15	82.38	12.43	B1	61	256.92	4.83	B3
16	83.90	20.91	B2	62	258.63	0.15	B1
17	85.95	1.67	B3	63	268.72	46.97	B2
18	86.44	1.16	B3	65	278.79	50.69	B2
19	86.98	54.49	B1	67	281.04	40.45	B3
21	90.10	32.10	B2	69	282.33	22.57	B1
22	94.08	0.01	B2	70	283.91	12.80	B2
23	102.21	0.00	B1	71	296.67	0.11	B1
25	105.35	0.16	B3	72	296.67	17.19	B3
26	110.14	21.23	B2	73	319.06	9.09	B3
27	110.86	18.94	B1	74	319.48	83.37	B1
28	110.92	4.26	B3	75	325.62	7.72	B1
29	113.54	5.36	B1	77	329.94	50.03	B2
30	114.27	15.47	B3	78	330.10	9.21	B3
31	117.24	9.69	B2	80	362.51	125.06	B2
33	123.10	0.00	B3	82	381.12	27.41	B2
34	123.14	4.18	B2	83	384.88	44.14	B1
36	127.50	3.94	B1	84	386.12	225.85	B3
37	130.21	40.03	B1	86	414.05	11.41	B2
38	133.20	23.82	B2	87	422.10	91.62	B1
40	140.33	8.18	B3	88	423.67	24.55	B3
42	145.92	9.94	B3	89	446.42	39.56	B2
43	147.39	0.08	B1	90	448.63	3.08	B3
44	158.07	7.23	B2	92	450.73	54.61	B1
45	168.33	26.17	B2	94	463.44	86.87	B3
46	171.80	1.31	B3	95	465.11	435.75	B1
48	184.56	1.02	B1	96	466.03	83.58	B2
49	187.44	7.33	B1	98	546.78	10.30	B2
51	191.86	3.19	B3	99	551.78	2.03	B1
52	195.10	17.08	B2	100	554.59	8.39	B3

101	563.19	9.65	B2	156	848.12	132.27	B3
102	563.83	3.24	B1	158	857.92	16.80	B1
103	564.23	50.71	B3	159	858.43	57.29	B2
106	614.52	47.92	B3	160	858.54	66.97	B3
107	619.85	484.19	B1	161	871.87	92.45	B2
109	623.96	31.83	B2	162	873.50	48.83	B3
110	624.95	91.62	B3	163	874.60	6.25	B1
111	627.24	194.04	B2	166	922.99	18.79	B1
112	629.46	15.99	B1	167	924.00	12.91	B3
113	641.76	288.20	B2	168	924.03	5.66	B2
114	642.69	201.33	B1	169	972.49	174.26	B3
115	647.13	24.92	B3	170	972.96	0.83	B2
118	667.99	94.77	B3	171	975.18	88.28	B1
119	671.88	414.74	B2	173	1012.87	1.68	B3
120	675.68	525.27	B1	174	1013.73	91.37	B2
121	685.11	79.96	B3	177	1015.16	41.33	B1
122	688.95	14.34	B1	178	1015.99	100.78	B2
123	691.94	13.54	B2	179	1016.36	4.14	B3
125	705.71	188.68	B2	180	1016.95	17.85	B1
127	708.78	83.97	B3	182	1058.55	0.14	B1
128	708.89	8.72	B1	183	1058.96	459.02	B3
130	714.49	5.98	B2	185	1060.51	115.42	B2
131	716.17	106.30	B1	186	1061.46	291.22	B2
132	720.72	1.98	B3	187	1061.61	207.15	B3
133	741.43	547.76	B1	188	1061.64	48.91	B1
134	743.37	15.88	B3	190	1073.47	1.13	B2
135	743.66	94.98	B2	191	1073.85	39.18	B3
137	745.90	3.56	B1	192	1075.29	182.94	B1
138	747.75	0.06	B2	193	1079.26	208.98	B1
140	761.25	9.27	B3	195	1082.15	1138.29	B2
141	783.44	0.05	B3	196	1092.56	85.27	B3
143	783.73	34.83	B1	197	1094.90	94.63	B3
144	784.36	0.45	B2	199	1096.22	59.48	B1
145	800.06	185.59	B1	200	1097.18	45.04	B2
147	801.26	191.96	B2	201	1104.54	236.95	B2
148	802.52	12.24	B3	203	1108.00	21.75	B1
149	840.70	112.43	B3	204	1108.41	161.60	B3
151	841.40	52.65	B2	206	1123.09	41.49	B1
152	841.82	0.00	B1	207	1126.54	2.78	B3
153	843.80	279.29	B2	208	1128.27	12.72	B2
155	846.16	15.09	B1	210	1160.21	10.45	B3

211	1160.56	242.20	B2	266	1399.88	19.28	B3
212	1160.85	145.36	B1	267	1400.80	84.47	B2
213	1197.30	109.76	B2	268	1401.13	2.55	B1
214	1197.94	0.33	B3	269	1420.67	96.83	B2
216	1200.51	3.42	B1	270	1421.32	59.11	B1
217	1221.12	35.41	B2	272	1421.58	30.67	B3
219	1223.26	0.01	B1	273	1438.32	75.34	B3
220	1225.79	83.01	B3	274	1438.73	7.54	B2
221	1228.42	17.82	B3	276	1442.40	27.07	B1
223	1231.35	1.71	B1	277	1457.94	226.97	B2
224	1236.49	69.78	B1	278	1460.83	43.66	B3
225	1236.92	33.18	B2	280	1463.81	444.02	B1
226	1238.71	0.01	B3	281	1464.28	0.53	B3
228	1239.52	20.00	B2	282	1465.66	74.06	B2
230	1253.13	4.39	B1	283	1465.76	51.31	B1
231	1254.50	4.66	B3	285	1473.61	78.19	B2
232	1255.22	53.39	B2	286	1473.74	38.40	B3
233	1272.24	104.16	B3	288	1476.57	1.96	B1
234	1272.79	93.45	B2	289	1490.07	338.83	B3
235	1276.59	0.78	B1	291	1493.36	14.41	B1
237	1285.82	14.91	B2	292	1493.70	6.71	B2
238	1287.89	21.91	B3	293	1596.11	305.49	B2
240	1292.82	95.81	B1	294	1597.85	253.30	B1
242	1302.68	481.70	B3	296	1604.28	157.67	B3
243	1303.83	22.37	B2	298	1656.68	942.74	B3
244	1305.51	0.69	B1	299	1681.68	1322.72	B2
245	1311.36	201.32	B3	300	1687.70	455.95	B1
247	1313.04	0.76	B2	302	2950.04	148.25	B1
248	1313.18	1.19	B1	303	2950.70	0.01	B3
249	1313.78	182.51	B1	304	2950.77	0.92	B2
250	1317.52	288.46	B2	305	2966.32	1.25	B3
252	1319.30	68.85	B3	306	2966.33	2.04	B2
254	1324.49	257.10	B2	307	2966.55	14.21	B1
255	1325.19	21.89	B3	310	2979.50	31.27	B1
256	1330.70	3.35	B1	311	2980.47	121.59	B2
258	1355.10	1.34	B3	312	2980.69	23.86	B3
259	1355.17	0.16	B1	314	2992.81	33.16	B1
260	1355.50	33.47	B2	315	2993.23	118.25	B2
262	1358.08	55.59	B1	316	2993.52	94.94	B3
263	1358.17	59.27	B3	317	2995.76	115.09	B2
264	1359.50	17.87	B2	318	2996.02	1.71	B3

319	2996.54	1.38	B1
321	3008.89	11.36	B1
323	3009.31	33.57	B2
324	3009.37	82.32	B3
325	3071.00	4756.28	B2
327	3080.59	3264.23	B3
328	3081.71	975.21	B1
329	3186.74	515.29	B3
331	3186.88	0.03	B1
332	3186.90	0.05	B2
333	3226.52	2321.33	B2
335	3230.52	5883.59	B3
336	3232.11	877.87	B1
338	3285.87	361.58	B3
339	3288.83	3336.36	B2
340	3295.96	1399.93	B1
341	3331.17	5069.87	B3
343	3331.62	276.21	B2
344	3333.72	61.04	B1
345	3530.29	1135.14	B2
347	3531.63	66.92	B3
348	3533.68	470.05	B1

Table E-2. Solid-state DFT Raman-active modes with frequencies (cm^{-1}), relative intensities (normalized to 1000), and mode symmetries for R-I full optimization at 78 K.

Mode Label (ν)	Frequency (cm^{-1})	Relative Intensity	Mode Symmetry	Mode Label (ν)	Frequency (cm^{-1})	Relative Intensity	Mode Symmetry
4	37.24	9.49	A	40	140.33	18.01	B3
5	39.19	0.15	B1	41	144.22	113.17	A
6	43.67	43.73	B2	42	145.92	20.57	B3
7	54.80	16.34	A	43	147.39	11.61	B1
8	57.28	3.56	B3	44	158.07	7.20	B2
9	64.66	6.30	B2	45	168.33	20.38	B2
10	72.23	31.94	B3	46	171.80	27.79	B3
11	72.71	43.72	B1	47	177.36	12.05	A
12	75.39	53.54	A	48	184.56	19.40	B1
13	79.62	16.84	A	49	187.44	26.98	B1
14	81.62	213.21	A	50	189.42	39.88	A
15	82.38	0.02	B1	51	191.86	14.03	B3
16	83.90	0.79	B2	52	195.10	0.35	B2
17	85.95	39.46	B3	53	213.97	8.49	A
18	86.44	18.27	B3	54	214.08	28.41	B2
19	86.98	27.71	B1	55	240.53	8.17	B3
20	88.17	49.22	A	56	242.93	5.94	B1
21	90.10	65.05	B2	57	244.95	7.14	A
22	94.08	10.33	B2	58	245.14	10.13	B1
23	102.21	1.22	B1	59	245.36	6.42	B2
24	105.23	40.84	A	60	246.49	0.12	B3
25	105.35	14.42	B3	61	256.92	5.88	B3
26	110.14	5.71	B2	62	258.63	24.02	B1
27	110.86	9.10	B1	63	268.72	1.43	B2
28	110.92	1.92	B3	64	269.54	23.42	A
29	113.54	26.61	B1	65	278.79	0.00	B2
30	114.27	0.02	B3	66	278.83	44.29	A
31	117.24	113.94	B2	67	281.04	6.96	B3
32	117.93	28.69	A	68	282.14	48.02	A
33	123.10	8.22	B3	69	282.33	0.02	B1
34	123.14	105.40	B2	70	283.91	11.72	B2
35	126.87	36.67	A	71	296.67	21.75	B1
36	127.50	105.85	B1	72	296.67	0.04	B3
37	130.21	101.81	B1	73	319.06	8.98	B3
38	133.20	247.02	B2	74	319.48	19.31	B1
39	136.88	35.88	A	75	325.62	0.00	B1

76	326.61	24.72	A	117	665.28	4.04	A
77	329.94	0.86	B2	118	667.99	0.91	B3
78	330.10	4.08	B3	119	671.88	0.67	B2
79	360.13	28.53	A	120	675.68	2.75	B1
80	362.51	2.56	B2	121	685.11	3.45	B3
81	380.10	163.07	A	122	688.95	32.57	B1
82	381.12	6.27	B2	123	691.94	3.41	B2
83	384.88	0.03	B1	124	699.25	26.70	A
84	386.12	0.26	B3	125	705.71	0.02	B2
85	413.73	4.89	A	126	707.74	81.90	A
86	414.05	24.30	B2	127	708.78	4.03	B3
87	422.10	23.84	B1	128	708.89	5.57	B1
88	423.67	0.13	B3	129	711.00	40.02	A
89	446.42	0.02	B2	130	714.49	1.60	B2
90	448.63	0.21	B3	131	716.17	13.57	B1
91	449.57	31.61	A	132	720.72	11.47	B3
92	450.73	41.19	B1	133	741.43	1.77	B1
93	462.30	15.01	A	134	743.37	1.82	B3
94	463.44	0.56	B3	135	743.66	9.55	B2
95	465.11	4.19	B1	136	744.17	14.09	A
96	466.03	11.50	B2	137	745.90	0.94	B1
97	544.00	29.32	A	138	747.75	23.62	B2
98	546.78	10.74	B2	139	753.85	6.36	A
99	551.78	3.39	B1	140	761.25	4.13	B3
100	554.59	24.45	B3	141	783.44	1.48	B3
101	563.19	2.74	B2	142	783.58	21.68	A
102	563.83	9.29	B1	143	783.73	3.97	B1
103	564.23	7.86	B3	144	784.36	3.13	B2
104	567.01	28.76	A	145	800.06	19.97	B1
105	614.36	16.86	A	146	800.15	24.23	A
106	614.52	0.82	B3	147	801.26	0.02	B2
107	619.85	3.43	B1	148	802.52	7.75	B3
108	621.34	35.09	A	149	840.70	0.37	B3
109	623.96	6.92	B2	150	841.39	72.59	A
110	624.95	24.57	B3	151	841.40	4.26	B2
111	627.24	0.22	B2	152	841.82	3.07	B1
112	629.46	12.09	B1	153	843.80	14.31	B2
113	641.76	0.43	B2	154	844.15	78.95	A
114	642.69	2.85	B1	155	846.16	5.24	B1
115	647.13	5.21	B3	156	848.12	6.28	B3
116	647.60	4.90	A	157	857.23	44.76	A

158	857.92	0.06	B1	199	1096.22	0.01	B1
159	858.43	12.67	B2	200	1097.18	3.59	B2
160	858.54	0.01	B3	201	1104.54	4.87	B2
161	871.87	16.16	B2	202	1106.76	15.80	A
162	873.50	0.16	B3	203	1108.00	0.00	B1
163	874.60	0.16	B1	204	1108.41	0.67	B3
164	875.20	81.95	A	205	1123.07	51.11	A
165	922.94	19.25	A	206	1123.09	1.06	B1
166	922.99	8.31	B1	207	1126.54	1.36	B3
167	924.00	17.87	B3	208	1128.27	22.12	B2
168	924.03	0.20	B2	209	1158.06	29.17	A
169	972.49	0.52	B3	210	1160.21	6.92	B3
170	972.96	5.57	B2	211	1160.56	7.78	B2
171	975.18	6.82	B1	212	1160.85	12.92	B1
172	975.20	84.85	A	213	1197.30	0.05	B2
173	1012.87	4.43	B3	214	1197.94	7.68	B3
174	1013.73	29.28	B2	215	1200.45	29.57	A
175	1014.36	77.78	A	216	1200.51	0.91	B1
176	1014.87	25.08	A	217	1221.12	11.96	B2
177	1015.16	6.85	B1	218	1221.92	25.33	A
178	1015.99	6.11	B2	219	1223.26	103.10	B1
179	1016.36	0.01	B3	220	1225.79	32.09	B3
180	1016.95	0.28	B1	221	1228.42	0.66	B3
181	1058.46	76.95	A	222	1230.88	64.97	A
182	1058.55	0.65	B1	223	1231.35	3.71	B1
183	1058.96	0.03	B3	224	1236.49	2.13	B1
184	1060.34	81.72	A	225	1236.92	0.06	B2
185	1060.51	5.80	B2	226	1238.71	18.02	B3
186	1061.46	0.44	B2	227	1239.01	51.19	A
187	1061.61	5.86	B3	228	1239.52	25.18	B2
188	1061.64	1.08	B1	229	1252.37	52.11	A
189	1073.29	97.34	A	230	1253.13	19.06	B1
190	1073.47	11.16	B2	231	1254.50	4.07	B3
191	1073.85	29.06	B3	232	1255.22	0.26	B2
192	1075.29	1.91	B1	233	1272.24	11.04	B3
193	1079.26	0.73	B1	234	1272.79	3.79	B2
194	1079.63	27.00	A	235	1276.59	0.09	B1
195	1082.15	2.43	B2	236	1277.84	6.94	A
196	1092.56	2.51	B3	237	1285.82	8.78	B2
197	1094.90	18.95	B3	238	1287.89	4.34	B3
198	1095.36	206.31	A	239	1289.95	43.49	A

240	1292.82	4.15	B1	281	1464.28	2.98	B3
241	1301.15	25.23	A	282	1465.66	0.08	B2
242	1302.68	25.34	B3	283	1465.76	3.44	B1
243	1303.83	1.22	B2	284	1466.36	35.72	A
244	1305.51	25.99	B1	285	1473.61	27.78	B2
245	1311.36	50.56	B3	286	1473.74	59.88	B3
246	1311.73	41.66	A	287	1475.42	17.19	A
247	1313.04	0.86	B2	288	1476.57	79.02	B1
248	1313.18	22.27	B1	289	1490.07	113.57	B3
249	1313.78	9.72	B1	290	1490.53	1000.00	A
250	1317.52	1.04	B2	291	1493.36	85.15	B1
251	1317.92	36.89	A	292	1493.70	113.51	B2
252	1319.30	1.76	B3	293	1596.11	22.37	B2
253	1322.06	38.08	A	294	1597.85	59.85	B1
254	1324.49	7.64	B2	295	1603.78	294.76	A
255	1325.19	7.84	B3	296	1604.28	60.65	B3
256	1330.70	4.11	B1	297	1655.27	148.09	A
257	1354.87	95.14	A	298	1656.68	30.08	B3
258	1355.10	0.44	B3	299	1681.68	4.59	B2
259	1355.17	3.29	B1	300	1687.70	4.19	B1
260	1355.50	0.01	B2	301	2950.00	197.99	A
261	1357.19	69.71	A	302	2950.04	0.53	B1
262	1358.08	4.40	B1	303	2950.70	87.46	B3
263	1358.17	1.54	B3	304	2950.77	27.59	B2
264	1359.50	11.89	B2	305	2966.32	56.45	B3
265	1398.92	15.46	A	306	2966.33	1.36	B2
266	1399.88	8.21	B3	307	2966.55	0.17	B1
267	1400.80	4.95	B2	308	2966.81	584.43	A
268	1401.13	22.28	B1	309	2979.45	72.15	A
269	1420.67	16.49	B2	310	2979.50	1.29	B1
270	1421.32	19.12	B1	311	2980.47	13.08	B2
271	1421.55	207.12	A	312	2980.69	22.97	B3
272	1421.58	19.25	B3	313	2992.56	31.51	A
273	1438.32	17.21	B3	314	2992.81	18.03	B1
274	1438.73	20.36	B2	315	2993.23	111.32	B2
275	1439.86	26.91	A	316	2993.52	0.87	B3
276	1442.40	1.11	B1	317	2995.76	12.93	B2
277	1457.94	18.02	B2	318	2996.02	0.21	B3
278	1460.83	2.88	B3	319	2996.54	4.99	B1
279	1461.39	106.60	A	320	2996.57	525.27	A
280	1463.81	1.19	B1	321	3008.89	116.07	B1

322	3008.96	114.95	A
323	3009.31	19.12	B2
324	3009.37	1.73	B3
325	3071.00	31.94	B2
326	3076.32	385.00	A
327	3080.59	14.86	B3
328	3081.71	161.65	B1
329	3186.74	0.13	B3
330	3186.87	165.26	A
331	3186.88	3.93	B1
332	3186.90	10.22	B2
333	3226.52	30.17	B2
334	3226.99	604.63	A
335	3230.52	63.81	B3
336	3232.11	47.84	B1
337	3281.82	92.58	A
338	3285.87	0.23	B3
339	3288.83	11.76	B2
340	3295.96	49.22	B1
341	3331.17	10.32	B3
342	3331.27	383.70	A
343	3331.62	39.48	B2
344	3333.72	131.97	B1
345	3530.29	12.19	B2
346	3531.31	36.79	A
347	3531.63	12.92	B3
348	3533.68	38.36	B1

Table E-3. Solid-state DFT IR-active modes with frequencies (cm^{-1}), intensities (km/mol), and mode symmetries for R-II full optimization.

Mode Label (ν)	Frequency (cm^{-1})	Intensity (km/mol)	Mode Symmetry	Mode Label (ν)	Frequency (cm^{-1})	Intensity (km/mol)	Mode Symmetry
6	34.22	0.22	B2	54	215.07	62.16	B3
7	40.40	0.55	B2	55	217.98	6.03	B1
8	41.01	0.96	B1	56	228.51	75.17	B2
10	50.40	0.14	B1	58	241.90	0.47	B3
11	51.88	0.11	B3	59	242.81	0.20	B2
12	58.73	2.29	B3	60	250.50	10.84	B1
13	59.75	1.76	B2	61	264.11	9.49	B2
14	63.46	1.32	B1	62	265.52	8.23	B3
15	69.91	16.74	B3	63	266.23	6.31	B1
17	77.69	0.52	B1	64	276.09	8.15	B1
18	82.77	20.72	B2	67	293.98	53.90	B2
20	86.40	1.21	B3	68	300.62	1.02	B3
21	93.39	12.72	B3	70	321.22	8.35	B3
23	95.67	16.63	B2	71	331.72	85.82	B2
24	97.52	1.98	B1	72	333.03	16.29	B1
25	104.28	21.31	B2	74	340.82	1.69	B2
26	106.41	0.94	B1	75	343.28	51.62	B3
28	118.16	0.04	B3	76	346.56	58.45	B1
29	119.21	45.56	B2	77	360.00	81.03	B3
30	120.09	0.25	B1	79	375.18	1.50	B1
32	131.51	9.26	B3	80	375.88	86.06	B2
33	132.43	0.21	B1	81	377.37	6.29	B2
35	138.92	13.07	B2	82	386.73	2.27	B1
36	139.97	6.97	B3	83	397.41	0.00	B3
37	141.72	0.07	B1	85	430.28	1.33	B1
39	147.61	1.43	B2	86	431.00	2.03	B2
40	148.66	18.35	B3	87	434.38	59.42	B3
41	160.39	5.16	B3	90	464.55	63.49	B3
42	166.43	1.80	B2	91	464.86	11.94	B1
43	167.88	28.96	B3	92	465.14	4.29	B2
44	168.71	33.64	B2	94	523.57	0.05	B1
46	172.33	0.01	B1	95	527.60	98.86	B2
47	177.08	0.02	B1	96	531.34	136.87	B3
49	182.66	11.25	B3	97	546.32	36.16	B1
51	199.46	85.96	B2	98	546.75	58.15	B2
52	201.17	10.14	B1	99	547.71	28.98	B3

101	581.73	24.20	B1	156	877.24	22.22	B2
102	583.10	187.96	B3	157	884.70	186.58	B2
104	588.70	1.23	B2	158	885.29	272.72	B1
106	593.78	12.06	B2	159	893.54	3.43	B3
107	596.07	615.58	B3	161	895.68	0.02	B2
108	599.72	4.57	B1	162	896.40	132.86	B1
109	652.21	44.32	B2	164	920.48	7.33	B3
110	652.28	48.66	B1	165	943.56	141.38	B2
112	652.84	8.78	B3	167	944.00	136.35	B1
113	659.73	550.21	B3	168	944.14	256.80	B3
114	660.10	15.10	B2	169	1003.87	16.19	B3
116	670.14	14.02	B1	170	1004.31	3.89	B2
117	681.15	77.78	B3	171	1005.44	0.88	B1
119	684.04	36.14	B2	174	1014.40	0.24	B3
120	686.58	175.47	B1	175	1017.33	366.81	B2
121	694.90	11.86	B3	176	1018.65	0.53	B1
123	709.42	7.71	B1	178	1019.94	110.80	B3
124	709.53	211.95	B2	179	1025.25	692.70	B1
126	716.79	23.31	B3	180	1025.73	21.27	B2
127	747.00	288.39	B2	181	1035.62	565.52	B2
128	749.43	121.12	B1	183	1037.34	89.74	B3
129	763.52	30.89	B3	184	1038.27	117.21	B1
131	766.59	83.05	B2	185	1045.40	649.26	B2
132	767.94	37.87	B1	187	1050.18	135.19	B1
133	777.33	15.28	B3	188	1052.12	137.67	B3
134	777.44	8.93	B2	189	1057.68	13.63	B2
136	778.60	0.40	B1	190	1057.73	15.66	B1
137	794.45	61.59	B2	192	1064.20	153.39	B3
138	794.82	86.34	B1	193	1070.77	150.61	B1
139	801.91	490.61	B3	194	1071.42	104.80	B2
142	816.94	362.59	B1	196	1072.70	3.47	B3
143	817.91	91.31	B2	197	1081.60	47.00	B3
144	819.54	234.60	B3	199	1085.68	28.49	B2
146	822.33	61.90	B3	200	1087.18	125.42	B1
147	822.54	61.81	B1	201	1094.97	125.46	B3
148	822.63	170.85	B2	203	1103.79	31.64	B2
149	863.42	27.61	B2	204	1104.15	61.88	B1
150	864.43	316.05	B3	205	1126.66	14.87	B3
152	868.69	6.93	B1	207	1128.34	437.81	B2
154	873.00	0.30	B3	208	1132.09	79.18	B1
155	876.72	50.35	B1	210	1168.44	158.96	B1

211	1169.28	142.91	B3	265	1393.24	57.83	B2
212	1169.36	101.10	B2	266	1393.89	40.40	B1
213	1204.63	140.54	B2	268	1394.48	20.52	B3
214	1205.28	52.15	B1	269	1412.70	0.74	B2
216	1208.54	14.52	B3	270	1412.71	0.58	B1
217	1209.33	0.82	B2	272	1414.22	117.22	B3
218	1209.59	61.92	B1	273	1427.81	122.24	B2
219	1213.58	46.63	B3	274	1428.24	0.00	B1
222	1223.36	92.81	B3	276	1431.73	25.96	B3
223	1228.81	5.43	B1	277	1453.35	22.85	B3
224	1229.78	9.01	B2	279	1458.61	310.75	B2
225	1244.37	0.07	B3	280	1458.87	112.73	B1
227	1249.76	287.88	B2	282	1466.23	228.22	B1
228	1253.08	59.53	B1	283	1466.42	656.53	B2
229	1261.17	3.70	B2	284	1469.46	55.63	B3
230	1261.21	18.63	B1	285	1473.84	1.90	B3
232	1268.32	126.03	B3	287	1478.17	465.01	B2
233	1272.97	162.23	B1	288	1480.38	150.17	B1
235	1278.11	142.67	B2	290	1490.80	11.98	B3
236	1279.49	159.12	B3	291	1492.82	120.65	B1
238	1298.91	25.29	B3	292	1493.35	12.87	B2
239	1299.67	60.49	B1	293	1591.95	51.34	B1
240	1300.87	29.98	B2	295	1596.67	559.96	B2
242	1308.86	74.30	B3	296	1599.64	38.50	B3
243	1313.71	28.98	B1	297	1628.26	695.09	B2
244	1313.97	7.53	B2	299	1631.45	2903.03	B1
245	1318.60	12.15	B3	300	1632.19	60.81	B3
247	1321.51	89.97	B2	301	2946.67	90.08	B3
248	1322.37	15.63	B1	303	2947.83	353.41	B1
249	1337.16	1.08	B3	304	2947.90	0.18	B2
251	1338.79	35.47	B1	305	2972.37	5234.97	B2
252	1338.87	0.66	B2	307	2976.29	80.39	B3
254	1343.52	31.81	B3	308	2978.69	52.43	B1
255	1351.19	9.75	B2	309	2992.47	1794.33	B2
256	1351.61	138.92	B1	310	2992.66	11.28	B1
257	1356.22	89.75	B1	312	2993.30	4513.95	B2
259	1356.83	6.64	B3	313	2994.16	351.73	B3
260	1357.26	0.00	B2	314	2994.74	3.52	B3
261	1360.56	62.46	B1	316	2999.30	0.47	B1
262	1360.71	0.27	B2	317	2999.40	21.70	B2
263	1367.57	11.84	B3	319	3001.81	131.85	B3

320	3012.70	398.54	B1
321	3016.00	18.86	B3
323	3016.88	92.03	B2
324	3019.21	329.21	B1
325	3047.65	239.85	B1
326	3047.99	154.75	B3
328	3048.03	48.57	B2
330	3061.90	7489.49	B1
331	3070.36	805.79	B2
332	3073.40	130.04	B3
334	3112.28	1252.65	B2
335	3113.31	5391.85	B3
336	3113.33	716.74	B1
337	3153.90	255.91	B2
338	3154.90	25.66	B3
340	3154.96	828.50	B1
342	3249.24	2503.04	B3
343	3274.06	4884.89	B2
344	3289.84	876.57	B1
345	3517.80	593.16	B2
347	3519.35	48.93	B1
348	3519.46	37.51	B3

Table E-4. Solid-state DFT Raman-active modes with frequencies (cm^{-1}), relative intensities (normalized to 1000), and mode symmetries for R-II full optimization at 78 K.

Mode Label (v)	Frequency (cm^{-1})	Relative Intensity	Mode Symmetry	Mode Label (v)	Frequency (cm^{-1})	Relative Intensity	Mode Symmetry
4	25.24	753.94	A	40	148.66	73.23	B3
5	33.09	9.49	A	41	160.39	3.65	B3
6	34.22	1.35	B2	42	166.43	0.64	B2
7	40.40	2.41	B2	43	167.88	4.91	B3
8	41.01	196.65	B1	44	168.71	2.82	B2
9	49.60	26.58	A	45	172.31	23.45	A
10	50.40	302.78	B1	46	172.33	3.44	B1
11	51.88	2.96	B3	47	177.08	2.21	B1
12	58.73	3.44	B3	48	180.91	14.18	A
13	59.75	13.72	B2	49	182.66	9.91	B3
14	63.46	18.10	B1	50	189.79	39.92	A
15	69.91	0.56	B3	51	199.46	6.62	B2
16	74.40	41.18	A	52	201.17	17.64	B1
17	77.69	39.58	B1	53	210.48	3.51	A
18	82.77	21.03	B2	54	215.07	5.33	B3
19	84.26	17.54	A	55	217.98	2.01	B1
20	86.40	3.00	B3	56	228.51	5.62	B2
21	93.39	0.89	B3	57	232.82	29.49	A
22	93.94	38.92	A	58	241.90	0.32	B3
23	95.67	2.53	B2	59	242.81	0.43	B2
24	97.52	1.21	B1	60	250.50	2.31	B1
25	104.28	0.66	B2	61	264.11	11.27	B2
26	106.41	26.14	B1	62	265.52	2.22	B3
27	109.28	54.49	A	63	266.23	19.45	B1
28	118.16	0.91	B3	64	276.09	0.53	B1
29	119.21	65.55	B2	65	277.54	7.85	A
30	120.09	2.99	B1	66	291.05	22.32	A
31	124.15	124.99	A	67	293.98	3.43	B2
32	131.51	43.53	B3	68	300.62	1.28	B3
33	132.43	32.44	B1	69	309.78	42.91	A
34	136.70	9.44	A	70	321.22	10.06	B3
35	138.92	30.44	B2	71	331.72	31.28	B2
36	139.97	3.21	B3	72	333.03	0.04	B1
37	141.72	0.32	B1	73	340.36	17.14	A
38	142.32	5.67	A	74	340.82	0.26	B2
39	147.61	613.56	B2	75	343.28	4.38	B3

76	346.56	21.50	B1	117	681.15	8.14	B3
77	360.00	8.49	B3	118	681.73	103.38	A
78	368.36	194.56	A	119	684.04	0.00	B2
79	375.18	12.61	B1	120	686.58	0.88	B1
80	375.88	1.10	B2	121	694.90	15.44	B3
81	377.37	1.32	B2	122	697.67	44.36	A
82	386.73	7.19	B1	123	709.42	37.77	B1
83	397.41	6.05	B3	124	709.53	0.03	B2
84	397.94	61.03	A	125	714.02	9.74	A
85	430.28	2.61	B1	126	716.79	0.03	B3
86	431.00	7.81	B2	127	747.00	4.15	B2
87	434.38	4.72	B3	128	749.43	23.95	B1
88	434.61	0.36	A	129	763.52	5.55	B3
89	463.68	35.03	A	130	763.63	12.76	A
90	464.55	33.81	B3	131	766.59	7.12	B2
91	464.86	2.00	B1	132	767.94	10.58	B1
92	465.14	0.02	B2	133	777.33	2.81	B3
93	523.17	49.22	A	134	777.44	3.95	B2
94	523.57	1.09	B1	135	778.08	6.54	A
95	527.60	24.75	B2	136	778.60	6.18	B1
96	531.34	0.44	B3	137	794.45	0.00	B2
97	546.32	23.02	B1	138	794.82	10.86	B1
98	546.75	2.13	B2	139	801.91	6.11	B3
99	547.71	10.75	B3	140	802.58	19.75	A
100	551.11	14.22	A	141	816.14	16.99	A
101	581.73	7.08	B1	142	816.94	4.23	B1
102	583.10	13.11	B3	143	817.91	0.37	B2
103	584.06	53.12	A	144	819.54	6.94	B3
104	588.70	1.12	B2	145	822.04	208.98	A
105	593.74	52.85	A	146	822.33	5.31	B3
106	593.78	3.57	B2	147	822.54	11.96	B1
107	596.07	0.01	B3	148	822.63	1.70	B2
108	599.72	12.93	B1	149	863.42	1.45	B2
109	652.21	3.70	B2	150	864.43	2.65	B3
110	652.28	2.09	B1	151	868.38	4.72	A
111	652.43	7.25	A	152	868.69	17.15	B1
112	652.84	0.04	B3	153	871.84	130.29	A
113	659.73	0.17	B3	154	873.00	0.19	B3
114	660.10	6.22	B2	155	876.72	2.78	B1
115	668.78	0.79	A	156	877.24	3.77	B2
116	670.14	0.73	B1	157	884.70	28.25	B2

158	885.29	0.20	B1	199	1085.68	0.34	B2
159	893.54	0.06	B3	200	1087.18	11.78	B1
160	893.92	5.19	A	201	1094.97	3.74	B3
161	895.68	0.16	B2	202	1095.00	41.31	A
162	896.40	7.99	B1	203	1103.79	0.44	B2
163	920.24	3.97	A	204	1104.15	3.48	B1
164	920.48	0.59	B3	205	1126.66	21.03	B3
165	943.56	1.52	B2	206	1126.67	28.66	A
166	943.87	110.27	A	207	1128.34	0.89	B2
167	944.00	0.01	B1	208	1132.09	1.68	B1
168	944.14	3.28	B3	209	1167.54	48.55	A
169	1003.87	9.78	B3	210	1168.44	1.08	B1
170	1004.31	0.00	B2	211	1169.28	27.81	B3
171	1005.44	1.45	B1	212	1169.36	25.17	B2
172	1005.54	72.65	A	213	1204.63	0.63	B2
173	1013.52	49.01	A	214	1205.28	0.02	B1
174	1014.40	3.73	B3	215	1207.57	58.86	A
175	1017.33	4.16	B2	216	1208.54	12.00	B3
176	1018.65	27.92	B1	217	1209.33	12.81	B2
177	1019.89	29.00	A	218	1209.59	3.77	B1
178	1019.94	1.26	B3	219	1213.58	0.36	B3
179	1025.25	0.77	B1	220	1214.58	18.73	A
180	1025.73	12.49	B2	221	1222.65	29.26	A
181	1035.62	0.58	B2	222	1223.36	2.44	B3
182	1037.13	239.09	A	223	1228.81	1.17	B1
183	1037.34	0.46	B3	224	1229.78	2.98	B2
184	1038.27	3.56	B1	225	1244.37	50.76	B3
185	1045.40	0.97	B2	226	1244.95	15.19	A
186	1049.82	66.77	A	227	1249.76	0.01	B2
187	1050.18	0.01	B1	228	1253.08	8.03	B1
188	1052.12	11.71	B3	229	1261.17	4.73	B2
189	1057.68	24.30	B2	230	1261.21	6.04	B1
190	1057.73	31.15	B1	231	1268.00	20.31	A
191	1063.99	40.41	A	232	1268.32	0.01	B3
192	1064.20	0.58	B3	233	1272.97	9.17	B1
193	1070.77	5.48	B1	234	1274.37	11.40	A
194	1071.42	1.81	B2	235	1278.11	3.53	B2
195	1072.11	244.68	A	236	1279.49	0.74	B3
196	1072.70	18.00	B3	237	1296.94	71.38	A
197	1081.60	6.00	B3	238	1298.91	5.11	B3
198	1082.75	38.71	A	239	1299.67	1.34	B1

240	1300.87	0.09	B2	281	1463.27	163.86	A
241	1307.90	7.76	A	282	1466.23	17.97	B1
242	1308.86	0.15	B3	283	1466.42	1.27	B2
243	1313.71	8.00	B1	284	1469.46	0.23	B3
244	1313.97	0.04	B2	285	1473.84	27.83	B3
245	1318.60	23.83	B3	286	1474.28	453.02	A
246	1319.04	13.00	A	287	1478.17	5.62	B2
247	1321.51	0.36	B2	288	1480.38	44.73	B1
248	1322.37	13.66	B1	289	1489.23	381.62	A
249	1337.16	8.78	B3	290	1490.80	43.45	B3
250	1337.68	37.82	A	291	1492.82	15.47	B1
251	1338.79	22.94	B1	292	1493.35	2.48	B2
252	1338.87	39.39	B2	293	1591.95	23.30	B1
253	1342.75	6.63	A	294	1592.02	242.18	A
254	1343.52	0.02	B3	295	1596.67	0.12	B2
255	1351.19	2.08	B2	296	1599.64	2.73	B3
256	1351.61	1.42	B1	297	1628.26	0.96	B2
257	1356.22	3.94	B1	298	1631.18	174.52	A
258	1356.56	108.56	A	299	1631.45	20.40	B1
259	1356.83	12.68	B3	300	1632.19	14.74	B3
260	1357.26	10.21	B2	301	2946.67	0.03	B3
261	1360.56	8.51	B1	302	2946.85	372.92	A
262	1360.71	13.76	B2	303	2947.83	6.77	B1
263	1367.57	1.00	B3	304	2947.90	15.28	B2
264	1368.26	25.23	A	305	2972.37	123.03	B2
265	1393.24	0.00	B2	306	2975.51	1000.00	A
266	1393.89	5.58	B1	307	2976.29	48.60	B3
267	1394.42	83.55	A	308	2978.69	21.32	B1
268	1394.48	2.69	B3	309	2992.47	4.27	B2
269	1412.70	19.25	B2	310	2992.66	122.69	B1
270	1412.71	1.42	B1	311	2992.91	422.09	A
271	1414.03	94.87	A	312	2993.30	1.04	B2
272	1414.22	0.92	B3	313	2994.16	12.68	B3
273	1427.81	28.95	B2	314	2994.74	157.81	B3
274	1428.24	4.77	B1	315	2994.75	21.49	A
275	1431.72	8.61	A	316	2999.30	0.52	B1
276	1431.73	1.05	B3	317	2999.40	2.97	B2
277	1453.35	0.84	B3	318	3001.59	115.86	A
278	1454.14	13.37	A	319	3001.81	28.61	B3
279	1458.61	4.48	B2	320	3012.70	19.61	B1
280	1458.87	8.72	B1	321	3016.00	9.67	B3

322	3016.13	163.81	A
323	3016.88	0.64	B2
324	3019.21	0.51	B1
325	3047.65	38.88	B1
326	3047.99	1.84	B3
327	3048.02	403.77	A
328	3048.03	66.65	B2
329	3060.84	428.18	A
330	3061.90	10.75	B1
331	3070.36	0.41	B2
332	3073.40	142.68	B3
333	3109.58	113.82	A
334	3112.28	0.20	B2
335	3113.31	38.63	B3
336	3113.33	152.49	B1
337	3153.90	0.35	B2
338	3154.90	55.89	B3
339	3154.96	177.67	A
340	3154.96	0.40	B1
341	3249.22	205.27	A
342	3249.24	65.51	B3
343	3274.06	41.03	B2
344	3289.84	124.31	B1
345	3517.80	5.85	B2
346	3519.28	93.30	A
347	3519.35	0.99	B1
348	3519.46	67.17	B3

Table E-5. Solid-state DFT IR-active modes with frequencies (cm^{-1}), intensities (km/mol), and mode symmetries for R-II fixed-lattice optimization.

Mode Label (ν)	Frequency (cm^{-1})	Intensity (km/mol)	Mode Symmetry	Mode Label (ν)	Frequency (cm^{-1})	Intensity (km/mol)	Mode Symmetry
6	32.74	0.04	B2	54	213.35	66.97	B3
7	39.50	0.94	B1	55	216.81	7.25	B1
8	40.06	0.67	B2	56	226.72	75.35	B2
10	50.35	0.23	B3	58	239.94	0.66	B3
11	51.72	0.29	B1	59	241.72	0.25	B2
12	58.49	2.51	B3	60	246.99	11.28	B1
13	59.07	1.80	B2	61	263.70	9.93	B2
14	61.89	0.83	B1	62	265.94	6.97	B1
15	68.11	16.98	B3	63	266.29	6.94	B3
17	75.00	0.35	B1	64	275.37	9.03	B1
18	79.61	20.58	B2	67	291.83	42.55	B2
20	84.87	1.12	B3	68	298.00	0.94	B3
21	91.29	12.16	B3	70	317.61	10.68	B3
23	93.81	12.21	B2	71	329.51	98.68	B2
24	95.19	1.59	B1	72	331.61	14.09	B1
25	104.22	18.04	B2	73	338.17	1.90	B2
26	108.14	1.61	B1	75	343.11	58.00	B3
28	116.66	0.49	B3	76	345.11	53.97	B1
29	116.95	53.61	B2	77	357.69	55.78	B3
30	117.05	0.30	B1	79	373.03	0.90	B1
32	129.55	0.09	B1	80	373.71	67.30	B2
33	130.26	7.46	B3	81	377.18	15.28	B2
35	135.51	7.39	B2	82	383.63	5.50	B1
36	137.22	9.46	B3	83	395.66	0.16	B3
38	140.78	0.11	B1	85	427.77	0.91	B1
39	145.78	1.44	B2	86	428.42	0.94	B2
40	146.36	12.57	B3	87	430.35	66.30	B3
41	158.75	8.23	B3	90	461.36	53.49	B3
42	165.39	30.51	B2	91	462.05	2.51	B2
43	165.78	21.86	B3	92	462.28	12.37	B1
44	166.92	7.36	B2	93	520.91	0.00	B1
46	170.01	0.14	B1	95	525.17	104.66	B2
47	174.95	0.02	B1	96	529.13	130.70	B3
49	182.17	13.70	B3	97	544.40	47.08	B2
51	197.61	75.33	B2	98	544.80	37.84	B1
52	199.75	9.53	B1	99	545.97	15.59	B3

101	583.84	13.59	B1	156	875.69	0.11	B2
102	583.93	43.50	B3	157	878.22	157.41	B2
104	588.02	7.85	B2	158	879.54	137.91	B1
106	597.11	2.88	B2	159	894.36	6.01	B3
107	598.47	746.60	B3	161	895.11	8.79	B2
108	600.78	8.74	B1	162	896.04	52.48	B1
109	652.71	48.60	B1	164	913.13	6.81	B3
111	652.94	47.03	B2	165	943.16	156.05	B2
112	653.35	34.92	B3	166	944.09	274.92	B3
113	661.42	563.98	B3	168	944.44	137.01	B1
114	661.83	5.04	B2	169	1003.35	10.75	B2
116	671.22	16.35	B1	170	1003.59	16.08	B3
117	677.65	94.15	B3	171	1004.44	3.00	B1
119	683.16	49.15	B2	174	1013.87	0.84	B3
120	685.65	167.65	B1	175	1018.31	354.78	B2
121	690.18	4.34	B3	176	1019.79	0.77	B1
123	707.98	226.88	B2	177	1019.94	106.64	B3
124	708.16	5.95	B1	179	1024.42	691.72	B1
126	714.38	23.52	B3	180	1024.77	28.20	B2
127	743.04	254.26	B2	181	1034.74	602.28	B2
128	744.95	130.33	B1	183	1037.18	85.03	B3
130	760.87	27.11	B3	184	1037.88	114.21	B1
131	763.48	78.10	B2	185	1043.90	614.10	B2
132	764.79	59.16	B1	186	1048.47	109.61	B1
133	778.04	5.47	B3	188	1051.29	145.30	B3
134	778.14	9.21	B2	189	1058.08	28.97	B2
136	779.03	0.85	B1	190	1058.30	7.33	B1
137	787.66	88.70	B1	192	1064.49	172.97	B3
138	787.72	23.43	B2	194	1071.44	168.95	B1
139	794.05	545.55	B3	195	1071.87	112.30	B2
141	814.48	380.12	B1	196	1073.41	3.30	B3
143	814.95	106.40	B2	197	1081.53	33.65	B3
144	817.23	254.01	B3	199	1085.85	35.43	B2
146	822.04	31.34	B1	200	1087.34	133.38	B1
147	822.17	0.68	B3	201	1095.71	113.74	B3
148	822.20	211.51	B2	203	1103.48	33.43	B2
149	864.37	47.15	B2	204	1104.26	53.28	B1
150	866.10	285.16	B3	206	1124.54	13.55	B3
151	869.62	137.94	B1	207	1126.31	466.94	B2
153	872.59	12.75	B3	208	1129.18	73.98	B1
155	874.57	122.68	B1	210	1168.36	153.52	B1

211	1169.27	108.76	B2	265	1392.75	61.82	B2
212	1169.63	134.10	B3	266	1394.14	40.10	B1
213	1203.56	146.88	B2	268	1394.83	31.98	B3
214	1204.21	57.00	B1	269	1412.63	1.65	B1
216	1207.41	9.48	B3	270	1412.92	0.88	B2
217	1208.64	6.17	B2	271	1414.06	99.65	B3
218	1208.92	59.37	B1	273	1425.43	112.78	B2
219	1212.66	46.79	B3	274	1425.92	0.24	B1
222	1223.14	99.95	B3	276	1429.00	24.23	B3
223	1228.96	5.04	B1	277	1450.43	24.47	B3
224	1230.06	11.34	B2	279	1455.22	232.93	B2
225	1244.72	0.78	B3	280	1456.25	66.27	B1
227	1251.12	273.73	B2	282	1464.57	260.97	B1
228	1254.20	57.10	B1	283	1465.88	740.87	B2
229	1262.09	5.25	B2	284	1467.52	25.71	B3
230	1262.27	18.16	B1	285	1470.68	15.59	B3
232	1269.31	126.42	B3	287	1475.95	433.80	B2
233	1272.83	177.22	B1	288	1478.21	152.50	B1
235	1278.48	164.74	B2	290	1488.82	11.65	B3
236	1279.53	146.03	B3	291	1489.53	139.64	B1
238	1299.21	30.76	B3	292	1490.46	4.97	B2
239	1301.07	59.30	B1	293	1591.96	46.99	B1
240	1301.21	17.87	B2	295	1596.36	623.06	B2
242	1309.90	52.57	B3	296	1599.53	28.53	B3
243	1315.39	23.06	B1	297	1626.52	697.91	B2
244	1315.51	25.45	B2	299	1630.17	2889.39	B1
246	1321.09	11.88	B3	300	1631.09	40.76	B3
247	1321.82	89.42	B2	301	2949.03	57.04	B3
248	1323.52	18.95	B1	303	2949.82	318.38	B1
250	1338.62	1.82	B3	304	2949.96	0.53	B2
251	1340.02	1.44	B2	305	2974.75	1380.30	B2
252	1340.07	42.30	B1	307	2977.68	13.60	B1
254	1344.10	26.61	B3	308	2977.74	5.95	B3
255	1349.49	11.40	B2	309	2992.81	16.55	B1
256	1350.77	91.51	B1	310	2992.92	8.74	B2
257	1355.55	1.37	B2	311	2993.82	25.87	B3
258	1356.14	9.59	B3	312	2994.45	161.17	B2
259	1356.16	56.57	B1	314	2995.29	0.01	B3
261	1360.24	104.54	B1	316	2995.48	11.08	B1
262	1360.84	0.02	B2	317	3007.00	9940.74	B2
263	1366.80	12.43	B3	319	3010.97	243.45	B3

320	3013.23	6.96	B2
322	3013.37	311.23	B3
323	3013.58	6.65	B1
324	3032.01	841.87	B1
326	3043.75	111.07	B2
327	3043.76	131.25	B3
328	3044.20	47.19	B1
330	3075.90	7309.11	B1
331	3084.09	754.85	B2
332	3086.96	86.60	B3
334	3128.52	1368.46	B2
335	3129.33	651.88	B1
336	3130.07	4871.64	B3
337	3154.42	247.52	B2
338	3154.55	835.59	B1
340	3155.83	61.94	B3
341	3266.48	2343.80	B3
343	3289.84	4857.17	B2
344	3305.10	842.86	B1
345	3516.17	608.14	B2
347	3517.13	44.43	B1
348	3517.96	24.23	B3

Table E-6. Solid-state DFT Raman-active modes with frequencies (cm^{-1}), relative intensities (normalized to 1000), and mode symmetries for R-II fixed-lattice optimization at 295 K.

Mode Label (ν)	Frequency (cm^{-1})	Relative Intensity	Mode Symmetry	Mode Label (ν)	Frequency (cm^{-1})	Relative Intensity	Mode Symmetry
4	24.01	1000.00	A	40	146.36	44.04	B3
5	31.66	19.86	A	41	158.75	4.33	B3
6	32.74	2.83	B2	42	165.39	0.77	B2
7	39.50	198.99	B1	43	165.78	3.20	B3
8	40.06	4.41	B2	44	166.92	0.51	B2
9	47.47	27.26	A	45	168.89	19.13	A
10	50.35	5.31	B3	46	170.01	5.07	B1
11	51.72	510.68	B1	47	174.95	0.80	B1
12	58.49	8.96	B3	48	179.98	11.67	A
13	59.07	6.75	B2	49	182.17	8.03	B3
14	61.89	12.04	B1	50	189.81	31.90	A
15	68.11	0.78	B3	51	197.61	3.99	B2
16	74.39	25.22	A	52	199.75	9.69	B1
17	75.00	38.15	B1	53	210.54	3.02	A
18	79.61	21.68	B2	54	213.35	3.52	B3
19	80.19	32.91	A	55	216.81	1.64	B1
20	84.87	2.52	B3	56	226.72	4.44	B2
21	91.29	1.54	B3	57	230.68	15.86	A
22	93.34	20.57	A	58	239.94	0.61	B3
23	93.81	2.61	B2	59	241.72	0.12	B2
24	95.19	4.72	B1	60	246.99	2.80	B1
25	104.22	0.91	B2	61	263.70	6.96	B2
26	108.14	24.92	B1	62	265.94	11.63	B1
27	109.17	77.10	A	63	266.29	1.99	B3
28	116.66	1.17	B3	64	275.37	0.57	B1
29	116.95	62.60	B2	65	276.49	4.98	A
30	117.05	1.83	B1	66	288.99	11.98	A
31	124.29	113.73	A	67	291.83	3.10	B2
32	129.55	35.66	B1	68	298.00	1.24	B3
33	130.26	36.28	B3	69	308.13	23.65	A
34	133.55	8.55	A	70	317.61	6.28	B3
35	135.51	55.61	B2	71	329.51	15.94	B2
36	137.22	0.21	B3	72	331.61	0.01	B1
37	140.09	5.61	A	73	338.17	0.41	B2
38	140.78	2.93	B1	74	340.52	11.41	A
39	145.78	476.69	B2	75	343.11	2.24	B3

76	345.11	13.51	B1	117	677.65	7.31	B3
77	357.69	3.86	B3	118	678.01	33.68	A
78	363.99	109.46	A	119	683.16	0.02	B2
79	373.03	6.16	B1	120	685.65	0.58	B1
80	373.71	1.04	B2	121	690.18	4.88	B3
81	377.18	0.54	B2	122	693.20	33.49	A
82	383.63	2.26	B1	123	707.98	0.05	B2
83	395.66	3.98	B3	124	708.16	17.86	B1
84	396.29	27.60	A	125	712.29	4.38	A
85	427.77	1.32	B1	126	714.38	0.02	B3
86	428.42	4.87	B2	127	743.04	2.08	B2
87	430.35	2.71	B3	128	744.95	13.31	B1
88	430.76	0.44	A	129	760.19	5.24	A
89	461.21	19.26	A	130	760.87	2.03	B3
90	461.36	15.52	B3	131	763.48	3.73	B2
91	462.05	0.00	B2	132	764.79	3.20	B1
92	462.28	0.74	B1	133	778.04	1.60	B3
93	520.91	0.52	B1	134	778.14	1.69	B2
94	521.29	24.07	A	135	778.53	2.99	A
95	525.17	11.73	B2	136	779.03	3.54	B1
96	529.13	0.26	B3	137	787.66	3.93	B1
97	544.40	0.66	B2	138	787.72	0.01	B2
98	544.80	10.69	B1	139	794.05	2.02	B3
99	545.97	6.01	B3	140	794.42	6.97	A
100	549.52	8.07	A	141	814.48	3.29	B1
101	583.84	2.32	B1	142	814.69	0.81	A
102	583.93	6.45	B3	143	814.95	0.04	B2
103	584.59	30.18	A	144	817.23	5.91	B3
104	588.02	1.35	B2	145	821.81	104.85	A
105	596.70	17.87	A	146	822.04	6.06	B1
106	597.11	0.64	B2	147	822.17	0.64	B3
107	598.47	0.34	B3	148	822.20	0.74	B2
108	600.78	8.36	B1	149	864.37	0.02	B2
109	652.71	1.40	B1	150	866.10	0.72	B3
110	652.87	3.90	A	151	869.62	9.90	B1
111	652.94	2.09	B2	152	870.22	23.10	A
112	653.35	0.13	B3	153	872.59	0.18	B3
113	661.42	0.17	B3	154	872.64	38.27	A
114	661.83	1.83	B2	155	874.57	0.00	B1
115	669.17	0.31	A	156	875.69	7.87	B2
116	671.22	0.30	B1	157	878.22	5.40	B2

158	879.54	0.20	B1	199	1085.85	0.10	B2
159	894.36	0.00	B3	200	1087.34	4.60	B1
160	894.87	1.67	A	201	1095.71	1.63	B3
161	895.11	1.06	B2	202	1096.53	19.14	A
162	896.04	2.99	B1	203	1103.48	0.12	B2
163	912.93	2.35	A	204	1104.26	1.60	B1
164	913.13	0.21	B3	205	1124.20	12.03	A
165	943.16	0.50	B2	206	1124.54	10.19	B3
166	944.09	0.89	B3	207	1126.31	0.40	B2
167	944.13	52.63	A	208	1129.18	0.70	B1
168	944.44	0.01	B1	209	1167.66	22.50	A
169	1003.35	0.00	B2	210	1168.36	0.30	B1
170	1003.59	4.33	B3	211	1169.27	9.68	B2
171	1004.44	0.39	B1	212	1169.63	13.14	B3
172	1004.53	37.88	A	213	1203.56	0.06	B2
173	1012.94	24.83	A	214	1204.21	0.01	B1
174	1013.87	1.92	B3	215	1206.78	25.73	A
175	1018.31	1.37	B2	216	1207.41	6.32	B3
176	1019.79	12.06	B1	217	1208.64	5.73	B2
177	1019.94	0.73	B3	218	1208.92	1.23	B1
178	1020.04	11.79	A	219	1212.66	0.15	B3
179	1024.42	0.40	B1	220	1214.04	9.29	A
180	1024.77	6.19	B2	221	1222.40	13.07	A
181	1034.74	0.19	B2	222	1223.14	1.22	B3
182	1036.98	104.92	A	223	1228.96	0.42	B1
183	1037.18	0.16	B3	224	1230.06	1.08	B2
184	1037.88	1.34	B1	225	1244.72	23.41	B3
185	1043.90	0.47	B2	226	1245.27	6.32	A
186	1048.47	0.02	B1	227	1251.12	0.02	B2
187	1048.78	30.26	A	228	1254.20	4.23	B1
188	1051.29	5.01	B3	229	1262.09	2.50	B2
189	1058.08	11.54	B2	230	1262.27	2.85	B1
190	1058.30	13.95	B1	231	1268.67	10.67	A
191	1064.31	16.66	A	232	1269.31	0.04	B3
192	1064.49	0.36	B3	233	1272.83	3.95	B1
193	1071.37	115.14	A	234	1273.98	5.20	A
194	1071.44	1.61	B1	235	1278.48	1.10	B2
195	1071.87	0.53	B2	236	1279.53	0.19	B3
196	1073.41	8.79	B3	237	1298.36	33.14	A
197	1081.53	2.73	B3	238	1299.21	2.37	B3
198	1082.84	15.76	A	239	1301.07	0.63	B1

240	1301.21	0.02	B2	281	1462.28	77.52	A
241	1309.41	2.59	A	282	1464.57	4.86	B1
242	1309.90	0.11	B3	283	1465.88	0.62	B2
243	1315.39	2.47	B1	284	1467.52	2.91	B3
244	1315.51	0.00	B2	285	1470.68	9.45	B3
245	1320.80	5.71	A	286	1471.39	181.39	A
246	1321.09	11.28	B3	287	1475.95	2.05	B2
247	1321.82	0.01	B2	288	1478.21	14.80	B1
248	1323.52	7.06	B1	289	1486.47	204.15	A
249	1338.49	20.56	A	290	1488.82	20.46	B3
250	1338.62	3.64	B3	291	1489.53	6.63	B1
251	1340.02	13.84	B2	292	1490.46	0.75	B2
252	1340.07	9.39	B1	293	1591.96	8.19	B1
253	1343.46	3.06	A	294	1592.00	115.75	A
254	1344.10	0.06	B3	295	1596.36	0.03	B2
255	1349.49	4.96	B2	296	1599.53	1.12	B3
256	1350.77	0.94	B1	297	1626.52	0.21	B2
257	1355.55	6.17	B2	298	1629.91	84.08	A
258	1356.14	5.72	B3	299	1630.17	7.64	B1
259	1356.16	2.72	B1	300	1631.09	6.85	B3
260	1356.37	40.18	A	301	2949.03	0.03	B3
261	1360.24	2.40	B1	302	2949.37	189.34	A
262	1360.84	3.02	B2	303	2949.82	3.39	B1
263	1366.80	0.35	B3	304	2949.96	7.31	B2
264	1367.22	13.11	A	305	2974.75	40.77	B2
265	1392.75	0.22	B2	306	2976.87	249.41	A
266	1394.14	1.36	B1	307	2977.68	13.09	B1
267	1394.68	31.22	A	308	2977.74	15.73	B3
268	1394.83	1.27	B3	309	2992.81	49.38	B1
269	1412.63	0.52	B1	310	2992.92	0.68	B2
270	1412.92	9.02	B2	311	2993.82	31.52	B3
271	1414.06	0.39	B3	312	2994.45	1.00	B2
272	1414.10	50.16	A	313	2994.95	164.59	A
273	1425.43	12.78	B2	314	2995.29	67.91	B3
274	1425.92	1.74	B1	315	2995.33	74.10	A
275	1428.97	3.31	A	316	2995.48	0.04	B1
276	1429.00	0.66	B3	317	3007.00	16.22	B2
277	1450.43	0.58	B3	318	3009.33	102.13	A
278	1450.65	4.34	A	319	3010.97	0.65	B3
279	1455.22	1.87	B2	320	3013.23	1.11	B2
280	1456.25	4.38	B1	321	3013.23	167.45	A

322	3013.37	1.53	B3
323	3013.58	7.20	B1
324	3032.01	8.27	B1
325	3043.48	182.75	A
326	3043.75	29.21	B2
327	3043.76	1.12	B3
328	3044.20	13.93	B1
329	3075.44	196.23	A
330	3075.90	2.79	B1
331	3084.09	0.01	B2
332	3086.96	65.03	B3
333	3126.44	62.66	A
334	3128.52	0.00	B2
335	3129.33	69.54	B1
336	3130.07	19.96	B3
337	3154.42	0.04	B2
338	3154.55	1.18	B1
339	3155.58	75.83	A
340	3155.83	22.38	B3
341	3266.48	30.24	B3
342	3266.54	96.03	A
343	3289.84	17.76	B2
344	3305.10	55.75	B1
345	3516.17	1.98	B2
346	3517.02	41.97	A
347	3517.13	0.20	B1
348	3517.96	32.32	B3
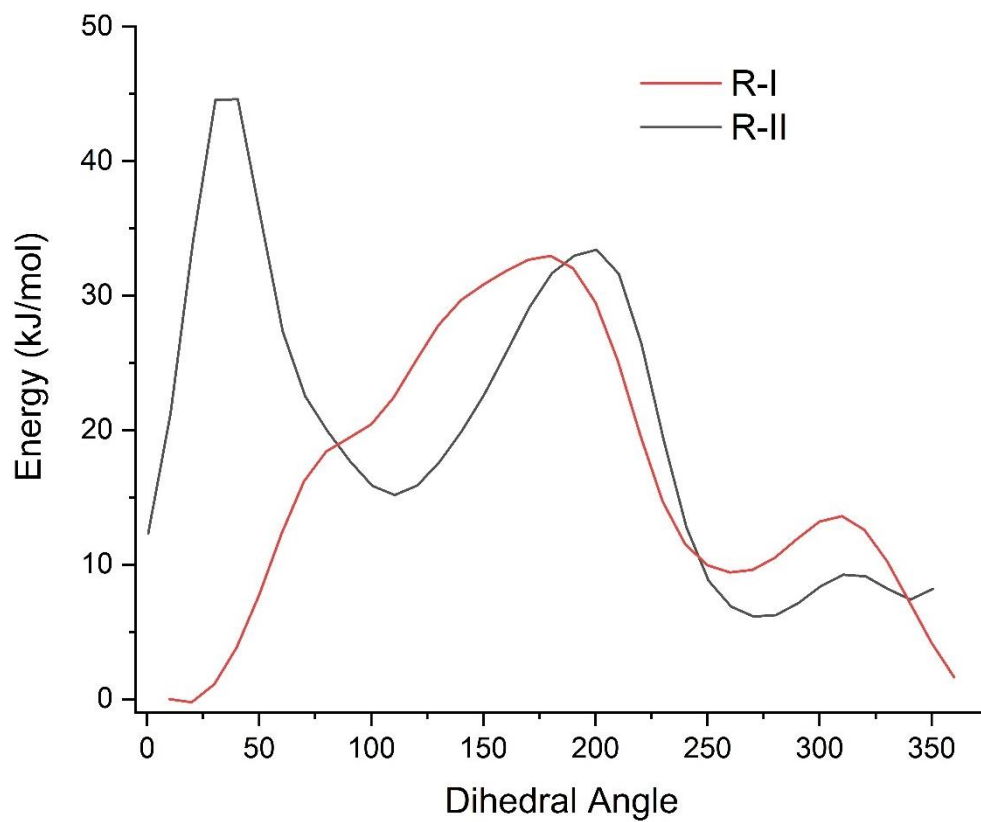
Figure E-6. Energy versus dihedral angle curves for R-I and R-II.

Table E-7. Coordinates for R-I final confirmation from Gaussian.

Atom Type	X	Y	Z
H	-0.121565	1.803718	0.371693
O	0.544470	2.525743	0.318756
C	1.698626	2.158644	1.047786
C	2.237840	0.763651	0.737356
C	2.169846	0.382765	-0.746266
C	1.795935	-1.116767	-0.727626
O	1.459198	-0.234116	1.452107
O	3.448174	0.596058	-1.357135
O	2.960756	-1.916004	-0.642667
H	1.538102	2.218613	2.141740
H	3.678071	-1.355967	-1.011350
H	1.170952	-1.412134	-1.589904
H	3.300993	0.880089	-2.274752
H	2.479603	2.891099	0.786883
H	1.205433	-2.240976	1.041915
H	1.388085	0.977403	-1.240351
H	3.282439	0.688199	1.086355
C	1.022349	-1.252232	0.592979
N	-0.435849	-1.159050	0.412518
C	-1.381287	-2.118949	0.569194
N	-2.579954	-1.626874	0.287853
C	-2.308230	-0.326752	-0.040346
C	-3.357305	0.670308	-0.425517
N	-4.608098	0.131164	-0.433043
H	-5.395693	0.725410	-0.661423
H	-1.149924	-3.132962	0.884419
N	-1.014519	-0.004524	0.021542
O	-3.091433	1.834413	-0.699834
H	-4.743528	-0.840263	-0.172483

Appendix F: Supporting Information for Chapter 9

Supporting Information Table of Contents

Supporting Information References

F-R1. Boles, M.; Girven, R., The Structures of Ampicillin: A Comparison of the Anhydrate and Trihydrate Forms. *Acta Crystallographica Section B: Structural Crystallography and Crystal Chemistry* **1976,** *32* (8), 2279-2284.

F-R2. Burley, J. C.; Streek, J.; Stephens, P. W., Ampicillin Trihydrate from Synchrotron Powder Diffraction Data. *Acta Crystallographica Section E: Structure Reports Online* **2006,** *62* (2), o797-o799.

F-R3. Boles, M.; Girven, R.; Gane, P., The Structure of Amoxycillin Trihydrate and a Comparison with the Structures of Ampicillin. *Acta Crystallographica Section B: Structural Crystallography and Crystal Chemistry* **1978,** *34* (2), 461-466.
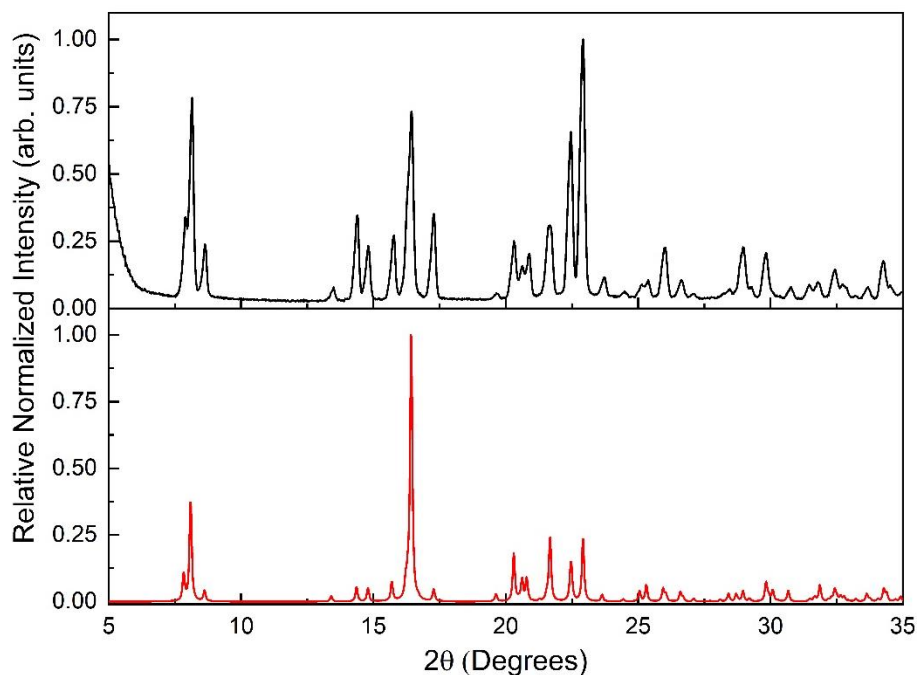
Figure F-1. The PXRD pattern of the ampicillin anhydrous sample (black) and the CSD data generated pattern[F-R1] (red).
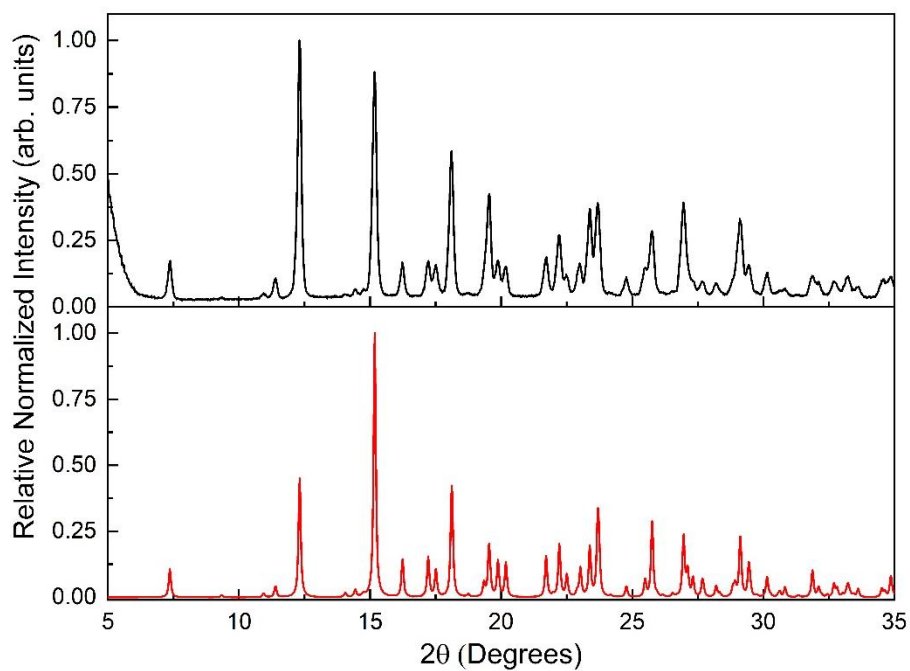
Figure F-2. The PXRD pattern of the ampicillin trihydrate sample (black) and the CSD data generated pattern[F-R2] (red).
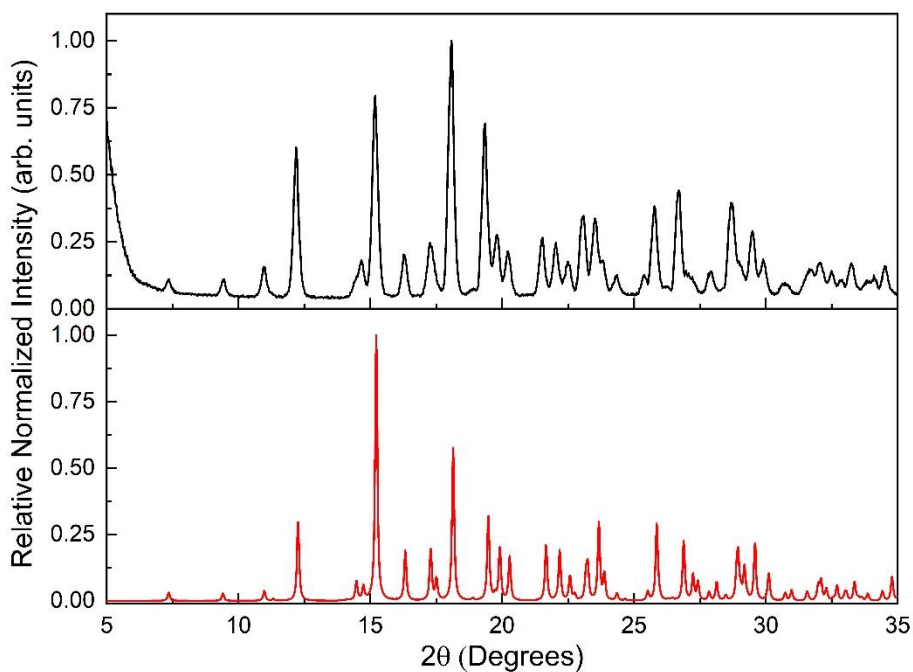

Figure F-3. The PXRD pattern of the amoxicillin trihydrate sample (black) and the CSD data generated pattern[F-R3] (red).

Margaret P. Davis

mdavis23@syr.edu • 716-597-8050
Syracuse, NY 13203

EDUCATION

Syracuse University, Syracuse, NY July 2022
Ph.D., Chemistry
Advisor: Dr. Timothy M. Korter
Dissertation: Evaluation of the Energetic Factors in Crystalline Pharmaceuticals using Solid-State Density Functional Theory and Low-Frequency Vibrational Spectroscopy

State University of New York at Geneseo, Geneseo, NY 2017
Bachelor of Science, Chemistry
Minors in Mathematics and Political Science

RESEARCH EXPERIENCE

Syracuse University, Syracuse, NY 2017 – Present
Ph.D. Candidate, Advisor: Dr. Timothy M. Korter
- Utilize CRYSTAL17, an *ab initio* solid-state density functional theory program (DFT), to simulate and analyze structure and vibrational spectra, and do energetic analyses on a variety of pharmaceutical crystals, including polymorphs and cocrystals, for the first time.
- Investigate low-frequency vibrations in pharmaceuticals using Terahertz time-domain spectroscopy and low-frequency Raman spectroscopy.
- Utilize single crystal X-ray diffraction and powder X-ray diffraction to confirm samples and identify structure and crystallinity for pharmaceutical samples as well as inorganic crystals for collaborators.

State University of New York at Geneseo, Geneseo, NY 2016 – 2017
Undergraduate Research, Advisor: Dr. Jeffrey J. Peterson
- Developed the first successful aqueous two-phase separation techniques at SUNY Geneseo to separate single-walled carbon nanotubes based on the unique electronic and structural properties of the different tube chiralities.
- Investigate the separate single-walled carbon nanotubes with absorption and emission spectroscopy and data analysis using ImageJ and Sigma Plot.

PUBLICATIONS

Mohara, M.; **Davis, M. P.**; Korter, T. M.; Shimura, K.; Ono, T.; Aiko, K., Study on Hydration and Dehydration of Ezetimibe by Terahertz Spectroscopy with Humidity-Controlled Measurements and Theoretical Analysis. *The Journal of Physical Chemistry A* **2022**.

Davis, M. P.; Korter, T. M., Evaluating Hydrogen Bonding in Organic Cocrystals Using Low-Frequency Raman Vibrational Spectroscopy and Quantum Mechanical Simulations. *Crystal Growth & Design* **2022**, *22* (3), 1922-1932.

Davis, M. P.; Mohara, M.; Shimura, K.; Korter, T. M., Simulation and Assignment of the Terahertz Vibrational Spectra of Enalapril Maleate Cocrystal Polymorphs. *The Journal of Physical Chemistry A* **2020,** *124* (47), 9793-9800.

Azzarelli, N.; Ponnala, S.; Aguirre, A.; Dampf, S. J.; **Davis, M. P.**; Ruggiero, M.; Lopez Diaz, V.; Babich, J.; Coogan, M.; Korter, T.; Doyle, R.P.; Zubieta, J. Defining the origins of multiple emission/excitation in Rhenium-bisthiazole complexes. *Inorg. Chim. Acta* **2019**, *489*, 301-309.

MANUSCRIPTS IN PREPARATION
Li, Q.; Kölbel, J.; **Davis, M. P.**; Korter, T. M.; Bond, A. D.; Threlfall, T.; Zeitler, J. A. In-Situ Observation of the Structure of Crystallising Magnesium Sulfate Heptahydrate Solutions with Terahertz Transmission Spectroscopy. **2022**. (Accepted)

Davis, M. P.; Korter, T.M. Low-Frequency Vibrational Spectroscopy and Quantum Mechanical Simulations of the Crystalline Polymorphs of the Antiviral Ribavirin. **2022**. (Manuscript in Preparation)

PRESENTATIONS
Davis, M. P.; Korter, T. M. Low-Frequency Vibrational Comparison of Amoxicillin and Ampicillin. The International Society of Infrared, Millimeter, and Terahertz Waves, Chengdu, Sichuan, China. (Virtual) September 2021.

Davis, M. P.; Korter, T. M. Low-Frequency Vibrational Spectroscopy and Quantum Mechanical Simulations of the Crystalline Polymorphs of the Antiviral Ribavirin. American Chemical Society Spring 2021 National Meeting & Exposition, San Antonio, TX. (Virtual) April 2021.

Davis, M. P.; Korter, T. M. Investigation Of 5-Fluorouracil Cocrystals By Low-Frequency Vibrational Spectroscopy And Solid-State Density Functional Theory. The International Society of Infrared, Millimeter, and Terahertz Waves, Buffalo, NY. (Virtual) November 2020.

Davis, M. P.; Mohara, M.; Shimura, K.; Korter, T. M. Simulation and Assignment of the Terahertz Spectra of Enalapril Maleate Cocrystal Polymorphs. The International Society of Infrared, Millimeter, and Terahertz Waves, Paris, France. September 2019.

Davis, M. P.; Korter, T. M. Low-Frequency Vibrational Spectroscopy and Quantum Mechanical Simulations of Cocrystallized Organic Molecules. Collaborative Computational Project for Computer Simulation of Condensed Phase Materials (CCP5) Summer School, Durham, UK. July 2019.

Davis, M. P.; Korter, T. M. Analysis of the Intermolecular Forces in Organic Cocrystals. 8th International Conference on Optical Terahertz Science and Technology 2019, Santa Fe, NM. March 2019. (Poster)

Davis, M. P.; Korter, T. M. Low-Frequency Vibrations of Tartaric Acid Cocrystals. *Ab initio* Modeling in Solid State Chemistry Workshop with CRYSTAL, Turin, Italy. September 2018. (Poster)

Davis, M. P.; Korter, T. M. Low-Frequency Vibrations of Tartaric Acid Cocrystals. 256th American Chemical Society National Meeting & Exposition, Boston, MA. August 2018. (Poster)

Davis, M. P.; Korter, T. M. Low-frequency vibrations of tartaric acid cocrystals with urea and glycine. CP2K Summer School, Warrington, UK. June 2018. (Poster)

SKILLS

Computational Skills:
- CRYSTAL17
- Gaussian and GaussView
- Vienna Ab initio Simulation Package (VASP)
- CP2K Open Source Molecular Dynamics
- Cambridge Structural Database (CSD) and Mercury
- Jmol

Laboratory Skills:
- Terahertz Time-Domain Spectroscopy
- Raman Spectroscopy
- Single Crystal and Powder X-Ray Diffraction
- Crystallization of a Variety of Polymorphs and Cocrystals

TEACHING EXPERIENCE

Department of Chemistry, Syracuse University, Syracuse, NY   Spring 2021 & 2022
Physical Chemistry Laboratory Teaching Assistant
- Assisted in teaching physical chemistry laboratory by leading multiple weekly laboratory sections including leading and developing experiments, grading of laboratory reports, and office hours.

Department of Chemistry, Syracuse University, Syracuse, NY   Summer 2020 & 2021
General Chemistry I & II Lecture Teaching Assistant
- Assisted in developing online instructions for general chemistry and holding office hours.

Department of Chemistry, Syracuse University, Syracuse, NY   Spring 2019
General Chemistry I Lecture Teaching Assistant
- Assisted in teaching general chemistry recitations by leading multiple weekly recitation sections of 20-25 students, holding office hours, and grading exams.

Department of Chemistry, Syracuse University, Syracuse, NY   Fall 2018 & 2019
Physical-Analytical Chemistry Laboratory Teaching Assistant
- Assisted in teaching physical chemistry laboratory by leading multiple weekly laboratory sections of 5-10 students that included laboratory lectures, experiments, and grading of written laboratory reports.

AWARDS AND FELLOWSHIPS

Finalist for the Presidential Management Fellows Program Class of 2022

CCP5 Runner-Up Student Talk Prize, Durham, UK. July 2019.

8th International Conference on Optical Terahertz Science and Technology Best Poster Award, Santa Fe, NM. March 2019.

Syracuse University Graduate Assistance in Areas of National Need Fellowship, 2017 – 2018.

Student Association & Geneseo Foundation Undergraduate Research Grant, 2016.

WORKSHOPS AND TRAININGS

1st online VASP workshop, Virtual. November 2021.

Collaborative Computational Project for Computer Simulation of Condensed Phase Materials (CCP5) Summer School, Durham, UK. July 2019.

Advanced Chemical Crystallography Applications Training, Madison, Wisconsin. October 29-30, 2018.

Ab initio Modeling in Solid State Chemistry Workshop with CRYSTAL, Turin, Italy. September 2018.

CP2K Summer School, Warrington, UK. June 2018.

Radiation Training, Syracuse University, Syracuse, NY. Spring 2018.